



Universiteit
Leiden
The Netherlands

Modeling of the cardiac sympathetic nervous system and the contribution of epicardium-derived cells

Ge, Y.

Citation

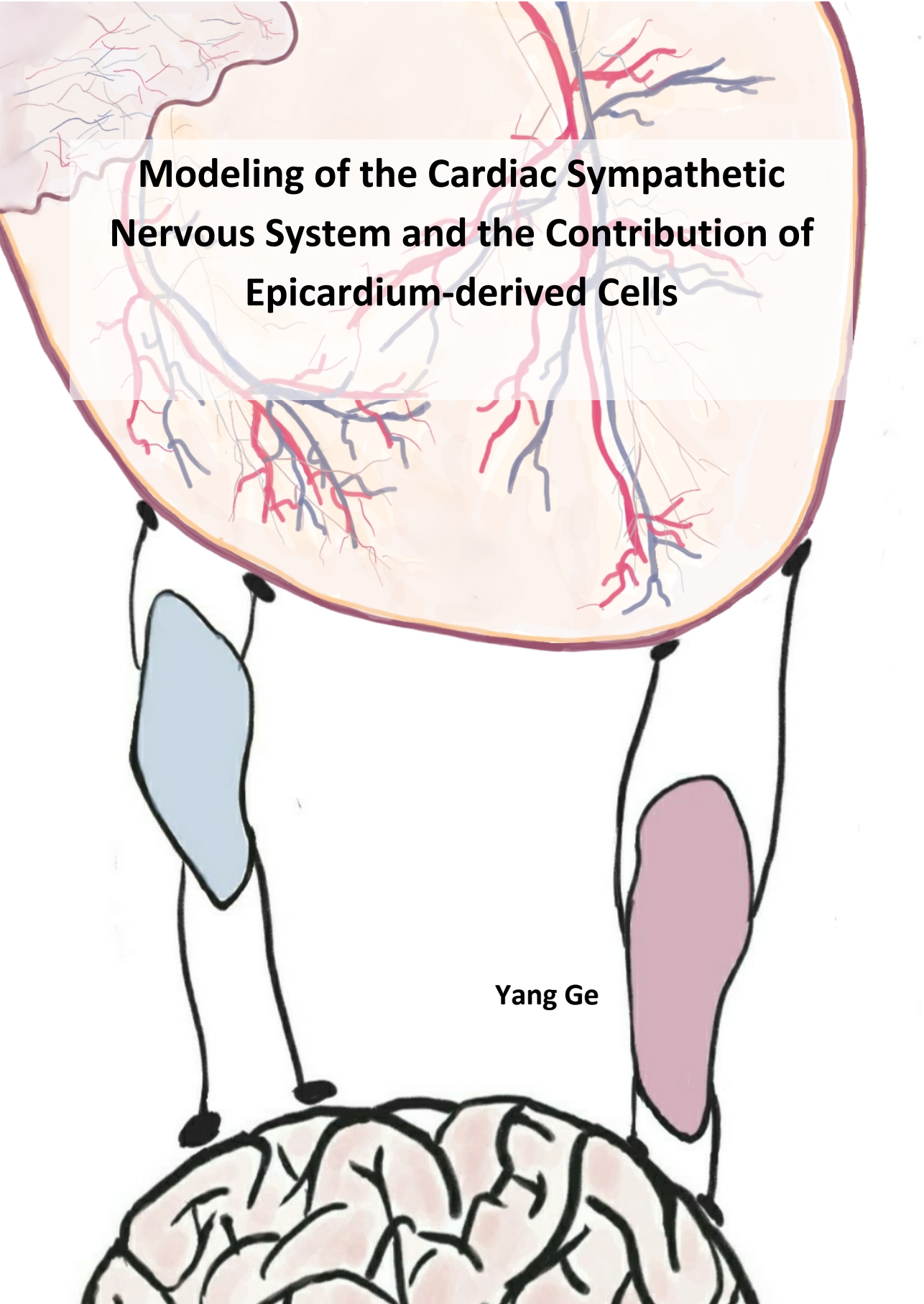
Ge, Y. (2021, December 15). *Modeling of the cardiac sympathetic nervous system and the contribution of epicardium-derived cells*. Retrieved from <https://hdl.handle.net/1887/3247258>

Version: Publisher's Version

License: [Licence agreement concerning inclusion of doctoral thesis in the Institutional Repository of the University of Leiden](#)

Downloaded from: <https://hdl.handle.net/1887/3247258>

Note: To cite this publication please use the final published version (if applicable).



The diagram illustrates the cardiac sympathetic nervous system. At the top, a cross-section of the heart is shown with a network of red and blue vessels. Below the heart, two elongated structures, a light blue one on the left and a light purple one on the right, represent the adrenal glands. At the bottom, a stylized brain is depicted with black lines representing neural pathways. These pathways connect the brain to the adrenal glands and then to the heart, indicating the neural control of the cardiac sympathetic system.

Modeling of the Cardiac Sympathetic Nervous System and the Contribution of Epicardium-derived Cells

Yang Ge

Modeling of the Cardiac Sympathetic Nervous System and the Contribution of Epicardium-derived Cells

Yang Ge

Modeling of the cardiac sympathetic nervous system and the contribution of epicardium-derived cells

© Yang Ge, Leiden, the Netherlands, 2021.

All rights reserved. No part of this book may be reproduced or transmitted, in any form or by any means, without written permission of the author

ISBN: 978-94-93270-31-2

Cover & chapter divider: Ganglia (parasympathetic and sympathetic ganglia) are important mediators between the central nervous system and the heart. Parasympathetic ganglia lie close to the heart. In contrast, sympathetic ganglia are usually located close to the spinal cord but more distant from the heart. These characteristics of parasympathetic and sympathetic ganglia are depicted as short (or long) legs and long (or short) arms of parasympathetic (or sympathetic) ganglia.

Layout, design and art work: Yang Ge

Printing: AIO proefschrift all in one | <https://proefschrift-aio.nl/>

The work presented in this thesis was carried out at the Department of Anatomy & Embryology and the Department of Cardiology of the Leiden University Medical Center

Modeling of the Cardiac Sympathetic Nervous System and the Contribution of Epicardium-derived Cells

Proefschrift

ter verkrijging van
de graad van doctor aan de Universiteit Leiden,
op gezag van rector magnificus prof.dr.ir. H. Bijl,
volgens besluit van het college voor promoties
te verdedigen op

woensdag 15 december 2021
klokke 10:00 uur

door

Yang Ge

geboren te Gansu, China in 1990

Promotores:

Prof. Dr. M.C. de Ruiter

Prof. Dr. M.J. Schalijs

Co-promotor:

Dr. M.R.M. Jongbloed

Leden promotiecommissie:

Prof. Dr. M.J.T.H. Goumans

Prof. Dr. D. Salvatori (Universiteit Utrecht)

Prof. Dr. R.L.A.W. Bleys (UMC Utrecht)

Dr. J.M. van Gils

To everyone who has offered help to make this thesis come true.

To my family and friends who have supported me spiritually.

Contents

Chapter 1

General introduction and thesis outline

Part I. Cardiac sympathetic innervation and EPDCs

Chapter 2

Human epicardium-derived cells reinforce cardiac sympathetic innervation

Chapter 3

The sex of epicardium-derived cells influences the outgrowth of cardiac sympathetic nerves in vitro

Part II. Breaking the limits of EPDCs

Chapter 4

Generation, characterization and application of inducible proliferative adult human epicardium-derived cells

Part III. Cardiac sympathetic nervous system remodeling after cardiac damage

Chapter 5

Acute myocardial infarction induces neuronal remodeling in murine superior cervical ganglia

Chapter 6

Low-input nucleus isolation and multiplexing with barcoded antibodies of mouse sympathetic ganglia for single-nucleus RNA sequencing

Chapter 7

Single-nucleus RNA sequencing reveals the cellular composition and molecular signature of murine superior cervical ganglia

Chapter 8

Systematic review and general discussion: The relevance of the superior cervical ganglion for cardiac autonomic innervation in health and disease: morphological considerations

Summary

Samenvatting

List of publications

Acknowledgements

Curriculum Vitae



1

GENERAL INTRODUCTION AND THESIS OUTLINE

1

The Development of a Functional Heart

A normal developed heart is a complex self-excitation organ that is composed of four chambers (two atria and two ventricles) [1]. The wall of the four-chamber heart consists of three layers: the endocardium, the myocardium and the epicardium [2]. The cardiac conduction system¹, consisting of myocardium cells with a distinct molecular signature from the working myocardium, generates and coordinates the electric signal by which mechanical activation by the sequential contraction of first the atria followed by the ventricles, is established [3, 4]. A functional heart is able to adapt to environmental changes (e.g. level of oxygen or stress) and body conditions (e.g. resting condition versus exercise) via adjusting the contraction rate and force. These cardiac adaptations are achieved by regulation of adrenaline release from the adrenal gland as well as by a controlled coordination of the parasympathetic and sympathetic cardiac activation, referred to as cardiac autonomic nervous system regulation [5, 6].

Development of the Heart and the Essential Role of Epicardium. During development, cardiogenesis begins with the formation of the cardiac crescent by E7.5 in mice and day 15 in human embryos [7, 8]. At this early stage two cardiac heart fields fuse in the ventral midline and give rise to the cardiac crescent, which will remodel into a single tube structure [8]. This primitive cardiac tube initially consists of two layers: the inner endocardium, which is a sheet of specialized epithelial cells that is in contact with the first blood cells, and the outer myocardium, which is a layer of cardiac muscle cells that starts to beat at day 22 in human embryos. Soon after the heart tube formation, around E8 in mice and day 23 in human embryos, the tube starts to elongate loop with an active blood circulation at E10 in mice and day 28 in human [7-10]. Subsequently, after cardiac looping and septation, a four-chamber heart with recognizable atrial and ventricular compartments is formed [11, 12].

The epicardium, the third layer, is formed after the cardiac looping. The epicardium originates from the so-called proepicardial organ (PEO) (**Figure 1**), which is an cauliflower-like cluster of extra-cardiac cells situated at the venous pole of the heart. The PEO is an outgrowth of the coelomic mesothelium at the ventro-caudal base of the developing heart around E8.5 in the mouse, and is composed of heterogeneous cell populations [13]. A subgroup of PEO cells, expressing Wilms' tumor 1 (WT1) transcription factor, T-box transcription factor 18 (Tbx18) and the basic helix-loop-helix Transcription Factor 21 (Tcf21), migrates along the inflow tract,

¹ Sinoatrial Node (SAN), Atrioventricular Node (AVN), Atrioventricular Bundle (AVB), left and right Bundle Branches (BBs), Peripheral Ventricular Conduction System (PVCS).

proliferates and gradually spreads to cover the heart to form an epithelial outer layer (**Figure 1**).

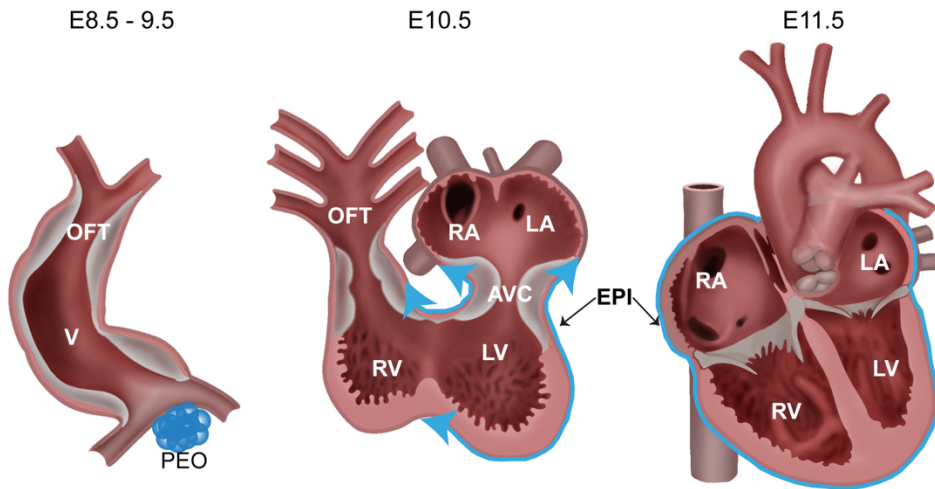


Figure 1. The proepicardial organ (PEO) and the development of epicardium. The expression of WT1 is indicated in blue. OFT, outflow tract; V, ventricle; PEO, proepicardium; RA, right atrium; RV, right ventricle; AVC, atrioventricular cushion; EPI, epicardium; LA, left atrium; LV, left ventricle.

Although initially consisting of only one cell layer, the epicardium plays an essential and critical role in cardiac development. Once the epicardium envelops the entire heart, part of the epicardial cells lose cell-cell contact, initiating the process of epithelial-to-mesenchymal transition (EMT), where after they are referred to as epicardium-derived cells (EPDCs) [14, 15]. EPDCs are deposited into the subepicardial space and subsequently migrate into the myocardium where they differentiate into multiple cardiac cells types, including interstitial fibroblasts, adventitial fibroblasts and smooth muscle cells of the coronary vessels [16-18] (**Figure 2**). Whether EPDC also differentiation into coronary endothelial cells and cardiomyocytes has been largely debated. Moreover, the role of the epicardium is not limited to a structural contribution to the cardiac lineages. EPDCs also possess paracrine functions critical for myocardial growth, as well as for coronary vessel [19-21]. As the heart matures, the epicardium becomes quiescent [17]. Inhibition of epicardium formation during cardiogenesis by mechanically removing the PEO, by obstructing the outgrowth of the PEO in the chicken embryo or by genetic knockdown methods in mice embryos results in (amongst others) a thin, noncompact ventricular myocardium and incomplete formation of coronary vasculature [22-24], which emphasizes the essential role of epicardium and EPDCs in heart development.

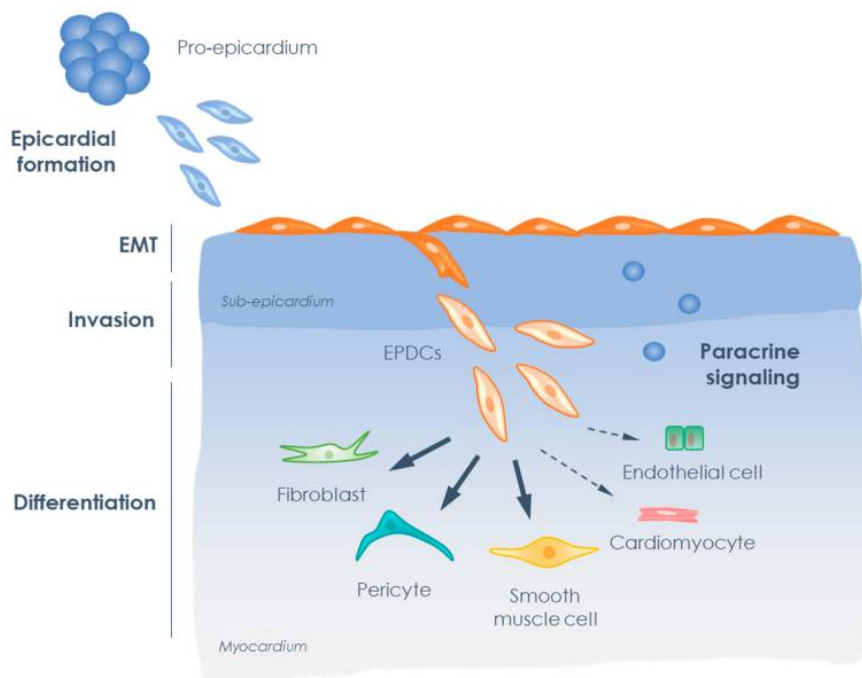


Figure 2. Schematic overview of epicardial development and differentiation during development. The figure is from Dronkers et al. Biomolecules. 2020

Cardiac Autonomic Nervous System and Its Development. A fully developed contractile heart is controlled by the autonomic nervous system (parasympathetic and sympathetic) to adapt to the body's demand for oxygenated blood under different conditions. The autonomic nervous system regulates the heart rate, blood pressure, respiration rate, body temperature, transpiration, as well as visceral activation to maintain homeostasis [25-27]. The cardiac autonomic nervous system is centrally coordinated by the thalamus at the top of the brain stem and the medulla oblongata within the brain stem. The peripheral autonomic system can be divided into a sympathetic and parasympathetic part. The sympathetic and parasympathetic system contain efferent (motor neurons) elements of the visceral peripheral nervous system (**Figure 3**).

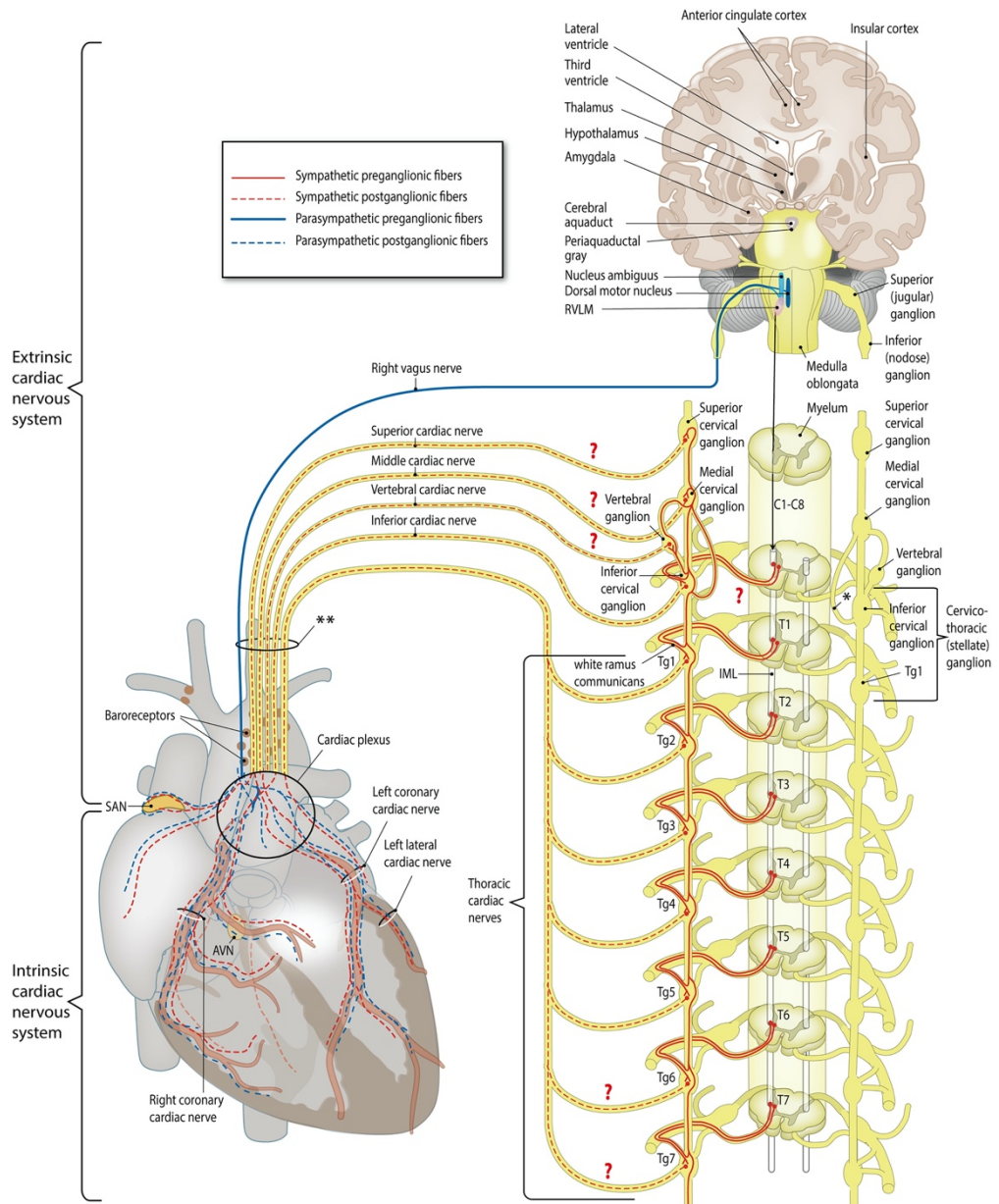


Figure 3. Schematic drawing of the cardiac autonomic nervous system. The figure is from Wink et al. Auton Neurosci. 2020.

The efferent portion of cardiac sympathetic nervous system includes short preganglionic nerves, cardiac sympathetic ganglia (cervical ganglia, stellate ganglia as well as upper thoracic ganglia of the sympathetic chain) and long postganglionic sympathetic nerves [25, 28] (**Figure 3**). Acetylcholine is used as pre-ganglionic sympathetic neurotransmitter, while norepinephrine (NE) is the post-ganglionic sympathetic neurotransmitter of the sympathetic nervous system. Activation of post-ganglionic nerves results in the release of NE from sympathetic nerve terminals to the synapse with cardiomyocytes. NE binds to the post-synaptic adrenergic beta-1 receptor in the cardiomyocytes of the working myocardium and conduction system, resulting in an increased heart rate, increased contractility as well as an increased AVN conduction velocity [5]. Tyrosine hydroxylase (TH) catalyzes the conversion of tyrosine to L-3,4-dihydroxyphenylalanine (L-DOPA), which can, through a series of downstream enzymatic reactions, be processed into dopamine and be further altered into NE [29-32]. Therefore, in the peripheral nervous system, TH can be used to identify sympathetic neurons.

In contrast, the efferent part of the cardiac parasympathetic nervous system is composed of long preganglionic nerves from the central nervous system, cardiac ganglia that are situated on the surfaced of the heart (centers where the majority of cardiac parasympathetic neurons interconnect), and short postganglionic parasympathetic nerve fibers [25, 28] (**Figure 3**). Acetylcholine is the neurotransmitter for both pre- and postganglionic parasympathetic nerves. Acetylcholine inhibits the contraction of cardiomyocytes by activating muscarinic receptors (M2) in cardiomyocytes [5]. The synthesis of acetylcholine in parasympathetic neurons is achieved by choline acetyltransferase (ChAT) that catalyzes the synthesis of acetylcholine from choline and acetyl-CoA [5]. Therefore, ChAT is usually used as a marker for postganglionic parasympathetic neurons in the peripheral nervous system.

The development of peripheral cardiac autonomic nervous system is a relatively late phenomenon. Sympathetic ganglia are formed as a result of trunk neural crest cells that migrate, proliferate and differentiate into mature sympathetic neurons [33, 34]. Parasympathetic neurons in cardiac ganglia, however, are derived from cardiac neural crest cells, which also participate in the septation of the outflow tract of the heart [34-37].

Cardiac innervation patterning is a very complex process, which is directed and modulated by a myriad of factors/signaling pathways, including chemo-attractants, like various neurotrophic factors (for instance, ET-1/NGF and NT-3 are critical for sympathetic, whereas GDNF regulates parasympathetic innervation²) [38-41] and neural chemorepellents (especially Sema3a³,

² NGF, nerve growth factor; ET-1, endothelin-1; GDNF, glial cell line–derived neurotrophic factor.

³ Sema3a, Semaphorin 3A.

strongly expressed in the developing heart at E12 in mouse and reduce gradually with development) [42, 43]. Crosstalk and balance between chemo-attractants and chemorepellents guide the proper innervation patterning in the heart.

Dynamic Changes in a Diseased Heart

Cardiovascular diseases (CVD) are the number one cause of death in the developed countries. An estimated 17.9 million people died from CVD in 2016, representing 31% of all global deaths. Of these deaths, 85% are due to heart attack and stroke (WHO 2017). Diminished flow of oxygenated blood to cardiac muscle, such as occurs by occlusion of the coronary arteries, is known as ischemic heart disease (IHD). IHD is the most common form of CVD. According to data published by the WHO in 2020, the number of deaths from IHD increased by more than 2 million since 2000, to nearly 9 million in 2019. IHD can eventually lead to a myocardial infarction (MI) which can further deteriorate outcome, including complications such as sudden cardiac death (SCD), ventricular tachycardia (VT) and heart failure.

Epicardium and Epicardium-derived Cells (EPDCs) in a Diseased Heart. MI induces damage and loss of cardiac tissue, caused especially by the death of cardiomyocytes. The loss of cardiac tissue may lead to loss of cardiac function which in turn can result in inadequate blood supply to the whole body by affecting cardiac output. After cardiac damage, a cascade of events occurs aimed at restoring of cardiac function in the acute phase of MI. One of these events is the (re)activation of epicardial cells.

In the adult mammalian heart the epicardium is, in contrast to the developmental state, a quiescent and single-cell layered tissue with squamous morphology. However, the epicardium is reactivated rapidly after cardiac damage and recapitulates its embryonic epicardial characteristics, including a cuboid morphology [16, 44]. The activation of epicardium begins within a day after MI, reaches its peak on the fifth day and gradually diminishes after 14 days [45-47]. Typical characteristics of the activated epicardium include: a) the transition of the epicardium from a single-cell layer into a multilayered tissue with cellular expansion and morphology change into a cuboidal shape, as indicated above [44, 47]; b) reactivation of expression of early embryonic epicardial genes, a.o. WT1, Tbx18, TCF21 and Raldh2 (Aldehyde dehydrogenase 1 family, member A2) [48-50].

Activated epicardium (epicardial cells) in the diseased heart thus recapitulates an embryonic phenotype and will undergo EMT, after which the cells are referred to as EPDCs [48, 51-54]. EPDCs can migrate into the subepicardial space and myocardium, where they can differentiate into coronary smooth muscle cells and cardiac fibroblasts in an effort of the heart for self-repair [17, 44, 47, 55]. The reactivated epicardium is also considered to serve as a source of

paracrine signaling to support repair, for example to reduce post-MI infarction size and improve heart function [47, 56, 57]. Remarkably, reactivated epicardium/EPDCs can modulate cellular and paracrine inflammatory process after cardiac damage, which is involved in the recruitment of cardiac macrophages and immunosuppressive regulatory T-cells [58-61].

Cardiac Autonomic Nervous System Changes in a Diseased Heart. An increasing amount of evidence indicates a change of cardiac innervation in cardiac disease states, not only after MI but also in a broad range of other cardiovascular disease, like hypertension, heart failure and pressure overload-induced cardiac hypertrophy [62-64]. These cardiac autonomic nervous changes include alterations in neurochemistry and activity (*functional*) as well as in innervation patterns (*structural*). Alterations of cardiac innervation can disturb the balance between sympathetic versus parasympathetic neuronal activity and may predispose patients lethal arrhythmias [65].

In contrast to the atria, cardiac ventricles are mainly innervated by sympathetic (efferent) nerves and only sparsely innervated by parasympathetic (efferent) nerves. In case of MI, cardiac tissue in the infarction and peri-infarction area will initially undergo functional and structural denervation, caused by death/degeneration of sympathetic fibers and by inflammatory cytokines (for example from the gp130 family) [66, 67]. Inflammatory cytokines can cause local suppression of TH, norepinephrine transporters as well as norepinephrine and can increase TH degradation [68-70]. After the initial denervation, both a functional and structural cardiac reinnervation occur which has been well characterized in animals and humans [71-74]. However, an overshoot of regeneration of sympathetic nerves can also occur, which is designated sympathetic hyperinnervation, defined as an increase of sympathetic fibers in the heart, and has been associated with ventricular arrhythmias and sudden cardiac death [75, 76]. Co-existence of sympathetic denervation and hyperinnervation can also trigger serious ventricular arrhythmias [77, 78]. The exact mechanism of the occurrence of hyperinnervation and its relation to cardiac arrhythmias is not clear yet. Neurotrophic factors released after MI likely play a key role in sympathetic re-/hyperinnervation, particularly NGF, which can be synthesized and released by cardiomyocytes, Schwann cells and inflammatory cells [40, 79-81]. Aside from the alterations of cardiac sympathetic innervation with regard to function and structural patterning, remodeling and transdifferentiation of neuronal cells has been reported [82-84]. These findings expand present mechanistic understanding of the cardiac nervous system in the pathological heart, and further investigations in this field could promisingly yield novel therapeutic targets for heart disease. In this thesis, we aim to further explore this by studying the remodeling of the autonomic nervous system after cardiac damage. We especially focus on the role of EPDCs in cardiac autonomic innervation.

Scope and Outline of the Thesis

Chapter 1 provides the context of this thesis with background information regarding the development of the heart, the critical contribution of the epicardium and its derived cells in cardiac development and the development of the cardiac autonomic nervous system. In addition, the cascade of events after cardiac damage, such as MI is discussed, including the occurrence of cardiac sympathetic hyperinnervation and its clinical sequelae.

Chapter 2 describes how human activated EPDCs can stimulate cardiac sympathetic innervation. We show that EPDCs significantly enhanced sympathetic neurite sprouting directionally towards damaged myocardium *in vitro*.

Chapter 3 demonstrates that sympathetic neurite outgrowth *in vitro*, is influenced by the sex of the donor of EPDCs. The data underlines the potential relevance of sex differences in post-MI cardiac hyperinnervation.

Chapter 4 describes the establishment of a polyclonal line of inducible proliferative human EPDCs (iEPDCs) cells, which was achieved by doxycycline-controlled expression of simian virus 40 large T antigen (LT) with a repressor-based lentiviral Tet-On system. As primary human EPDCs have very limited proliferation ability *in vitro*, iEPDCs are highly useful for *in-vitro* studies that take advantage of EPDCs in the experimental design.

Chapter 5 addresses the neuronal remodeling of murine superior cervical ganglion (SCG) and the proximate carotid body in sequential time point after myocardial infarction. The results demonstrate an overt neuronal remodeling that occurs in the SCG as well as in the carotid body, suggesting an interaction of these 2 structures after MI, that might contribute to pathological cardiac hyperinnervation.

Chapter 6 provides a detailed protocol of low-input nucleus isolation and multiplexing with barcoded antibodies used for single nucleus RNA sequencing (snRNA-seq) of murine SCG. This method enables long-term sample preservation maintaining an adequate RNA quality when samples cannot be fully collected within a short period of time. Moreover, hashtag barcoding antibody-oligos (HTOs) staining enables demultiplexing and the trace-back of distinct ganglionic samples during the subsequent single nucleus analysis.

In **Chapter 7** We aimed to reveal the cellular composition and molecular signature of healthy murine superior cervical ganglia (SCG) by using snRNA-seq. The analysis is focused on the cellular heterogeneity of neurons and satellite glial cells. Analysis of sex and laterality differences of SCG is also included in this chapter. The data provides a useful resource for further disease-oriented studies.

Chapter 8 provides a general discussion on the relevance of the SCG in health as well as in cardiac disease. The discussion focuses on morphological evidence of a contribution of the SCG in cardiac innervation in different animal species including human.

REFERENCES

- [1] A. Moorman, S. Webb, N.A. Brown, W. Lamers, R.H. Anderson, Development of the heart: (1) formation of the cardiac chambers and arterial trunks, *Heart (British Cardiac Society)* 89(7) (2003) 806-14.
- [2] A. Arackal, K. Alsayouri, *Histology, Heart, StatPearls*, Treasure Island (FL), 2020.
- [3] V.M. Christoffels, A.F.M. Moorman, Development of the Cardiac Conduction System Why Are Some Regions of the Heart More Arrhythmogenic Than Others?, *Circ-Arrhythmia Elec* 2(2) (2009) 195-207.
- [4] R.H. Anderson, J. Yanni, M.R. Boyett, N.J. Chandler, H. Dobrzynski, The anatomy of the cardiac conduction system, *Clinical anatomy (New York, N.Y.)* 22(1) (2009) 99-113.
- [5] R. Gordan, J.K. Gwathmey, L.H. Xie, Autonomic and endocrine control of cardiovascular function, *World journal of cardiology* 7(4) (2015) 204-14.
- [6] H.K. Jamali, F. Waqar, M.C. Gerson, Cardiac autonomic innervation, *Journal of nuclear cardiology : official publication of the American Society of Nuclear Cardiology* 24(5) (2017) 1558-1570.
- [7] S.D. Vincent, M.E. Buckingham, How to make a heart: the origin and regulation of cardiac progenitor cells, *Current topics in developmental biology* 90 (2010) 1-41.
- [8] L. Wolpert, *Principles of development*, 2015.
- [9] G.C.B.S.B.P.R.F.-W.P.H.L.W.J. Schoenwolf, *Larsen's human embryology*, (2015).
- [10] K.E. McGrath, A.D. Koniski, J. Malik, J. Palis, Circulation is established in a stepwise pattern in the mammalian embryo, *Blood* 101(5) (2003) 1669-1675.
- [11] A.C. Gittenberger-de Groot, M.M. Bartelings, M.C. Deruiter, R.E. Poelmann, Basics of Cardiac Development for the Understanding of Congenital Heart Malformations, *Pediatric Research* 57(2) (2005) 169-176.
- [12] M.F.J. Buijtendijk, P. Barnett, M.J.B. van den Hoff, Development of the human heart, *American journal of medical genetics. Part C, Seminars in medical genetics* 184(1) (2020) 7-22.
- [13] T.C. Katz, M.K. Singh, K. Degenhardt, J. Rivera-Feliciano, R.L. Johnson, J.A. Epstein, et al., Distinct compartments of the proepicardial organ give rise to coronary vascular endothelial cells, *Developmental cell* 22(3) (2012) 639-50.
- [14] A. Wessels, J.M. Pérez-Pomares, The epicardium and epicardially derived cells (EPDCs) as cardiac stem cells, *The anatomical record. Part A, Discoveries in molecular, cellular, and evolutionary biology* 276(1) (2004) 43-57.
- [15] A.C. Gittenberger-de Groot, M.P. Vrancken Peeters, M.M. Mentink, R.G. Gourdie, R.E. Poelmann, Epicardium-derived cells contribute a novel population to the myocardial wall and the atrioventricular cushions, *Circulation research* 82(10) (1998) 1043-52.
- [16] A.M. Smits, E. Dronkers, M.-J. Goumans, The epicardium as a source of multipotent adult cardiac progenitor cells: Their origin, role and fate, *Pharmacological Research* 127 (2018) 129-140.
- [17] P. Quijada, M.A. Trembley, E.M. Small, The Role of the Epicardium During Heart Development and Repair, 126(3) (2020) 377-394.
- [18] R. Carmona, J.A. Guadix, E. Cano, A. Ruiz-Villalba, V. Portillo-Sánchez, J.M. Pérez-Pomares, et al., The embryonic epicardium: an essential element of cardiac development, *J Cell Mol Med* 14(8) (2010) 2066-2072.
- [19] T. Chen, T.C. Chang, J.O. Kang, B. Choudhary, T. Makita, C.M. Tran, et al., Epicardial induction of fetal cardiomyocyte proliferation via a retinoic acid-inducible trophic factor, *Developmental biology* 250(1) (2002) 198-207.
- [20] I. Stuckmann, S. Evans, A.B. Lassar, Erythropoietin and retinoic acid, secreted from the epicardium, are required for cardiac myocyte proliferation, *Developmental biology* 255(2) (2003) 334-49.
- [21] H.E. Olivey, E.C. Svensson, Epicardial–Myocardial Signaling Directing Coronary Vasculogenesis, 106(5) (2010) 818-832.

- [22] A.C. Gittenberger-de Groot, M.P. Vrancken Peeters, M. Bergwerff, M.M. Mentink, R.E. Poelmann, Epicardial outgrowth inhibition leads to compensatory mesothelial outflow tract collar and abnormal cardiac septation and coronary formation, *Circulation research* 87(11) (2000) 969-71.
- [23] I. Eralp, H. Lie-Venema, M.C. DeRuiter, N.M. van den Akker, A.J. Bogers, M.M. Mentink, et al., Coronary artery and orifice development is associated with proper timing of epicardial outgrowth and correlated Fas-ligand-associated apoptosis patterns, *Circulation research* 96(5) (2005) 526-34.
- [24] H. Lie-Venema, A.C. Gittenberger-de Groot, L.J. van Empel, M.J. Boot, H. Kerkdijk, E. de Kant, et al., Ets-1 and Ets-2 transcription factors are essential for normal coronary and myocardial development in chicken embryos, *Circulation research* 92(7) (2003) 749-56.
- [25] J.A. Waxenbaum, V. Reddy, M. Varacallo, *Anatomy, Autonomic Nervous System*, StatPearls, Treasure Island (FL), 2020.
- [26] W. Boron, E.J.G.S. Boulpaep, *Medical Physiology: a cellular and molecular approach*. 2003, (2005).
- [27] D.P. Zipes, P. Libby, R.O. Bonow, D.L. Mann, G.F. Tomaselli, *Braunwald's heart disease e-book: A textbook of cardiovascular medicine*, Elsevier Health Sciences 2018.
- [28] H.K. Jamali, F. Waqar, M.C. Gerson, Cardiac autonomic innervation, *Journal of Nuclear Cardiology* 24(5) (2017) 1558-1570.
- [29] P.F. Fitzpatrick, Tetrahydropterin-Dependent Amino Acid Hydroxylases, 68(1) (1999) 355-381.
- [30] X. Chen, L. Xu, P. Radcliffe, B. Sun, A.W.J.M.p. Tank, Activation of tyrosine hydroxylase mRNA translation by cAMP in midbrain dopaminergic neurons, 73(6) (2008) 1816-1828.
- [31] N.M. Gervasi, S.S. Scott, A. Aschrafi, J. Gale, S.N. Vohra, M.A. MacGibeny, et al., The local expression and trafficking of tyrosine hydroxylase mRNA in the axons of sympathetic neurons, 22(6) (2016) 883-895.
- [32] K.R. Melia, A. Trembleau, R. Oddi, P.P. Sanna, F.E.J.E.n. Bloom, Detection and regulation of tyrosine hydroxylase mRNA in catecholaminergic terminal fields: possible axonal compartmentalization, 130(2) (1994) 394-406.
- [33] K. Kimura, M. Ieda, K. Fukuda, Development, Maturation, and Transdifferentiation of Cardiac Sympathetic Nerves, 110(2) (2012) 325-336.
- [34] W. Hasan, Autonomic cardiac innervation: development and adult plasticity, *Organogenesis* 9(3) (2013) 176-193.
- [35] T.L. Creazzo, R.E. Godt, L. Leatherbury, S.J. Conway, M.L. Kirby, Role of cardiac neural crest cells in cardiovascular development, *Annual review of physiology* 60 (1998) 267-86.
- [36] K. Waldo, M. Zdanowicz, J. Burch, D.H. Kumiski, H.A. Stadt, R.E. Godt, et al., A novel role for cardiac neural crest in heart development, *The Journal of clinical investigation* 103(11) (1999) 1499-507.
- [37] Y. Tomita, K. Matsumura, Y. Wakamatsu, Y. Matsuzaki, I. Shibuya, H. Kawaguchi, et al., Cardiac neural crest cells contribute to the dormant multipotent stem cell in the mammalian heart, *The Journal of cell biology* 170(7) (2005) 1135-46.
- [38] C. Crowley, S.D. Spencer, M.C. Nishimura, K.S. Chen, S. Pitts-Meek, M.P. Armanini, et al., Mice lacking nerve growth factor display perinatal loss of sensory and sympathetic neurons yet develop basal forebrain cholinergic neurons, *Cell* 76(6) (1994) 1001-11.
- [39] A.M. Fagan, H. Zhang, S. Landis, R.J. Smeyne, I. Silos-Santiago, M. Barbacid, TrkA, but not TrkC, receptors are essential for survival of sympathetic neurons in vivo, *The Journal of neuroscience : the official journal of the Society for Neuroscience* 16(19) (1996) 6208-18.
- [40] M. Ieda, K. Fukuda, Y. Hisaka, K. Kimura, H. Kawaguchi, J. Fujita, et al., Endothelin-1 regulates cardiac sympathetic innervation in the rodent heart by controlling nerve growth factor expression, *The Journal of clinical investigation* 113(6) (2004) 876-84.
- [41] N. Sharma, C.D. Deppmann, A.W. Harrington, C. St Hillaire, Z.Y. Chen, F.S. Lee, et al., Long-distance control of synapse assembly by target-derived NGF, *Neuron* 67(3) (2010) 422-34.
- [42] M. Ieda, H. Kanazawa, K. Kimura, F. Hattori, Y. Ieda, M. Taniguchi, et al., Sema3a maintains normal heart rhythm through sympathetic innervation patterning, *Nature medicine* 13(5) (2007) 604-12.

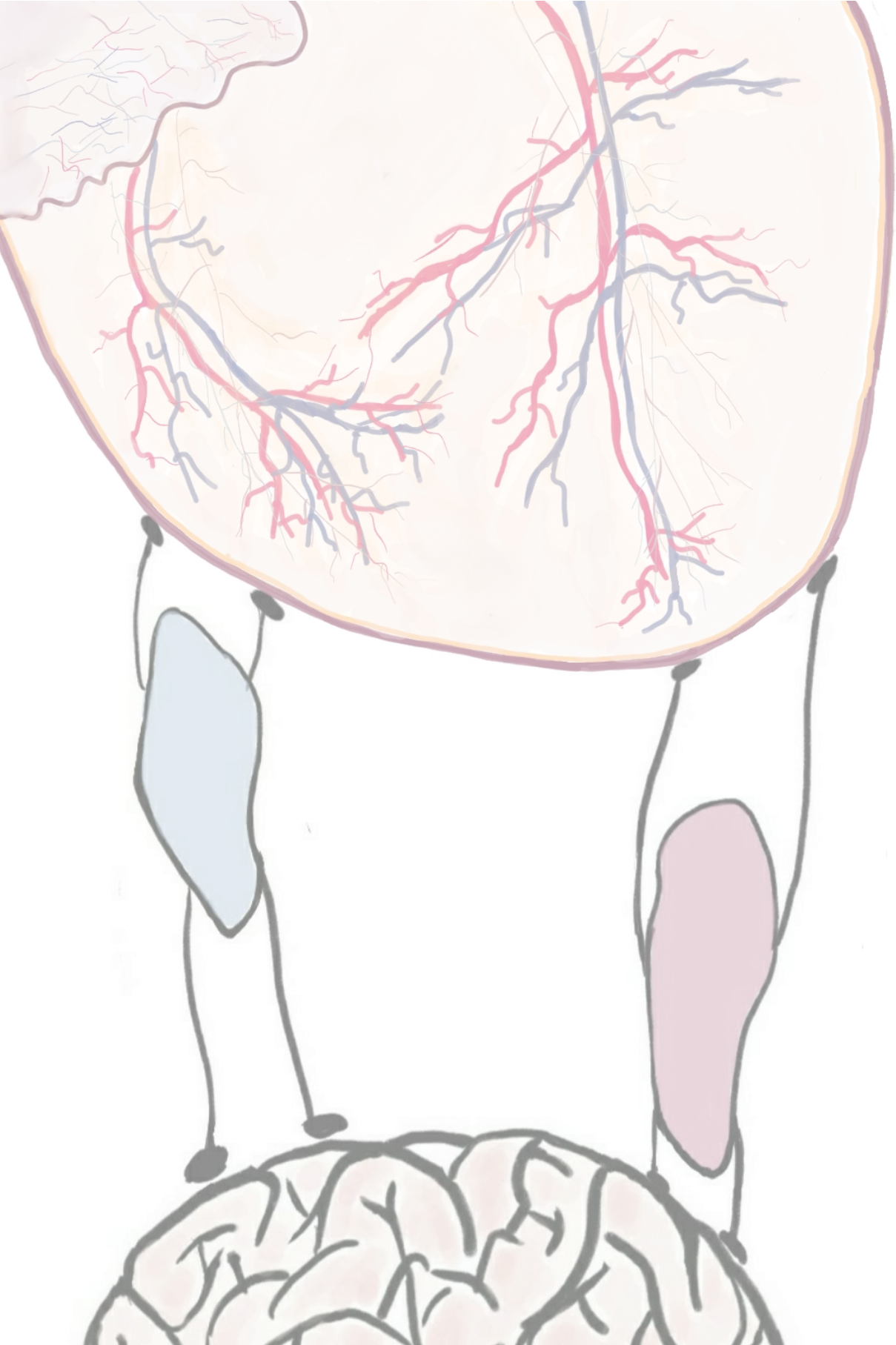
- [43] M. Taniguchi, S. Yuasa, H. Fujisawa, I. Naruse, S. Saga, M. Mishina, et al., Disruption of semaphorin III/D gene causes severe abnormality in peripheral nerve projection, *Neuron* 19(3) (1997) 519-30.
- [44] A.M. Smits, P.R. Riley, Epicardium-Derived Heart Repair, *J Dev Biol* 2(2) (2014) 84-100.
- [45] F. Limana, C. Bertolami, A. Mangoni, A. Di Carlo, D. Avitabile, D. Mocini, et al., Myocardial infarction induces embryonic reprogramming of epicardial c-kit⁺ cells: Role of the pericardial fluid, *Journal of Molecular and Cellular Cardiology* 48(4) (2010) 609-618.
- [46] G.N. Huang, J.E. Thatcher, J. McAnally, Y. Kong, X. Qi, W. Tan, et al., C/EBP Transcription Factors Mediate Epicardial Activation During Heart Development and Injury, 338(6114) (2012) 1599-1603.
- [47] B. Zhou, L.B. Honor, H. He, Q. Ma, J.-H. Oh, C. Butterfield, et al., Adult mouse epicardium modulates myocardial injury by secreting paracrine factors, *The Journal of clinical investigation* 121(5) (2011) 1894-1904.
- [48] B. van Wijk, Q.D. Gunst, A.F.M. Moorman, M.J.B. van den Hoff, Cardiac regeneration from activated epicardium, *PLoS One* 7(9) (2012) e44692-e44692.
- [49] C.M. Braitsch, O. Kanisicak, J.H. van Berlo, J.D. Molkentin, K.E. Yutzey, Differential expression of embryonic epicardial progenitor markers and localization of cardiac fibrosis in adult ischemic injury and hypertensive heart disease, *Journal of molecular and cellular cardiology* 65 (2013) 108-119.
- [50] M. Masters, P.R. Riley, The epicardium signals the way towards heart regeneration, *Stem Cell Res* 13(3 Pt B) (2014) 683-692.
- [51] J. Duan, C. Gherghe, D. Liu, E. Hamlett, L. Srikantha, L. Rodgers, et al., Wnt1/ β catenin injury response activates the epicardium and cardiac fibroblasts to promote cardiac repair, 31(2) (2012) 429-442.
- [52] A.T. Moerkamp, K. Lodder, T. van Herwaarden, E. Dronkers, C.K.E. Dingenouts, F.C. Tengstrom, et al., Human fetal and adult epicardial-derived cells: a novel model to study their activation, *Stem Cell Res Ther* 7 (2016).
- [53] O. Saifi, B. Ghandour, D. Jaalouk, M. Refaat, R. Mahfouz, Myocardial regeneration: role of epicardium and implicated genes, *Molecular Biology Reports* 46(6) (2019) 6661-6674.
- [54] B. Zhou, W.T. Pu, Epicardial epithelial-to-mesenchymal transition in injured heart, *J Cell Mol Med* 15(12) (2011) 2781-2783.
- [55] E.M. Winter, A.C. Gittenberger-de Groot, Epicardium-derived cells in cardiogenesis and cardiac regeneration, *Cellular and molecular life sciences : CMLS* 64(6) (2007) 692-703.
- [56] F.C. Simões, P.R. Riley, The ontogeny, activation and function of the epicardium during heart development and regeneration, 145(7) (2018) dev155994.
- [57] E.M. Winter, R.W. Grauss, B. Hogers, J. van Tuyn, R. van der Geest, H. Lie-Venema, et al., Preservation of left ventricular function and attenuation of remodeling after transplantation of human epicardium-derived cells into the infarcted mouse heart, *Circulation* 116(8) (2007) 917-27.
- [58] S.M. Stevens, A. von Gise, N. VanDusen, B. Zhou, W.T. Pu, Epicardium is required for cardiac seeding by yolk sac macrophages, precursors of resident macrophages of the adult heart, *Developmental biology* 413(2) (2016) 153-159.
- [59] G.N. Huang, J.E. Thatcher, J. McAnally, Y. Kong, X. Qi, W. Tan, et al., C/EBP transcription factors mediate epicardial activation during heart development and injury, *Science (New York, N.Y.)* 338(6114) (2012) 1599-603.
- [60] A.R. Pinto, J.W. Godwin, A. Chandran, L. Hersey, A. Illykh, R. Debuque, et al., Age-related changes in tissue macrophages precede cardiac functional impairment, *Aging* 6(5) (2014) 399-413.
- [61] V. Ramjee, D. Li, L.J. Manderfield, F. Liu, K.A. Engleka, H. Aghajanian, et al., Epicardial YAP/TAZ orchestrate an immunosuppressive response following myocardial infarction, *The Journal of clinical investigation* 127(3) (2017) 899-911.
- [62] D.M. Kaye, G. Vaddadi, S.L. Gruskin, X.-J. Du, M.D. Esler, Reduced Myocardial Nerve Growth Factor Expression in Human and Experimental Heart Failure, 86(7) (2000) e80-e84.

- [63] J.P. Fisher, J.F. Paton, The sympathetic nervous system and blood pressure in humans: implications for hypertension, *Journal of human hypertension* 26(8) (2012) 463-75.
- [64] K. Kimura, M. Ieda, H. Kanazawa, T. Yagi, M. Tsunoda, S.-i. Ninomiya, et al., Cardiac Sympathetic Rejuvenation, 100(12) (2007) 1755-1764.
- [65] K. Fukuda, H. Kanazawa, Y. Aizawa, J.L. Ardell, K. Shivkumar, Cardiac Innervation and Sudden Cardiac Death, *Circulation research* 116(12) (2015) 2005-2019.
- [66] D.P. Zipes, Influence of Myocardial-Ischemia and Infarction on Autonomic Innervation of Heart, *Circulation* 82(4) (1990) 1095-1105.
- [67] W. Li, D. Knowlton, D.M. Van Winkle, B.A. Habecker, Infarction alters both the distribution and noradrenergic properties of cardiac sympathetic neurons, *Am J Physiol-Heart C* 286(6) (2004) H2229-H2236.
- [68] J.G. Cheng, D. Pennica, P.H. Patterson, Cardiotrophin-1 induces the same neuropeptides in sympathetic neurons as do neurotrophic cytokines, *Journal of neurochemistry* 69(6) (1997) 2278-84.
- [69] M.S. Rao, Y. Sun, J.L. Escary, J. Perreau, S. Tresser, P.H. Patterson, et al., Leukemia inhibitory factor mediates an injury response but not a target-directed developmental transmitter switch in sympathetic neurons, *Neuron* 11(6) (1993) 1175-85.
- [70] Y. Sun, R.E. Zigmond, Involvement of leukemia inhibitory factor in the increases in galanin and vasoactive intestinal peptide mRNA and the decreases in neuropeptide Y and tyrosine hydroxylase mRNA in sympathetic neurons after axotomy, *Journal of neurochemistry* 67(4) (1996) 1751-60.
- [71] J. Hartikainen, J. Kuikka, M. Mäntysaari, E. Lämsä, K. Pyörälä, Sympathetic reinnervation after acute myocardial infarction, *The American journal of cardiology* 77(1) (1996) 5-9.
- [72] S.L. Nori, M. Gaudino, F. Alessandrini, E. Bronzetti, P. Santarelli, Immunohistochemical evidence for sympathetic denervation and reinnervation after necrotic injury in rat myocardium, *Cellular and molecular biology (Noisy-le-Grand, France)* 41(6) (1995) 799-807.
- [73] S. Zhou, L.S. Chen, Y. Miyauchi, M. Miyauchi, S. Kar, S. Kangavari, et al., Mechanisms of cardiac nerve sprouting after myocardial infarction in dogs, *Circulation research* 95(1) (2004) 76-83.
- [74] Y.S. Oh, A.Y. Jong, D.T. Kim, H. Li, C. Wang, A. Zemljic-Harpf, et al., Spatial distribution of nerve sprouting after myocardial infarction in mice, *Heart rhythm* 3(6) (2006) 728-36.
- [75] C.Y. Li, Y.G. Li, Cardiac Sympathetic Nerve Sprouting and Susceptibility to Ventricular Arrhythmias after Myocardial Infarction, *Cardiol Res Pract* 2015 (2015) 698368.
- [76] T. Yokoyama, J.K. Lee, K. Miwa, T. Opthof, S. Tomoyama, H. Nakanishi, et al., Quantification of sympathetic hyperinnervation and denervation after myocardial infarction by three-dimensional assessment of the cardiac sympathetic network in cleared transparent murine hearts, *PLoS One* 12(7) (2017) e0182072.
- [77] T. Yokoyama, J.K. Lee, K. Miwa, T. Opthof, S. Tomoyama, H. Nakanishi, et al., Quantification of sympathetic hyperinnervation and denervation after myocardial infarction by three-dimensional assessment of the cardiac sympathetic network in cleared transparent murine hearts, *PLoS One* 12(7) (2017).
- [78] C.U. Lorentz, D.C. Parrish, E.N. Alston, M.J. Pellegrino, W.R. Woodward, B.L. Hempstead, et al., Sympathetic denervation of peri-infarct myocardium requires the p75 neurotrophin receptor, *Experimental neurology* 249 (2013) 111-9.
- [79] H. Zhang, X. Yuan, P.F. Jin, J.F. Hou, W. Wang, Y.J. Wei, et al., Alteration of parasympathetic/sympathetic ratio in the infarcted myocardium after Schwann cell transplantation modified electrophysiological function of heart: a novel antiarrhythmic therapy, *Circulation* 122(11 Suppl) (2010) S193-200.
- [80] W. Hasan, A. Jama, T. Donohue, G. Wernli, G. Onyszchuk, B. Al-Hafez, et al., Sympathetic hyperinnervation and inflammatory cell NGF synthesis following myocardial infarction in rats, *Brain research* 1124(1) (2006) 142-54.

- [81] G. Wernli, W. Hasan, A. Bhattacharjee, N. van Rooijen, P.G. Smith, Macrophage depletion suppresses sympathetic hyperinnervation following myocardial infarction, *Basic research in cardiology* 104(6) (2009) 681-93.
- [82] A. Olivas, R.T. Gardner, L. Wang, C.M. Ripplinger, W.R. Woodward, B.A. Habecker, Myocardial Infarction Causes Transient Cholinergic Transdifferentiation of Cardiac Sympathetic Nerves via gp130, 36(2) (2016) 479-488.
- [83] O.A. Ajijola, D. Yagishita, N.K. Reddy, K. Yamakawa, M. Vaseghi, A.M. Downs, et al., Remodeling of stellate ganglion neurons after spatially targeted myocardial infarction: Neuropeptide and morphologic changes, *Heart rhythm* 12(5) (2015) 1027-35.
- [84] B.L. Nguyen, H. Li, M.C. Fishbein, S.F. Lin, C. Gaudio, P.S. Chen, et al., Acute myocardial infarction induces bilateral stellate ganglia neural remodeling in rabbits, *Cardiovascular pathology : the official journal of the Society for Cardiovascular Pathology* 21(3) (2012) 143-8.

PART I

CARDIAC SYMPATHETIC INNERVATION AND EPDCs



2

HUMAN EPICARDIUM-DERIVED CELLS REINFORCE CARDIAC SYMPATHETIC INNERVATION

Yang Ge^{1,2}, Anke M. Smits³, J. Conny van Munsteren¹, Adriana C. Gittenberger-de Groot², Robert E. Poelmann², Thomas J. van Brakel², Martin J. Schalij², Marie-José T.H. Goumans³, Marco C. DeRuiter¹, Monique R.M. Jongbloed^{1,2}

2

a. Department of Anatomy & Embryology, Leiden University Medical Center, Einthovenweg 20, 2333 ZC Leiden, The Netherlands;

b. Department of Cardiology and Thoracic Surgery, Leiden University Medical Center, Albinusdreef 2, 2333 ZC Leiden, The Netherlands;

c. Department of Cell and Chemical Biology, Leiden University Medical Center, Einthovenweg 20, 2333 ZC Leiden, The Netherlands;

ABSTRACT

Rationale: After cardiac damage, excessive neurite outgrowth (sympathetic hyperinnervation) can occur, which is related to ventricular arrhythmias/sudden cardiac death. Post-damage reactivation of epicardium causes epicardium-derived cells (EPDCs) to acquire a mesenchymal character, contributing to cardiac regeneration. Whether EPDCs also contribute to cardiac re/hyperinnervation, is unknown.

Aim: To investigate whether mesenchymal EPDCs influence cardiac sympathetic innervation.

Methods and results: Sympathetic ganglia were co-cultured with mesenchymal EPDCs and/or myocardium, and neurite outgrowth and sprouting density were assessed. Results showed a significant increase in neurite density and directional (i.e. towards myocardium) outgrowth when ganglia were co-cultured with a combination of EPDCs and myocardium, as compared to cultures with EPDCs or myocardium alone. In absence of myocardium, this outgrowth was not directional. Neurite differentiation of PC12 cells in conditioned medium confirmed these results via a paracrine effect, in accordance with expression of neurotrophic factors in myocardial explants co-cultured with EPDCs. Of interest, EPDCs increased the expression of nerve growth factor (NGF) in cultured, but not in fresh myocardium, possibly due to an “ischemic state” of cultured myocardium, supported by TUNEL and Hif1 α expression. Cardiac tissues after myocardial infarction showed robust NGF expression in the infarcted, but not remote area.

Conclusion: Neurite outgrowth and density increases significantly in the presence of EPDCs by a paracrine effect, indicating a new role for EPDCs in the occurrence of sympathetic re/hyperinnervation after cardiac damage.

Keywords

Epicardium-derived cells (EPDCs); Nerve growth factor (NGF); Neurite outgrowth; Semaphorin 3A (SEMA3A); Sympathetic hyperinnervation.

INTRODUCTION

Cardiac function is influenced by the cardiac autonomic nervous system tone. Cardiac sympathetic stimulation increases heart rate, contraction force and atrioventricular conduction velocity, whereas parasympathetic stimulation largely results in opposite effects. Balanced cardiac sympathetic and parasympathetic activity is critical for maintaining normal cardiac function. Excessive sympathetic activation can be pro-arrhythmogenic, whereas parasympathetic activation is considered to be cardioprotective [1,2]. An accumulating amount of reports indicate a relation between ventricular arrhythmias, sudden cardiac death and activity of the sympathetic autonomic nervous system [3,4]. Although sudden cardiac death after myocardial infarction (MI) is in general attributed to heterogeneous conduction in the infarct border zone [5], autonomic hyperinnervation after MI is also related to sudden cardiac death in numerous reports [6,7]. In addition, sympathetic hyperinnervation has been described in other states of cardiac damage/overload, such as hypertension, RV overload and pulmonary hypertension [8,9].

The definition of post-MI sympathetic hyperinnervation is most often linked to an increase of sympathetic nerve sprouting which can be observed between 3h to several months after the cardiac event [10]. The increased sympathetic nerve density is considered to result from sprouting from cardiac sympathetic ganglia, clusters of neuron cell bodies located bilaterally to the spinal cord at cervical and upper thoracic levels [11].

During development, ventricular innervation develops in close relationship with ventricular vascularization and axons use the developing coronary veins as guides. Neurotrophic factors secreted by coronary veins/epicardium-derived smooth muscle cells guide this process [12,13].

The epicardium is a monolayer of tissue covering the heart. Although it is predominantly quiescent in the healthy adult heart, in the fetal phase it is a multipotent population with various functions. Cells derived from the epicardium, so called epicardium-derived cells (EPDCs), function as a powerful population of cardiac progenitor cells [14–16]. EPDCs expressing e.g. Tbx18, Tcf21 and WT1 can undergo a process known as epithelial-to-mesenchymal transition (EMT) [17,18]. These post-EMT EPDCs acquire mesenchymal cell characteristics and the ability to migrate and populate the subepicardial space by differentiating into different cell types [16]. Of interest, the fetal epicardium also transiently expresses the β_2 -adrenergic receptor (β_2 -AR), and was shown to be essential for the early autonomic response [19].

In the adult, epicardium can get reactivated after cardiac damage such as MI. After reactivation, EPDCs regain an embryonic phenotype with an enrichment of EPDCs in the

infarcted area [15,20,21]. Exogenous administrated adult-derived mesenchymal EPDCs have also been shown to migrate to the infarcted area where they contribute to neovascularization and amelioration of left ventricular function [22]. Whether EPDCs also contribute to cardiac re-innervation as is shown after MI, is currently not known.

The current study is aimed at exploring the effect of adult-derived mesenchymal EPDCs on cardiac sympathetic innervation and demonstrates that these potent cells promote sympathetic nerve sprouting towards “damaged” cultured adult myocardium in vitro.

MATERIALS AND METHODS

A detailed overview of methodology for all sections described below, is provided in the Supplemental Materials.

Experimental animals

C57BL/6 J (Jackson Laboratory) adult mice (n = 42) and mice embryos of embryonic day (E) 18.5 (n = 81) were used. All animal experiments were carried out according to the Guide for the Care and Use of Laboratory Animals published by NIH and approved by the Animal Ethics Committee of the Leiden University (License number AVD1160020185325), Leiden, The Netherlands).

MI induction

8-week male C57BL/6 J mice (n = 4) were anesthetized with isoflurane 5% for induction and 1.5–2% for maintenance. MI was induced by permanent ligation of left anterior descending coronary artery for 7 days [22].

Isolation and culture of human EPDCs

EPDCs were isolated from adult human cardiac tissue and EMT was induced as previously described [23,24]. Briefly, the epicardium was carefully peeled off and cells were dissociated, to exclude contamination with other cells. Isolated EPDCs of epithelial state have a typical cuboidal morphology, therefore EPDCs can readily be distinguished from other cell types. Only cultures that displayed a clear epithelial morphology were used for further experiments to ensure their derivation from the epicardium. Mesenchymal EPDCs were obtained after several days of TGF β stimulation and were cultured for several passages in an mesenchymal state. Mesenchymal post-EMT EPDC are characterized by their morphology and gene expression pattern (**Supplemental fig. S1**). Human mesenchymal EPDCs of passage 6 to 9 were prepared into aggregates and cultured for 4 days until ready for further co-culture. All experiments were

performed according to the guidelines of the Leiden University Medical Centre (Leiden, The Netherlands) and according to the Dutch regulations on the use of human tissues. The study was conducted according to the principles of the Declaration of Helsinki (64th WMA General Assembly, Fortaleza, Brazil, October 2013) and national and institutional guidelines, regulations and acts.

Dissection and culture of adult murine myocardium

Pregnant mice were euthanized in a CO₂ chamber. Left ventricular myocardium was isolated from mother mice and processed into pieces of similar size of 0.1mm³. To induce myocardial damage, processed myocardium pieces were cultured in a cell incubator (at 37 °C and 5% CO₂) for 7 days before subsequent culturing.

Isolation of murine embryonic sympathetic ganglia

After resection of the uteri of euthanized pregnant mice, embryos were collected and euthanized in cold PBS. Superior cervical ganglia (SCG) were isolated from E18.5 embryos and kept in cold PBS. Each SCG was processed into 3–4 pieces for subsequent culturing.

Sympathetic ganglion culture and neurite outgrowth assay

Collagen gel was used to provide a 3-dimensional environment for neurite projection from ganglia explants. Freshly isolated SCG explants were randomly cultured under 5 different conditions in complete medium for 6 days before fixation and further staining.

Immunostaining of ganglion explants in gel

All SCG cultured in gel were whole-mount immuno-stained with anti- β -Tubulin III (Tubb3) to visualize outgrowth. Expression of the enzyme Tyrosine hydroxylase (TH), that is part of the catecholamine biosynthesis pathway necessary for stimulating myocardial contraction, was used to demonstrate the sympathetic phenotype of these ganglia [25]. To verify that growing sympathetic SCG were of a similar phenotype as those freshly isolated, whole-mount anti-TH immunostaining was performed in cultured growing SCG as well as in freshly isolated SCG. Growing SCG show a similar TH expression profile as compared to freshly isolated SCG (Supplemental Fig. S2A,B). In addition, post-ganglionic varicosities, the site in the axon where the neurotransmitters are contained and released, forming the site of the synapses [26,27] were detected in our co-cultured ganglionic neurites (Supplemental Fig. S2C).

Quantification of neurite outgrowth

The work flow of outgrowth quantification is illustrated in supplemental Fig. S3A. Tubb3+ images of cultured SCG were used to quantify the neurite outgrowth according to the presence of neurite outgrowth and its directional preference. For directional outgrowth, a method to quantify the length and density of directional neurites was developed based on different existing plugins in ImageJ: briefly, Quadrant picking was used to identify the quadrant showing directional outgrowth towards myocardium/EPDCs; NeuriteJ was utilized to count the directional neurites length and density in this quadrant. To correct for potential differences in amount of myocardium used in each experiment, all data were normalized for myocardial volume. The myocardial volume was measured and calculated by applying z-stack in confocal imaging. The normalized directional neurite outgrowth was calculated as: Normalized directional neurite number = Counted neurite number/ Relative myocardium volume.

PC12 neurite outgrowth assay

Serum-free conditioned media were collected after 48-hour culturing. PC12 cells were cultured in low-serum media (with/without the addition of NGF) or conditioned media supplemented with 1% FBS. After culturing, the PC12 cells were immuno-stained with anti- β -Tubulin III (tubb3) and neurite differentiation of PC12 in each condition was quantified.

Real time PCR and immuno-blotting

Left-ventricular myocardium explants (freshly isolated or cultured for 7 days in vitro) were cultured exclusively or co-cultured with EPDCs for 2 days. Fresh and cultured myocardial explants were collected for gene expression analysis by real time PCR and protein expression analysis by dot blotting and WES (automated Western Blots).

TUNEL assay and immuno-staining in myocardium sections

Sections of freshly isolated, in-vitro cultured (for 7 days) left-ventricular myocardium explants and 7-day post-MI hearts were stained (see Supplement for further details) with TUNEL, anti-NGF and anti-Wilms' tumor 1 (WT-1) antibodies. NGF expression in myocardium explants and post-MI hearts was quantified with ImageJ.

RESULTS

Adult mesenchymal EPDCs enhance neurite outgrowth of sympathetic ganglia

To investigate the relationship of EPDCs with the establishment and remodeling of cardiac sympathetic innervation, murine sympathetic superior cervical ganglia (SCG) of late embryonic

stages (E18.5) were isolated and cultured with human-derived mesenchymal EPDCs in a 3D-culture system. To mimic the in-vivo absence of direct neuron-EPDC communication (cell-cell contact) and determine the paracrine potential, cellular contact between EPDCs and SCG was prevented by preparing the mesenchymal EPDCs as aggregates in collagen gel. In this way, EPDC aggregates were formed, 4 days prior to co-culturing them with E18.5 ganglia in vitro. Each of these EPDC-ganglion co-cultures was allowed to sprout for 6 days, followed by staining to detect the effects of EPDCs on nerve sprouting of SCG in vitro (**Fig. 1A**).

The SCG explants cultured in the vehicle condition (**Fig. 1B**) showed very limited neurite outgrowth, with either absent or very short neurites. SCG explants in +EPDCs condition (**Fig. 1C**) exhibited robust neurite outgrowth with regard to both density and length of neurites. Comparison of the occurrence of neurite outgrowth (regardless of the length and density of neurites) between SCG in vehicle condition and in +EPDCs condition demonstrated that EPDCs significantly increase the neurite outgrowth of sympathetic ganglia (**Fig. 1F**).

Directional sympathetic nerve sprouting is induced by myocardium and this effect is amplified by EPDCs

Communication between target organs and nerve cells contributes to the innervation of target organs [28]. To study whether adult mesenchymal EPDCs participate in facilitating sympathetic neurite sprouting to target tissue (i.e. the heart), ventricular myocardium was included into the co-culture. Adult-derived murine ventricular myocardium explants were prepared and were cultured in-vitro for 7 days prior to co-culture with SCG explants, after which similar procedures were followed as described (**Fig. 1A**). The SCG explants cultured in the +EPDCs+M condition showed not only abundant but also directionally sprouted neurites towards ventricular myocardium explants (**Fig. 1D**) compared to the abundant but non-directional neurite outgrowth of SCG in the +EPDCs condition (**Fig. 1C**).

To clarify the separate roles as well as potential interactions of mesenchymal EPDCs and myocardium affecting ganglionic outgrowth, SCG explants isolated from the same embryos were randomly divided and cultured in either +EPDCs+M or +M conditions. After a matched co-culture period of 6 days, anti-Tubb3 staining showed directionally sprouted neurites towards myocardium explants in both co-culture conditions (**Fig. 1D, E**). However, the sprouting density of neurites appeared higher in the +M+EPDCs compared to the +M group.

When comparing the +M+EPDCs group and the +EPDCs group (**Fig. 1F**), no difference in the total occurrence of outgrowth from the ganglia was detected but neurite outgrowth showed a significant increase in occurrence of directional outgrowth in the +M+EPDCs condition compared to +EPDCs condition (**Fig. 2A**).

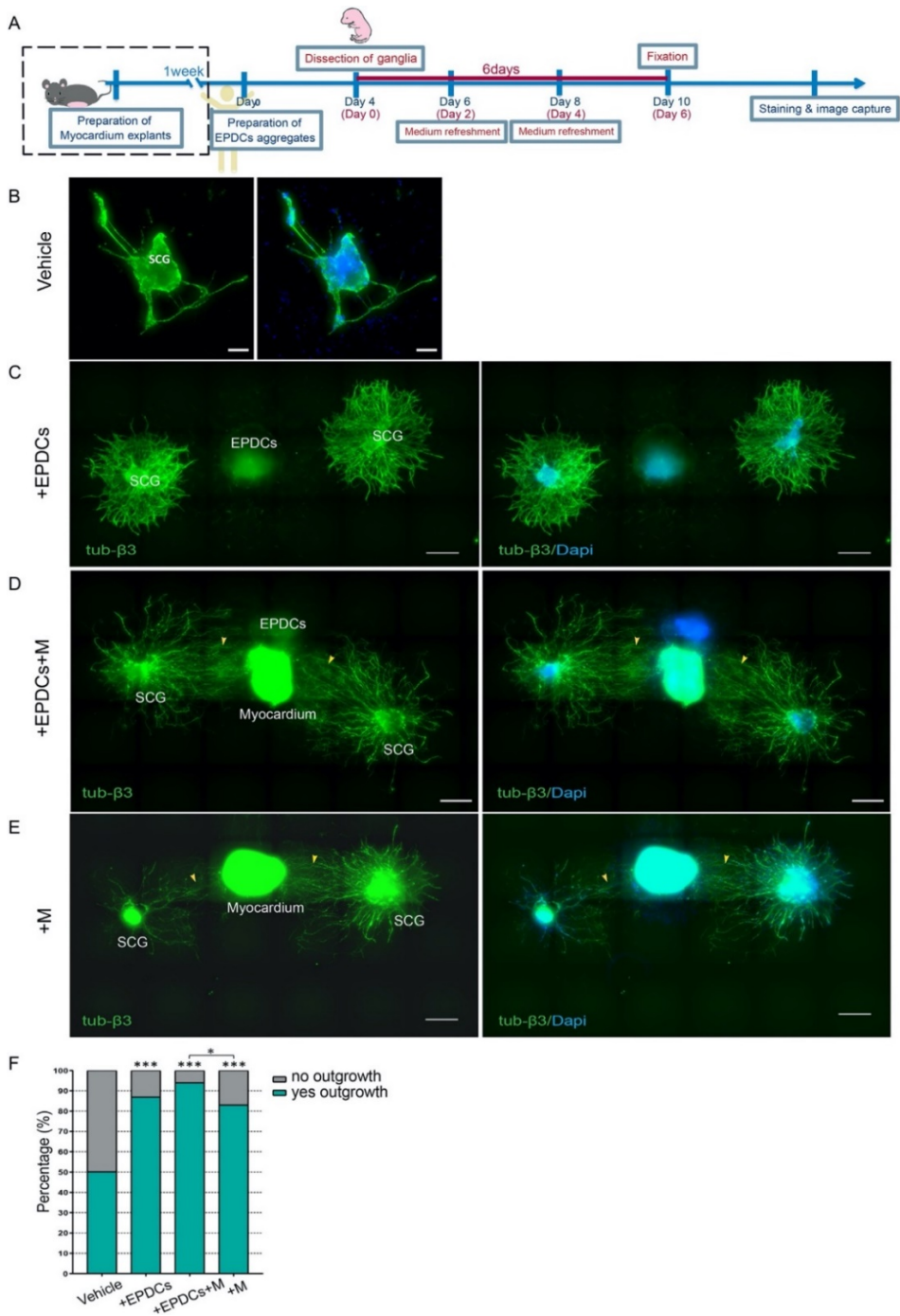


Fig. 1. Mesenchymal EPDCs enhance the outgrowth of sympathetic ganglia. A. Schematic timeline of events in co-culturing superior cervical ganglia (SCG) with mesenchymal EPDCs or with mesenchymal EPDCs and ventricular myocardium (indicated in the dashed square). B-E. Outgrowth of SCG after 6-days of culturing in indicated conditions. Both EPDCs and cultured ventricular myocardium increase the outgrowth of SCG. Directionally organized neurite outgrowth of SCG (indicated by arrowheads in D and E) are detected in +EPDCs+M (panel D) and +M (panel E) co-culturing conditions. Scale bar represents 100 μm in B and 500 μm in C-E. F. Quantification of the percentage of SCG showing neurite outgrowth shows significant increase of neurite outgrowth in ganglia co-cultured with mesenchymal EPDCs and/or ventricular myocardium as compared to vehicle $n = 48$ for vehicle condition; $n = 38$ for +EPDCs condition; $n = 96$ for +EPDCs+M condition; $n = 95$ for +M condition. Chi-square test was applied to detect the difference among groups, * $P < .05$, *** $P < .001$.

Quantification of neurite density shows significant increase in growth and branching of directional neurites in presence of EPDCs

As a next step the density of directional sprouting of neurites towards myocardium was quantified in both groups (i.e. +M versus +EPDCs +M).

Quadrants in anti-Tubb3 images were determined and #1 was assigned to the quadrant showing neurites outgrowth towards myocardium/EPDCs (**supplemental Fig. S3A, Fig. 2B**). Outgrowth was designated as “directional outgrowth” when denser and longer neurites were observed in quadrant 1 (as is depicted in the graphs of **Supplemental Fig. S3B** as red lines). Likewise, neurites sprouting in quadrant 1 were named “directional neurites”. When each quadrant showed a similar neurite density and length, as was the case when SCG were co-cultured with EPDCs only, the outgrowth was designated as “non-directional”. In this case, the colored lines in **Supplemental Fig. S3C** depicting the different quadrants overlap, as is shown.

Subsequently, once SCG explants in +M+EPDCs and +M conditions showed directional outgrowth, the directional neurites were semi-automatically quantified and normalized for myocardium volume in each corresponding co-culture. The normalized number of directional neurites at each length (from 100 μm to 1600 μm) projecting from the SCG explants is shown in a heatmap (**Fig. 2C**, relative myocardium volume is shown in **supplemental Fig. S3D**). As is demonstrated in the heat map, directional neurites with high density (red areas) are predominantly encountered in +M+EPDCs condition. Addition of EPDCs also resulted in a significant increase in growth and branching of directional neurites (**Fig. 2D**).

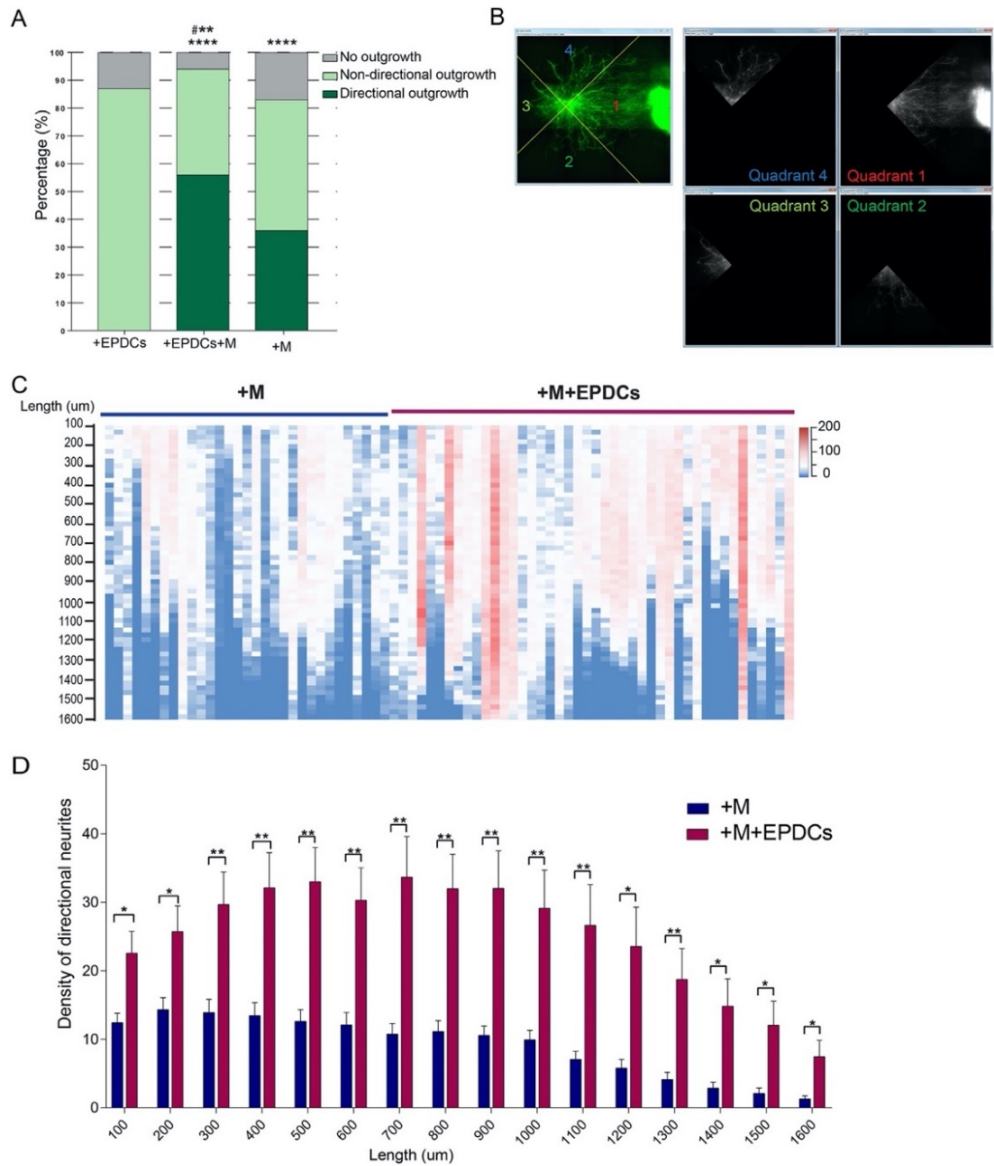


Fig. 2. Mesenchymal EPDCs enhance directional neurite growth of SCG towards ventricular myocardium. A. Cultured myocardium triggers directional outgrowth (compare +M condition with +EPDCs condition). EPDCs augment this occurrence of directional outgrowth (compare +M condition with +EPDCs+M condition). +EPDCs+M condition $n = 96$, +M condition $n = 95$. Chi-square test was applied to detect the difference among conditions, **** $p < .0001$ compared to +EPDCs group; *** $p < .01$ compared to +M group. B. To define directional outgrowth, Tubb3+ images with detectable neurite outgrowth were first processed by Quadrant picking in ImageJ, which divided the image in 4 quadrants according to the ganglion-myocardium position (SCG explants shown in Fig. 1D are shown as an example). The quadrants

were numbered 1 to 4, where quadrant 1 is always the one facing the myocardium/EPDC aggregate, followed clockwise by quadrant 2, 3 and 4. C. The normalized density of directional neurites (i.e. the neurites in quadrant 1) at the indicated length is shown as a heatmap. Neurite density increases from blue (lowest density) to dark red (high density). D. Statistical analysis indicates a significant difference of neurite density (y-axis) between directional neurite outgrowth in the +M condition and in the +M+EPDCs condition at each distance (x-axis) ($n = 32$ for +M group, $n = 45$ for +M+EPDCs group). Multiple t-test was applied to detect the difference between +M and +M +EPDCs, * $p < .05$, ** $p < .01$.

EPDCs and myocardium augment neurite outgrowth via a paracrine effect

In the SCG/myocardium/EPDC co-cultures, the most dense and elongated neurites were observed in quadrant 1, while outgrowth/ density was less in quadrant 2 and 4 and least in quadrant 3 (**supplemental Fig. S3B**), suggesting a potential paracrine effect. Therefore, the next experiments used conditioned medium of the different culture groups. PC12 cells, derived from rat adrenal medullary tumor, have been shown as an adequate model to study neurite outgrowth in vitro [29,30]. After exposure to NGF, PC12 cells are induced to switch from a proliferating phenotype to a neuron-like phenotype, i.e. neurite differentiation [31]. Conditioned medium of mesenchymal EPDCs (EPDCs med), ventricular myocardium (M med) and co-cultured myocardium with EPDCs (M+EPDCs med) was collected to study the effect on neurite differentiation of PC12 cells. As PC12 cells need a “trigger” to switch to a differentiating phenotype, the cells were first triggered by exposure to 50 ng/ml NGF followed by culturing in different conditioned mediums to study their outgrowth (**Supplemental table 2**). All conditioned media could induce clear neurite differentiation of PC12 cells after 2-day triggering with NGF (**Fig. 3A**). PC12 cells triggered by NGF and subsequently cultured in vehicle medium served as a negative control (NGF+/-) and showed limited neurite differentiation. In contrast, PC12 cells cultured in different conditioned mediums after pre-treatment with NGF showed different degrees of augmentation of neurite differentiation. This was significantly different from the PC12 cells in the negative control (NGF+/-) condition, but comparable to the cells in a positive control (NGF+/+) condition (**Fig. 3A,B**). Quantification showed a significantly higher neurite differentiation in combined M+EPDCs medium as compared to cells cultured exclusively with either M medium or EPDCs medium (**Fig. 3B**), in concordance with findings in the SCG co-cultures (**Fig. 2D**). Culturing PC12 cells with conditioned media without pre-treatment of NGF showed no significant neurite differentiation (**Supplemental table 1, Supplemental Fig. S4A**).

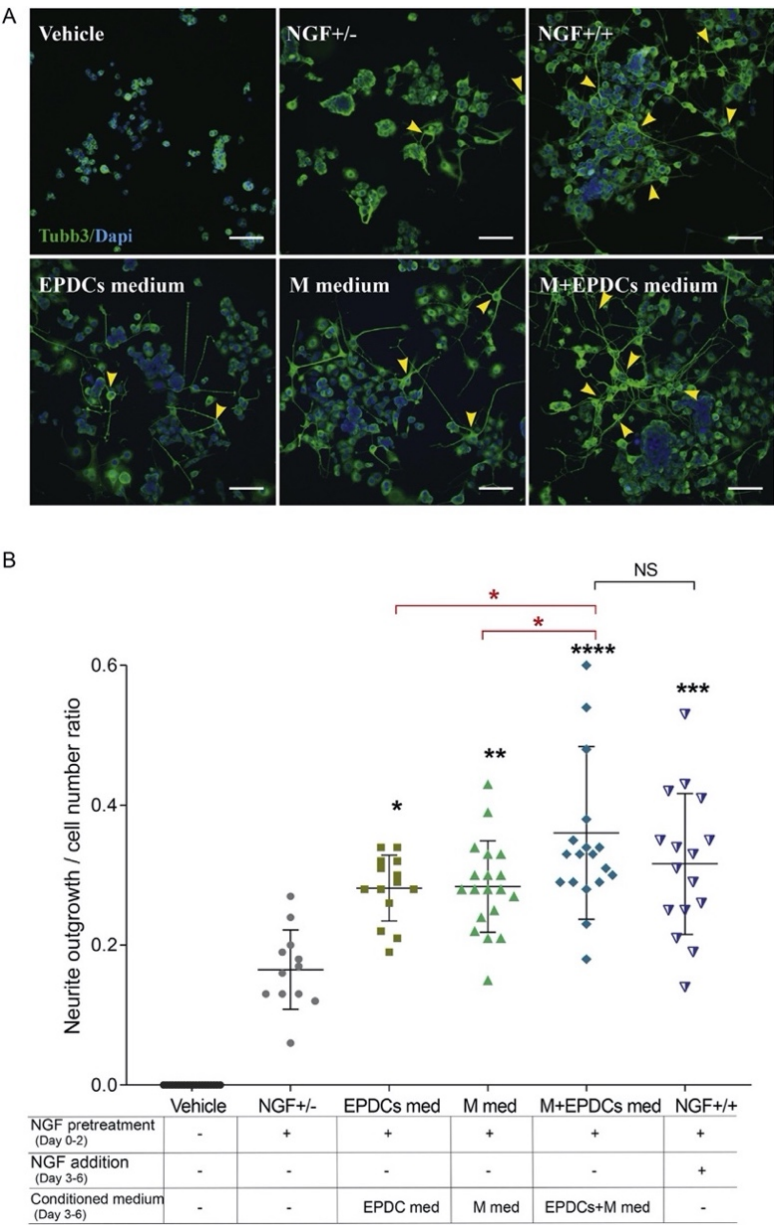


Fig. 3. EPDCs and myocardium augment neurite outgrowth via a paracrine effect. A. Tubb3 staining of PC12 cells cultured under different conditions as indicated (also see **supplemental Table 2**). Differentiated PC12 cells and neurites are indicated by arrow heads. Scale bar = 100 μ m. B. Neurite outgrowth of PC12 cells cultured in the indicated conditions (shown in the table below the graph) is

quantified and displayed as mean \pm SD. One-way ANOVA was applied to detect differences in neurite outgrowth among conditions, and Post Hoc Test (Tukey's multiple comparisons test) in one-way ANOVA was performed to detect the specific difference between groups, * $p < .05$, ** $p < .01$, *** $p < .001$ **** $p < .0001$ compared to NGF+/- condition.

EPDCs increase the expression of NGF in cultured myocardium compared to fresh myocardium

In contrast to the robust neurite sprouting of SCG co-cultured with pre-cultured myocardium, co-culturing SCG with freshly isolated myocardium (+fresh M), showed strikingly less directional outgrowth and only limited density of directional neurites (**Fig. 4A**). TUNEL assay revealed apoptosis in cultured myocardium but not in freshly isolated myocardium. (**Fig. 5A, B**). Hif1a (hypoxia-inducible factor 1-alpha), known to regulate the cellular and systemic homeostatic response to hypoxia and activate genes involving energy metabolism and apoptosis, plays a critical role in adaption of ischemic disease [32,33]. Its expression was increased in the ex-vivo cultured myocardium explants, especially in the myocardium co-cultured with EPDCs (**Supplemental Fig. S4B**). This led to the hypothesis that cultured myocardium explants might show signs of ischemia related cell death leading to the release of factors stimulating neuronal outgrowth. Therefore as a next step several neurotrophic factors known to induce innervation, including *Gdnf*, *Ntf3* and *Igfbp6* were examined by RT-PCR, but were not significantly changed in cultured myocardium. The expression of these genes was not significantly altered by the presence of EPDCs either (**Supplemental Fig. S4B**). However, expression of other genes, like *Bmp2*, *Fgf2*, *Tgfb1* and *Tgfb3* was significantly increased in cultured myocardium (**Supplemental Fig. S4B**). These genes are known to be involved in various events including cardiac development (i.e. epicardial EMT and differentiation), angiogenesis, neuron differentiation/growth and peripheral nerve regeneration.

In addition to the neurotrophic factors mentioned above, expression of NGF was studied, as it is one of the most critical factors for neuronal survival and nerve growth and has been shown to increase under hypoxic conditions and is released acutely from ischemic myocardium [34,35]. Its induction is regulated by ET-1 via the endothelin receptor A (ETA), which participates in cardiac sympathetic nerve growth during development [36]. As we previously found an increase of ET-1 in re-activated mesenchymal human EPDCs (**Supplemental Fig. S4C**), we first examined the expression of gene Endothelin receptor A (*EdnrA*) in myocardium. Increased *EdnrA* expression was observed in cultured myocardium as compared to fresh isolated myocardium (**Fig. 4B**). As a next step, NGF expression in cultured versus fresh myocardium was examined by real time PCR. Results showed that NGF in cultured myocardium was significantly upregulated compared to fresh isolated myocardium (**Fig. 4B**). SEMA3A, a chemorepellent of axonal outgrowth critical for the formation of normal cardiac innervation, was also examined and a decline of SEMA3A expression was detected in the cultured

myocardial tissue at mRNA level (Fig. 4B). Both NGF and SEMA3A were further confirmed at protein level by WES (automated Western Blotting) and showed more outspoken alterations in cultured myocardium at protein level (Fig. 4C, D). After co-culturing of myocardium explants with EPDCs, NGF protein was further upregulated in myocardium explants (Fig. 4C).

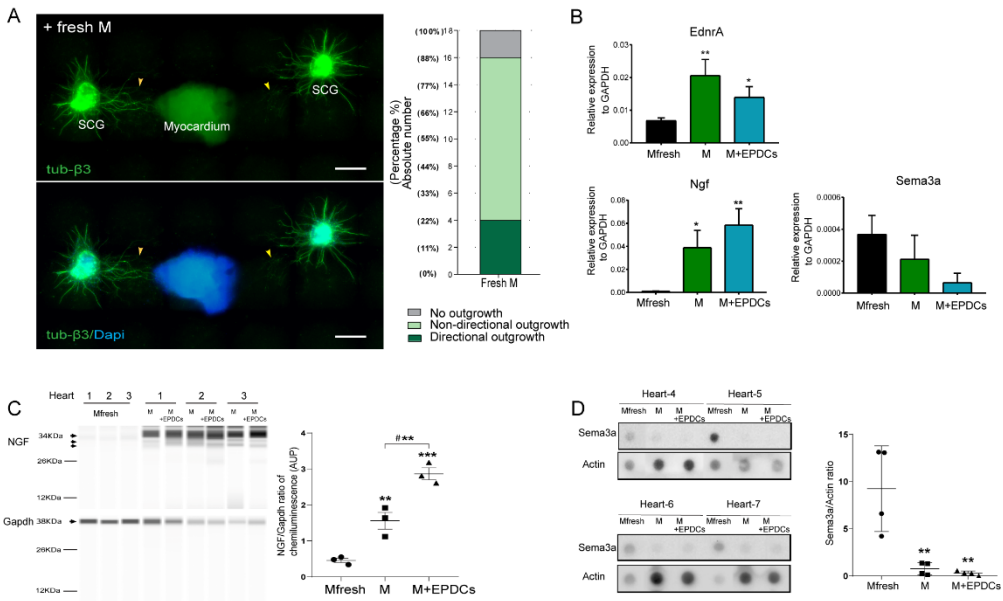


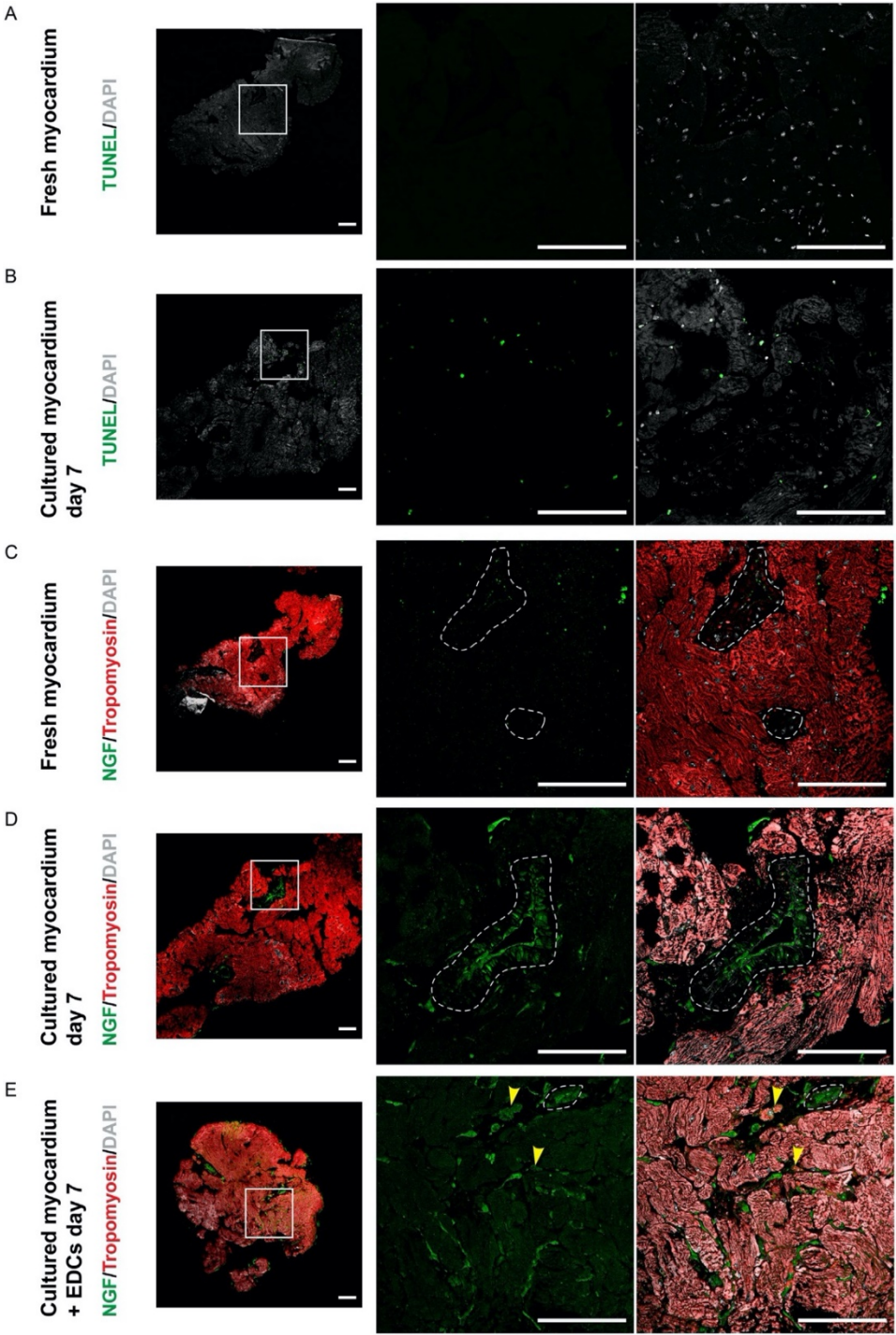
Fig. 4. EPDCs increase the expression of neurotrophic factors in cultured myocardium. **A.** SCG co-cultured with freshly isolated myocardium explants (left panel) and the quantification of outgrowth (right panel). Directional neurite outgrowth is indicated with arrowheads. Scale bar = 500μm. **B.** Real time PCR results of *Ngf*, *Sema3a* and *EdnrA* expression in freshly isolated myocardium, cultured myocardium and myocardium co-cultured with EPDCs (n = 6). Mfresh = freshly isolated myocardium; Mculture = cultured myocardium ** p < .01 compared to Mfresh. **C.** The expression of NGF protein in cultured myocardium and in myocardium co-cultured with EPDCs (n = 3), determined by WES (automated western blots). Mfresh = freshly isolated myocardium; M = cultured myocardium; M+EPDCs = the myocardium co-cultured with EPDCs. * p < .05, ** p < .01 compare to Mfresh, *** p < .01 compared to M+EPDCs with M. **D.** SEMA3A protein in myocardium explants as determined by dot-blotting (n = 4). * p < .05, ** p < .01 compared to Mfresh. Mfresh = freshly isolated myocardium; M = cultured myocardium; M+EPDCs = the myocardium co-cultured with EPDCs. One-way ANOVA and Post Hoc Test (Tukey's multiple comparison test) were performed to detect the differences.

To confirm the finding of NGF at the tissue level, fresh and cultured myocardial explants as well as explants co-cultured with EPDCs from the same mouse were sectioned and stained

with anti-NGF antibody. In fresh myocardium, only a very limited amount of anti-NGF staining was detected (**Fig. 5C**). In cultured myocardium however, robust staining of NGF was detected, mainly observed in non-cardiomyocyte cells, like cells in vessels with slightly increased NGF detection in cardiomyocytes (**Fig. 5D**). The presence of EPDCs, as is shown in **Fig. 5E**, further increased the expression of NGF, which could be widely detected in both cardiomyocytes and non-cardiomyocytes of cultured myocardium. To compare with the in-vivo situation, sections of cardiac tissue after myocardial infarction were studied (**Fig. 6**). As expected, activation of epicardium was observed with expression of WT-1 in the epicardium (**Fig. 6A,B**) as reported previously [20]. In the ischemic zone, NGF expression was observed in cardiomyocytes and non-cardiomyocytes including the activated epicardial cells, similar to the findings in myocardium explants co-cultured with EPDCs in vitro (**Fig. 6C**). In contrast, in the area remote from the infarction, only a low amount of NGF expression was observed similar to the pattern in fresh isolated healthy myocardium explants (**Fig. 6D,E**), supporting a role of EPDCs on upregulation of NGF in “damaged” myocardium. Quantification of NGF protein confirmed a significant increase in both the myocardial explants co-cultured with EPDCs and in the ischemic area of post-MI hearts (**Fig. 6F, G**).

(Figure 5 is on the next page)

Fig. 5. Cultured myocardium explants shows apoptosis and expression of NGF. A-B. Detection of apoptosis in fresh and 7-day cultured myocardium explants with TUNEL assay. Scale bar = 100µm. C-E. Anti-NGF staining in fresh myocardium explants, in cultured myocardium explants and in myocardium explants co-cultured with EPDCs. Anti-Tropomyosin was performed to label cardiomyocytes. Arrowheads indicate cardiomyocytes with NGF staining of high intensity. Dash lined-circles indicate vessels. Scale bar = 100µm.



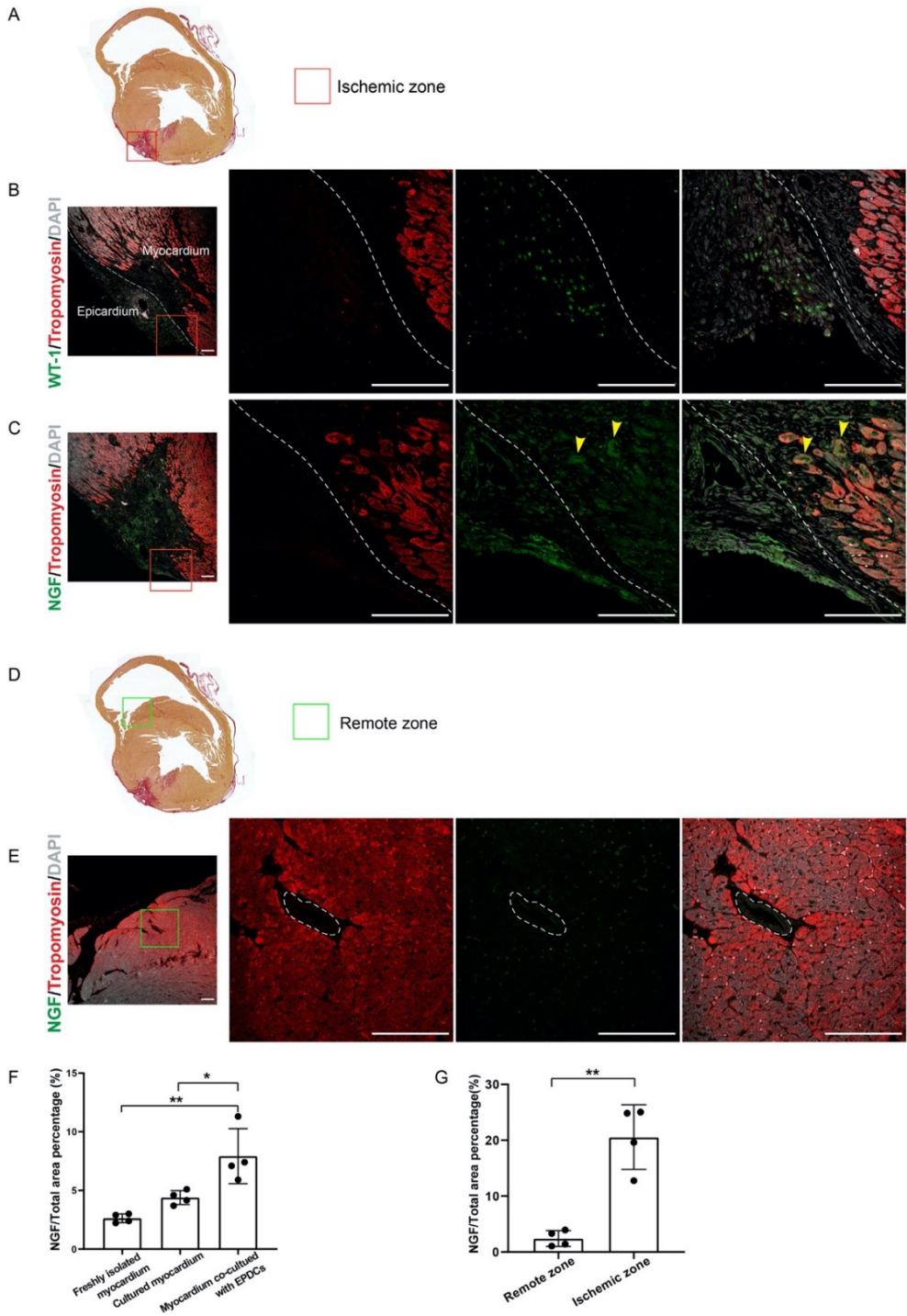


Fig. 6. Expression of NGF at Ischemic zone of infarcted heart. A,D Sirius red staining of infarcted murine heart (7 days after ligation of the left anterior descending coronary artery). The red square indicates the ischemic zone shown in B and C. B. Activation of epicardium in the infarcted murine heart with the re-expression of WT-1 in epicardial cells. The dashed line indicates the borderline of epicardium at ischemic zone. Scale bar = 100 μ m. C. Anti-NGF and anti-tropomyosin staining of the ischemic zone. Arrowheads indicate cardiomyocytes with NGF staining of high intensity. The dashed line indicates the borderline of epicardium at the ischemic zone. Scale bar = 100 μ m. D, E. Anti-NGF and anti-tropomyosin staining of remote zone. The dash lined-circle indicates the vessel. Scale bar = 100 μ m. D. Sirius red staining of the infarcted murine heart (7 days after ligation of the left anterior descending coronary artery). The green square indicates the remote (un-infarcted) zone shown in E. E. Anti-NGF and anti-tropomyosin staining of the remote (un-infarcted) zone. The dash lined-circle indicates the vessel. F. Quantification of NGF expression in freshly isolated myocardium, cultured myocardium and the myocardium co-cultured with EPDCs in vitro for 7 days (n = 4). G. Quantification of NGF expression at ischemic zone and remote zone of ischemic murine hearts (n = 4). * P < .05, ** P < .01.

DISCUSSION

Ventricular tachyarrhythmias secondary to myocardial infarction (MI) are a major risk factor for sudden cardiac death and have been increasingly associated with ventricular sympathetic hyperinnervation [7,37]. For ventricular (hyper)innervation to occur, axons must grow out of sympathetic chain ganglia towards the heart [11]. Likely, factors from the heart in response to ischemia/hypoxia cause retrograde stimulation of ganglia to induce axonal outgrowth [38]. In the current study, we aimed to explore a potential role of EPDCs in this process.

The epicardium is composed of multifunctional, multipotent progenitor cells with important roles during fetal development [14,15,39]. Of interest, the fetal epicardium transiently expresses the autonomic β 2-adrenergic receptor, and the presence of this mono-layer on the surface of the myocardium was shown to be essential for the early autonomic response [19]. However, whether and how epicardium or EPDCs participate in the establishment of cardiac sympathetic innervation, especially in the remodeling of sympathetic innervation in states of cardiac damage is largely unknown. Although mesenchymal EPDCs are able to differentiate into several cell types, including cardiac fibroblasts, which have been suggested to induce cardiac sympathetic hyperinnervation after MI [40], there is no direct evidence linking EPDCs to sympathetic innervation, as yet.

During development, cardiac autonomic ganglia and nerve fibers have their origin in the neural crest [41], multipotent cells that derive from the embryonic neural plate. Ventricular autonomic innervation develops in parallel with ventricular vascularization, guided by neurotrophic factors [12]. In the current study, in which we co-cultured mouse sympathetic chain ganglia with myocardium and human EPDCs in a collagen based 3D co-culture system, we found evidence for a role of EPDCs in stimulating neuronal outgrowth. This observation opens up a novel approach to understanding of the regulation of the autonomic innervation

of the heart. In all circumstances, adding EPDCs to the ganglion cultures induced a synergistic effect as compared to culturing ganglia with either EPDCs or myocardium alone. The mutual interaction between myocardium and EPDCs has been demonstrated by our group as well in other circumstances, where EPDCs influenced for instance the proper maturation and alignment of myocardium [18,42].

The question remains why healthy murine ganglia, started to show an increase in outgrowth in our in vitro culturing model. We postulated that ischemia/hypoxia induced conditions mimicked a condition of cardiac damage. This was supported by the ganglia-EPDC co-cultures with fresh myocardium, that showed remarkably less outgrowth. These findings are in line with observations in other cell culture systems, showing that even concentrations of oxygen in the physiological range may exert a significant negative impact on cells in culture [43]. Our data on the possible role of induction of “cardiac damage” was further supported by the increase of levels of Hypoxia-inducible factor 1-alpha (*Hif1a*) in cultured myocardial cells, already starting after 1 day of culture. *Hif1a* is known to regulate the cellular and systemic homeostatic response to hypoxia and activate genes involving energy metabolism and apoptosis, and plays a critical role in adaption to ischemic disease [32,33].

Paracrine effect of mesenchymal EPDCs on neurite outgrowth. The current culturing experiments using PC12 cells cultured with conditioned media of myocardium, EPDCs and both, confirmed a paracrine effect of EPDCs on the differential potential of neurons. PC12 cells are derived from rat adrenal medullary tumor cells and have been shown an adequate model to study neurite outgrowth in vitro [29,30]. In line with the in vitro results of ganglion cultures, a synergistic effect of the addition of EPDC medium to the PC12 cell culture was observed, with an increase in neurite sprouting as compared to cultures with either myocardium or EPDCs medium alone. It is well established that epicardium and its EPDCs exert effects on the heart through paracrine signaling via secreted factors [44], which is considered crucial in the regenerative role of EPDCs after MI [16], although a potential effect on neuronal outgrowth has not been described to date. Interestingly, comparable like the in vivo situation after MI, where neurons only start growing fast after an “ischemic hit”, PC12 cells are in a “default” dormant proliferating state and only start differentiating and sprouting when triggered by addition of NGF. NGF is a critical neurotrophic factor supporting neuron survival and axonal growth. Levels of myocardial NGF increased substantially in the presence of EPDCs, demonstrated at both mRNA and protein level. NGF has two main isoforms in vivo; it is initially synthesized as a precursor, proNGF (a complex of alpha, beta and gamma unit) and can be cleaved into a mature functional beta NGF [45]. We only found a low amount of mature NGF staining in fresh myocardium, consistent with a previous report describing the absence of mature NGF in most healthy tissues in both mouse and human [46]. In vivo, anti-mature NGF

staining in epicardium-activated hearts (7-day post-MI) supported our findings that EPDCs increase the NGF expression in both non-cardiomyocyte cells as well as in cardiomyocytes in the myocardium.

Similar results in our study were found for other factors involved in regulation of cardiac innervation. Endothelin 1, increasing cardiac innervation via NGF in animal models [36], was upregulated in myocardium in the presence of EPDCs. In contrast, axonal repellent factor, SEMA3A, that guides the establishment of normal epicardium-to-endocardium cardiac sympathetic innervation [47], was decreased in cultured myocardium, the effect of which was again augmented by the presence of mesenchymal EPDCs. This decrease in SEMA3 expression could underline an increased potential for neuronal growth, as SEMA3A has a suppressive function on neuronal growth [48]. Conversely, overexpression of SEMA3A in either the ischemic border zone of myocardium or in sympathetic ganglia was able to diminish cardiac sympathetic hyperinnervation in the damaged heart [47,49].

Besides a modulation of myocardial NGF and SEMA3A expression by EPDCs, an upregulation of transcriptional expression of *Bmp2*, *Fgf2*, *Tgfb1* and *Tgfb3* was also detected. These genes have various functions including their role as growth factors for multiple cell types, participating in cardiac development, directing cells differentiation, as well as promoting peripheral nerve regeneration [50–53].

STUDY LIMITATIONS

Murine ganglia and myocardium were cultured with human adult EPDCs. In an ideal setting tissues of the same species (preferably human) would be used. The use of our setup was partly directed by the difficulties encountered of culturing murine EPDCs in vitro. In addition, acquiring fresh ventricular human tissues and ganglia suitable for prolonged culture is challenging. On the other hand, the use of human cells is beneficial from a translational point of view. In other studies we also successfully cultured murine and human tissues [22,54], as was also reported by other researchers [55].

As EPDCs are derived from human adult cells, obtained as anonymous surplus operation tissues, we were blinded to any patient information. This may explain some of the variations we encountered in our cell cultures. In the future, we strive to obtain immortalized/ clonal cell lines, that would provide a solution for these interindividual variations. On the other hand, the current study more closely mimics the situation encountered in clinical settings, where individuals factor will always play a role in outcome.

CONCLUSIONS AND CLINICAL PERSPECTIVE

In conclusion, in the current paper we propose a new role for EPDCs extending their potential role in cardiac regeneration in states of ischemia to include an effect on cardiac (re)innervation. Because of its complexity, the autonomic nervous system is in many respects still enigmatic and the pathways regulating neural growth and differentiation, especially in disease states are complex and largely unresolved. We show that the promotional effect of mesenchymal EPDCs on sympathetic neurite sprouting is via paracrine signaling, and indicate a role of NGF, Endothelin-1 and SEMA3A in the process. This response may be in essence beneficial *in vivo*, restoring loss of functional nerves after damage, but given the occurrence of hyperinnervation-related lethal arrhythmias, an “overshoot” may occur, with adverse effect on prognosis after cardiac damage. Which of those factors released by the ventricular myocardium and/or EPDCs are crucial in promoting nerve outgrowth, requires further exploration including metabolomics/proteomics. Our findings warrant more extensive molecular studies, aimed at exploring the neural-myocardial-epicardial axis such as RNA sequencing of ganglionic, myocardial and epicardial tissues in normal and disease states, exploring other signaling pathways involved.

ACKNOWLEDGEMENTS

We thank T. van Herwaarden and Esther Dronkers (Department of Cell and Chemical Biology, LUMC, Leiden, the Netherlands) for their help with isolating and culturing of human EPDCs, and A. Végh (Department of Cell and Chemical Biology, LUMC, Leiden, the Netherlands) for technical assistance.

REFERENCES

- [1] M. Vaseghi, J. Gima, C. Kanaan, O.A. Ajijola, A. Marmureanu, A. Mahajan, et al. Cardiac sympathetic denervation in patients with refractory ventricular arrhythmias or electrical storm: intermediate and long-term follow-up, *Heart Rhythm* 11(3) (2014) 360-6.
- [2] M.J. Shen, D.P. Zipes, Role of the autonomic nervous system in modulating cardiac arrhythmias, *Circ Res* 114(6) (2014) 1004-21.
- [3] D.P. Zipes, M. Rubart, Neural modulation of cardiac arrhythmias and sudden cardiac death, *Heart Rhythm* 3(1) (2006) 108-13.
- [4] M. Vaseghi, K. Shivkumar, The role of the autonomic nervous system in sudden cardiac death, *Prog Cardiovasc Dis* 50(6) (2008) 404-19.
- [5] J.M.T. Debakker, F.J.L. Vancapelle, M.J. Janse, S. Tasserone, J.T. Vermeulen, N. Dejonge, J.R. Lahpor, Slow Conduction in the Infarcted Human Heart - Zigzag Course of Activation, *Circulation* 88(3) (1993) 915-926.
- [6] T. Yokoyama, J.K. Lee, K. Miwa, T. Opthof, S. Tomoyama, H. Nakanishi, A. Yoshida, et al. Quantification of sympathetic hyperinnervation and denervation after myocardial infarction by three-dimensional assessment of the cardiac sympathetic network in cleared transparent murine hearts, *PLoS One* 12(7) (2017) e0182072.
- [7] C.Y. Li, Y.G. Li, Cardiac Sympathetic Nerve Sprouting and Susceptibility to Ventricular Arrhythmias after Myocardial Infarction, *Cardiol Res Pract* 2015 (2015) 698368.
- [8] T.M. Lee, C.C. Chen, N.C. Chang, Cardiac sympathetic hyperinnervation in deoxycorticosterone acetate-salt hypertensive rats, *Clin Sci (Lond)* 123(7) (2012) 445-57.
- [9] K. Kimura, M. Ieda, H. Kanazawa, T. Yagi, M. Tsunoda, S. Ninomiya, H. Kurosawa, K. Yoshimi, H. Mochizuki, K. Yamazaki, S. Ogawa, K. Fukuda, Cardiac sympathetic rejuvenation: a link between nerve function and cardiac hypertrophy, *Circ Res* 100(12) (2007) 1755-64.
- [10] Y.S. Oh, A.Y. Jong, D.T. Kim, H.M. Li, C. Wang, A. Zemljic-Harpe, et al. Spatial distribution of nerve sprouting after myocardial infarction in mice, *Heart Rhythm* 3(6) (2006) 728-736.
- [11] T. Kawashima, The autonomic nervous system of the human heart with special reference to its origin, course, and peripheral distribution, *Anat Embryol* 209(6) (2005) 425-438.
- [12] J. Nam, I. Onitsuka, J. Hatch, Y. Uchida, S. Ray, S. Huang, W. Li, H. Zang, P. Ruiz-Lozano, Y.S. Mukoyama, Coronary veins determine the pattern of sympathetic innervation in the developing heart, *Development* 140(7) (2013) 1475-85.
- [13] E. Manousiouthakis, M. Mendez, M.C. Garner, P. Exertier, T. Makita, Venous endothelin guides sympathetic innervation of the developing mouse heart, *Nature Communications* 5 (2014).
- [14] A.C. Gittenberger-de Groot, E.M. Winter, M.M. Bartelings, M.J. Goumans, M.C. DeRuiter, R.E. Poelmann, The arterial and cardiac epicardium in development, disease and repair, *Differentiation* 84(1) (2012) 41-53.
- [15] N. Smart, K.N. Dube, P.R. Riley, Epicardial progenitor cells in cardiac regeneration and neovascularisation, *Vascul Pharmacol* 58(3) (2013) 164-73.
- [16] A.M. Smits, E. Dronkers, M.J. Goumans, The epicardium as a source of multipotent adult cardiac progenitor cells: Their origin, role and fate, *Pharmacol Res* 127 (2018) 129-140.
- [17] A. von Gise, W.T. Pu, Endocardial and Epicardial Epithelial to Mesenchymal Transitions in Heart Development and Disease, *Circ Res* 110(12) (2012) 1628-1645.
- [18] E.A.F. Mahtab, M.C.E.F. Wijffels, N.M.S. Van den Akker, N.D. Hahurij, H. Lie-Venema, L.J. Wisse, M.C. DeRuiter, et al. Cardiac malformations and myocardial abnormalities in Podoplanin knockout mouse embryos: Correlation with abnormal epicardial development, *Dev Dynam* 237(3) (2008) 847-857.

- [19] T.P. Kelder, S.N. Duim, R. Vicente-Steijn, A.M.D. Vegh, B.P.T. Kruithof, A.M. Smits, et al. The epicardium as modulator of the cardiac autonomic response during early development, *Journal of Molecular and Cellular Cardiology* 89 (2015) 251-259.
- [20] A.C. Gittenberger-de Groot, E.M. Winter, R.E. Poelmann, Epicardium-derived cells (EPDCs) in development, cardiac disease and repair of ischemia, *J Cell Mol Med* 14(5) (2010) 1056-1060.
- [21] E.M. Winter, A.C. Gittenberger-de Groot, Epicardium-derived cells in cardiogenesis and cardiac regeneration, *Cell Mol Life Sci* 64(6) (2007) 692-703.
- [22] E.M. Winter, R.W. Grauss, B. Hogers, J. van Tuyn, R. van der Geest, H. Lie-Venema, et al. Preservation of left ventricular function and attenuation of remodeling after transplantation of human epicardium-derived cells into the infarcted mouse heart, *Circulation* 116(8) (2007) 917-927.
- [23] E. Dronkers, A.T. Moerkamp, T. van Herwaarden, M.J. Goumans, A.M. Smits, The Isolation and Culture of Primary Epicardial Cells Derived from Human Adult and Fetal Heart Specimens, *Jove-J Vis Exp* (134) (2018).
- [24] A.T. Moerkamp, K. Lodder, T. van Herwaarden, E. Dronkers, C.K.E. Dingenouts, F.C. Tengstrom, T.J. van Brakel, et al. Human fetal and adult epicardial-derived cells: a novel model to study their activation, *Stem Cell Res Ther* 7 (2016).
- [25] R.E. Zigmond, Y. Ben-Ari, Electrical stimulation of preganglionic nerve increases tyrosine hydroxylase activity in sympathetic ganglia, *Proc Natl Acad Sci U S A* 74(7) (1977) 3078-80.
- [26] V. Prando, F. Da Broi, M. Franzoso, A.P. Plazzo, N. Pianca, M. Francolini, et al. Dynamics of neuroeffector coupling at cardiac sympathetic synapses, *J Physiol-London* 596(11) (2018) 2055-2075.
- [27] M.R. Bennett, A. Cheung, K.L. Brain, Sympathetic neuromuscular transmission at a varicosity in a syncytium, *Microsc Res Techniq* 42(6) (1998) 433-450.
- [28] M.E. Schwab, R. Heumann, H. Thoenen, Communication between Target Organs and Nerve-Cells - Retrograde Axonal-Transport and Site of Action of Nerve Growth-Factor, *Cold Spring Harb Sym* 46 (1981) 125-134.
- [29] L.A. Greene, A.S. Tischler, Establishment of a Noradrenergic Clonal Line of Rat Adrenal Pheochromocytoma Cells Which Respond to Nerve Growth-Factor, *P Natl Acad Sci USA* 73(7) (1976) 2424-2428.
- [30] N.M. Radio, W.R. Mundy, Developmental neurotoxicity testing in vitro: Models for assessing chemical effects on neurite outgrowth, *Neurotoxicology* 29(3) (2008) 361-376.
- [31] S.C. Kao, R.K. Jaiswal, W. Kolch, G.E. Landreth, Identification of the mechanisms regulating the differential activation of the MAPK cascade by epidermal growth factor and nerve growth factor in PC12 cells, *J Biol Chem* 276(21) (2001) 18169-18177.
- [32] G.L. Semenza, Hypoxia-Inducible Factor 1 and Cardiovascular Disease, *Annu Rev Physiol* 76 (2014) 39-56.
- [33] G.L. Semenza, Hypoxia-inducible factor 1: Regulator of mitochondrial metabolism and mediator of ischemic preconditioning, *Bba-Mol Cell Res* 1813(7) (2011) 1263-1268.
- [34] J.O. Hiltunen, A. Laurikainen, A. Vakeva, S. Meri, M. Saarma, Nerve growth factor and brain-derived neurotrophic factor mRNAs are regulated in distinct cell populations of rat heart after ischaemia and reperfusion, *J Pathol* 194(2) (2001) 247-53.
- [35] T. Abe, D.A. Morgan, D.D. Gutterman, Protective role of nerve growth factor against postischemic dysfunction of sympathetic coronary innervation, *Circulation* 95(1) (1997) 213-220.
- [36] M. Ieda, K. Fukuda, Y. Hisaka, K. Kimura, H. Kawaguchi, J. Fujita, K. Shimoda, E. Takeshita, et al. Endothelin-1 regulates cardiac sympathetic innervation in the rodent heart by controlling nerve growth factor expression, *J Clin Invest* 113(6) (2004) 876-884.
- [37] K. Fukuda, H. Kanazawa, Y. Aizawa, J.L. Ardell, K. Shivkumar, Cardiac Innervation and Sudden Cardiac Death, *Circulation Research* 116(12) (2015) 2005-2019.

- [38] G.W. O'Keeffe, H. Gutierrez, L. Howard, C.W. Laurie, C. Osorio, N. Gavalda, S.L. Wyatt, A.M. Davies, Region-specific role of growth differentiation factor-5 in the establishment of sympathetic innervation, *Neural Dev* 11 (2016).
- [39] A. Wessels, J.M. Perez-Pomares, The epicardium and epicardially derived cells (EPDCs) as cardiac stem cells, *Anat Rec Part A* 276a(1) (2004) 43-57.
- [40] C. Mias, C. Coatrieux, C. Denis, G. Genet, M.H. Seguelas, N. Laplace, et al. Cardiac Fibroblasts Regulate Sympathetic Nerve Sprouting and Neurocardiac Synapse Stability, *Plos One* 8(11) (2013) e79068.
- [41] R. Lumb, Q. Schwarz, Sympathoadrenal neural crest cells: the known, unknown and forgotten?, *Dev Growth Differ* 57(2) (2015) 146-57.
- [42] A. Weeke-Klump, N.A.M. Bax, A.R. Bellu, E.M. Winter, J. Vrolijk, J. Plantinga, S. Maas, M. Brinker, et al. Epicardium-derived cells enhance proliferation, cellular maturation and alignment of cardiomyocytes, *Journal of Molecular and Cellular Cardiology* 49(4) (2010) 606-616.
- [43] A.K. Balin, A.J. Fisher, M. Anzelone, I. Leong, R.G. Allen, Effects of establishing cell cultures and cell culture conditions on the proliferative life span of human fibroblasts isolated from different tissues and donors of different ages, *Exp Cell Res* 274(2) (2002) 275-287.
- [44] M. Masters, P.R. Riley, The epicardium signals the way towards heart regeneration, *Stem Cell Res* 13(3) (2014) 683-692.
- [45] B. Bax, T.L. Blundell, J. MurrayRust, N.Q. McDonald, Structure of mouse 7S NGF: a complex of nerve growth factor with four binding proteins, *Structure* 5(10) (1997) 1275-1285.
- [46] M. Fahnstock, G. Yu, M.D. Coughlin, ProNGF: a neurotrophic or an apoptotic molecule?, *Prog Brain Res* 146 (2004) 101-10.
- [47] R.H. Chen, Y.G. Li, K.L. Jiao, P.P. Zhang, Y. Sun, L.P. Zhang, et al. Overexpression of *Sema3a* in myocardial infarction border zone decreases vulnerability of ventricular tachycardia post-myocardial infarction in rats, *J Cell Mol Med* 17(5) (2013) 608-16.
- [48] T. Toyofuku, J. Yoshida, T. Sugimoto, H. Zhang, A. Kumanogoh, M. Hori, et al. FARP2 triggers signals for *Sema3A*-mediated axonal repulsion, *Nat Neurosci* 8(12) (2005) 1712-1719.
- [49] L.C. Yang, P.P. Zhang, X.M. Chen, C.Y. Li, J. Sun, J.W. Hou, et al. Semaphorin 3a transfection into the left stellate ganglion reduces susceptibility to ventricular arrhythmias after myocardial infarction in rats, *Europace* 18(12) (2016) 1886-1896.
- [50] T. Schlange, B. Andree, H.H. Arnold, T. Brand, BMP2 is required for early heart development during a distinct time period, *Mech Develop* 91(1-2) (2000) 259-270.
- [51] Y. Morikawa, A. Zehir, E. Maska, C.X. Deng, M.D. Schneider, Y. Mishina, et al. BMP signaling regulates sympathetic nervous system development through Smad4-dependent and -independent pathways, *Development* 136(21) (2009) 3575-3584.
- [52] W. Sulaiman, D.H. Nguyen, Transforming growth factor beta 1, a cytokine with regenerative functions, *Neural Regen Res* 11(10) (2016) 1549-1552.
- [53] E. Nusayr, T. Doetschman, Cardiac development and physiology are modulated by FGF2 in an isoform-and sex-specific manner, *Physiological Reports* 1(4) (2013).
- [54] M.C. den Haan, R.W. Grauss, A.M. Smits, E.M. Winter, J. van Tuyn, D.A. Pijnappels, et al. Cardiomyogenic differentiation-independent improvement of cardiac function by human cardiomyocyte progenitor cell injection in ischaemic mouse hearts, *J Cell Mol Med* 16(7) (2012) 1508-1521.
- [55] Y. Oh, G.S. Cho, Z. Li, I. Hong, R.J. Zhu, M.J. Kim, Y.J. Kim, E. Tampakakis, et al. Functional Coupling with Cardiac Muscle Promotes Maturation of hPSC-Derived Sympathetic Neurons, *Cell Stem Cell* 19(1) (2016) 95-106.

SUPPLEMENTAL FIGURES

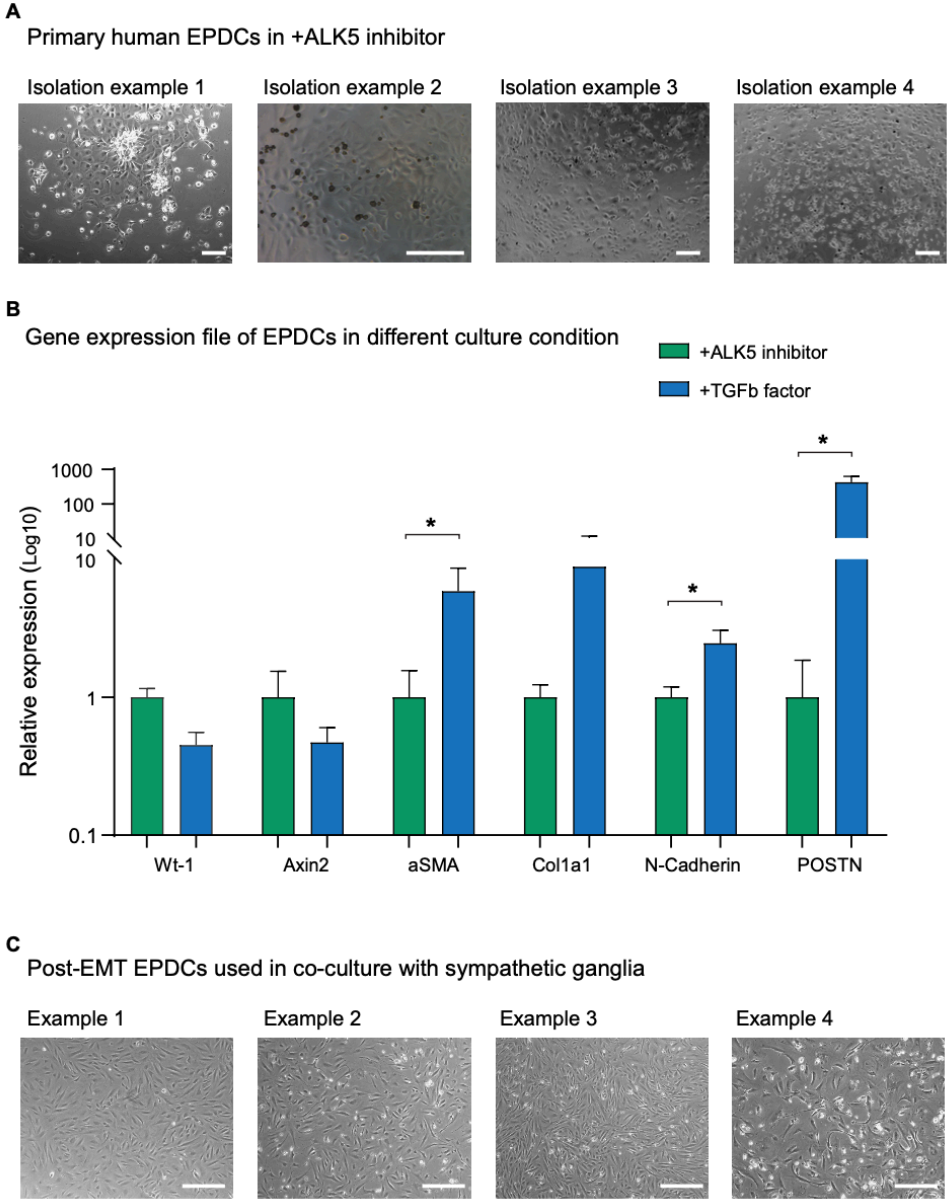


Figure S1. Supplemental information of EPDCs used in the experiment. A. Representative example bright view images of primary human EPDCs with cobblestone morphology in a culture condition supplemented with ALK5 inhibitor. Scale bar=200µm. B. Gene expression profile of cobblestone EPDCs (+ALK5 inhibitor) and EPDCs undergoing EMT (+TGFb). The graph is shown as mean±SD, a paired T-test was

applied (n=2). C. Representative example bright view images of human post-EMT mesenchymal EPDCs with spindle-like morphology. Scale bar=200μm.

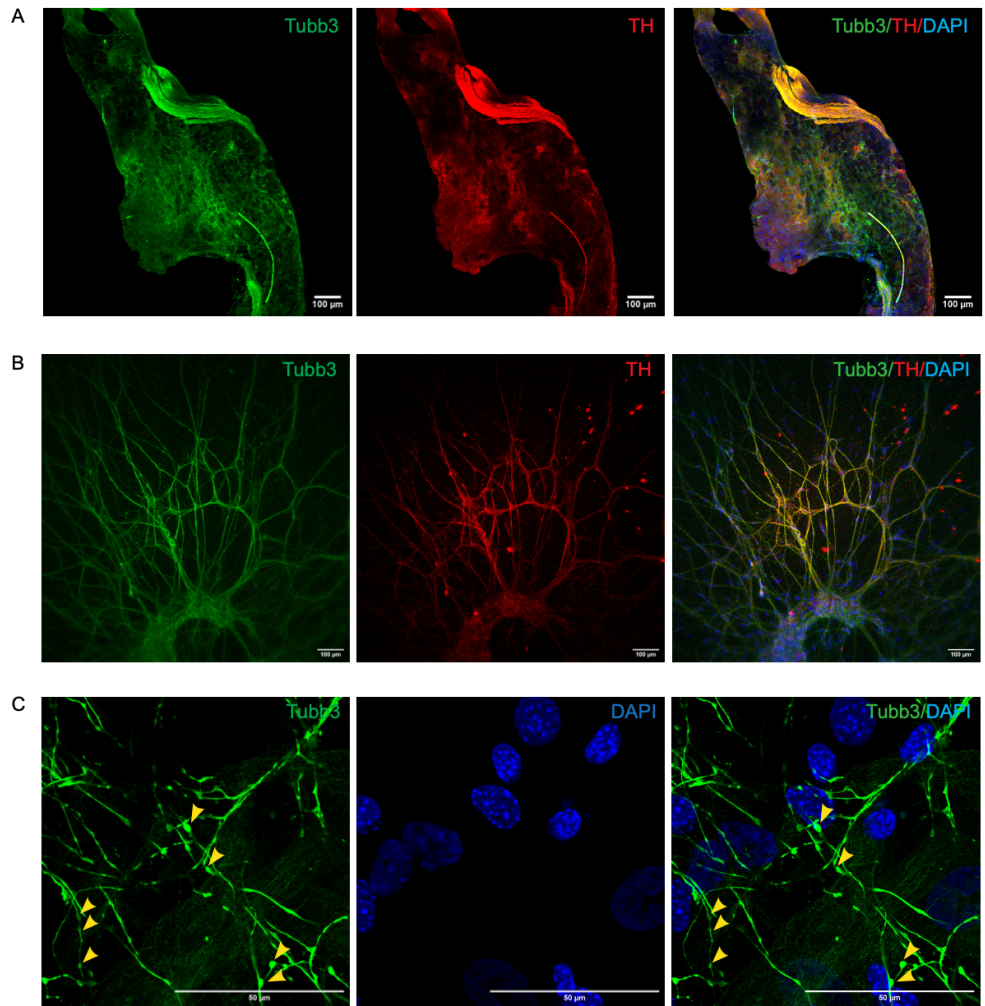


Figure S2. Sympathetic phenotype and varicosities in cultured cervical ganglia. A. Freshly isolated mouse superior cervical ganglia (SCG) that fixed immediately after isolation, whole-mount immunofluorescent staining was applied. Scale bar=100μm. B. Mouse SCG that co-cultured with myocardium and EPDCs in vitro for 6days, whole-mount immunofluorescent staining was performed after fixation. Scale bar=100μm. C. Mouse SCG that co-cultured with EPDCs in a monolayer to visualize sympathetic varicosities (indicated with arrowheads). Scale bar=50μm.

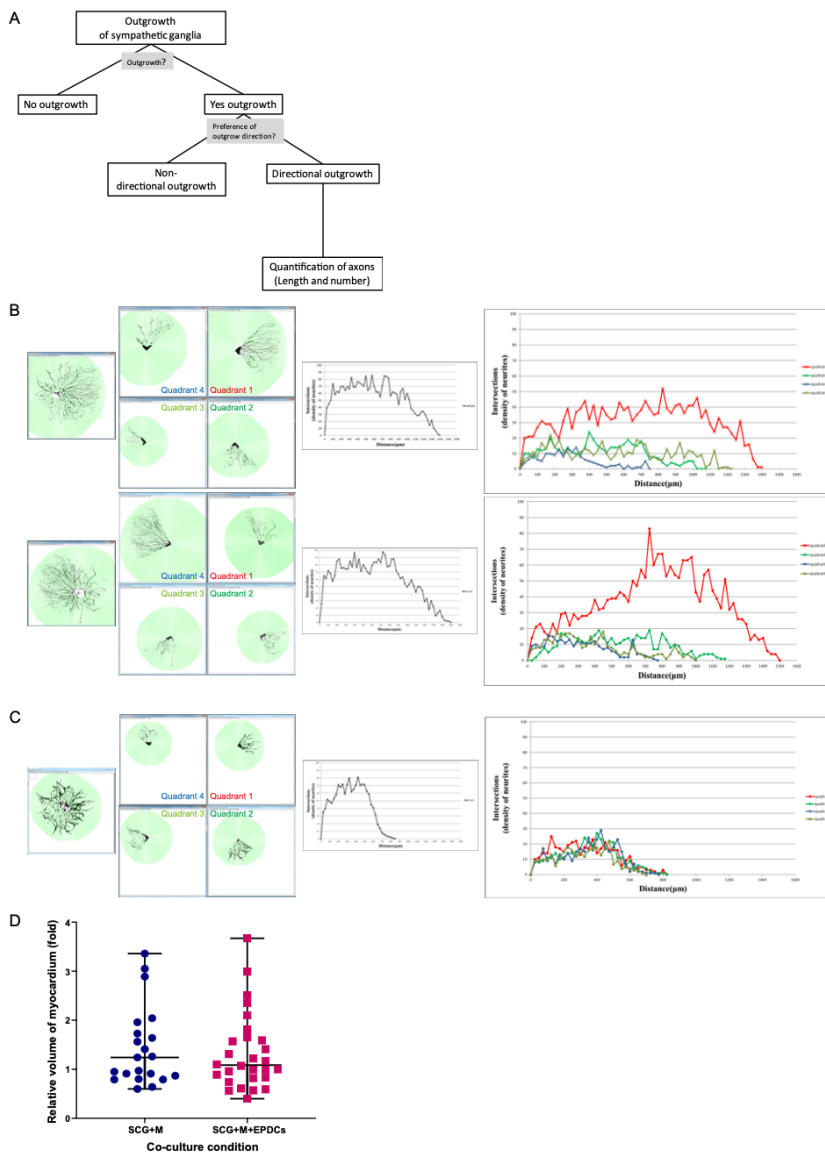


Figure S3. Quantification of neurites density in quadrants. A. Flow diagram of the work procedure. B. Neurite numbers in each quadrants-split image were quantified with NeuriteJ. The results of each quadrant were depicted in a graph. Outgrowth was designated as “directional” when outgrowth of denser and longer neurites sprouting towards the myocardium/EPDCs was observed in quadrant 1 (depicted here as the red lines in the graph on the right side of panel B). C. When each quadrant showed a similar neurite density and length, as was the case when SCG were co-cultured with EPDCs only, the outgrowth was designated “non-directional”. In this case, lines depicting the different quadrants (indicated by different colors) overlap in the graph shown on the right side of panel C. D. Relative volume

of myocardium used in each co-culture is shown as medium±range. SCG+M: superior cervical ganglia with only myocardium; SCG+M+EPDCs: SCG co-culture with myocardium and EPDCs.

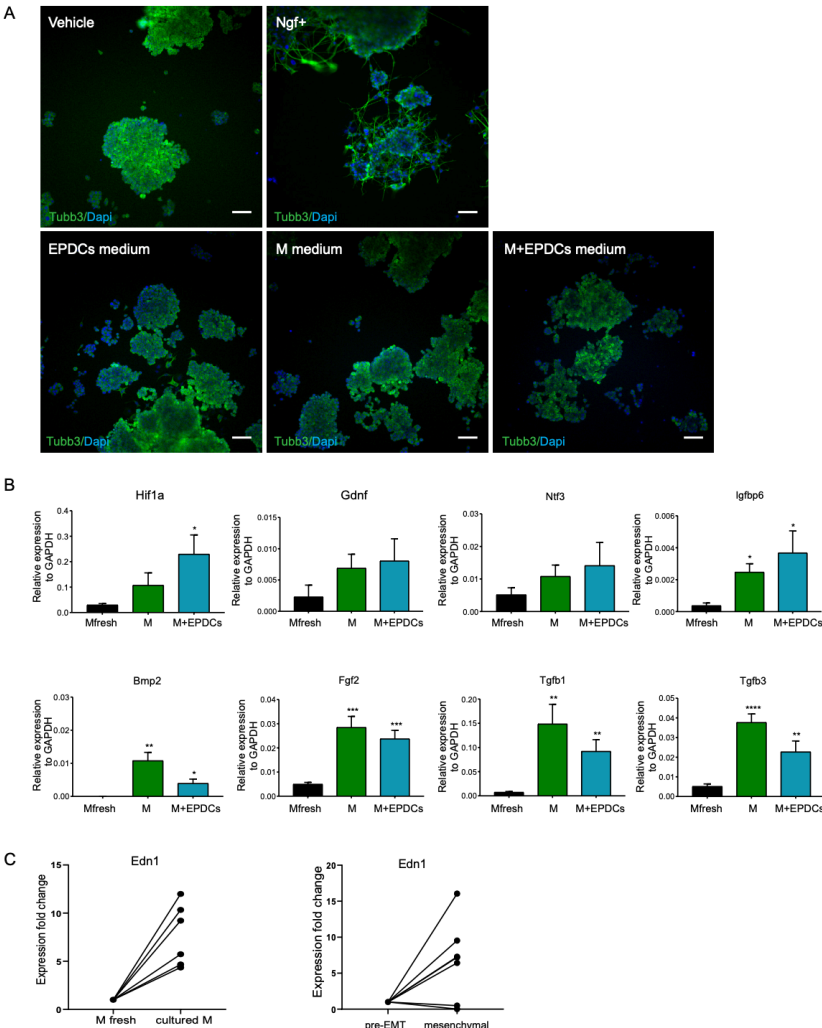


Figure S4. Related to figure 3 and figure 4. EPDCs increase neurite outgrowth by NGF in paracrine fashion. A. Tubb3 staining of PC12 cells cultured in conditioned medium as is indicated in the graph without the pre-treatment of NGF. Scale bar =100µm. B. Gene expression in fresh isolated myocardium, cultured myocardium and the myocardium co-cultured with EPDCs (n=6). Mfresh = freshly isolated myocardium; M = cultured myocardium; M+EPDCs = myocardium co-cultured with EPDCs. * p<0.05, ** p<0.01 compare to Mfresh. C. Expression of endothelin 1 (EDN1) as examined with real time PCR in cultured myocardium (cultured M) compared to freshly isolated myocardium(Mfresh) and in mesenchymal EPDCs compared to pre-EMT EPDCs. P <0.05 in both.

SUPPLEMENTAL METHODS

Experimental animals

C57BL/6J (the Jackson Laboratory) adult mice (n=42) and embryos of embryonic day (E) 18.5 (n=81) were used. All animal experiments were carried out according to the Guide for the Care and Use of Laboratory Animals published by NIH and approved by the Animal Ethics Committee of the Leiden University (Leiden, The Netherlands, license number AVD1160020185325).

MI induction

MI was induced in 8-week C57BL/6J mice (n=4) by permanent ligation of left anterior descending artery. Mice were anesthetized with isoflurane 5% for induction and 1.5-2% for maintenance. Mice were placed in a supine position on a controlled heating pad, intubated and ventilated mechanically (Harvard Ventilator) with a tidal volume of 240 μ L and a frequency of 200/min. The thoracic cavity was opened in the fifth intercostal space. After opening of the pericardial sac, the left anterior descending coronary artery (LAD) was visualized and permanently ligated using 7.0 suture (Prolene, Johnson and Johnson, New Brunswick, NJ, USA) [1].

Human cardiac tissue collection for EPDCs

EPDC were derived from human auricle specimens, obtained as redundant material during cardiac surgery. Patients gave informed consent for use of these tissues for research purposes. All experiments were performed according to the guidelines of the Leiden University Medical Centre (Leiden, The Netherlands) and approved by the local Medical Ethics Committee.

Isolation and culture of human EPDCs

EPDCs were isolated from adult human cardiac tissue as previously described [2]. Briefly, epicardium was dissected from underlying myocardium and processed into small pieces followed by 0.25% Trypsin /EDTA (1:1; Serva and USH products) digestion for 30 min at 37°C. After digestion, the cell suspension was passed through a 100- μ m cell strainer (BD Falcon), resuspended and plated on 0.1% gelatine-coated dishes. The freshly isolated EPDCs were first cultured in the complete medium supplemented with ALK5-kinase inhibitor SB431542 (5–10 μ m; Tocris Bioscience, Ellisville, MO, USA) to keep EPDCs at epithelial state. EPDCs were passaged twice with 0.05% Trypsin-EDTA (Invitrogen) when reaching confluency. Complete medium is a mixed medium of Dulbecco's modified Eagle's medium (DMEM-low glucose; Invitrogen) and Medium 199 (M199; Invitrogen) in 1:1 with 10% heat-inactivated fetal calf

serum (FCS; Gibco), and 1% penicillin/streptomycin (Gibco). To obtain EPDCs of mesenchymal state, EPDCs were induced to undergo EMT by further culturing in complete medium supplemented with 1 ng/ml transforming growth factor beta 3 (TGFβ3) for 5 days. All EPDCs used in the described experiments were of between 6 to 9 passages. RNA was isolated from EPDCs after 5-day culture in ALK5-kinase inhibitor or in TGFβ3. Gene expression of epithelial EPDCs marker and mesenchymal markers were examined by real time PCR.

Preparation of human EPDCs aggregates

Human mesenchymal EPDCs around passage 6 to 9 were collected and split into sterilized microtubes at a density of 10^4 cells per tube. After centrifugation at 1,000 rpm for 4 min, the supernatant was removed and 4 μl collagen gel mix was added to each cell pellet attached to the tube bottom without mixing. Microtubes were incubated for 10 min in a cell incubator after which 80 μl complete medium was carefully added. The aggregates were then cultured for 4 days.

Dissection and culture of adult murine myocardium

Pregnant mice were sacrificed in a CO₂ chamber. Uteri containing the E18.5 embryos were removed and transferred to cold PBS for short time storage on ice. The heart of the mother mouse was dissected and transferred into cold PBS as well. Atria, epicardium and endocardium were first removed from the ventricles. Subsequently, left ventricular myocardium was processed into small pieces of similar size of 0.1 mm³ under a stereo microscope. All myocardial explants were first allowed to attach to the bottom of 24-well plate by incubating at 37°C for 20 minutes, supplying a drop of complete medium to avoid tissue dehydration. All myocardial explants were then cultured in 500 ul/well complete medium in a cell incubator (at 37°C and 5% CO₂) for 7 days to induce myocardial damage and subsequently used for co-culture assays.

Dissection of embryonic sympathetic ganglia

After resection of the uteri with the E18.5 embryos, the embryos were collected and euthanized in cold PBS. To isolate superior cervical ganglia (SCG), the embryonic skin was opened along the midline of the neck using a sharp forceps, exposing the bilateral bifurcations of the common carotid arteries. This was used as reference to indicate the location of cervical ganglia by removing ventral cervical muscle tissue. Cervical ganglia were first dissected together with carotid arteries and placed in cold PBS. Thereafter, vascular and connective tissues were removed. Each isolated SCG was subsequently processed into 3-4 tiny pieces under a stereo microscope for subsequent culturing.

Sympathetic ganglion culture and neurite outgrowth assay

General ganglion culture methods. To provide a 3-dimensional environment for neurite projections from ganglia, we used a similar gel culture method of ganglia as reported in 1997 [3]. In the current study, type I collagen gel mix (Corning 35429) 1,5 ml, 10X PBS 500 μ l, 1N NaOH 34.5 μ l and complete medium 3 ml were mixed under sterile conditions and handled on ice. For ganglion explant cultures, 20 μ l collagen gel mix was placed at the bottom of 24-well plates. Once collagen gel got solidified (10 min in a cell incubator), cervical ganglion pieces with or without other co-culture cells/tissue were transferred onto the solidified gel drops and another 50 μ l collagen gel mix was added to encapsulate the ganglion explants. The plate was kept in the incubator for 20 min before 500 μ l complete culture medium was added. For purpose of high magnification imaging of neurites, cervical ganglion pieces were co-cultured with EPDCs as a monolayer in a 48-well plate with coverslips. Briefly, ganglia pieces were first allowed to attach to the surface of coverslips in 48-well plate by incubating at 37°C for 20 minutes, supplying a drop of complete medium to avoid tissue dehydration. Then 200 μ l complete medium containing 2×10^4 EPDCs were added.

Neurite outgrowth assay. To detect the function of EPDCs on neurite outgrowth and extension, ganglion explants from embryos were randomly cultured in 5 conditions:

Vehicle: 1-2 ganglia explants cultured in gel; +EPDCs: 2 ganglion explants co-cultured with 1 EPDCs aggregate; +M+EPDCs: 2 ganglion explants with 1 EPDCs aggregate and 1 cultured myocardial (M) piece; +M: 2 ganglion explants with 1 piece of cultured adult myocardium; and +M-fresh: 2 ganglion explants co-cultured with 1 freshly dissected piece of adult myocardium (M fresh).

Immunostaining of ganglion explants

After 6-day culture, the medium in the culture plates was removed followed by rinsing with PBS and fixation with 4% PFA for 30 min (10 min for ganglia co-cultured with EPDCs in a monolayer). To make the explants better accessible for antibodies the gels were treated with 0.5% Tween 20 for 30 min (10 min for monolayer) after which blocking with 1% BSA in PBS with 0.05% Tween 20 was carried out for 1 hr. The cultures were stained with primary antibody rabbit anti β -Tubulin III (anti-Tubb3) (Sigma T2200; 1:500) (a general staining for autonomic nerve fibers), Tyrosine hydroxylase (anti-TH) (ThermoFisher PA14679; 1:500) overnight at 4°C. After 3 times rinsing with PBS, visualization of the primary antibodies was done with Alexa Fluor-488 donkey anti-rabbit IgG(H+L) (Life Technology A-21206; 1:250), Alexa Fluor-568 donkey anti-sheep IgG(H+L) (Life Technology A21099; 1:250). After 2,5 hr incubation (1 hr for monolayer) with the secondary antibodies at room temperature, the explants were rinsed

again with PBS. DAPI was used to stain nuclei. Images of ganglia were captured with Leica AF6000 microscope and Leica SP8 confocal microscope.

Whole-mount immunofluorescent staining and clearing of freshly isolated sympathetic ganglion

Freshly isolated cervical ganglia were fixed with 4% PFA at 4°C overnight followed by a treatment with 0.5% Tween 20 for 40 min. After the blocking in 1% BSA in PBS with 0.05% Tween 20 for 1 hr, the ganglia were incubated with primary antibody: rabbit anti β -Tubulin III (anti-Tubb3) (Sigma T2200; 1:500) (a general staining for autonomic nerve fibers) and Tyrosine hydroxylase (anti-TH) (ThermoFisher PA14679; 1:500) for 24 hr at 4°C. After 3 times rinsing with PBS, visualization of the primary antibodies was done with Alexa Fluor-488 donkey anti-rabbit IgG(H+L) (Life Technology A-21206; 1:250) and Alexa Fluor-568 donkey anti-sheep IgG(H+L) (Life Technology A21099; 1:250) at 4°C overnight. DAPI was used to stain nuclei. Images were immediately captured with Leica SP8 confocal microscope after tissue clearing with BABB solution[4]. Briefly, the ganglia were dehydrated in 70% and 100% methanol for 5min after staining. Methanol was first replaced first with 50% (vol/vol) BABB/ methanol then 100% BABB, let ganglia stay in 100%BABB for a few minute until clear.

Quantification of neurite outgrowth

A method to quantify “directional” (i.e towards myocardium) outgrowth of neurites was developed based on different existing plugins (Quadrant Picking and NeuriteJ) in ImageJ. To measure the length of neurites, as well as the density of neurites in each culture condition, ImageJ 1.51s software (National Institutes of Health, Bethesda, MD) was used to process and analyze all β -Tubulin III+ (Tubb3+) images. First, all outgrowth results were classified into 3 groups (no outgrowth, non-directional outgrowth and directional outgrowth) according to the presence of neurite outgrowth and its directional preference as is illustrated in Fig. S3A. Once directional outgrowth was detected, anti-Tubb3 images were processed by the Quadrant picking plug-in, which divided the image in 4 quadrants according to the ganglion-myocardium position. The quadrants were numbered 1 to 4, where Quadrant 1 was the one facing the myocardium/EPDC aggregate, followed clockwise by quadrant 2 to 4 (Fig. 2B). Thereafter, the neurites sprouting towards myocardium/EPDCs were quantified with NeuriteJ as described by Torres-Espin at al. [5]. Briefly, SCG explants were identified and circles (with an interval of 25 μ m) surrounding SCG were produced automatically in NeuriteJ (as is shown in the left panel of Fig. S3B, C). The number of directional neurites was automatically calculated by counting cross point of neurites and circles.

To correct for potential differences in amount of myocardium used in each experiment, all data were normalized for myocardial volume. The myocardial volume was calculated based on confocal images. The normalized directional neurite outgrowth was calculated as: Normalized directional neurite number = Counted neurite number/Relative myocardium volume. The volume of each myocardium used in each co-culture were measured with a confocal microscope (Leica SP8) by detecting autofluorescence of myocardium. Z-stack (10 μ m per step) and tile scan options of confocal microscopy were applied during imaging. Volume of myocardium = stacked area of all stacks * thickness per step (10 μ m). The myocardium volume of the myocardium used in the first co-culture was considered as reference volume, and the relative myocardium volume of the rest of the myocardium was calculated. Normalized directional neurite number = Counted neurite number/Relative myocardium volume.

Collection of conditioned medium

To collect condition medium, isolated left ventricular myocardium tissues (after removal of epicardium and endocardium) were either co-cultured with mesenchymal EPDCs or cultured exclusively in complete medium (as is described above) for 4 days. Next, the tissues and cells were cultured with serum-free DMEM/F12 medium for 48 hr for the purpose of collecting serum-free conditioned medium. The collection of conditioned medium was repeated 3 times with a 1-day culturing interval with complete medium between each collection.

The collected serum-free medium included: EPDCs medium (derived from culturing only EPDCs); EPDCs+M medium (of co-cultured myocardium and EPDCs) and M medium (of cultured myocardium only).

PC12 neurite outgrowth assay

PC12 cells were cultured in proliferation medium (DMEM medium supplemented with 10% HS (Horse serum, Gibco), 5% FCS(Gibco) and 1% penicillin/streptomycin (Gibco)) prior to the neurite outgrowth assay for expansion. To examine the differentiation of PC12, PC12 cells were seeded on a 48 well-plate pre-coated with 50 ng/ml type I collagen at a density of 2,000 cells per well in proliferation medium overnight and then cultured in vehicle medium (DMEM/F12 medium, 1% FCS, 1% penicillin/streptomycin), NGF differentiation medium (supplemented with 50 ng/ml NGF), or the medium mixed with 1/3 volume of DMEM/F12 medium and 2/3 volume of conditioned medium, 1% FCS, 1% penicillin/streptomycin. Replicates of each culture condition were applied. The media were refreshed once on the second day and the PC12 cells in each medium were fixed with 4% PFA on the fourth day. The PC12 cells were permeabilized with 0.5% Tween-PBS for 10 min and blocked in 1% BSA/0.05% Tween-PBS for 1 hr at room temperature. The cells were afterwards incubated with rabbit

anti- β -Tubulin III (Sigma T2200; 1:500) overnight at 4°C and with Alexa Fluor-488 donkey anti-rabbit IgG(H+L) (Life Technology A-21206;1/200) for 1 hr at room temperature. DAPI was used to visualize nuclei. Fluorescence images of entire wells were captured with an EVOS cell imaging system and used for neurite differentiation quantification of PC12 cells. To calculate the ratio of neurite numbers/total cell numbers of each culture condition, 6 fields in each well were used for counting neurites and cells, using ImageJ software. Representative images were captured with an Leica AF6000 fluorescent imaging system.

Supplemental table 1. Experimental setup of PC12 cells cultured in conditioned medium without pre-treatment with NGF.

Condition	Day 0 - 6
Vehicle	- NGF
NGF50+	+ NGF
EPDCs med	EPDCs med
M med	M med
M+EPDCs med	M+EPDCs med

Supplemental table 2. Experimental setup of PC12 cells cultured in conditioned medium with 2-day pre-treatment with NGF.

Condition	Day 0 - 2	Day 3 - 6
Vehicle	- NGF	- NGF
Ngf50+/-	+ NGF (trigger)	- NGF
Ngf50+/+	+ NGF (trigger)	+ NGF
EPDCs med	+ NGF (trigger)	- NGF + EPDCs med
M med	+ NGF (trigger)	- NGF + M med
M+EPDCs med	+ NGF (trigger)	- NGF + M+EPDCs med

Real time PCR (RT-PCR)

To study the impact of mesenchymal EPDCs on the expression of nerve growth related genes in myocardium, left-ventricular myocardium explants (fresh isolated or cultured for 7 days in vitro) were cultured exclusively or co-cultured with EPDC aggregates for 2 days. Afterwards, myocardial explants were collected for gene expression analysis. Briefly, RNA was extracted with NucleoSpin RNA (Macherey-Magel). After treatment with DNase (DNA-free kit, Invitrogen) and cDNA synthesis (iScript DNA synthesis kit, Bio-Rad), RT-PCR was performed by using SYBR Green (Bio-Rad) and run on Real-time system (Bio-Rad) for 44 cycles and checked by electrophoresis on a 2% agarose gel. Primers used for RT-PCR are shown in Supplement table3.

Supplemental table 3. Primer sequences

Gene		Sequence
Gapdh	Forward	TTGATGGCAACAATCTCCAC
	Reverse	CGTCCCGTAGACAAAATGGT
Ngf	Forward	ATGGTGGAGTTTGGCCTGT
	Reverse	GTACGCCGATCAAAAACGCA
SEMA3A	Forward	AGAAATGACCGTCTTCCGGG
	Reverse	TGCACAGGCTTTGCCATAGA
Edn1	Forward	GGCCCAAAGTACCATGCAGA
	Reverse	TGCTATTGCTGATGGCCCTCC
Gdnf	Forward	TATCACTCCCTTTGTGGCTGC
	Reverse	GGGTGTGGAACCATGCGAA
Ntf3	Forward	GGAGTTTGCCGGAAGACTCTC
	Reverse	GGGTGCTCTGGTAATTTTCCTTA
Hif1α	Forward	TGCTGAAGACACAGAGGCA
	Reverse	TCATCAGTGGTGGCAGTTGTG
FGF2	Forward	GCCAACCGGTACCTTGCTAT
	Reverse	GTCCCGTTTTGGATCCGAGT
Tgb1	Forward	GTCACTGGAGTTGTACGGCA
	Reverse	GTTTGGGGCTGATCCCGTT
Igfbp6	Forward	TGCTAATGCTGTTGTTTCGCTG
	Reverse	CACGGTTGTCCCTCTCTCCT
Bmp2	Forward	TGCTAGATCTGTACCGCAGG
	Reverse	GGCCGTTTTCCCACTCATCT
Tgfb1	Forward	GTCACTGGAGTTGTACGGCA
	Reverse	GTTTGGGGCTGATCCCGTT
Tgfb3	Forward	TGTCACACCTTCAGCCCCAA
	Reverse	GGGTGTGGTGATCCTTTTGC
EdnrA	Forward	TACAAGGGCGAGCTGCATAG
	Reverse	CCGTTCTCTCTGTTGAGCAT

WES (automated Western Blots) procedure

WES system (ProteinSimple) and 2-40 KDa Separation Modules (ProteinSimple, SM-W012) were applied to detect NGF protein in fresh myocardium and cultured myocardium samples. Total protein was extracted from myocardium samples with RIPA buffer (Thermo Fischer Scientific). Total protein was measured with BCA assay and diluted with 0.1x sample buffer into the desired concentration (around 0.5 $\mu\text{g}/\mu\text{l}$). All procedures were performed by following the manufacturer's instruction. In brief, 4 volumes of protein sample were mixed with 1 volume of 5X Fluorescent Master Mix and heated at 95°C for 5 min. First antibody, rabbit anti-NGF (Sigma, N6655) and rabbit anti-GAPDH (abcam, ab9485) were separately prepared 1:10 in antibody diluent. The samples, antibody diluent (ProteinSimple, DM-001), primary antibodies (in antibody diluent), HRP-conjugated secondary antibodies (ProteinSimple, DM-001) and chemiluminescent substrate (ProteinSimple, DM-001) were dispensed into the specific wells of the separation module with the volumes recommended in the instruction. When the separation module and capillary cartridge were loaded in the WES system, default settings of the instruments were applied to the run under the control of Compass software. The chemiluminescent peaks were identified automatically and were checked in electropherograms in Compass. The results of area under the peak (AUP) were exported, and NGF/GAPDH ratio of AUP of each sample was afterwards calculated.

Dot blotting

SEMA3A protein expression in myocardium was examined and quantified by dot blotting. 5 μg of total protein extracted from myocardium samples were loaded on the PVDF membrane within bio-dot apparent (bio-rad) and incubated for 1 min. The protein samples were subsequently filtered on the membrane by vacuum. The membrane was washed twice and incubated in blocking buffer for 1hr at RT. Next the membrane was incubated with rabbit anti-SEMA3A antibody (Abcam ab199475; 1:1000) and mouse anti-actin antibody (Millipor BV MAB1501; 1:2000) overnight at 4°C followed by an incubation with HRP-linked antibody (cell signalling #7074; 1:10,000) and anti-mouse IgG HRP-linked antibody (cell signalling #7076; 1:10,000) for 1hr at RT. SEMA3A protein was finally visualized with a WesternBright kit (Isogen life science) and images were captured by C500 western blot imaging system (Azure biosystems). The results were quantified by ImageJ.

TUNEL assay and immuno-staining of cultured myocardium explants

Left-ventricular myocardium was isolated from adult mice and processed into small pieces with the same methods of preparing myocardium explants for co-culture with ganglia. Part of the myocardium explants were fixed with 4% PFA immediately after isolation. The rest of the

myocardium explants were mono-cultured or co-cultured with mesenchymal EPDCs in complete medium for 7 days in vitro, and then fixed with 4% PFA. After embedding with paraffin, 5 µm-thick myocardium sections were made and deparaffined in xylene and ethanol. To detect apoptosis and necrosis in myocardium explants, sections of fresh and cultured myocardium explants were stained with TUNEL (TUNEL in situ cell death detection kit; Sigma Aldrich) for 90 min at 37°C. To detect NGF protein, deparaffined sections were first heated in Tris/EDTA buffer (10mM Tris PH=9.0, 1mM EDTA, 0.05% Tween) at 98°C for 15 min to unmask antigen. The sections were afterwards blocked in blocking buffer (1% BSA, 0.05% Tween in PBS) for 30min at room temperature and incubated with first antibody, rabbit-anti-beta NGF antibody (abcam ab6199; 1:100) and mouse-anti-Tropomyosin (Sigma T9283; 1:200) at 4°C overnight. The sections were rinsed 3 times in PBS and 0.05% Tween-PBS and incubated with fluorescence-labelled secondary antibody, Alexa Fluor 488 goat-anti-rabbit IgG(H+L) (Life technology A-11034; 1:200) and Alexa Fluor 568 goat-anti-mouse IgG1 (Life technology A-21124; 1:200) at room temperature for 1 hr. Nuclei were stained with DAPI and the sections were mounted with Prolong Gold antifade reagent (Life technology P36965). Images were captured with Leica SP8 confocal microscope. To evaluate the NGF expression in myocardium explants and post-MI hearts, 3 sections of each myocardium explants and 3 sections of each post-MI hearts were chosen for quantification. NGF expression in 3 areas of each sections was quantified in ImageJ, averaged and calculated as the percentage NGF area out of the total tissue area.

Sirius red and Immuno-staining of post-MI hearts

7 days after MI surgery, mice were euthanized and the hearts were isolated. The MI hearts were fixed in 4% PFA and paraffin embedded. 5µm-thick heart sections were first deparaffined with xylene and ethanol and then processed with Sirius red staining and immunofluorescence staining with first antibodies: rabbit anti-beta NGF (Abcam ab6199; 1:100), mouse anti-Tropomyosin (Sigma T9283; 1:200), rabbit anti-Wilms tumor 1 (anti-WT-1) (Abcam ab89901; 1:100).

To perform Sirius red staining, deparaffined sections were first stained with Weigert's iron haematoxylin for 10min followed by Picro-Sirius red (0.1% Sirius red in saturated picric acid) staining for 60min. The sections were washed twice in acidified water (2.5 ml acetic acid in 500 ml distilled H₂O), dehydrated and mounted with Entellan.

To perform immunofluorescence staining, deparaffined the sections were first treated with Tris/EDTA buffer (10mM Tris PH=9.0, 1mM EDTA, 0.05% Tween) at 98°C for 15 min. After cooling down at room temperature, the sections were rinsed in PBS and 0.05% Tween-PBS, then the section were incubated with first antibodies (diluted in 1% BSA, 0.05% Tween-PBS

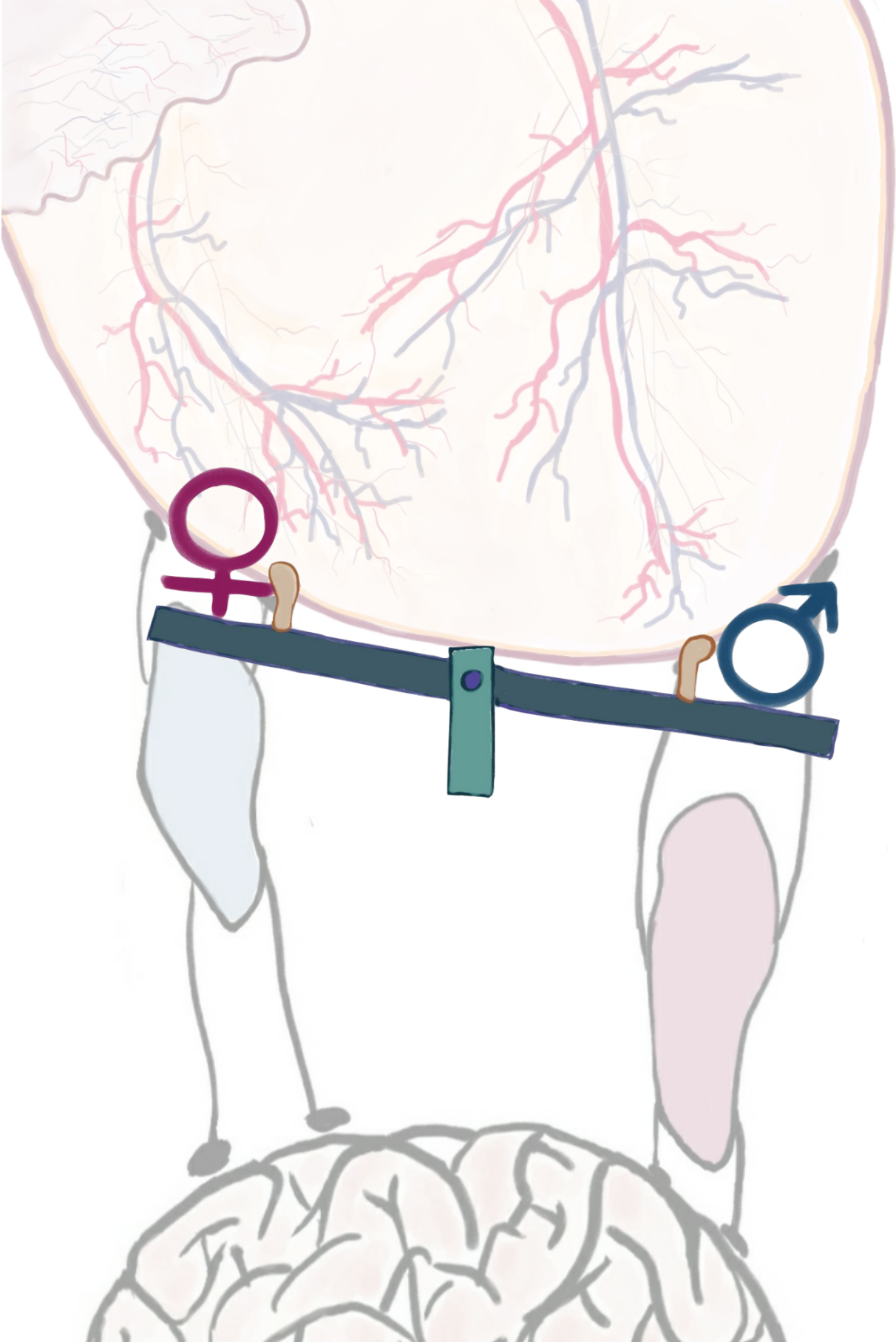
into desired concentration as is described above) at 4°C overnight. On the next day, the sections were rinsed with PBS and 0.05% Tween-PBS followed by the incubation of fluorescence labelled secondary antibodies according to the species of first antibody at room temperature for 1 hr. Secondary antibodies used included: Alexa Fluor 488 donkey-anti-rabbit IgG(H+L) (Life technology A-21206; 1:200), Alexa Fluor 594 goat-anti-mouse IgG(H+L) (Life technology A-21203; 1:200). Nuclei were stained with DAPI and the sections were mounted with Prolong Gold antifade reagent (Life technology P36965). Images were captured with Leica SP8 confocal microscope.

Statistics

Graphs are presented as mean \pm SEM. The presence of neurite outgrowth in control and EPDCs co-culture groups were compared using a Chi-square test. The Chi-square test was also used to compare the proportion of neurite outgrowth between the different co-culture groups (ganglion/myocardium, ganglion/myocardium/EPDC co-cultures). Neurites density at different lengths in the Myocardium condition and Myocardium-EPDCs condition were compared using an independent Student's t test (two-sided). PC12 neurite outgrowth in different conditioned media were compared using one-way ANOVA. Gene and protein expression in myocardium were compared using one-way ANOVA. Results were considered significant when the p value was <0.05. GraphPad Prism (GraphPad Software, San Diego, CA, USA; version 6) was used for statistical analysis.

REFERENCE

- [1] E.M. Winter, R.W. Grauss, B. Hogers, J. van Tuyn, R. van der Geest, H. Lie-Venema, R.V. Steijn, S. Maas, M.C. DeRuiter, A.A.F. de Vries, P. Steendijk, P.A. Doevendans, A. van der Laarse, R.E. Poelmann, M.J. Schalij, D.E. Atsma, A.C. Gittenberger-de Groot, Preservation of left ventricular function and attenuation of remodeling after transplantation of human epicardium-derived cells into the infarcted mouse heart, *Circulation* 116(8) (2007) 917-927.
- [2] E. Dronkers, A.T. Moerkamp, T. van Herwaarden, M.J. Goumans, A.M. Smits, The Isolation and Culture of Primary Epicardial Cells Derived from Human Adult and Fetal Heart Specimens, *Jove-J Vis Exp* (134) (2018).
- [3] S.E. Blackshaw, S. Arkison, C. Cameron, J.A. Davies, Promotion of regeneration and axon growth following injury in an invertebrate nervous system by the use of three-dimensional collagen gels (vol 264, pg 657, 1997), *P Roy Soc B-Biol Sci* 264(1384) (1997) 1101-1102.
- [4] T. Yokomizo, T. Yamada-Inagawa, A.D. Yzaguirre, M.J. Chen, N.A. Speck, E. Dzierzak, Whole-mount three-dimensional imaging of internally localized immunostained cells within mouse embryos, *Nat Protoc* 7(3) (2012) 421-431.
- [5] A. Torres-Espin, D. Santos, F. Gonzalez-Perez, J. del Valle, X. Navarro, Neurite-J: An Image-J plug-in for axonal growth analysis in organotypic cultures, *J Neurosci Meth* 236 (2014) 26-39.



3

THE SEX OF EPICARDIUM-DERIVED CELLS INFLUENCES THE OUTGROWTH OF CARDIAC SYMPATHETIC NERVES IN VITRO

Yang Ge^{1,2}, Janine M. van Gils^{5*}, Ruben Methorst^{1*}, J. Conny van Munsteren¹, Anke M. Smits³, Marie-José T.H. Goumans³, Thomas J. van Brakel⁴, Martin J. Schalij², Marco C. DeRuiter^{1#}, Monique RM. Jongbloed^{1,2#}

* Shared authorship

Shared senior authorship

1. Department of Anatomy & Embryology, Leiden University Medical Center, Einthovenweg 20, 2333 ZC Leiden, The Netherlands;
2. Department of Cardiology, Leiden University Medical Center, Albinusdreef 2, 2333 ZC Leiden, The Netherlands;
3. Department of Cell and Chemical Biology, Leiden University Medical Center, Einthovenweg 20, 2333 ZC Leiden, The Netherlands;
4. Department of Thoracic Surgery, Leiden University Medical Center, Albinusdreef 2, 2333 ZC Leiden, The Netherlands;
5. Department of Nephrology, Leiden University Medical Center, Albinusdreef 2, 2333 ZC Leiden, The Netherlands;

Ready for submission

ABSTRACT

In the past decades, attention on sex differences in the prevalence and outcomes of a wide range of cardiac diseases has increased. Next to overt sex differences in disease presentation and outcome, also differences in autonomic function between males and females have been exposed. After myocardial infarction (MI), male patients have an increased risk for ventricular arrhythmias and sudden cardiac death. Part of these arrhythmias have been attributed to an increase in cardiac sympathetic nerve fibers occurring after cardiac damage. Although mechanical studies of post-MI cardiac sympathetic hyperinnervation have raised growing awareness on the role of the autonomic nervous system in arrhythmogenesis, data on the role of sex herein are still scarce and not conclusive. Here we show that male co-cultures of superior cervical ganglia with male myocardium and mesenchymal epicardium-derived cells (EPDCs) resulted in significant higher neurite directional outgrowth towards myocardium compared to entirely female co-cultures. Moreover, male EPDCs in a female setting enhanced the female neurite outgrowth comparable to an entire male environment. RNA sequencing of male and female EPDCs revealed that female EPDCs have a higher expression of the axon-repellent guidance cue SLIT2, which was also confirmed at the protein level. Our results confirm the stimulating effect of EPDCs on neurite outgrowth and also demonstrate that sympathetic nerve outgrowth and density differs between male and female in vitro which can be equalized by changing the sex of the EPDCs. Our data underlines the potential relevance of sex differences in post-MI cardiac hyperinnervation.

Keywords

Sex differences, sympathetic hyperinnervation, epicardium-derived cells, superior cervical ganglion, ventricular myocardium

INTRODUCTION

Cardiovascular disease is the most important cause of death in Western countries. Sudden cardiac death is a worldwide public health challenge, and is commonly associated with ischemic heart disease [1, 2]. In the past decades, attention on the influence of sex in the prevalence and outcomes of a wide range of cardiac diseases has increased. Next to overt sex differences in cardiovascular disease presentation and outcome [3, 4], also differences in autonomic function between males and females have been exposed [5-7]. Although ischemic cardiovascular disease occurs more often and seems prone to an adverse outcome in males, females seem to obtain a similar risk at cardiovascular events at higher age [3, 8-10]. Partly, this has been attributed to changes in hormonal status, related to menopause, hypothesizing that the lack of estrogens provide a more “male environment” with a concomitant higher cardiovascular risk profile [11].

After myocardial infarction (MI), patients are at increased risk for ventricular arrhythmias and sudden cardiac death. Part of these arrhythmias have been attributed to the phenomenon of cardiac sympathetic hyperinnervation, an increase in sympathetic nerve fibers in the heart which occurs after cardiac damage [12-14]. Several studies have reported sex related differential gene expression in sympathetic genes, as well as differential neurotransmitter contents in rodent studies [15, 16]. Although mechanical studies of post-MI sympathetic hyperinnervation have raised growing awareness on the role of the autonomic nervous system in arrhythmogenesis, data on the role of sex herein is still deficient.

Previously we have reported a stimulating effect of activated mesenchymal epicardium-derived cells (EPDCs) on neurite outgrowth of sympathetic ganglia [17]. The outer layer of the heart, or epicardium, is composed of multifunctional and multipotential progenitor cells with important roles during heart development [18, 19]. In the healthy adult heart these cells are quiescent, but they can become activated in response to pathological triggers, such as MI [18, 19]. Epicardial cells then migrate into the subepicardial space and myocardium, whereafter they are referred to as EPDCs. These cells can differentiate into a.o. coronary smooth muscle cells and cardiac fibroblasts [19, 20]. In our previous study, we showed increased directional outgrowth of sympathetic ganglia towards myocardium in vitro in the presence of human mesenchymal EPDCs [17]. No sex comparison was included as the sex of the used human EPDCs obtained from surgical procedures was unknown to us. To explore whether the stimulating role of EPDC in neurite outgrowth is sex dependent we designed new co-culture experiments including the biological sex origin. RNA sequencing of both male and female EPDCs were performed to find first clues in found differences between male and female hyperinnervation.

MATERIALS AND METHODS

Experimental animals and tissue isolation

C57BL/6J (Charles River) adult mice ($n = 30$) and mice embryos of embryonic day (E) 18.5 ($n = 119$) were used. All animal experiments were carried out according to the Guide for the Care and Use of Laboratory Animals published by NIH and approved by the Animal Ethics Committee of the Leiden University (License number AVD1160020185325, Leiden, The Netherlands).

For the dissection and pre-culture of adult murine myocardium, female mice and male mice were euthanized in a CO₂ chamber. Left ventricular myocardium was isolated and cut into pieces of 0.1mm³. The myocardium pieces were cultured in EPDC medium (at 37 °C and 5% CO₂) for 7 days before subsequent co-culturing. EPDC medium is a 1:1 mixture of low glucose Dulbecco's modified Eagle's medium (10567014; Thermo Fisher Scientific) and medium 199 (31150022; Thermo Fisher Scientific) with 10% heat-inactivated fetal bovine serum (FBS; S1860-500; Biowest) and 1% 100× penicillin/streptomycin solution (15140122; Thermo Fisher Scientific).

For the isolation of murine embryonic superior cervical ganglia, pregnant mice were euthanized with CO₂, whereafter E18.5 embryos were collected and euthanized in cold PBS. The sex of embryos were determined based on the internal genitalia and confirmed by PCR. To isolate superior cervical ganglia (SCG), the embryonic skin was opened along the midline of the neck to expose the bilateral bifurcations of the common carotid arteries. Cervical ganglia were first dissected together with carotid arteries and placed in cold PBS. Thereafter, vascular and connective tissues were removed from SCG under a stereomicroscope. Each SCG was processed into 4 pieces for subsequent co-culturing and kept in cold PBS for further application.

Isolation and culture of human EPDCs

Adult human atrial samples (auricles) were collected as surgical waste material, and further processed anonymously with only the sex of the donor known. Handling of human heart tissues was carried out according to the Dutch regulation for responsible use of human tissues for medical research purposes, and the institutional Medical Ethics Committee ruled that the Medical Research Involving Human Subject Act (WMO) does not apply to the use of surgical waste material (reference number B12.017). EPDCs were isolated from the auricles and EMT was induced to obtain mesenchymal EPDCs, as previously described [21]. Briefly, the epicardium was carefully removed from the underlying myocardium and cut into small pieces followed by three incubations in 0.25% Trypsin-EDTA (25200056; Thermo Fisher Scientific) at

37 °C for 30 min in total. After digestion, the cell suspension was passed through a series of syringes of decreasing internal diameter (19G to 22G) and through a 100-µm BD Falcon cell strainer (BD Biosciences). Next, the cells were plated on 0.1% porcine gelatin coated dishes (G1890; Sigma-Aldrich) and cultured in EPDC medium. To ensure that the cells were derived from the epicardium, only cultures that displayed a clear epithelial morphology were used for further experiments. Mesenchymal EPDCs were obtained after five days of TGFβ (1 ng/ml) stimulation, cultured for a few passages in a mesenchymal state and cryo-preserved in freezing medium (10% DMSO, 25% FBS and 65% EPDC medium) in liquid nitrogen until further use. Cryo-preserved human mesenchymal EPDCs were thawed and cultured for a week before use in the co-cultures.

Co-cultures and neurite outgrowth assay

As indicated in **Figure 1A**, ventricular myocardium explants and cryo-preserved male and female EPDC aggregates were prepared 4 days prior to co-culturing with SCG in a 3D collagen gel in vitro. EPDCs of passage 6 to 9 were collected and split into sterilized microtubes at a density of 10^4 cells per tube. After centrifugation at 1,000 rpm for 4 minutes, the supernatant was carefully removed and 4 µl collagen gel mix was added in each tube without mixing. Microtubes were incubated for 10 minutes in a cell incubator followed by the addition of 80 µl complete medium in each tube. To make gel mix, 1.5 ml type I collagen gel (Corning 35429), 500 µl 10X PBS and 34.5 µl 1N NaOH were added into 3 ml culture medium and kept on ice. To perform co-culturing, 50 µl of collagen gel mix was placed in the center of 24-well plates and allowed to solidify at 37°C. Once collagen gel was solidified after 20 minutes, cervical ganglion pieces with or without other co-culture cells/tissue were transferred onto the solidified gel drops and another 50 µl collagen gel mix was added to encapsulate the tissue explants. The plate was kept in the incubator for 20 minutes before 500 µl complete culture medium was added. According to the cell/tissue components employed in the (co-)culture condition, a total of 4 conditions were included in the study (**Fig. 1B**): *control condition* (only SCG explants); *EPDCs condition* (SCG co-culturing with EPDCs); *M condition* (SCG co-culturing with pre-cultured myocardium) and *M+EPDCs condition* (SCG co-culturing with both pre-cultured myocardium and EPDCs). All the co-cultures were allowed to sprout for 6 days, after which the cultures were fixed and neurite outgrowth was quantified.

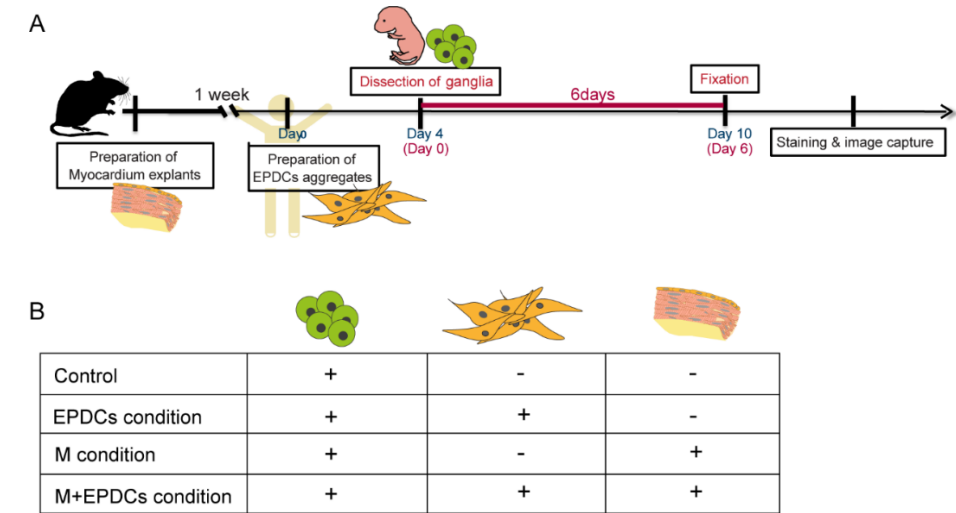


Figure. 1 Experimental workflow and co-culture conditions. A. Schematic timeline of events in co-culturing superior cervical ganglia (SCG) with solely mesenchymal EPDCs or with mesenchymal EPDCs in co-culture of left ventricular myocardium. B. Schematic illustration of co-culture conditions.

Quantification of neurite outgrowth

After 6-day culture, the medium in the culture plates was removed followed by rinsing with PBS and fixed with 4% PFA for 30 minutes at room temperature (RT). Next, the samples were permeabilized with 0.5% Tween 20 for 30 minutes and blocked with 1% BSA in PBS with 0.05% Tween 20 for 1 hour at RT. The samples were incubated with primary antibody rabbit anti β -Tubulin III (anti-Tubb3) (Sigma T2200; 1:500) (a general staining for autonomic nerve fibers) overnight at 4°C. After 3 rinses with PBS, the samples were incubated with Alexa Fluor-488 donkey anti-rabbit IgG(H+L) (Life Technology A-21206; 1:250) for 2.5 hours. DAPI was stained after secondary antibody incubation to indicate nuclei. Images of ganglia were captured with a Leica AF6000 microscope.

To quantify “*directional neurite outgrowth*” (i.e. outgrowth towards the myocardium), first all outgrowth results were classified into 3 groups (no outgrowth, non-directional outgrowth and directional outgrowth) according to the presence of neurite outgrowth and its directional preference as was illustrated previously [17]. In short, once directional outgrowth was detected, anti-Tubb3 images were processed by the Image J Quadrant picking plug-in (ImageJ version 1.52p, National Institutes of Health, Bethesda, MD), which divided the image in 4 quadrants according to the ganglion-myocardium position. The quadrant facing the myocardium/EPDC aggregate was selected, and the neurites sprouting towards the myocardium/EPDC aggregate in the selected quadrant were quantified using the NeuriteJ

plug-in, as described by Torres-Espin et al. [22]. Briefly, SCG explants were identified and circles (with an interval of 25 μm) surrounding SCG were produced automatically in NeuriteJ. The number of directional neurites was automatically calculated by counting cross points of neurites and circles.

To correct for potential differences in the amount of myocardium used in each experiment, all data were normalized for myocardial volume. The volume of each myocardial sample used in each co-culture was measured with a confocal microscope (Leica SP8 or Dragonfly 200) by detecting autofluorescence of myocardium. Z-stack (10 μm per step) and tile scan options of confocal microscopy were applied during imaging.

Volume of myocardium = stacked area of all stacks \times thickness per step

The myocardium volume of the myocardium used in the first co-culture was considered as reference volume, and the volumes of the rest of the myocardium was calculated relative to this reference volume.

The normalized directional neurite outgrowth was calculated as:

$$\text{Normalized directional neurite density} = \frac{\text{Counted neurite density}}{\text{Relative myocardium volume}}$$

RNA sequencing and differential gene expression analysis

Human mesenchymal EPDCs for RNA sequencing were isolated and cultured for 5 days using the same protocol as described above. 4 male and 2 female cryo-preserved mesenchymal EPDCs were isolated and subsequent RNA isolation was performed using the Qiagen mini kit (Qiagen, Hilden, Germany) according to the manufacturers protocol. The final concentration of RNA in each sample was 35 ng/ μl . PolyA selection was performed before sequencing. Paired-end sequencing was performed using the Illumina NovaSeq6000 sequencing (Illumina, San Diego, USA) aiming for 20 million paired-end reads per sample. Transcripts were mapped to GRCh37.p13 and Ensemble TranscriptID were annotated using STAR [23]. Quality control was performed using FastQC. A large count table was generated containing raw counts of each transcript. The R package DESeq2 v3.13 was used for differential expression analysis of male versus female EPDCs [24]. A custom design matrix was produced to extract male and female samples only from the count table. Four cryo-preserved male samples were compared to 2 cryo-preserved female samples in the current study. We filtered for >10 total counts per transcript to remove any low count genes. Next, we performed differential gene expression analysis based on negative binomial distribution using the functions provided by the DESeq2 package. Genes were considered differentially expressed if the adjusted p-value was < 0.05.

Pairwise comparisons of cryo-preserved versus non-cryopreserved samples

RNA isolation of human mesenchymal EPDCs was split into two groups: A group in which RNA was isolated from non-cryopreserved EPDCs, and a group in which RNA isolation was performed 5 days after culturing of thawed EPDCs. RNA isolation, sequencing, and quality control was performed as described above. In total, 4 pairs of cryo-preserved and non-cryopreserved samples were used for sequencing.

Next, differential gene expression between cryo-preserved and non-cryopreserved samples were compared per individual sample to exclude inter-individual differences. A custom script was used to analyze the data in a pairwise manner. All raw counts were added by 1 to prevent infinite values in logarithmic fold change values (LogFC). Next, raw counts were annotated with gene name and gene length. This allowed for transformation of raw counts to transcripts per million (TPM). Subsequently, only protein-coding genes with a mean TPM-expression of 5 were included for further analysis. We determined logFC for each pair. Hereafter, 2x2 tables were generated (TPM of gene x + the mean TPM of given sample for 'non-cryo' and 'cryo') and a Fisher Exact test was performed for each gene including multiple testing correction using FDR correction. Gene Ontology pathway enrichment was performed per pair to identify pathways enriched in non-cryopreserved mesenchymal EPDCs compared to cryo-preserved mesenchymal EPDCs using the standard pipeline [25].

Western blotting

Western blotting was performed on both EPDCs supernatant and on cell lysates. Male (n=5) and female (n=4) mesenchymal EPDCs were cultured in a 6-well plate. From confluent cultures the supernatants were collected and samples diluted in Novex Tris-Glycine SDS sample buffer (ThermoFisher, LC2676) and denatured using DTT at 70°C for 10 minutes. After washing in ice cold PBS, EPDCs were lysed with Novex Tris-Glycine SDS sample buffer (ThermoFisher, LC2676) and denatured using DTT at 70°C for 10 minutes. Equal amounts of proteins were size separated using 4-15% Mini-PROTEAN gels (Biorad, 4561084) and transferred to nitrocellulose membranes (Biorad, 1704158) using the Trans-Blot Turbo system of Biorad. Membranes were blocked with 5% milk in TBST and incubated overnight with primary antibody against Slit2 (1:100, Santa Cruz Biotechnology, SC-28945), or Actin (1:1000, Sigma, C6198). After incubation with Horseradish peroxidase (HRP-)conjugated secondary antibodies (1:5000, DAKO) membranes were developed with SuperSignal Western blot Enhancer (ThermoFisher, 46640) and visualized with the ChemiDoc Touch Imaging System (Biorad). Pictures were analyzed using ImageLab software (Biorad) and expression was quantified using ImageJ software from the NIH.

Statistics

Graphs are presented as mean \pm SEM. The presence of neurite outgrowth in different conditions was compared using a Chi-square test. Neurites density at different lengths in the M condition and M+EPDCs condition were compared using a paired Student's t-test. Results were considered significant when the p value was < 0.05 . GraphPad Prism (GraphPad Software, San Diego, CA, USA; version 9) was used for statistical analysis. RNA sequencing analyses were performed in R version 4.1.1. Scripts are available upon request.

RESULTS

Cryo-preserved EPDCs enhance directional neurite outgrowth towards myocardium

We previously demonstrated enhancing effects of non-cryopreserved human mesenchymal EPDCs on sympathetic neurite outgrowth [17]. For logistic reasons related to limited availability of tissue samples of surgical rest material in past years, we used cryo-preserved EPDCs in the current study. As a first step in our experimental design, we therefore tested whether cryo-preserved EPDCs can also induce directional neurite outgrowth of mouse sympathetic ganglia towards mouse myocardium in co-cultures. While the SCG explants in the control condition showed limited neurite outgrowth, with either absent or short neurites (**Fig. 2A**). The SCG explants cultured in the presence of EPDC (+EPDCs, **Fig. 2B**), myocardium (+M, **Fig. 2C**) or both EPDCs and myocardium (+M+EPDCs, **Fig. 2D**) displayed a clear increase in neurite outgrowth, with regard to both density and length, as compared to the control (SCG only) condition. We also observed strong directional sympathetic neurite outgrowth towards myocardium when culturing SCG in +M and +M+EPDCs conditions (**Fig. 2C, D, E**). Comparison of the occurrence of neurite outgrowth of SCG among the 4 conditions, regardless of the length and density of neurites, confirmed our previous results that EPDCs significantly increase the prevalence of sympathetic directional neurite outgrowth (**Fig. 2E**). For quantification of these results, neurite density was normalized to the myocardial volume in each corresponding co-culture to exclude a potential influence of myocardial volume on neurite outgrowth. The quantification data confirmed that the addition of cryo-preserved EPDCs resulted in a significant increase in directional outgrowth of neurites towards myocardium (**Fig. 2F**), which is in line with our previously published data with non-cryopreserved EPDCs [17].

In contrast to non-cryopreserved EPDCs in our previous experiment [17], SCG co-cultures with cryo-preserved mesenchymal EPDCs alone showed directional neurite outgrowth towards EPDCs in approximately 30% of co-cultures (**Fig. 2C, F**). RNA sequencing of both groups of EPDCs (cryo-preserved vs. non-cryopreserved) detected several differential expressed genes involved in axonogenesis, such as SEMA4D and PTPRO, which might be related to the neurite

outgrowth differences observed between cryo- and non-cryopreserved EPDCs co-cultures (Supplemental Fig. 1A, B).

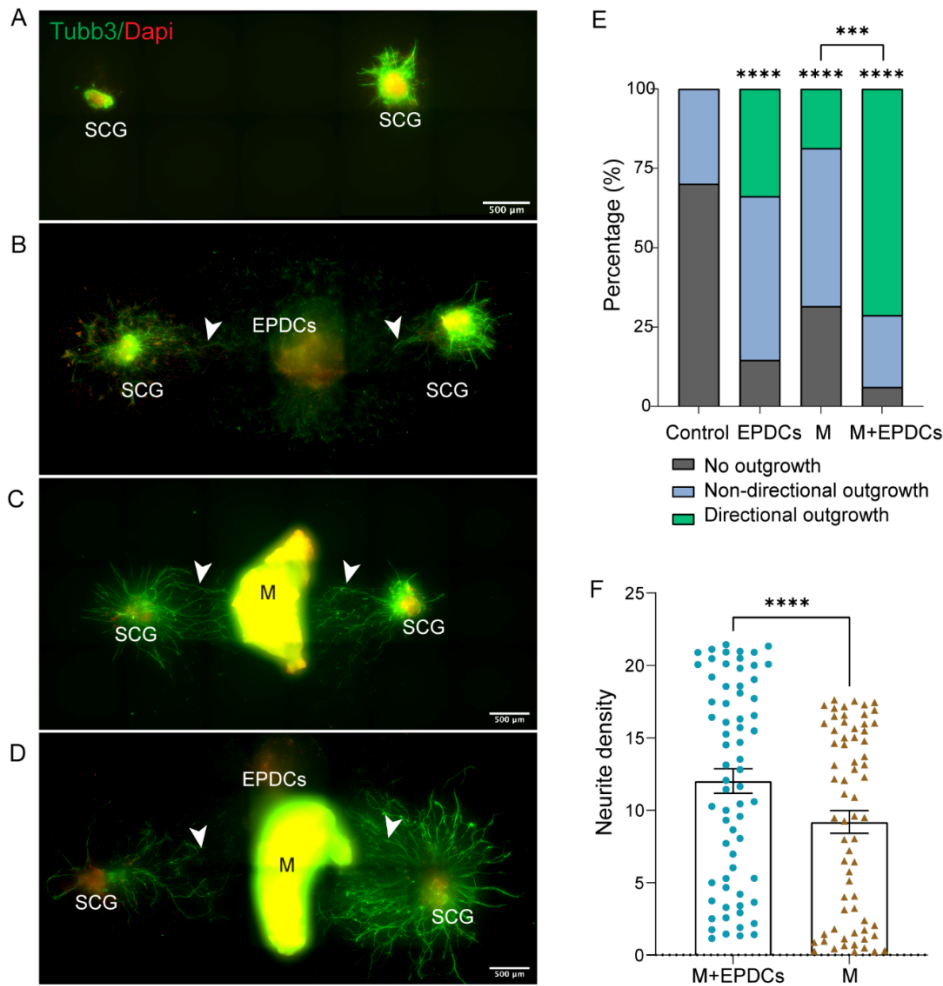


Figure 2. Cryo-preserved EPDCs enhance the directional neurite outgrowth towards myocardium. A-D. Outgrowth of SCG after 6-days of culturing in indicated conditions. A. Control culture of SCG with none or very limited outgrowth. Cryo-preserved EPDCs increase the neurite outgrowth of SCG. Directionally organized neurite outgrowth of SCG towards myocardium are indicated by arrowheads in B, C and D. Scale bar represents 500 μ m. E. Quantification of the percentage of SCG showing either no outgrowth (gray), non-directional outgrowth (blue), or directional outgrowth (green). $n = 187$ for control condition; $n = 192$ for +EPDCs condition; $n = 241$ for +M condition; $n = 230$ for +M+EPDCs condition. Chi-square test was applied to detect the difference among groups, *** $P < .001$, **** $P < .0001$ compared to control. F. In +M and +M+EPDCs conditions, when directional outgrowth was detected (green bars in E), the density of directional neurite sprouting towards myocardium was quantified with NeuriteJ. The normalized

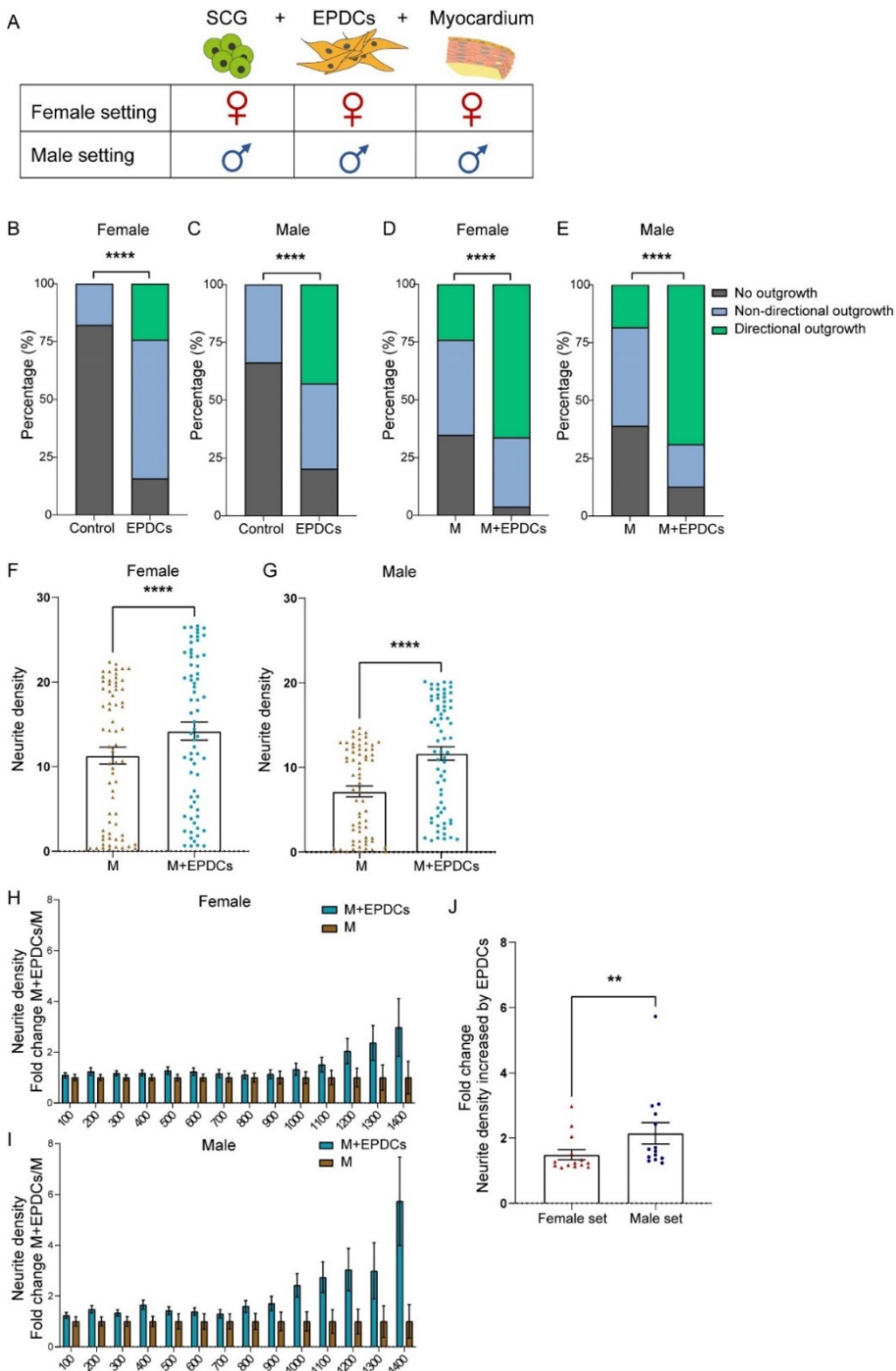
density of directional neurites at the length from 50 μm to 1700 μm (interval=25 μm) is shown as a bar plot; each dot represents an average neurite density at each length. $n=48$ for +M, $n=144$ for +M+EPDCs. Paired t-test was applied to detect the difference, **** $P < .0001$.

Directional neurite outgrowth is significantly higher in male than in female setting

In order to study sex differences in outgrowth of sympathetic neurites, including the enhancing effect of EPDCs on directional neurite outgrowth towards myocardium, we compared co-cultures with an all-female setting and an all-male setting (Fig. 3A). In both the female and male settings, co-cultures of ganglia and EPDCs showed that EPDCs significantly increase sympathetic neurite outgrowth (Fig. 3B, C). Co-culture with myocardium and EPDCs showed significant promotional effects of the EPDCs on the occurrence of directional neurite outgrowth in both female and male sets (Fig. 3D, E).

Quantification of the density of neurites growing directionally towards the myocardium in the absence of EPDCs (+M) or presence of EPDCs (+M+EPDCs) in either a female or male setting, is shown in Fig. 3F and 3G. These experiments confirmed that EPDCs significantly enhance directional neurite outgrowth towards myocardium in both female and male settings. However, the directional neurite outgrowth increased by EPDCs seemed more prominent in the male setting (Fig. 3F, G). Indeed, comparing male and female neurite density (+M+EPDCs condition) showed a significantly more promotional effect of EPDCs on directional neurite outgrowth in the male compared to the female setting, with on average over the total neurite length a 2 fold increase in males, compared to 1.5 fold increase in females (Fig. 3H-J).

Figure. 3 The promotional effects of EPDCs on directional neurite growth is significantly higher in male. A. Schematic representation of the sex information of SCG, EPDCs and myocardium (M) that was utilized in each co-culture group (male and female settings). B-C. Comparison of the percentage of SCG showing neurite outgrowth in the SCG only (control) condition and in the SCG with EPDCs (+EPDCs) condition in the female group and male group. B. Female group, $n=78$ for control, $n=70$ for +EPDCs condition. C. Male group, $n=77$ for control, $n=84$ for +EPDCs condition. Chi-square test was applied to detect the difference among groups, **** $P < .0001$. D-E. Comparison of the percentage of SCG showing neurite outgrowth in SCG in the presence of myocardium (+M) or SCG in the presence of myocardium and EPDCs (+M+EPDCs) in female and male groups. D. Results in the female group, $n=95$ for +M, $n=80$ for +M+EPDCs. E. Results in the male group, $n=87$ for +M, $n=87$ for +M+EPDCs. Chi-square test was applied to detect the difference among groups, **** $P < .0001$. F-G. In +M and +M+EPDCs conditions, the normalized density of directional neurites at the length from 50 μm to 1700 μm (interval=25 μm) is shown in the bar plot; each dot represents an average neurite density at each length. F. In the female group, $n=22$ for +M, $n=49$ for +M+EPDCs. G. In the male group, $n=18$ for +M, $n=59$ for +M+EPDC. Paired t-test was applied to detect the difference between +M and +M+EPDCs conditions, **** $p < .0001$. H-I. Directional neurite density sprouted from SCG cultured in M+EPDCs condition normalized to the averaged directional neurites density of the +M condition in female and male groups. J. Increase of the directional neurite sprouting by EPDCs at the length from 100 μm to 1400 μm (interval=100 μm) is shown in the bar plot. Paired t-test was applied, ** $p < 0.01$. (Figure.3 is on the next page)

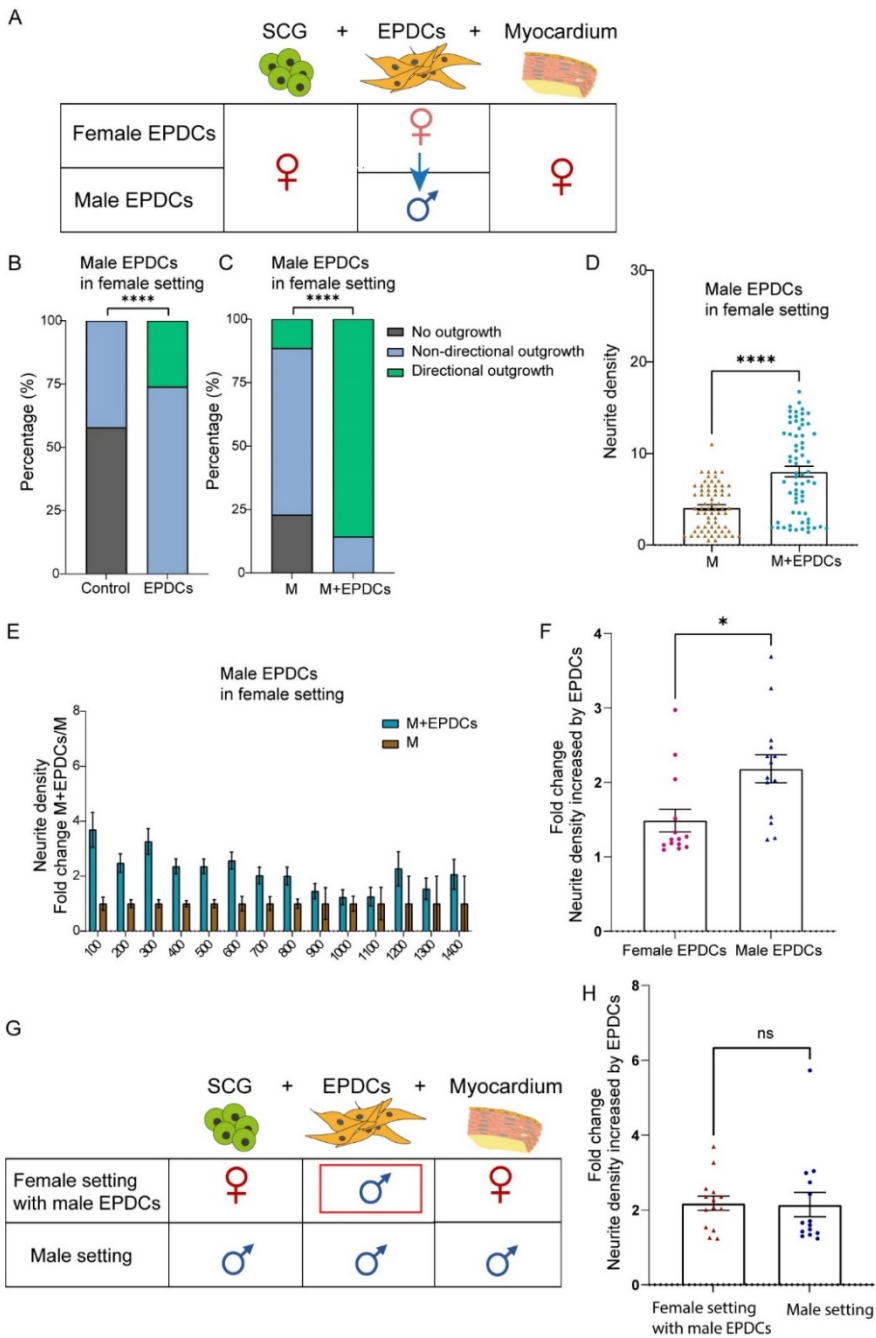


Male EPDCs in a female setting result in an increased sympathetic neurite growth towards myocardium

As we found a significant larger promotional effect of EPDC on directional neurite outgrowth in the male experimental setting, we hypothesized that male EPDCs would have a similar effect in a female experimental setting. To assess this, we replaced the EPDCs in the female setting with male EPDCs, as illustrated in **Fig. 4A**. Results show that the outgrowth of female sympathetic neurite outgrowth could also be significantly induced by the presence of male EPDCs (**Fig. 4B**), and these male EPDCs in the female setting also displayed significant enhancing effects on the occurrence of directional neurite outgrowth towards myocardium (**Fig. 4C and 4D**), similar to what was seen in the all-male setting. Comparing the neurite density between male and female EPDCs in a female setting, we observed a higher sympathetic neurite outgrowth towards myocardium in the presence of male EPDCs (**Fig. 4E and 4F**). Moreover, comparing this co-culture containing male EPDCs in a female setting with an all-male setting showed no difference in the neurite density of the directional sympathetic outgrowth towards myocardium induced by male EPDCs (**Fig. 4G and 4H**). Collectively, these data demonstrate that the enhancing effect of male EPDCs in a female setting on sympathetic neurite growth towards myocardium, is not due to a lack of neurite outgrowth capacity of the female SCG, but rather due to a less robust promotional effect of female EPDCs as compared to male EPDCs on neurite outgrowth.

3

Figure. 4 Male EPDCs in a female setting highly promote sympathetic neurite growth towards myocardium. A. Schematic representation of the sex information of SCG, EPDCs and myocardium (M) that was used in each co-culture group (male or female EPDCs in female setting). B. Comparison of the percentage of SCG showing neurite outgrowth in the control condition and in the EPDC condition in the male EPDCs (in a female setting) group. n=19 for control, n=23 for +EPDCs condition. C. Comparison of the percentage of SCG showing neurite outgrowth in the presence of myocardium (+M) or SCG in the presence of myocardium and male EPDCs (+M+EPDCs) in the female setting. n=35 for +M, n=35 for +M+EPDCs. Chi-square test was applied to detect the difference among groups, ****P < .0001. D. In +M and +M+EPDCs conditions of male EPDCs group (in a female setting), the normalized density of directional neurites at the length from 50 μ m to 1400 μ m (interval=100 μ m) is shown in the bar plot; each dot represents an average neurite density at each length. n= 4 for +M, n= 20 for +M+EPDC. Paired t-test was applied to detect the difference between +M and +M +EPDCs conditions, **** p < .0001. E. Directional neurite density sprouted from SCG cultured in M+EPDCs condition normalized to the averaged directional neurites density of the +M condition in male EPDCs group. F. The increase of the directional neurite sprouting by male EPDCs at the length from 100 μ m to 1400 μ m (interval=100 μ m) is shown. Paired t-test was applied, * p<0.05. G-H. Comparison of male EPDCs in the female setting, with the male setting. ns, no significant difference. (Figure.4 is on the next page)



Differential expression of SLIT2 between male and female EPDCs

As we found a more robust capacity of male EPDCs to stimulate neurite outgrowth in comparison to female EPDCs, we next assessed the difference in gene expression between male and female EPDC by RNA sequencing and differential gene expression analysis. This revealed differentially higher and lower expressed genes in males compared to female EPDCs (**Supplemental Table 1**), which might contribute to the sex difference of EPDCs in promoting directional neurite growth. One of the genes showing a differential expression was SLIT2, that is known to regulate axon growth during central nervous system development [26, 27]. Immunoblot analysis confirmed that female EPDCs had more cell-associated SLIT2 protein (**Fig. 5**), which was paralleled by more SLIT2 in cell culture supernatants of female EPDCs compared to cell culture supernatants of male EPDCs (**Fig. 5**).

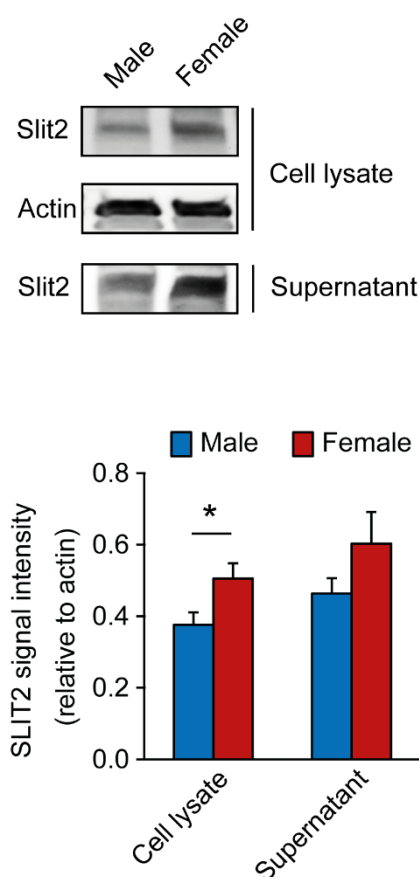


Figure. 5 Western blotting of SLIT2 in male and female EPDCs. Western blot images and analysis of SLIT2 expression in male (n=5) and female (n=4) mesenchymal EPDCs and secreted SLIT2 in corresponding culturing supernatant. * P<0.05.

DISCUSSION

The influence of sex in the prevalence and outcomes of cardiovascular disease has increasingly been recognized over the past decades. In line with this, a growing number of researchers acknowledges the relevance of taking sex into account in both clinical and basic science. We have previously shown a stimulating role of mesenchymal EPDCs on outgrowth of SCG *in vitro* [17], but did not take sex of the cell donor into account yet. In the present study we performed co-cultures of sympathetic ganglia with myocardium and mesenchymal EPDCs to specifically study the effect of the sex of EPDCs on cardiac innervation. Key findings of our study are: i) Cryo-preserved EPDCs promote sympathetic neurite outgrowth *in vitro* and increase the directional neurite projection towards myocardium; ii) In the presence of EPDCs, male SCG exhibit higher cardiac sympathetic outgrowth than female SCG; iii) Male EPDCs in a female setting can increase the cardiac sympathetic neurite outgrowth to a level that is comparable to the level of outgrowth in an entirely male environment; And iv) The SLIT2/ROBO-pathway is proposed as a potential candidate influencing these differential findings in male and female EPDCs.

Findings of the current study have potential clinical implications. There are overt sex-differences in the occurrence of clinical arrhythmias, with a general higher tendency of ventricular tachycardia and sudden cardiac death to occur in males [28]. In addition, sex differences in autonomic function, of relevance for a.o. cardiac repolarization, have been shown [29, 30]. This is of interest in the light of the phenomenon of sympathetic hyperinnervation, that is increasingly recognized as a mechanism of ventricular tachycardia and sudden cardiac death in structural heart disease [31, 32].

Cardiac autonomic ganglia and nerve fibers have their developmental origin in the neural crest, multipotent cells that derive from the crest of the embryonic neural plate [33, 34]. Already in utero, sex differences in autonomic cardiac function have been observed [35]. Ventricular autonomic innervation develops in parallel with ventricular vascularization, guided by neurotrophic factors [36]. We have previously shown a pivotal role of the epicardium in the development of the cardiac autonomic nerve system [37], a study that initiated the concept of a potential role of the epicardium in cardiac autonomic innervation. Whereas in the healthy adult heart the epicardium is considered as a quiescent layer, which can become activated in response to pathological triggers, such as MI [38]. In mouse models, experimentally-induced MI re-activates the epicardium, both endogenous and transplanted exogenous human EPDCs migrate to the infarcted area and contribute to neovascularization and amelioration of LV function [38-41]. In many of these animal studies, sex has not been taken into account. As MI is still the number one cause of death in the western countries, not only in men, but at higher age, after menopause, also in women [42], this is certainly a subject that deserves

attention, as is increasingly recognized [43]. Reperfusion therapy after MI has significantly reduced mortality and morbidity, but there is still a high risk of early ventricular arrhythmias and mortality. Next to the mechanism of re-entry in the border zone [44], this has in the past decades increasingly been associated with sympathetic hyperinnervation, also an early event after MI, starting within a few hours to several weeks after the ischemic event. Sympathetic hyperinnervation, defined as a superfluous increase of sympathetic fibers in the heart after MI, has been linked to sympathetic overactivity with a risk of ventricular arrhythmias [45-47]. Although data is still scarce, several studies have indicated that post-MI arrhythmias induced by sympathetic hyperinnervation are more severe in males than in females [6, 48]. Although our experiments were performed in an *in-vitro* non-MI setting, results of our co-cultures of sympathetic autonomous ganglia with ventricular myocardium and activated EPDCs, are in line with these clinical observations, showing a higher directional sympathetic neurite projection towards the myocardium in male than in female.

In addition to the evaluation of sex differences in sex-matched conditions (the so-called female setting and male setting), we aimed to study whether the observed difference in outgrowth between male and female tissues was attributable to a diminished capacity of female ganglia to grow, or whether this was caused by the “female” environment. We therefore tested the hypothesis that female ganglia would show a similar growth capacity as male ganglia, in the presence of male EPDCs. Results showed that co-culturing male EPDCs in a female environment (i.e. with female myocardium and female SCG) causes an increase in cardiac sympathetic neurite outgrowth to a level that is comparable to the level of outgrowth in an entirely male environment. In line with this, we observed a lower expression of SLIT2 in male EPDCs as compared to female EPDCs. SLIT2 is a member of a family of large extracellular matrix (ECM) glycoproteins and has been described as a chemorepellent factor for axonogenesis in motor neurons [49-52]. Inhibition studies of the SLIT2/ROBO signaling pathway will be necessary to determine its exact role in epicardial stimulation of cardiac innervation and the role of sex therein.

Cryo-preserved versus non-cryopreserved EPDCs. For quantification of our results, we have used so called “directional outgrowth” as parameter, defined as the outgrowth in the quadrant bordering the target tissue, i.e. the myocardium. In our previous study, using non-cryopreserved EPDCs, we did not observe directional outgrowth towards EPDCs, but only towards the myocardium [17]. Of interest, in our current study design, we used cryopreserved EPDCs, due to a lack of sufficient supply of fresh EPDCs in the past years, partly attributable to the downscaling of surgical procedures during the Covid19 pandemic. As expected, both cryo-preserved EPDCs and non-cryopreserved EPDCs could promote sympathetic neurite outgrowth. However, in contrast to our previous study, we observed that cryo-preserved

EPDCs could also attract neurite projections, i.e. directional outgrowth was observed in the EPDC-SCG cultures, in the absence of myocardium. As these findings might indicate a differential expression of axonal guidance and attraction related factors in cryo-preserved versus non-cryopreserved EPDCs, we performed RNA seq of both types (i.e. cryo- versus non-cryopreserved EPDCs). RNA sequencing and DGE analysis of 4 pairs of cryo-preserved EPDCs versus non-cryopreserved EPDCs indeed indicated differentially expressed axonogenesis related genes, including SEMA4D, PTPRO. PTPRO (protein tyrosine phosphatase receptor type O), is known to support axonogenesis of the nervous system as well as NGF-dependent neuronal outgrowth [53, 54], and this transmembrane receptor is required in growing neurons. The role of PTPRO in EPDCs is currently unknown. SEMA4D, as a member of Semaphorin family of soluble and transmembrane proteins, participates in multiple key cellular functions including axon guidance and morphogenesis [55]. Although not the focus of our current study, further research is needed to evaluate potential effects of cryo-preservation on neurotrophic function of EPDCs.

Conclusions, clinical implications and future perspectives

In summary, in the current study, we show a stimulatory effect of cryopreserved EPDCs on neurite outgrowth *in vitro*. Our co-cultures in female and male settings demonstrate that sympathetic nerve outgrowth and density differs between male and female, with a higher stimulatory effect of male - as compared to female - EPDCs. This differential effect could be neutralized by changing the sex of the EPDCs. We propose the SLIT2/ROBO pathway as a potential candidate involved in these sex-differences observed.

Although our results are preliminary and require validation in broader experimental settings, our data underline the potential relevance of sex differences in post-MI arrhythmias related cardiac hyperinnervation. In addition, results indicate that the sex of the individuals that EPDCs are derived from can influence the response significantly with respect to the amount of outgrowth and neurite density. Considering the current focus on cell therapy, including induced pluripotent stem cells, cardiomyocyte progenitor cells and EPDCs, in preserving heart function after cardiac damage [56, 57], we propose that sex should be taken into account when considering injection of cells for cell therapy in male and female patients.

Future directions. In the present study we focused on the influence of the sex of EPDCs in cardiac sympathetic innervation *in vitro*, using 3D co-cultures with sympathetic ganglia, myocardium and EPDCs. As a next step, we aim to further validate our results by performing SLIT2 knock down and overexpression in male and female EPDCs and evaluate the presence of the receptors of Slit2 (ROBO receptors) on cardiac sympathetic autonomous ganglia. In addition, the role of hormones deserve more attention. Whether these sex differences are

detectable in cardiac sympathetic activity *in vivo* or affect prognosis of patients suffering MI also requires further study and validation.

AUTHOR CONTRIBUTIONS

All authors contributed to the study conception and design. The experiments were designed and performed by Y.G. and J.M.v.G., analyzed by Y.G and supervised by M.R.M.J. and M.C.d.R. RNA-seq analysis was performed by R.M and Y.G. The first draft of the manuscript was written by Y.G., J.M.v.G., M.R.M.J., M.C.d.R. All authors commented on the manuscript. All authors have read and agreed to the published version of the manuscript.

FUNDING

This work is supported by the Netherlands Organization for Scientific Research (NWO) [016.196.346 to M.R.M.J.] and in part by European Research Area Network on Cardiovascular Diseases and Dutch Heart Foundation [038 MISsCVD 2018T095 to J.M.v.G.] and ZonMW [84920 Size Matters to M.C.d.R].

ACKNOWLEDGMENTS

We are grateful to Tessa van Herwaarden (Department of Cell and Chemical Biology, LUMC, Leiden, The Netherlands) for her help with isolating primary human EPDCs.

CONFLICTS OF INTEREST

The authors declare no conflict of interest.

REFERENCES

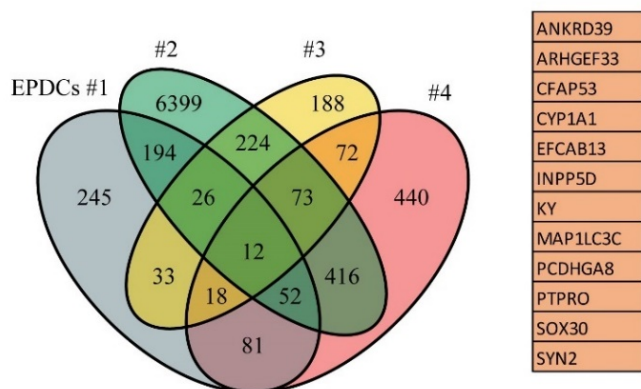
1. Zipes, D.P. and H.J. Wellens, *Sudden cardiac death*. Circulation, 1998. 98(21): p. 2334-51.
2. Myerburg, R.J. and M.J. Junttila, *Sudden cardiac death caused by coronary heart disease*. Circulation, 2012. 125(8): p. 1043-52.
3. Davis, E., et al., "*Mind the gap*" acute coronary syndrome in women: A contemporary review of current clinical evidence. International Journal of Cardiology, 2017. 227: p. 840-849.
4. EUGenMed, T., et al., *Gender in cardiovascular diseases: impact on clinical manifestations, management, and outcomes*. European Heart Journal, 2015. 37(1): p. 24-34.
5. Burger, I.A., et al., *Age- and sex-dependent changes in sympathetic activity of the left ventricular apex assessed by 18F-DOPA PET imaging*. PLoS One, 2018. 13(8): p. e0202302.
6. Dart, A.M., X.-J. Du, and B.A. Kingwell, *Gender, sex hormones and autonomic nervous control of the cardiovascular system*. Cardiovascular Research, 2002. 53(3): p. 678-687.
7. Smetana, P. and M. Malik, *Sex differences in cardiac autonomic regulation and in repolarisation electrocardiography*. Pflügers Archiv - European Journal of Physiology, 2013. 465(5): p. 699-717.
8. Regitz-Zagrosek, V., et al., *Gender in cardiovascular diseases: impact on clinical manifestations, management, and outcomes*. Eur Heart J, 2016. 37(1): p. 24-34.
9. Curtis, A.B. and D. Narasimha, *Arrhythmias in women*. Clin Cardiol, 2012. 35(3): p. 166-71.
10. Kannel, W.B., et al., *Sudden coronary death in women*. Am Heart J, 1998. 136(2): p. 205-12.
11. Wittnich, C., et al., *Sex differences in myocardial metabolism and cardiac function: an emerging concept*. Pflügers Archiv - European Journal of Physiology, 2013. 465(5): p. 719-729.
12. Ajijola, O.A., et al., *Extracardiac Neural Remodeling in Humans With Cardiomyopathy*. 2012. 5(5): p. 1010-1116.
13. Nguyen, B.L., et al., *Acute myocardial infarction induces bilateral stellate ganglia neural remodeling in rabbits*. Cardiovasc Pathol, 2012. 21(3): p. 143-8.
14. Ajijola, O.A., et al., *Remodeling of stellate ganglion neurons after spatially targeted myocardial infarction: Neuropeptide and morphologic changes*. Heart Rhythm, 2015. 12(5): p. 1027-35.
15. Bayles, R.G., et al., *Transcriptomic and neurochemical analysis of the stellate ganglia in mice highlights sex differences*. Sci Rep, 2018. 8(1): p. 8963.
16. Bayles, R.G., et al., *Sex differences in sympathetic gene expression and cardiac neurochemistry in Wistar Kyoto rats*. PLoS One, 2019. 14(6): p. e0218133.
17. Ge, Y., et al., *Human epicardium-derived cells reinforce cardiac sympathetic innervation*. J Mol Cell Cardiol, 2020. 143: p. 26-37.
18. Cao, J. and K.D. Poss, *The epicardium as a hub for heart regeneration*. Nature reviews. Cardiology, 2018. 15(10): p. 631-647.
19. Smits, A.M., E. Dronkers, and M.-J. Goumans, *The epicardium as a source of multipotent adult cardiac progenitor cells: Their origin, role and fate*. Pharmacological Research, 2018. 127: p. 129-140.
20. Quijada, P., M.A. Trembley, and E.M. Small, *The Role of the Epicardium During Heart Development and Repair*. Circulation Research, 2020. 126(3): p. 377-394.
21. Dronkers, E., et al., *The Isolation and Culture of Primary Epicardial Cells Derived from Human Adult and Fetal Heart Specimens*. J Vis Exp, 2018(134).
22. Torres-Espín, A., et al., *Neurite-J: an image-J plug-in for axonal growth analysis in organotypic cultures*. J Neurosci Methods, 2014. 236: p. 26-39.
23. Dobin, A., et al., *STAR: ultrafast universal RNA-seq aligner*. Bioinformatics, 2013. 29(1): p. 15-21.

24. Love, M.I., W. Huber, and S. Anders, *Moderated estimation of fold change and dispersion for RNA-seq data with DESeq2*. *Genome Biol*, 2014. 15(12): p. 550.
25. Mi, H., et al., *PANTHER version 14: more genomes, a new PANTHER GO-slim and improvements in enrichment analysis tools*. *Nucleic Acids Res*, 2019. 47(D1): p. D419-d426.
26. Lin, L., Y. Rao, and O. Isacson, *Netrin-1 and slit-2 regulate and direct neurite growth of ventral midbrain dopaminergic neurons*. *Mol Cell Neurosci*, 2005. 28(3): p. 547-55.
27. Battisti, A.C., et al., *A subset of chicken statoacoustic ganglion neurites are repelled by Slit1 and Slit2*. *Hear Res*, 2014. 310: p. 1-12.
28. Ehdaie, A., et al., *Sex Differences in Cardiac Arrhythmias: Clinical and Research Implications*. *Circ Arrhythm Electrophysiol*, 2018. 11(3): p. e005680.
29. Dart, A.M., X.J. Du, and B.A. Kingwell, *Gender, sex hormones and autonomic nervous control of the cardiovascular system*. *Cardiovasc Res*, 2002. 53(3): p. 678-87.
30. Smetana, P. and M. Malik, *Sex differences in cardiac autonomic regulation and in repolarisation electrocardiography*. *Pflugers Arch*, 2013. 465(5): p. 699-717.
31. Nederend, I., et al., *Postnatal Cardiac Autonomic Nervous Control in Pediatric Congenital Heart Disease*. *Journal of cardiovascular development and disease*, 2016. 3(2): p. 16.
32. Zipes, D.P. and M. Rubart, *Neural modulation of cardiac arrhythmias and sudden cardiac death*. *Heart rhythm*, 2006. 3(1): p. 108-113.
33. Lumb, R. and Q. Schwarz, *Sympathoadrenal neural crest cells: the known, unknown and forgotten?* *Dev Growth Differ*, 2015. 57(2): p. 146-57.
34. Végh, A.M.D., et al., *Part and Parcel of the Cardiac Autonomic Nerve System: Unravelling Its Cellular Building Blocks during Development*. *J Cardiovasc Dev Dis*, 2016. 3(3).
35. Gonçalves, H., et al., *Gender-specific evolution of fetal heart rate variability throughout gestation: A study of 8823 cases*. *Early Hum Dev*, 2017. 115: p. 38-45.
36. Nam, J., et al., *Coronary veins determine the pattern of sympathetic innervation in the developing heart*. *Development*, 2013. 140(7): p. 1475-85.
37. Kelder, T.P., et al., *The epicardium as modulator of the cardiac autonomic response during early development*. *J Mol Cell Cardiol*, 2015. 89(Pt B): p. 251-9.
38. Winter, E.M., et al., *Preservation of left ventricular function and attenuation of remodeling after transplantation of human epicardium-derived cells into the infarcted mouse heart*. *Circulation*, 2007. 116(8): p. 917-27.
39. Smart, N., K.N. Dubé, and P.R. Riley, *Epicardial progenitor cells in cardiac regeneration and neovascularisation*. *Vascul Pharmacol*, 2013. 58(3): p. 164-73.
40. Limana, F., M.C. Capogrossi, and A. Germani, *The epicardium in cardiac repair: from the stem cell view*. *Pharmacol Ther*, 2011. 129(1): p. 82-96.
41. van Wijk, B., et al., *Cardiac regeneration from activated epicardium*. *PLoS One*, 2012. 7(9): p. e44692.
42. WHO. *The top 10 causes of death*. 2020; Available from: <https://www.who.int/news-room/fact-sheets/detail/the-top-10-causes-of-death>.
43. Korzick, D.H. and T.S. Lancaster, *Age-related differences in cardiac ischemia-reperfusion injury: effects of estrogen deficiency*. *Pflugers Arch*, 2013. 465(5): p. 669-85.
44. de Bakker, J.M., et al., *Slow conduction in the infarcted human heart. 'Zigzag' course of activation*. *Circulation*, 1993. 88(3): p. 915-26.
45. Zhou, S., et al., *Mechanisms of Cardiac Nerve Sprouting After Myocardial Infarction in Dogs*. *Circulation Research*, 2004. 95(1): p. 76-83.
46. Chen, P.-S., et al., *Sympathetic nerve sprouting, electrical remodeling and the mechanisms of sudden cardiac death*. *Cardiovascular Research*, 2001. 50(2): p. 409-416.

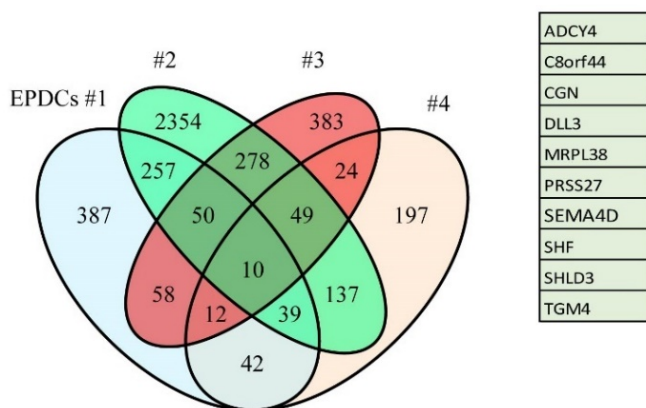
47. Yokoyama, T., et al., *Quantification of sympathetic hyperinnervation and denervation after myocardial infarction by three-dimensional assessment of the cardiac sympathetic network in cleared transparent murine hearts*. PLoS One, 2017. 12(7): p. e0182072.
48. Du, X.J., et al., *Sympathetic activation triggers ventricular arrhythmias in rat heart with chronic infarction and failure*. Cardiovasc Res, 1999. 43(4): p. 919-29.
49. Ba-Charvet, K.T.N., et al., *Slit2-Mediated Chemorepulsion and Collapse of Developing Forebrain Axons*. Neuron, 1999. 22(3): p. 463-473.
50. Niclou, S.P., L. Jia, and J.A. Raper, *Slit2 is a repellent for retinal ganglion cell axons*. The Journal of neuroscience : the official journal of the Society for Neuroscience, 2000. 20(13): p. 4962-4974.
51. Tanno, T., et al., *Expression of a chemorepellent factor, Slit2, in peripheral nerve regeneration*. Biosci Biotechnol Biochem, 2005. 69(12): p. 2431-4.
52. Li, Y., et al., *Slit2/Robo1 promotes synaptogenesis and functional recovery of spinal cord injury*. Neuroreport, 2017. 28(2): p. 75-81.
53. Beltran, P.J., J.L. Bixby, and B.A. Masters, *Expression of PTPRO during mouse development suggests involvement in axonogenesis and differentiation of NT-3 and NGF-dependent neurons*. J Comp Neurol, 2003. 456(4): p. 384-95.
54. Chen, B. and J.L. Bixby, *A novel substrate of receptor tyrosine phosphatase PTPRO is required for nerve growth factor-induced process outgrowth*. J Neurosci, 2005. 25(4): p. 880-8.
55. Koncina, E., et al., *Role of semaphorins during axon growth and guidance*. Adv Exp Med Biol, 2007. 621: p. 50-64.
56. Abdelwahid, E., et al., *Stem cell therapy in heart diseases: a review of selected new perspectives, practical considerations and clinical applications*. Curr Cardiol Rev, 2011. 7(3): p. 201-12.
57. Hashimoto, H., E.N. Olson, and R. Bassel-Duby, *Therapeutic approaches for cardiac regeneration and repair*. Nature Reviews Cardiology, 2018. 15(10): p. 585-600.

SUPPLEMENTAL FIGURES

A



B



Supplemental Fig. 1 Differential gene expression analysis between cryo-preserved versus non-cryopreserved EPDCs. A. Venn diagram of 4 donate-derived EPDCs (EPDCs#1, #2, #3, #4) shows 12 common protein-coding genes that up-regulated in cryo-preserved EPDCs compared to non-cryo-preserved EPDCs. B. Venn diagram of 4 donor-derived EPDCs (EPDCs#1, #2, #3, #4) shows the 10 common protein-coding genes down-regulated in cryo-preserved EPDCs compared to non-cryo-preserved EPDCs. The detected up- and down-regulated genes are listed in the right panels.

Genes	adjusted P value	LogFC
ERVV-1	5,68E-05	24,02632
UPK3B	4,12E-02	6,216895
LRRN4	6,74E-03	5,726742
HTT	9,73E-03	4,135993
KRT19	2,31E-02	3,035461
ITGA7	1,70E-02	2,529226
SLIT2	4,84E-02	1,134702
PKD1P5	2,35E-02	-3,29221
ID1	2,40E-03	-3,49841
EIF1AY	6,59E-03	-7,8285
NLGN4Y	6,59E-03	-7,87928
TXLNGY	6,04E-03	-7,92583
KDM5D	2,03E-03	-8,43109
ZFY	2,03E-03	-8,45093
RPS4Y1	2,03E-03	-8,47819
USP9Y	1,28E-03	-8,84273

Supplemental Table. 1 DGE analysis of male EPDCs between female EPDCs. Highly differentially expressed genes in male EPDCs as compared to female EPDCs are shown in the table. Green highlights indicate the genes are lower expressed in male EPDCs while the red indicate the higher expressed gene in male than in female.

PART II

BREAKING THE LIMITS OF EPDCs



4

GENERATION, CHARACTERIZATION AND APPLICATION OF INDUCIBLE PROLIFERATIVE ADULT HUMAN EPICARDIUM-DERIVED CELLS

Yang Ge^{*1,2}, Anke M. Smits^{*3}, Jia Liu^{2,4}, Juan Zhang², Daniel Pijnappels¹, Thomas van Brakel⁵, Marie-José T.H. Goumans^{3§}, Monique RM. Jongbloed^{**1,2}, Antoine A.F. de Vries^{**2},

* Authors contributed equally

** Authors contributed equally

§ Corresponding author

1. Department of Anatomy & Embryology, Leiden University Medical Center, Einthovenweg 20, 2333 ZC Leiden, The Netherlands;

2. Department of Cardiology, Leiden University Medical Center, Albinusdreef 2, 2333 ZA Leiden, The Netherlands;

3. Department of Cell and Chemical Biology, Leiden University Medical Center, Einthovenweg 20, 2333 ZC Leiden, The Netherlands;

4. Central Laboratory, Longgang District People's Hospital of Shenzhen & The Third Affiliated Hospital of The Chinese University of Hong Kong, 518172 Shenzhen, China;

5. Department of Thoracic Surgery, Leiden University Medical Center, Albinusdreef 2, 2333 ZC Leiden, The Netherlands;

Cells. 2021 Aug 12;10(8):2064. doi: 10.3390/cells10082064.

ABSTRACT

Rationale: In recent decades, the great potential of human epicardium-derived cells (EPDCs) as an endogenous cell source for cardiac regeneration has been recognized. The limited availability and low proliferation capacity of primary human EPDCs and phenotypic differences between EPDCs obtained from different individuals hampers their reproducible use for experimental studies.

Aim: To generate and characterize inducible proliferative adult human EPDCs for use in fundamental and applied research.

Methods and results: Inducible proliferation of human EPDCs was achieved by doxycycline-controlled expression of simian virus 40 large T antigen (LT) with a repressor-based lentiviral Tet-On system. In the presence of doxycycline, these inducible EPDCs (iEPDCs) displayed high and long-term proliferation capacity. After doxycycline removal, LT expression ceased and the iEPDCs regained their cuboidal epithelial morphology. Similar to primary EPDCs, iEPDCs underwent an epithelial-to-mesenchymal transition (EMT) after stimulation with transforming growth factor β 3. This was confirmed by reverse transcription-quantitative polymerase chain reaction analysis of epithelial and mesenchymal marker gene expression and (immuno) cytochemical staining. Collagen gel-based cell invasion assays demonstrated that mesenchymal iEPDCs, like primary EPDCs, possess increased invasion and migration capacities as compared to their epithelial counterparts. Mesenchymal iEPDCs co-cultured with sympathetic ganglia stimulated neurite outgrowth similarly to primary EPDCs.

Conclusion: Using an inducible LT expression system, inducible proliferative adult human EPDCs were generated displaying high proliferative capacity in the presence of doxycycline. These iEPDCs maintain essential epicardial characteristics with respect to morphology, EMT ability, and paracrine signaling following doxycycline removal. This renders iEPDCs a highly useful new in vitro model for studying human epicardial properties.

Keywords

epicardium-derived cells (EPDCs); conditional immortalization; simian virus 40 large T antigen (LT); epithelial-to-mesenchymal transition (EMT)

INTRODUCTION

The cardiac outer layer, or epicardium, is composed of multifunctional and multipotent cells with important roles during fetal development [1–3]. In the healthy adult heart, epicardial cells are quiescent and have a squamous (flat) morphology. Studies in animal models have shown that epicardial cells become activated in response to pathological triggers, such as myocardial infarction [4–6]. Epicardial cells then adopt a cuboidal appearance, undergo epithelial-to-mesenchymal transition (EMT), migrate into the subepicardial space, and subsequently into the myocardium [4]. After migration, epicardial cells are referred to as epicardium-derived cells (EPDCs). These EPDCs can differentiate into coronary smooth muscle cells and cardiac fibroblasts [5,7]. In addition, EPDCs have strong paracrine effects, and factors secreted by EPDCs have been shown to promote angiogenesis, reduce infarct size, and improve cardiac function [8].

Given the ability of EPDCs to (i) contribute to different cardiac cell lineages, (ii) produce beneficial paracrine factors for heart development and (iii) recapitulate an embryonic epicardial phenotype after cardiac damage in adult hearts, they are a highly interesting study object from a cardiac developmental and regenerative perspective. An increased understanding of epicardial cell properties and behavior could not only provide new insights into certain (congenital) heart diseases but also generate additional knowledge about the ability of epicardial cells to participate in human cardiac repair [9,10]. Our research group has previously established cell culture models based on primary human EPDCs that allowed us to investigate processes like EMT [11–13]. Furthermore, we found that the injection of human EPDCs into mouse infarcted myocardium improves cardiac function, leads to scar reduction, and induces angiogenesis likely through a paracrine mechanism [5,14,15]. Co-culturing human EPDCs with neuronal tissue showed that human EPDC-derived factors can influence the outgrowth of cardiac autonomic ganglia [16]. Human epicardial cells thus hold strong potential for cardiac regeneration therapy, but there are several challenges and pitfalls when using these cells. First, the relative scarcity of human epicardium and EPDC sources hampers the deeper investigation of EPDC function and their potential for cardiac repair. Furthermore, although we developed a reliable method for the isolation and expansion of EPDCs from human specimens [17], EPDCs possess limited proliferation capacity and tend to lose their epithelial phenotype within a few passages. In addition, the application of EPDCs derived from different patients and with different passage numbers, has likely contributed to the variable results obtained in *in vitro* experiments. These considerations inspired us to investigate whether conditional immortalization would allow the generation of lines of highly proliferative adult human EPDCs with preserved functionality. At present, the only immortalized EPDCs available are of rodent origin, isolated from transgenic mouse embryos obtained by crossing

wild type or Sm22 α -lacZ mice with the ImmortoMouse line, which harbors an H-2Kb promoter-driven expression unit directing the synthesis of a temperature-sensitive version of the simian virus 40 (SV40) large T antigen (LT) [18–20]. This is the first study to generate a polyclonal line of human EPDCs by applying a lentiviral vector (LV) expressing wild type LT in a doxycycline (Dox)-dependent manner. We designated the resulting cells inducible EPDCs (iEPDCs) and studied their proliferation capacity, their LT expression in the presence and absence of Dox, and their expression of epicardial genes after treatment with modulators of transforming growth factor β (TGF β) signaling. In addition, known functions of EPDCs, including EMT, migration and invasion, and simulation of neurite outgrowth, were explored to determine whether iEPDCs maintain the phenotypic and functional properties of the primary cells from which they are derived.

METHODS

LV production

Primary human EPDCs were conditionally immortalized using the self-inactivating, vesicular stomatitis virus G protein-pseudotyped LV named LV.iHsUBC.LT-WT (for a map of the corresponding LV shuttle plasmid, see **Supplemental Figure S1**). LV.iHsUBC.LT-WT directs the Dox-dependent expression of wild type SV40 LT and only differs from the previously described LV.iHsUBC.LT-tsA58 [21] by harboring the coding sequence of wild type SV40 LT instead of the temperature-sensitive SV40 LT mutant tsA58. The production, purification, and concentration of LV particles was done essentially as described in [22].

Isolation and culture of primary human EPDCs

This study was conducted in accordance with the Ethical Principles of the Declaration of Helsinki 2013. Adult human atrial samples (auricles) were strictly anonymously collected as surgical waste material, transferred to an unlabeled tube, and delivered to the researcher without any additional information to guarantee the full anonymity of the tissues so as not to include or identify human subjects. Handling of human heart tissues was carried out according to the Dutch regulation for responsible use of human tissues for medical research purposes and the institutional Medical Ethics Committee ruled that the Medical Research Involving Human Subject Act (WMO) does not apply to the use of surgical waste material (reference number B12.017). Human EPDCs were dissociated from the specimens as previously described [17]. Briefly, the epicardium was carefully removed from the underlying myocardium and cut into small pieces followed by three rounds of 0.25% Trypsin-EDTA (25200056; Thermo Fisher Scientific, Bleiswijk, The Netherlands) incubation at 37 °C for 30 min in total. After digestion, the cell suspension was passed through a series of syringes of decreasing internal diameter

(19G to 22G) and through a 100- μ m BD Falcon cell strainer (BD Biosciences, Vianen, The Netherlands). Next, the cells were plated on dishes coated with 0.1% porcine gelatin (G1890; Sigma-Aldrich, St. Louis, MO, USA). Successful isolation of epithelial EPDCs was indicated by the recovery of cells with a cuboidal morphology. EPDCs were cultured in complete medium supplemented with the ALK5 kinase inhibitor SB431542 (SB, 10 μ M; Tocris Bioscience, Ellisville, MO, USA) to maintain an epithelial state. Complete medium is a 1:1 mixture of low glucose Dulbecco's modified Eagle's medium (10567014; Thermo Fisher Scientific) and medium 199 (31150022; Thermo Fisher Scientific) with 10% heat-inactivated fetal bovine serum (FBS; S1860-500; Biowest, Nuaille, France) and 1% 100 \times penicillin/streptomycin solution (15140122; Thermo Fisher Scientific).

Transduction of human EPDCs

The primary human EPDCs were first expanded for three passages to create a seed stock. Next, the cells were transduced with LV.HsUBC.LT-WT in the presence of 5 μ g/mL of DEAE-dextran (4198; Carl Roth, Karlsruhe, Germany) [23] to facilitate vector uptake. Twenty four hours after transduction, the LV-containing medium was replaced by complete medium supplemented with 10 μ M SB and 50 ng/mL Dox (D9891; Sigma-Aldrich) to induce LT expression. The medium containing SB and Dox was refreshed every two days. LT expression in iEPDCs in the presence of Dox was visualized by immunofluorescence staining.

Analysis of cell growth of primary and transduced EPDCs

Both primary and transduced EPDCs were cultured in medium supplemented with SB and 50 ng/mL Dox. When the cultures approached confluence, the cells were passaged at a splitting ratio of 1:8 (iEPDCs) or 1:2 (primary EPDCs). To compile cell growth curves, numbers of population doublings (PDs) were plotted against days in culture until the EPDCs lost their epithelial phenotype (i.e., cobblestone-like cell morphology).

To assess the cell proliferation rate of iEPDCs under different conditions, a Cell Counting Kit-8 (Dojindo Molecular Technologies, Rockville, MD, USA) was applied according to the manufacturer's protocol using cells of PD28. The iEPDCs were first cultured in complete medium supplemented with Dox and SB or only with SB for eight days. Next, the cells were seeded into 96-well culture plates at a density of 1000 cells/well and exposed to different culture conditions. At culture day 0, 1, 3, 5, 7, and 9, the production of WST-8 formazan in each well ($n = 3$ per condition) was measured as an indicator of viable cell number (**Figure 1E**).

Inducible LT expression upon Dox addition

To study the dynamical changes in LT expression following Dox removal, iEPDCs that had been maintained in complete medium with SB and Dox were seeded into a 96-well culture plate and given complete medium supplemented with SB but without Dox. After the indicated times of culture in Dox-free medium, the cells were fixed with 4% paraformaldehyde (104005; Merck Millipore, Darmstadt, Germany) for subsequent immunostaining with an LT-specific monoclonal antibody (see below). In parallel, iEPDCs that had been kept in Dox-free medium for 8 days were seeded into a 96-well culture plate and exposed for different time periods to Dox-containing complete medium with SB before being fixed for LT staining.

EMT assay

Primary EPDCs and iEPDCs were seeded in 96-well plates (for staining) and 6-well plates (for RNA isolation). After five days of culture in Dox-free complete medium without additives or in Dox-free complete medium supplemented with either SB (10 μ M; to maintain an epithelial phenotype) or TGF β 3 (1 ng/mL; to induce EMT), the cells were either processed for (immuno)cytochemical staining or used for RNA extraction. Total cellular RNA was isolated using the RNeasy Mini Kit (QIAGEN Benelux, Venlo, The Netherlands) according to the manufacturer's instruction. Afterwards, cDNA was synthesized with the aid of the iScript cDNA Synthesis Kit (Bio-Rad Laboratories, Lunteren, The Netherlands). Reverse transcription quantitative polymerase chain reactions (RT-qPCRs) were performed using iQ SYBR Green Supermix (Bio-Rad Laboratories) and the primer pairs (obtained from Integrated DNA Technologies, Leuven, Belgium) shown in **Supplemental Table S1**. The forward and reverse primer in each primer pair were targeting different exons and their specificity was confirmed by melting curve analysis and agarose gel electrophoresis of the amplification products. PCR amplification was performed in a CFX384 Touch Real-Time PCR Detection System (Bio-Rad Laboratories). For each primer pair, the amplification efficiency was determined using serial dilutions of target RNAs. The three most stable reference genes were chosen based on geNORM [24]. For each sample and for each target gene, RT-qPCR was performed in triplicate. Target gene expression was calculated using the amplification efficiency of the PCR product and normalized to the geometric mean of three reference genes (i.e., GAPDH, TBP, B2M) [24,25]. Depending on the experiment, samples were normalized to the SB-treated sample and results are shown as relative expression. Moreover, the RT-qPCR data of iEPDCs in **Supplemental Figure S3** are average values derived from the analysis of cells at PD25, -28, -30, and -35, i.e., each bar in this figure represents four biological replicates.

Scratch wound healing assay

Eight days after removal of Dox, the iEPDCs were cultured for five days in complete medium containing SB (10 μ M) or TGF β 3 (1 ng/mL) to keep epithelial iEPDCs or obtain mesenchymal iEPDCs, respectively. Next, the iEPDCs were seeded into a 96-well culture plate for a scratch wound healing assay at a density of 20,000 cells/well. Twenty four hours before making a scratch, the epithelial iEPDCs were given complete medium with or without SB while the mesenchymal EPDCs received complete medium with or without TGF β 3. The IncuCyte S3 Live Cell Analysis System (Sartorius Stedim Netherlands, Amersfoort, The Netherlands) was used to make the scratch and to image and analyze the cell migration according to the manufacturer's instructions.

Invasion assay

Eight days after removal of Dox, the iEPDCs were cultured for five days in complete medium containing SB (10 μ M) or TGF β 3 (1 ng/mL) to keep epithelial iEPDCs or obtain mesenchymal iEPDCs, respectively. Next, aggregates of 20,000 epithelial iEPDCs, mesenchymal iEPDCs, or primary EPDCs with a total volume of 30 μ L were formed by the hanging drop technique. Twenty four hours before the invasion assay started, the epithelial iEPDCs in the hanging drop were given complete medium with or without SB while the clumps of mesenchymal EPDCs received complete medium with or without TGF β 3. To measure their invasion ability, aggregates of primary EPDCs and of iEPDCs were placed in drops of 3 mg/mL rat tail collagen I (354236; Corning Life Sciences, Amsterdam, The Netherlands) and cultured for the indicated time periods in EPDC culture medium. Time-lapse images were captured immediately with the EVOS FL Auto 2 Imaging System (Thermo Fisher Scientific). The invasion distances of the cells away from the aggregates were measured with ImageJ 1.52p (National Institutes of Health [NIH], Bethesda, MA, USA).

Co-culture of primary EPDCs and iEPDCs with sympathetic ganglia

To further test the experimental applicability of iEPDCs, co-cultures of mesenchymal iEPDCs with sympathetic ganglia ($n = 10$) were performed, as was done previously with primary EPDCs [16]. Superior cervical ganglia were isolated from (E) 18.5-day C57BL/6J mouse embryos (Charles River Laboratories, 's-Hertogenbosch, The Netherlands, $n = 5$) and co-cultured with mesenchymal EPDCs (primary EPDCs of PD8 or iEPDCs of PD30 that had been cultured without Dox for 15 days) as described previously [16]. Ganglionic outgrowth was determined after six days of co-culturing by immunochemical staining for β 3 tubulin. All animal experiments were carried out according to the Guide for the Care and Use of Laboratory Animals published by

the NIH and approved by the Animal Ethics Committee of the Leiden University Medical Center (Leiden, The Netherlands, license number AVD1160020185325).

Immunofluorescence staining

Cells were fixed with 4% paraformaldehyde in phosphate-buffered saline (PBS), permeabilized with 0.5% Tween 20 (822184, Merck Millipore, Darmstadt, Germany) in PBS and non-specific epitopes were blocked with PBS containing 1% bovine serum albumin (A8022; Sigma-Aldrich) and 0.05% Tween 20. The monocultures of EPDCs were stained with the following primary antibodies: mouse anti-SV40 LT (Santa Cruz Biotechnology, Heidelberg, Germany; SC-147; 1:400) or rabbit anti-Wilms tumor 1 (WT1, marker for epicardial tissues) (Abcam, Cambridge, MA, USA; ab89901; 1:100). The co-cultures of EPDCs and neurons were stained with rabbit anti β 3 tubulin (Tubb3, marker for neural tissues) antibodies (Sigma-Aldrich; T2200; 1:500) overnight at 4 °C. After three rinses with 0.05% Tween 20 in PBS, bound primary antibodies were detected by incubation with Alexa Fluor 594-conjugated donkey anti-mouse IgG(H + L) (Thermo Fisher Scientific; A-21203; 1:250) or Alexa Fluor 488-conjugated donkey anti-rabbit IgG(H + L) (Thermo Fisher Scientific; A-21206; 1:250). For the detection of F-actin, Alexa Fluor 594-conjugated phalloidin (Thermo Fisher Scientific; A12381, 1:200) was used. Incubation with the secondary anti-bodies was done at room temperature and lasted for 1 hour (monocultures) or for 2.5 hours (co-cultures) and was followed by a single wash with PBS. DAPI (300 nM; D3571; Thermo Fisher Scientific) was used to stain nuclei. All images were captured with a Leica TCS SP8 confocal laser scanning microscope (Leica Microsystems, Wetzlar, Germany).

Statistics

Graphs are presented as mean \pm standard error of the mean (SEM). Gene expression, cell migration, and invasion were compared using one-way analysis of variance (ANOVA) (plus Tukey's multiple comparison test). The presence of neurite outgrowth in vehicle and EPDC co-culture groups was compared using a Chi-square test. GraphPad Prism (GraphPad Software, San Diego, CA, USA; version 8) was used for statistical analysis.

RESULTS

Generation of iEPDCs

Primary adult human EPDCs at PD3 were transduced with an LV mediating Dox-dependent expression of wild type LT to generate a polyclonal line of EPDCs with inducible proliferation capacity (**Supplemental Figure S1**). Immunofluorescence staining of primary and transduced EPDCs that were cultured in the presence of Dox showed LT expression in the transduced

EPDCs, while no LT was detected in the primary EPDCs (Figure 1A). In an attempt to preserve their epithelial phenotype, both the primary EPDCs and the iEPDCs were cultured in medium supplemented with the ALK5 kinase inhibitor SB to block endogenous TGF β signaling. This, however, could not prevent the primary EPDCs from undergoing EMT after only a few cell divisions, causing them to lose their epithelial cobblestone-like morphology as early as at PD5 (**Supplemental Figure S2A**). The phenotypic change of the primary EPDCs was accompanied by a strong reduction in proliferation capacity (**Figure 1B**). In contrast, the transduced cells (iEPDCs) were able to proliferate long-term without losing their cuboidal morphology. For iEPDCs, the earliest signs of EMT and loss of epithelial cobblestone-like morphology only occurred after PD51 (**Figure 1B, Supplemental Figure S2B**). These changes in iEPDC behavior coincided with an increase in the percentage of senescent cells as assessed by β -galactosidase staining (**Supplemental Figure S2C**).

To study the kinetics of Dox-dependent LT expression, iEPDCs were transferred from Dox-containing culture medium to Dox-free culture medium or vice versa and analyzed by immunostaining before (day 0) and 2, 4, 6, 8, and 10 days after medium change. While LT was highly expressed in iEPDCs cultured in the presence of Dox (**Figure 1C**, day 0), the omission of Dox resulted in a gradual decrease in the LT level in the first 4 days, and no obvious LT expression could be detected from day 6 onwards (**Figure 1C**). The addition of Dox to the culture medium of iEPDCs that had been maintained for 8 days in Dox-free culture medium induced LT expression. As is shown in Figure 1D, LT expression was first detectable 4 days after Dox addition and further increased afterwards to reach a plateau between day 8 and day 10 of culture in Dox-free medium.

Subsequently, the proliferation rate of iEPDCs in the presence and absence of Dox was quantified colorimetrically by measuring the bioreduction of WST-8. In primary adult human EPDCs, the addition of SB allows short-term in vitro expansion while maintaining their cuboidal epithelial morphology. Conversely, activation of the TGF β signaling cascade in primary adult human EPDCs stimulates the transition from an epithelial to a mesenchymal cell type and inhibits epicardial cell proliferation. [26] We therefore also tested the effects of SB and TGF β 3 treatment on the proliferation capacity of iEPDCs cultured in the presence and absence of Dox, as shown in **Figure 1E**. Exposure of iEPDCs to Dox invariably resulted in cell proliferation with the highest proliferation rate observed in the cells that were also treated with SB. The addition of TGF β 3 to the culture medium stimulated iEPDCs to undergo EMT and lowered the cell proliferation induced by Dox (**Figure 1F**). In contrast to the iEPDCs that were cultured with Dox, iEPDCs did not show apparent proliferation when kept in Dox-free medium (**Figure 1F**). Consistent with the kinetics of Dox-induced LT expression (**Figure 1D**), iEPDC proliferation started around four days after exposure to Dox (**Figure 1F**).

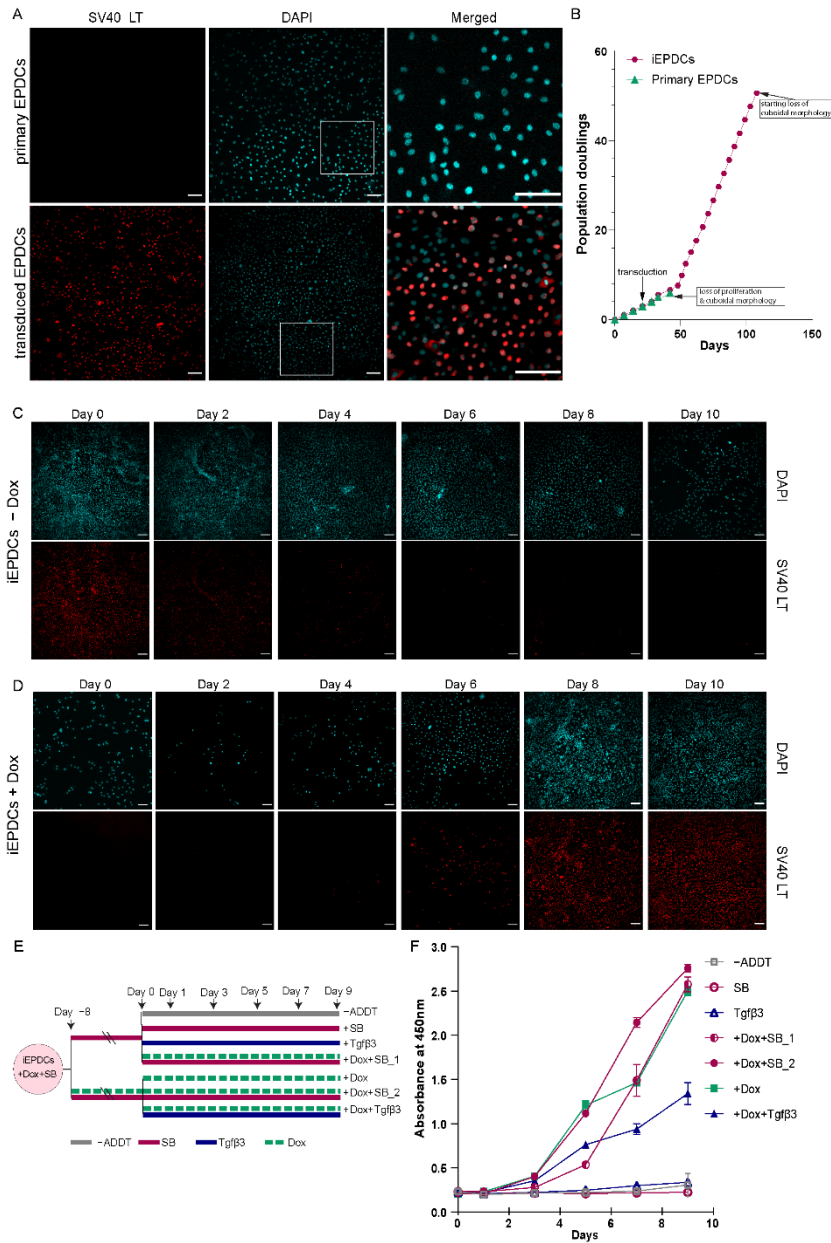


Figure 1. Generation of iEPDCs. (A) Confirmation of LT expression in iEPDCs (PD10) in the presence of Dox by immunofluorescent staining with anti-SV40 LT antibodies. (B) Growth curves of primary EPDCs and iEPDCs cultured in the presence of Dox. Recordings were ended when the EPDCs started to lose their cuboidal epithelial morphology. (C,D) Timeline of LT expression in iEPDCs after switching from Dox-containing to Dox-free culture medium (C) and vice versa (D). (E) Overview of the different pretreatments

and culture conditions to which the iEPDCs were exposed for cell proliferation analysis. (F) Quantification of the proliferation of iEPDCs under the conditions indicated in (E). Scale bar = 100 μ m. –ADDT = no additive.

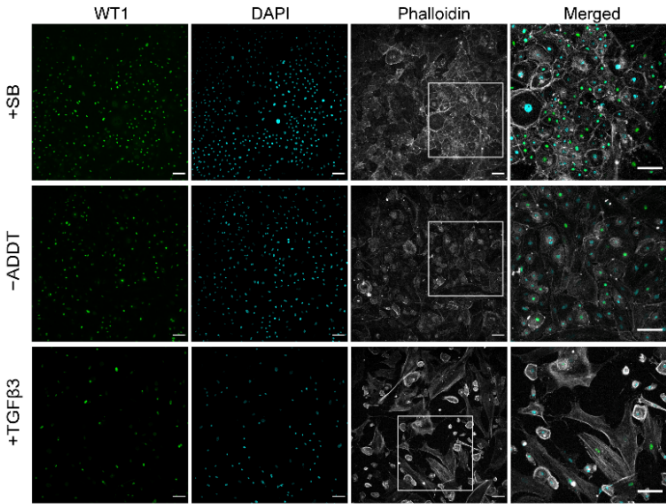
iEPDCs undergo EMT and show a mesenchymal phenotype upon TGF β 3 stimulation

EMT of EPDCs starts with the loss of their cuboidal epithelial (cobblestone-like) phenotype and of their cell-cell junctions [4,27–29]. Subsequently, epithelial EPDCs acquire a spindle-shaped mesenchymal cell morphology and mesenchymal characteristics with upregulated expression of α -smooth muscle actin (ACTA2), fibronectin (FN1), collagen type I α 1 (COL1A1) and N-cadherin (CDH2). The upregulation of mesenchymal markers is accompanied by down-regulation of WT1, E-cadherin (CDH1), and other epicardial genes, like basonuclin1 (BNC1) [12,30,31] and aldehyde dehydrogenase 1 family member A2 (ALDH1A2) [32,33], which were previously found to be enriched in both developing epicardium and in in vitro cultured primary adult human EPDCs.

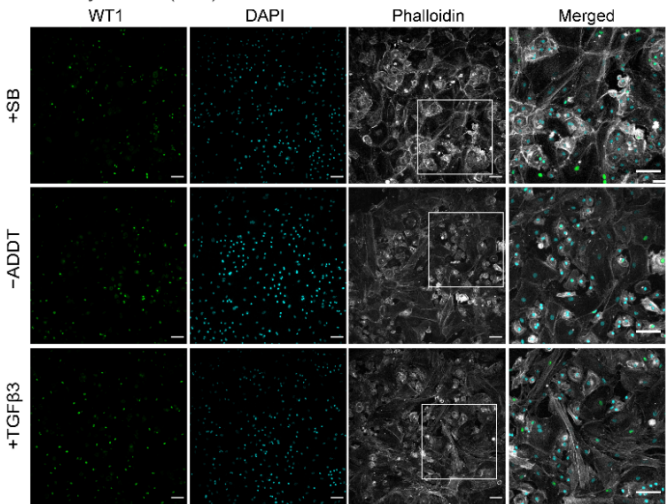
To study the ability of iEPDCs to undergo EMT, we exposed iEPDCs of PD15 and -30 to Dox-free medium without additives (control conditions) or supplemented with either SB or TGF β 3 for five days and compared the cell morphology and the protein level of the epithelial marker WT1 with those of similarly treated primary EPDCs of PD3 and -5. To eliminate the possible effects of residual LT expression, Dox was removed from the iEPDC culture medium 4–8 days before SB or TGF β 3 supplementation. As expected, the primary EPDCs and iEPDCs displayed a cuboidal cell morphology and higher WT1 protein expression in the presence of SB than under control conditions (**Figures 2A,B and 3A,C**). After culturing for five days in the absence of SB, neither primary EPDCs nor iEPDCs showed morphological signs of EMT (**Figures 2A,B and 3A,C**). Upon TGF β 3 stimulation, both primary EPDCs and iEPDCs transformed into spindle-shaped mesenchymal cells and showed redistribution of F-actin as assessed by phalloidin staining from the cortical cytoskeleton to stress fibers, which is indicative of the occurrence of EMT (**Figures 2A,B and 3A,C**). EMT was further confirmed in both primary EPDCs and iEPDCs by RT-qPCR analysis, which showed downregulation of epithelial marker genes like WT1 and BNC1 and upregulation of mesenchymal marker genes, e.g., ACTA2 and FN1, when comparing SB- with TGF β 3-treated cells (**Figures 2C and 3B,D**). The expression of the epithelial marker genes WT1 and CDH1 was similarly affected in primary EPDCs of PD5 as in iEPDCs of PD15 and -30 (WT1) and of PD15 (CDH1). Five days after SB removal, all cells displayed an increase in expression of the mesenchymal marker genes CDH2, ACTA2, COL1A1, and FN1 (**Figures 2C and 3B,D**). Culturing of the cells for 5 days in the presence of TGF β 3, led in most cases to a strong further increase in mesenchymal marker gene expression (**Figures 2C and 3B,D**). Comparison of both epithelial and mesenchymal marker genes between primary EPDCs of PD5 and iEPDCs of PD25, -28, -30 and -35 (corresponding to four biological replicates) demonstrated similar gene

expression levels and revealed similar changes in expression pattern after removal of SB or addition of TGF β for most of the genes. However, CDH1 in particular was expressed at lower levels in iEPDCs when compared to primary EPDCs under all conditions. (**Supplemental Figure S3A**). Expression of epithelial and mesenchymal markers was confirmed at the protein level by Western blotting. As shown in **Supplemental Figure S3B**, iEPDCs and primary EPDCs displayed very similar changes in the levels of E-cadherin, N-cadherin, α -smooth muscle actin, and fibronectin upon induction of EMT.

A Primary EPDCs (PD3)



B Primary EPDCs (PD5)



C

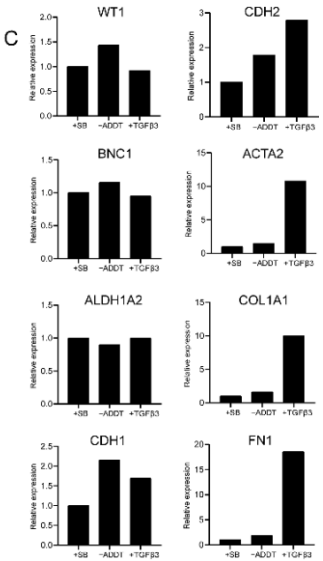


Figure 2. Primary human EPDCs undergo EMT and show a mesenchymal phenotype upon TGFβ3 stimulation. (A) Immunostaining showing that SB-treated primary human EPDCs of PD3 display a typical cuboidal epithelial morphology (indicated by phalloidin staining) and nuclear WT1 expression. TGFβ3-treated primary EPDCs undergo EMT, acquire a spindle-like appearance, which is accompanied by a large decrease in the percentage of WT1-positive cells. Culture without the additives SB or TGFβ3 causes a small fraction of PD3 EPDCs to lose their cuboidal morphology and nuclear WT1 expression. (B) Immunofluorescent staining of primary human EPDCs of PD5 subjected to the same treatments as in (A). Irrespective of the specific culture conditions, primary human EPDCs of PD5 show a low percentage of WT1-positive cells and display signs of EMT. (C) Assessment by RT-qPCR of epithelial and mesenchymal marker gene expression in primary human EPDCs of PD5 cultured under different conditions. Technical replicates: 3, biological replicates: 1. Scale bar = 100 μm. –ADDT = no additive.

Proliferating iEPDCs show a reduced propensity to undergo EMT upon TGFβ3 stimulation

As mentioned previously, TGFβ can induce EMT in EPDCs while inhibition of TGFβ signaling can prevent EMT of these cells. Interestingly, in *in-vitro* cultures we observed a PD-dependent propensity for primary human EPDCs to undergo EMT. This change in phenotype could not be prevented by TGFβ-ALK5 pathway inhibition and was often accompanied by a decreased proliferation rate of the cells.

Therefore, we tested the response of iEPDCs to TGFβ treatment in the presence of Dox to maintain a high proliferation rate and in its absence to induce cell cycle arrest. As depicted in **Figure 4A**, iEPDCs cultured in the presence or absence of Dox (designated iEPDCs +Dox and iEPDCs –Dox, respectively) were exposed to complete medium containing SB, TGFβ, or neither of the two additives (control conditions) for the indicated times after which cells were judged morphologically for their tendency to undergo EMT.

After four days of culture in the absence of Dox and with SB, iEPDCs stopped proliferating and had a similar morphology to primary EPDCs cultured in SB-containing medium (**Figure 4B**, panels B-Day 2 (+SB) and B-Day 4 (+SB)). iEPDCs that were cultured for four days in the presence of Dox and with SB continued to divide (compare **Figure 4B**, panel A-Day 2 (+SB) with A-Day 4 (+SB)) and did not undergo EMT. Subsequent removal of SB from the culture medium did not induce EMT in iEPDCs +Dox or iEPDCs –Dox based on morphological observations (**Figure 4B**, panels Aa1&2 and Ba1&2, **Supplemental Figure S4**). However, iEPDCs +Dox and iEPDCs –Dox showed markedly different responses to TGFβ3 stimulation. Compared to the typical transformation of iEPDCs –Dox after five days of stimulation with TGFβ3 into spindle-shaped mesenchymal EPDCs, the iEPDCs +Dox were not fully transformed upon TGFβ3 treatment (compare **Figure 4B**, panel Bc1 with Ac1). Continued culture in medium with or without TGFβ3 did not induce additional changes in the cell morphology of iEPDCs –Dox (**Figure 4B**, panels Bc2&3 and Bc2' & 3'). After prolonged TGFβ3 stimulation (up to 15 days), iEPDCs +Dox still

did not acquire a typical mesenchymal morphology (Figure 4B, panels Ac2 and Ac3). Furthermore, when removing TGFβ3 after 10 days of stimulation, iEPDCs +Dox reacquired a cobblestone-like appearance (Figure 4B, panels Ac2' and Ac3').

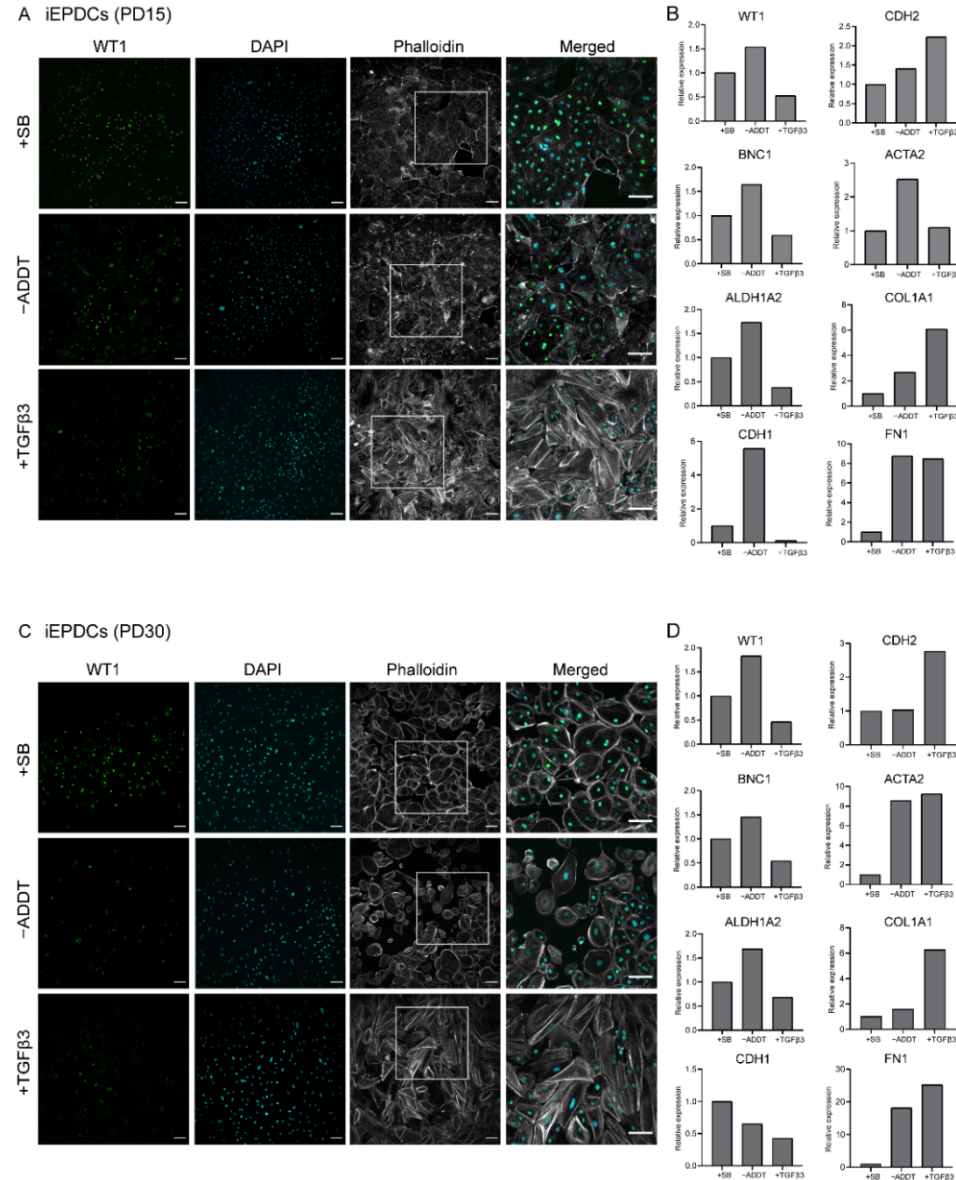


Figure 3. iEPDCs undergo EMT and show a mesenchymal phenotype upon TGFβ3 stimulation. (A) Immunostaining of iEPDCs of PD15 cultured in Dox-free medium containing SB (10 μM), TGFβ3 (1 ng/mL), or neither of the two additives. The iEPDCs show similar morphological characteristics and WT1

expression profiles as equally treated primary human EPDCs of PD3. (B) Assessment by RT-qPCR of epithelial and mesenchymal marker gene expression in iEPDCs of PD15 following different treatments. (C) Immunostaining of iEPDCs of PD30 cultured in Dox-free medium containing SB, TGF β 3, or neither of the two additives. The iEPDCs show similar morphological characteristics and WT1 expression profiles as equally treated primary human EPDCs of PD3. (D) Assessment by RT-qPCR of epithelial and mesenchymal marker gene expression in iEPDCs of PD30 following different treatments. Technical replicates: 3, biological replicates: 1. Scale bar = 100 μ m. -ADDT = no additive.

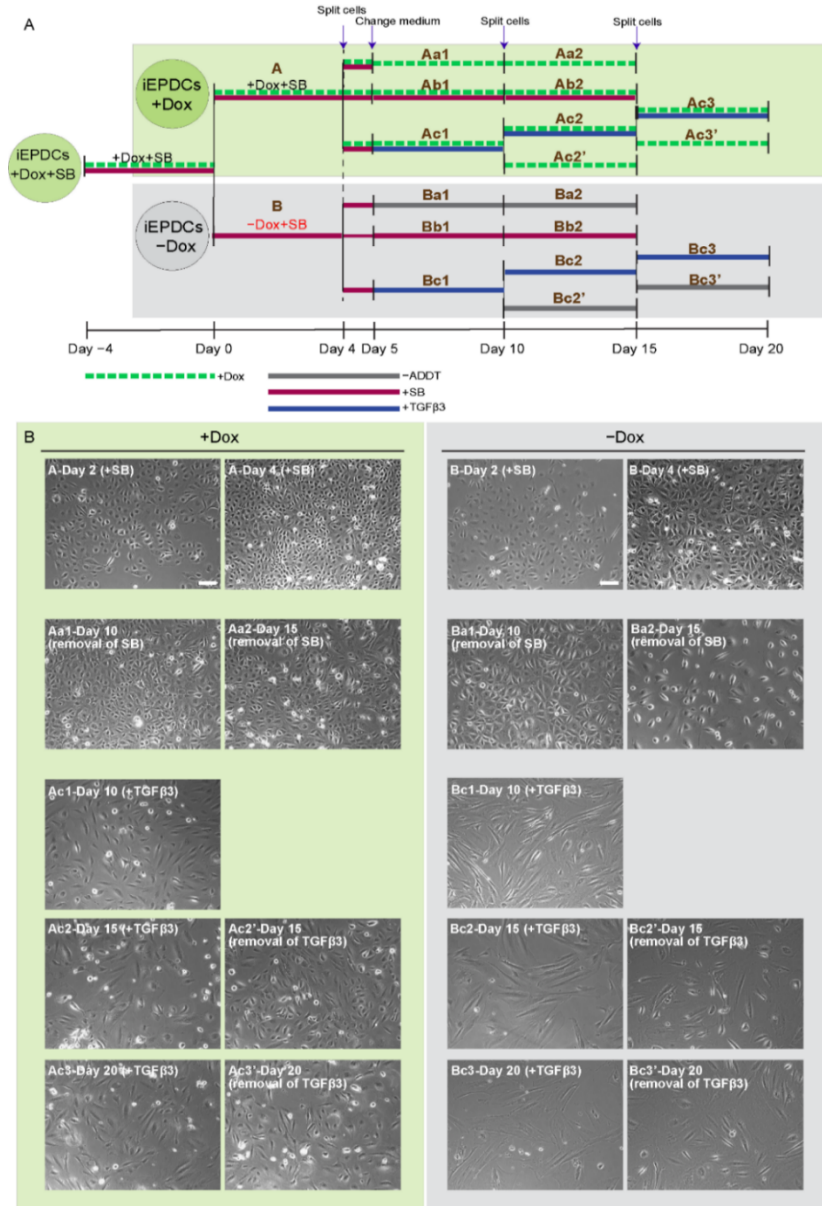


Figure 4. Proliferating iEPDCs show a reduced propensity to undergo EMT upon TGF β 3 stimulation. (A) Diagram of the experimental protocol used to examine EMT of actively proliferating (+dox) and cell cycle-arrested (–dox) iEPDCs following exposure to TGF β 3 (1 ng/ml) or various control conditions. (B) Representative phase contrast images of iEPDCs subjected to the treatment regimens shown in (A). The images on the left panel display the morphology of actively proliferating iEPDCs under each condition, the images in the right panel show the morphology of cell cycle-arrested iEPDCs under each condition. While TGF β 3 treatment readily induces EMT in non-dividing iEPDCs, dividing cells only displayed signs of EMT after prolonged exposure to TGF β 3. Scale bar = 100 μ m. –ADDT = no additive.

Mesenchymal iEPDCs show robust migration and invasion ability

Critical to their participation in heart development and cardiac regeneration, is the ability of a subset of epicardial cells to (i) undergo EMT, (ii) acquire migration capacity, and (iii) invade the subepicardial space and myocardium to subsequently differentiate into cardiac fibroblasts and vascular smooth muscle cells [34–36].

To compare the migration ability of non-proliferating epithelial iEPDCs with that of non-proliferating mesenchymal iEPDCs, a classical scratch wound healing assay was performed. As shown in **Figure 5A**, both epithelial and mesenchymal iEPDCs (gray area) migrate into the cell-free zone (cyan area) and gradually close the wound. Although the difference was rather small, wound closure occurred faster in the epithelial iEPDC cultures compared to the mesenchymal iEPDC cultures. Quantification of the wound closure rate showed it to be fastest for epithelial iEPDCs cultured without SB during the assay (**Figure 5B**), which is consistent with our previous findings in primary human EPDCs [12]. Analyzing the cell migration patterns in more detail, we found that epithelial iEPDCs closed the wound by migrating as a cell sheet, whereas mesenchymal iEPDCs tended to migrate individually into the cell-free zone (Figure 5A, Supplemental videos). The migration speed of mesenchymal iEPDCs based on the quantification of relative wound density may therefore be underestimated, especially in the beginning of the assay because individual cell migration cannot be recognized as easily as cell sheet-like migration. The specific migration pattern of epithelial iEPDCs observed in the scratch wound healing assay is reminiscent of the behavior of epicardial cells during cardiac development when they gradually cover the whole heart as a cell sheet.

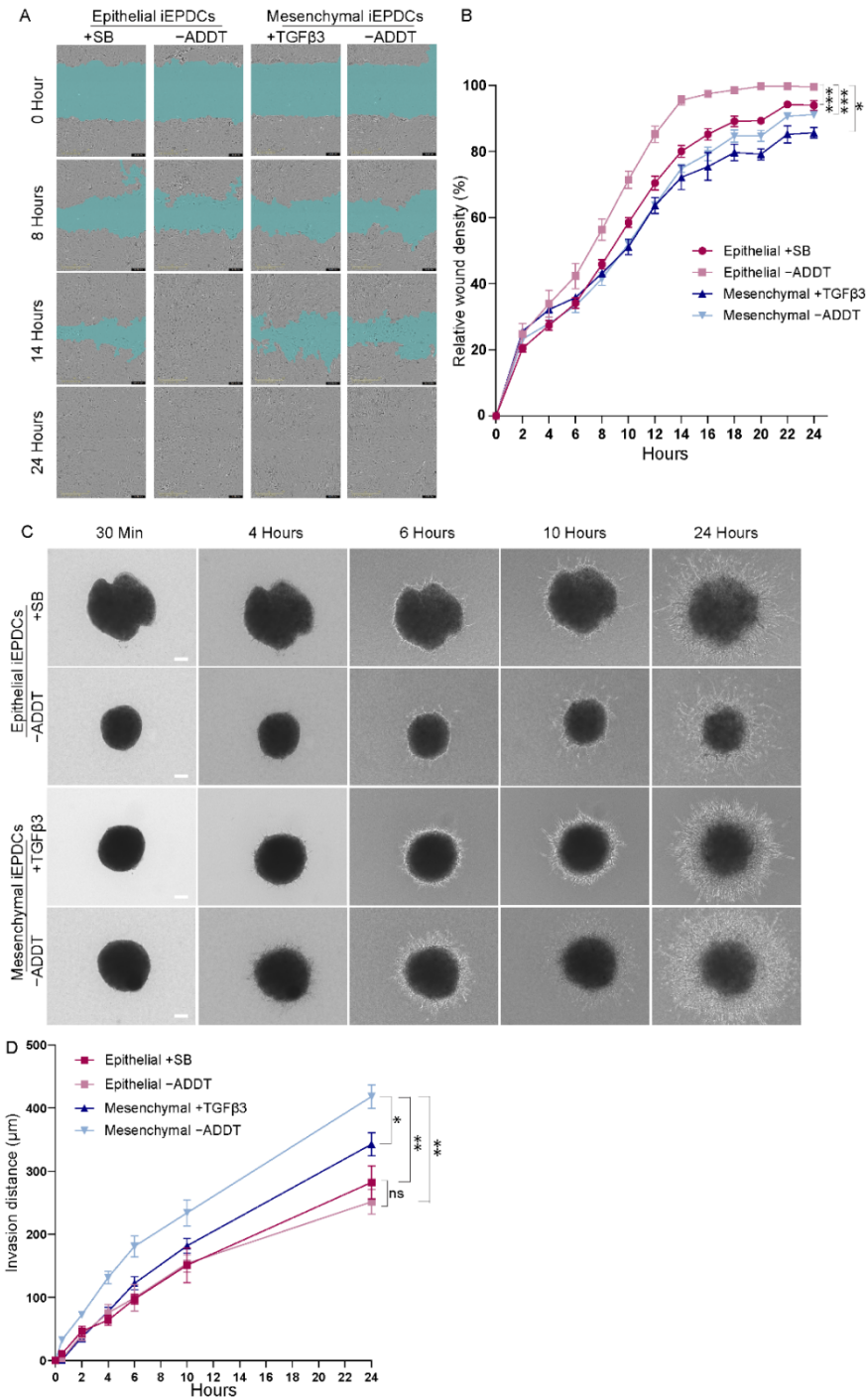


Figure 5. Mesenchymal iEPDCs show robust migration and invasion ability. (A) Representative phase contrast images of iEPDC migration in a scratch wound healing assay. Scale bar = 400 μm . (B) Quantification of iEPDC migration in a scratch wound healing assay. (C). Representative images of iEPDC aggregates in a 3D collagen gel-based invasion assay. Scale bar = 100 μm . (D). Quantification of EPDC invasion distance within 24 hours. The assay was performed in Dox-free complete medium with the indicated additives using either epithelial iEPDCs (i.e., iEPDCs pretreated with SB (10 μM) to preserve their cuboidal epithelial morphology) or with mesenchymal iEPDCs (i.e., iEPDCs pretreated for five days with TGF β 3 (1 ng/mL) to induce a spindle-like morphology). * $p < 0.05$, ** $p < 0.01$, *** $p < 0.001$. –ADDT = no additive.

Another key function of EPDCs is their ability to invade the underlying myocardium after EMT. We employed a 3D invasion assay in order to further investigate this function of epithelial and mesenchymal iEPDCs. As can be appreciated in **Figure 5C**, iEPDCs gradually migrate out of cell aggregates and invade the surrounding collagen gel, moving further away from the aggregates. Mesenchymal iEPDCs cultured in the absence of TGF β 3 during the assay spread through the collagen gel significantly faster than epithelial iEPDCs or TGF β 3-stimulated mesenchymal iEPDCs (**Figure 5D**). No difference in cell migration was observed between epithelial iEPDCs that were cultured in medium with or without SB during the time of this assay, indicating that inhibition of TGF β -ALK5 signaling did not affect epithelial EPDCs' invasion capacity. The presence of TGF β 3 during the assay decreased the cell invasion ability of the mesenchymal EPDCs, which may be the result of the continuing differentiation of the mesenchymal EPDCs by lasting TGF β stimulation. TGF β is known to transiently induce EMT in vivo during development, and both in vitro and in vivo studies have shown that TGF β signaling promotes EPDC differentiation and their contribution to heart development and regeneration [13,37,38]. The phenotype (epithelial or mesenchymal) and TGF β -ALK5 signaling (with or without SB or TGF β 3)-dependent changes in invasion capacity of iEPDCs mimicked those observed in primary adult human EPDCs (**Supplemental Figure S5**). Interestingly, both mesenchymal and epithelial iEPDCs displayed a much higher capacity to invade collagen gels in comparison to their primary counterparts. To investigate whether this might be linked to the lower CDH1 expression in iEPDCs (**Supplemental Figure S3**), the cells were transduced with an LV encoding human E-cadherin. After confirmation of E-cadherin overexpression by immunofluorescence microscopy (**Supplemental Figure S6A**), the invasion capacity of epithelial and mesenchymal subtypes of these iEPDCs was investigated in the 3D invasion assay. As shown in Supplemental Figure S6B, E-cadherin overexpression only slightly reduced the invasion capacity of both epithelial and mesenchymal iEPDCs.

Mesenchymal iEPDCs promote neurite outgrowth from sympathetic ganglia

We recently showed that primary adult human mesenchymal EPDCs promote neurite outgrowth from sympathetic ganglia in vitro by a paracrine effect [16]. To study whether the same results could be obtained using iEPDCs, primary EPDCs and iEPDCs derived from the

same patient were treated with TGF β 3 for five days to induce EMT and passaged twice in Dox-free medium without TGF β 3. Next, the EPDCs were co-cultured with superior cervical ganglion (SCG) explants for six days without additive. Consistent with our previous findings, less than 50% of the SCG explants showed limited outgrowth when cultured without EPDCs (**Figure 6A,B**) [16]. In contrast, co-culture of SCG with both mesenchymal primary EPDCs and with iEPDCs robustly stimulated ganglionic outgrowth (**Figure 6A,B**).

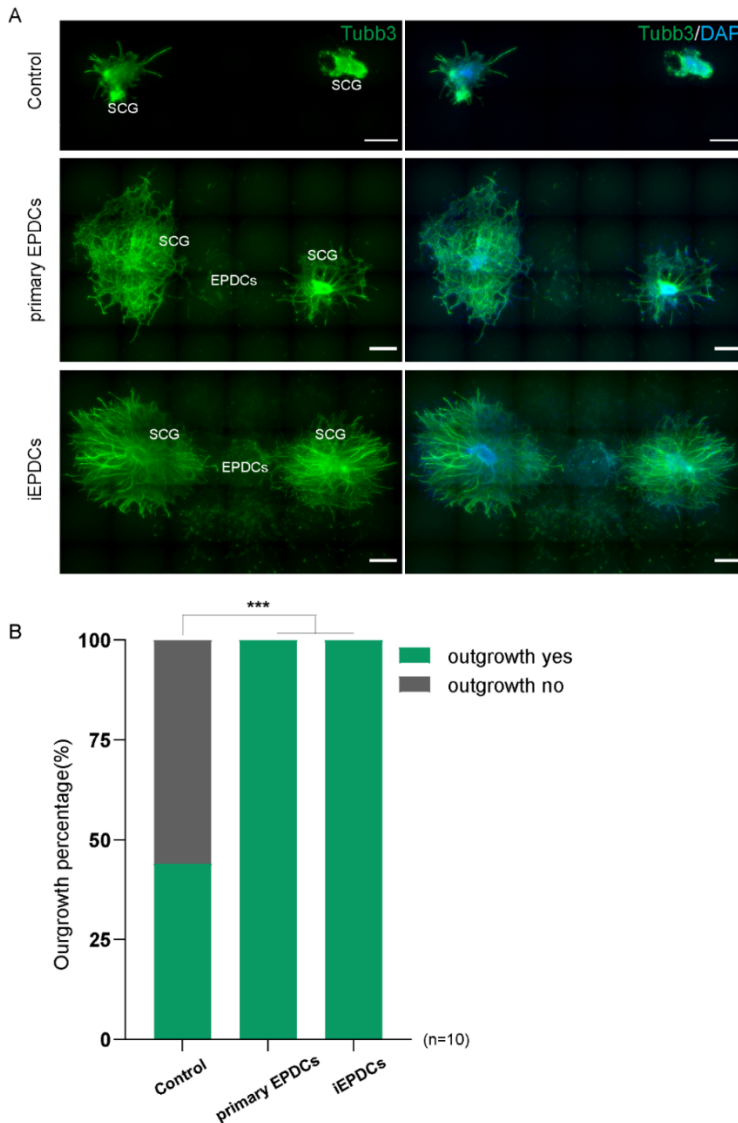


Figure 6. Mesenchymal iEPDCs promote neurite outgrowth of sympathetic ganglia. (A). Representative immunofluorescence images (Tubb3 staining) of embryonic superior cervical ganglia (SCG) outgrowth after six days of culture alone or together with primary human EPDCs or iEPDCs in a 3D culture setup. Upper panel: No or hardly any neurite outgrowth is observed when SCG are cultured without EPDCs. Co-culture with primary human EPDCs (PD8, middle panel) or iEPDCs (PD30, lower panel) promotes neurite outgrowth from SCG. (B). Quantification of the percentage of SCG showing neurite outgrowth when cultured alone or co-cultured with primary human EPDCs or iEPDCs. Scale bar = 500 μm . *** $p < 0.001$.

DISCUSSION

The interest in the epicardium has strongly increased during recent decades due to its (i) key role in heart development, (ii) involvement in cardiac injury responses, and (iii) potential to contribute to myocardial regeneration both through paracrine signaling and by differentiation of its cellular descendants into cardiac fibroblasts and vascular smooth muscle cells [10]. To facilitate human EPDC research, our research teams previously developed methods to isolate and culture primary human epicardial cells for in vitro studies and xenogeneic transplantation experiments [11,12,14,17]. Further characterization of EPDCs to better understand their contribution to myocardial fibrosis and to fully exploit their cardioregenerative potential is, however, hampered by (i) the limited availability of human epicardium and EPDCs for research purposes, (ii) the highly variable properties of EPDCs obtained from different donors, and (iii) the fact that primary EPDCs stop dividing and lose their epithelial phenotype after a few passages in vitro. The availability of a well-characterized line of human EPDCs phenotypically resembling primary human EPDCs would greatly expedite epicardial research and allow high-throughput studies, e.g., to identify (novel) drugs that can modulate EPDC function. Here, we introduce the first adult human epicardial cell line with Dox-inducible proliferation capacity via ex-expression of SV40 LT using a repressor-based Tet-On system. This human epicardial cell line recapitulates key properties of primary epicardial cells and overcomes important challenges that come with the use of primary EPDCs.

There are various options to extend the proliferative capacity of primary mammalian cells [39,40]. Viral oncoproteins of DNA tumor viruses (in particular the SV40 LT + small t antigen [st], the human papillomavirus type 16/18 E6 and E7 proteins and the human adenovirus type 2/5 E1A and E1B proteins) have been extensively used for this purpose [41]. This has, amongst other things, resulted in the generation of multiple lines of human endothelial cells [42], hepatocytes [43], lung epithelial cells [44], and keratinocytes [45]. The first lines of human mesothelial cells were published in 1989 [46] and were generated by transfection of cells isolated from pleural fluid with a plasmid encoding the early gene products (i.e., LT, 17kT and st) of SV40. This extended the replicative life span of the cells from 15 PDs to up to 60-70 PDs and gave rise to a single clone of permanently immortalized mesothelial cells with a cuboidal epithelial morphology designated MeT-5A. Subsequently, several other lines of human pleural

and peritoneal mesothelial cells were generated (see, e.g., Fischereder et al. 1997 [47]; Pruett et al. 2020 [48]). However, the present paper is the first to describe the generation of a human epicardial mesothelial cell line.

In the mesothelial cell lines generated by Ke et al. [46] and Fischereder et al. [47], LT expression is under the control of constitutively active promoters. For many cell types, continuous LT expression/cell proliferation negatively affects their functional properties. We therefore employed a repressor-based lentiviral Tet-On system allowing tight control of LT expression by Dox to generate the iEPDCs described in this study. We have previously used very similar conditional cell immortalization systems to generate lines of neonatal rat atrial cardiomyocytes with preserved cardiomyogenic differentiation capacity [22] and for producing adipogenic lines of murine and human brown preadipocytes (designated iBPAs) [21]. The latter study nicely illustrated the advantage of inducible over permanent immortalization gene expression, as the human iBPAs could only differentiate into fat cells in the absence of Dox, i.e., after switching off LT expression. In congruence with these findings, iEPDCs displayed a reduced ability to undergo TGF β 3-induced EMT in the presence of Dox.

For the application of iEPDCs, it is mandatory that they possess similar characteristics to primary human EPDCs with regard to morphology, molecular signature, and function. Morphologically, early passage SB-treated primary human EPDCs strongly resemble SB-treated iEPDCs and both cell types undergo EMT adapting a spindle-like appearance after exposure to TGF β 3. Moreover, comparative gene expression analysis between primary human EPDCs and iEPDCs showed that the epithelial marker genes WT1, BNC1, and ALDH1A2 were expressed at very similar levels in both cell types and that mesenchymal marker gene expression was affected similarly upon treatment of primary human EPDCs and iEPDCs with EMT modulators. One exception was the epithelial marker gene CDH1, which showed a lower expression in iEPDCs as compared to primary human EPDCs under all experimental conditions. CDH1 codes for E-cadherin, which is responsible for the tight cell-cell contact in adherent junctions connecting neighboring EPDCs. During EMT, expression of junctional proteins including E-cadherin is lost, which results in the disruption of intercellular junctions and together with other changes in cell behavior, allows EPDCs to migrate into the myocardium [10,49]. Consistent with their decreased E-cadherin expression, iEPDCs displayed a higher invasion capacity in 3D collagen hydrogels than primary human EPDCs. While CDH1 overexpression reduced the invasion ability of iEPDCs, it remained higher than that of primary human EPDCs, indicating that additional factors contribute to the increased motility of iEPDCs. Although loss of E-cadherin has been associated with the initiation of EMT, non-TGF β 3-stimulated iEPDCs maintained a cuboidal epithelial phenotype, suggesting that their E-cadherin levels are high enough to prevent EMT.

The iEPDCs started to lose their cuboidal epithelial appearance at PD51, which was accompanied by a slowing of the cell division rate. It will be of interest to determine the reason(s) for this change in cell morphology and doubling time. Conceivably, iEPDCs gradually accumulate telomeric and non-telomeric DNA damage due to exposure to the high atmospheric O₂ level and/or to the high replication rate imposed by LT, which, in combination with telomere shortening, result in the induction of cellular senescence. If so, combined overexpression of LT and telomerase reverse transcriptase and measures to reduce DNA damage during in vitro culture might further expand the replicative life span of epithelial iEPDCs, especially when derived from older patients. Alternatively, the changes in cell morphology observed at late passages of the iEPDCs are caused by the progressive loss of the epigenetic determinants of their epithelial cell identity [50]. To prevent this from happening will require the identification of the epigenetic memory initiating factors responsible for the maintenance of the cuboidal epithelial appearance of EPDCs [51].

The fact that proliferation of the iEPDCs is strictly Dox-dependent allowed us to investigate the relationship between proliferation and EMT of EPDCs. As mentioned above, continuous proliferation induced by Dox inhibited the ability of iEPDCs to undergo EMT in response to TGFβ₃ stimulation. Moreover, iEPDCs cultured in the presence of Dox re-acquired epithelial characteristics when exposure to TGFβ₃ was stopped. This is in line with the previous description of competition between cell growth and differentiation in normal, genetically unmodified somatic (stem) cells [52–54] and may suggest that EMT and proliferation are competing processes in iEPDCs, where high proliferation is accompanied by low EMT, and vice versa. This finding is consistent with our observation that primary human EPDCs spontaneously undergo EMT in the absence of TGFβ₃ after entering a low proliferation state in vitro. Studies in other cell types support the existence of a possible relationship between cell proliferation and EMT, e.g., in tumor cells EMT has been shown to inhibit cell proliferation whereas inhibition of EMT promotes tumor cell proliferation [55,56]. However, since SV40 can induce malignant mesotheliomas in rodents [57] and this effect is linked to expression of LT, caution should be exercised in drawing definitive conclusions about the relationship between cell proliferation and EMT in EPDCs due to possible direct effects of LT on EMT.

Taken together, in this study we have shown that human EPDCs can be endowed with inducible proliferation capacity and massively expanded without loss of their cuboidal epithelial morphology and characteristic (functional) properties by Dox-controlled expression of SV40 LT using a lentiviral repressor-based Tet-On system. Similar to primary human EPDCs, iEPDCs underwent EMT upon TGFβ₃ stimulation as evidenced by the acquisition of a spindle-shaped appearance and by the upregulation of mesenchymal marker genes. Moreover, functional collagen gel-based cell invasion assays demonstrated that mesenchymal iEPDCs,

just like primary human EPDCs had an increased capacity for invasion and migration as compared to their epithelial counterparts. Finally, mesenchymal iEPDCs were shown to stimulate neurite outgrowth from sympathetic ganglia by paracrine signaling similar to primary human EPDCs [16]. In conclusion, iEPDCs provide a plentiful cell source for fundamental and translation EPDC research and as such represent a valuable new addition to the existing epicardial model systems.

AUTHOR CONTRIBUTIONS

All authors contributed to the study conception and design. The experiments were designed and performed by Y.G., J.L., A.M.S., and A.A.F.d.V. Data collection and analysis were performed by Y.G. and supervised by M.R.M.J., A.A.F.d.V., M.J.T.H.G., and A.M.S. The first draft of the manuscript was written by Y.G. and M.R.M.J. and all authors commented on previous versions of the manuscript. All authors have read and agreed to the published version of the manuscript.

FUNDING

This work is supported by the Dutch Heart Foundation [2017T059 to A.M. S], The Netherlands Organization for Scientific Research (NWO) [016.196.346 to M.R.M.J.], the National Natural Science Foundation of China [81900264 to J.L.], The Netherlands Organization for Health Research and Development (ZonMw) the Dutch Society for the Replacement of Animal Testing (dsRAT) [MKMD project 114022503 to A.A.F.d.V.], and the Leiden Regenerative Medicine Platform Holding (LRMPH project 8212/41235 to A.A.F.d.V.).

ACKNOWLEDGMENTS

We are grateful to Tessa van Herwaarden (Department of Cell and Chemical Biology, LUMC, Leiden, The Netherlands) for her help with isolating primary human EPDCs. We thank Cindy Bart (Laboratory of Experimental Cardiology, LUMC, Leiden, The Netherlands) for her technical support with LV (shuttle plasmid) production.

CONFLICTS OF INTEREST

The authors declare no conflict of interest.

REFERENCE

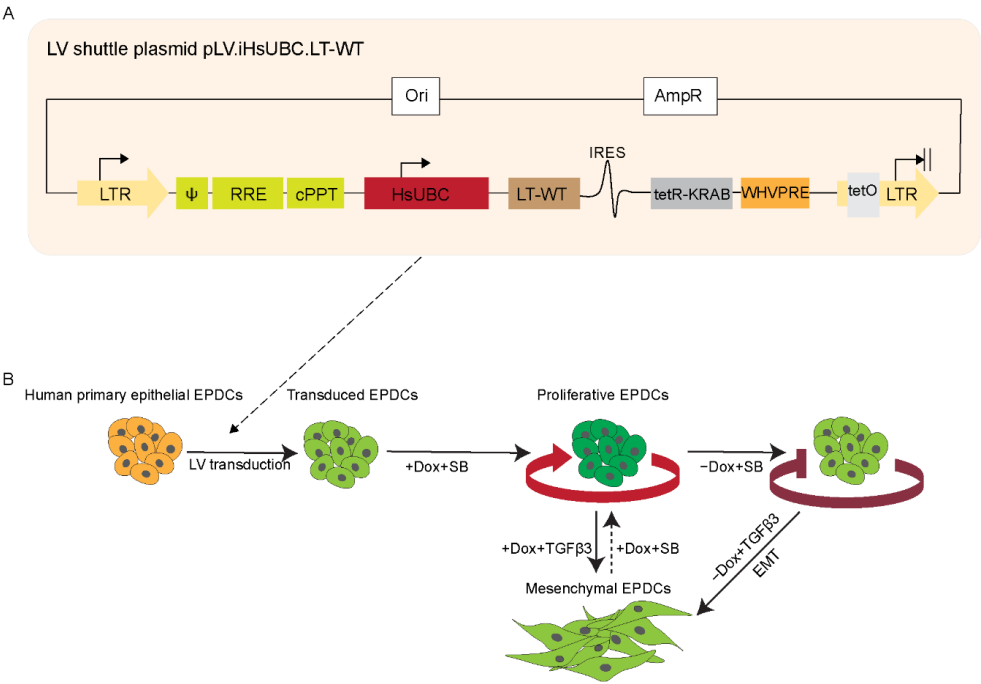
1. Zhou, B.; Ma, Q.; Rajagopal, S.; Wu, S.M.; Domian, I.; Rivera-Feliciano, J.; Jiang, D.; von Gise, A.; Ikeda, S.; Chien, K.R.; et al. Epicardial progenitors contribute to the cardiomyocyte lineage in the developing heart. *Nature* 2008, 454, 109–113, doi:10.1038/nature07060.
2. Kolditz, D.P.; Wijffels, M.C.; Blom, N.A.; van der Laarse, A.; Hahurij, N.D.; Lie-Venema, H.; Markwald, R.R.; Poelmann, R.E.; Schalij, M.J.; Gittenberger-de Groot, A.C. Epicardium-derived cells in development of annulus fibrosis and persistence of accessory pathways. *Circulation* 2008, 117, 1508–1517, doi:10.1161/circulationaha.107.726315.
3. Gittenberger-de Groot, A.C.; Vrancken Peeters, M.P.; Mentink, M.M.; Gourdie, R.G.; Poelmann, R.E. Epicardium-derived cells contribute a novel population to the myocardial wall and the atrioventricular cushions. *Circ. Res.* 1998, 82, 1043–1052, doi:10.1161/01.res.82.10.1043.
4. von Gise, A.; Pu, W.T. Endocardial and epicardial epithelial to mesenchymal transitions in heart development and disease. *Circ. Res.* 2012, 110, 1628–1645, doi:10.1161/circresaha.111.259960.
5. Smits, A.M.; Riley, P.R. Epicardium-derived heart repair. *J. Dev. Biol.* 2014, 2, 84–100, doi:10.3390/jdb2020084.
6. Duan, J.; Gherghe, C.; Liu, D.; Hamlett, E.; Srikantha, L.; Rodgers, L.; Regan, J.N.; Rojas, M.; Willis, M.; Leask, A.; et al. Wnt1/ β catenin injury response activates the epicardium and cardiac fibroblasts to promote cardiac repair. *EMBO J.* 2012, 31, 429–442, doi:10.1038/emboj.2011.418.
7. van Wijk, B.; Gunst, Q.D.; Moorman, A.F.; van den Hoff, M.J. Cardiac regeneration from activated epicardium. *PLoS ONE* 2012, 7, e44692, doi:10.1371/journal.pone.0044692.
8. Zhou, B.; Honor, L.B.; He, H.; Ma, Q.; Oh, J.H.; Butterfield, C.; Lin, R.Z.; Melero-Martin, J.M.; Dolmatova, E.; Duffy, H.S.; et al. Adult mouse epicardium modulates myocardial injury by secreting paracrine factors. *J. Clin. Invest.* 2011, 121, 1894–1904, doi:10.1172/jci45529.
9. Gittenberger-de Groot, A.C.; Winter, E.M.; Goumans, M.J.; Bartelings, M.M.; Poelmann, R.E. The arterial epicardium: A developmental approach to cardiac disease and repair. In *Etiology and Morphogenesis of Congenital Heart Disease: From Gene Function and Cellular Interaction to Morphology*; Nakanishi, T., Markwald, R.R., Baldwin, H.S., Keller, B.B., Srivastava, D., Yamagishi, H., Eds.; Tokyo, 2016; pp. 11–18.
10. Quijada, P.; Trembley, M.A.; Small, E.M. The role of the epicardium during heart development and repair. *Circ. Res.* 2020, 126, 377–394, doi:10.1161/CIRCRESAHA.119.315857.
11. van Tuyn, J.; Atsma, D.E.; Winter, E.M.; van der Velde-van Dijke, I.; Pijnappels, D.A.; Bax, N.A.M.; Knaän-Shanzer, S.; Gittenberger-de Groot, A.C.; Poelmann, R.E.; van der Laarse, A.; et al. Epicardial cells of human adults can undergo an epithelial-to-mesenchymal transition and obtain characteristics of smooth muscle cells in vitro. *Stem Cells* 2007, 25, 271–278, doi:10.1634/stemcells.2006-0366.
12. Moerkamp, A.T.; Lodder, K.; van Herwaarden, T.; Dronkers, E.; Dingenouts, C.K.E.; Tengstrom, F.C.; van Brakel, T.J.; Goumans, M.J.; Smits, A.M. Human fetal and adult epicardial-derived cells: A novel model to study their activation. *Stem Cell Res. Ther.* 2016, 7, doi:10.1186/s13287-016-0434-9.
13. Dronkers, E.; Wauters, M.M.M.; Goumans, M.J.; Smits, A.M. Epicardial TGF β and BMP signaling in cardiac regeneration: What lesson can we learn from the developing heart? *Biomolecules* 2020, 10, doi:10.3390/biom10030404.
14. Winter, E.M.; Grauss, R.W.; Hogers, B.; van Tuyn, J.; van der Geest, R.; Lie-Venema, H.; Steijn, R.V.; Maas, S.; DeRuiter, M.C.; deVries, A.A.; et al. Preservation of left ventricular function and attenuation of remodeling after transplantation of human epicardium-derived cells into the infarcted mouse heart. *Circulation* 2007, 116, 917–927, doi:10.1161/circulationaha.106.668178.
15. Smits, A.M.; Dronkers, E.; Goumans, M.-J. The epicardium as a source of multipotent adult cardiac progenitor cells: Their origin, role and fate. *Pharmacol. Res.* 2018, 127, 129–140, doi:10.1016/j.phrs.2017.07.020.

16. Ge, Y.; Smits, A.M.; van Munsteren, J.C.; Gittenberger-de Groot, A.C.; Poelmann, R.E.; van Brakel, T.J.; Schalij, M.J.; Goumans, M.J.; DeRuiter, M.C.; Jongbloed, M.R.M. Human epicardium-derived cells reinforce cardiac sympathetic innervation. *J. Mol. Cell. Cardiol.* 2020, 143, 26–37, doi:10.1016/j.yjmcc.2020.04.006.
17. Dronkers, E.; Moerkamp, A.T.; van Herwaarden, T.; Goumans, M.-J.; Smits, A.M. The isolation and culture of primary epicardial cells derived from human adult and fetal heart specimens. *J. Vis. Exp.* 2018, doi:10.3791/57370.
18. Jat, P.S.; Noble, M.D.; Ataliotis, P.; Tanaka, Y.; Yannoutsos, N.; Larsen, L.; Kioussis, D. Direct derivation of conditionally immortal cell lines from an H-2Kb-tsA58 transgenic mouse. *Proc. Natl. Acad. Sci. USA* 1991, 88, 5096–5100, doi:10.1073/pnas.88.12.5096.
19. Austin, A.F.; Compton, L.A.; Love, J.D.; Barnett, J.V. Immortalized mouse epicardial cells undergo differentiation in response to TGF α . *FASEB J.* 2007, 21, A973–A973, doi:10.1096/fasebj.21.6.A973-b.
20. Zhang, J.C.; Kim, S.; Helmke, B.P.; Yu, W.W.; Du, K.L.; Lu, M.M.; Strobeck, M.; Yu, Q.; Parmacek, M.S. Analysis of SM22 α -deficient mice reveals unanticipated insights into smooth muscle cell differentiation and function. *Mol. Cell. Biol.* 2001, 21, 1336–1344, doi:10.1128/mcb.2001.21.4.1336-1344.2001.
21. Liu, J.; Kuipers, E.N.; Sips, H.C.M.; Dorleijn, J.C.; van Dam, A.D.; Christodoulides, C.; Karpe, F.; Zhou, G.Q.; Boon, M.R.; Rensen, P.C.N.; et al. Conditionally immortalized brown preadipocytes can switch between proliferative and differentiated states. *BBA-Mol. Cell Biol. Lipids* 2019, 1864, doi:10.1016/j.bbalip.2019.08.007.
22. Liu, J.; Volkers, L.; Jangsanthong, W.; Bart, C.I.; Engels, M.C.; Zhou, G.; Schalij, M.J.; Ypey, D.L.; Pijnappels, D.A.; de Vries, A.A.F. Generation and primary characterization of iAM-1, a versatile new line of conditionally immortalized atrial myocytes with preserved cardiomyogenic differentiation capacity. *Cardiovasc. Res.* 2018, 114, 1848–1859, doi:10.1093/cvr/cvy134.
23. Denning, W.; Das, S.; Guo, S.; Xu, J.; Kappes, J.C.; Hel, Z. Optimization of the transductional efficiency of lentiviral vectors: Effect of sera and polycations. *Mol. Biotechnol.* 2013, 53, 308–314, doi:10.1007/s12033-012-9528-5.
24. Vandesompele, J.; De Preter, K.; Pattyn, F.; Poppe, B.; Van Roy, N.; De Paepe, A.; Speleman, F. Accurate normalization of real-time quantitative RT-PCR data by geometric averaging of multiple internal control genes. *Genome Biol.* 2002, 3, re-search0034.0031, doi:10.1186/gb-2002-3-7-research0034.
25. Hellemans, J.; Mortier, G.; De Paepe, A.; Speleman, F.; Vandesompele, J. qBase relative quantification framework and software for management and automated analysis of real-time quantitative PCR data. *Genome Biol.* 2007, 8, R19, doi:10.1186/gb-2007-8-2-r19.
26. Bax, N.A.; van Oorschot, A.A.; Maas, S.; Braun, J.; van Tuyn, J.; de Vries, A.A.; Groot, A.C.; Goumans, M.J. In vitro epithelial-to-mesenchymal transformation in human adult epicardial cells is regulated by TGF β -signaling and WT1. *Basic Res. Cardiol.* 2011, 106, 829–847, doi:10.1007/s00395-011-0181-0.
27. von Gise, A.; Zhou, B.; Honor, L.B.; Ma, Q.; Petryk, A.; Pu, W.T. WT1 regulates epicardial epithelial to mesenchymal transition through β -catenin and retinoic acid signaling pathways. *Dev. Biol.* 2011, 356, 421–431, doi:10.1016/j.ydbio.2011.05.668.
28. Martinez-Estrada, O.M.; Lettice, L.A.; Essafi, A.; Guadix, J.A.; Slight, J.; Velecela, V.; Hall, E.; Reichmann, J.; Devenney, P.S.; Hohenstein, P.; et al. Wt1 is required for cardiovascular progenitor cell formation through transcriptional control of Snail and E-cadherin. *Nat. Genet.* 2010, 42, 89–93, doi:10.1038/ng.494.
29. Velecela, V.; Torres-Cano, A.; Garcia-Melero, A.; Ramiro-Pareta, M.; Muller-Sanchez, C.; Segarra-Mondejar, M.; Chau, Y.Y.; Campos-Bonilla, B.; Reina, M.; Soriano, F.X.; et al. Epicardial cell shape and maturation are regulated by Wt1 via transcriptional control of Bmp4. *Development* 2019, 146, doi:10.1242/dev.178723.

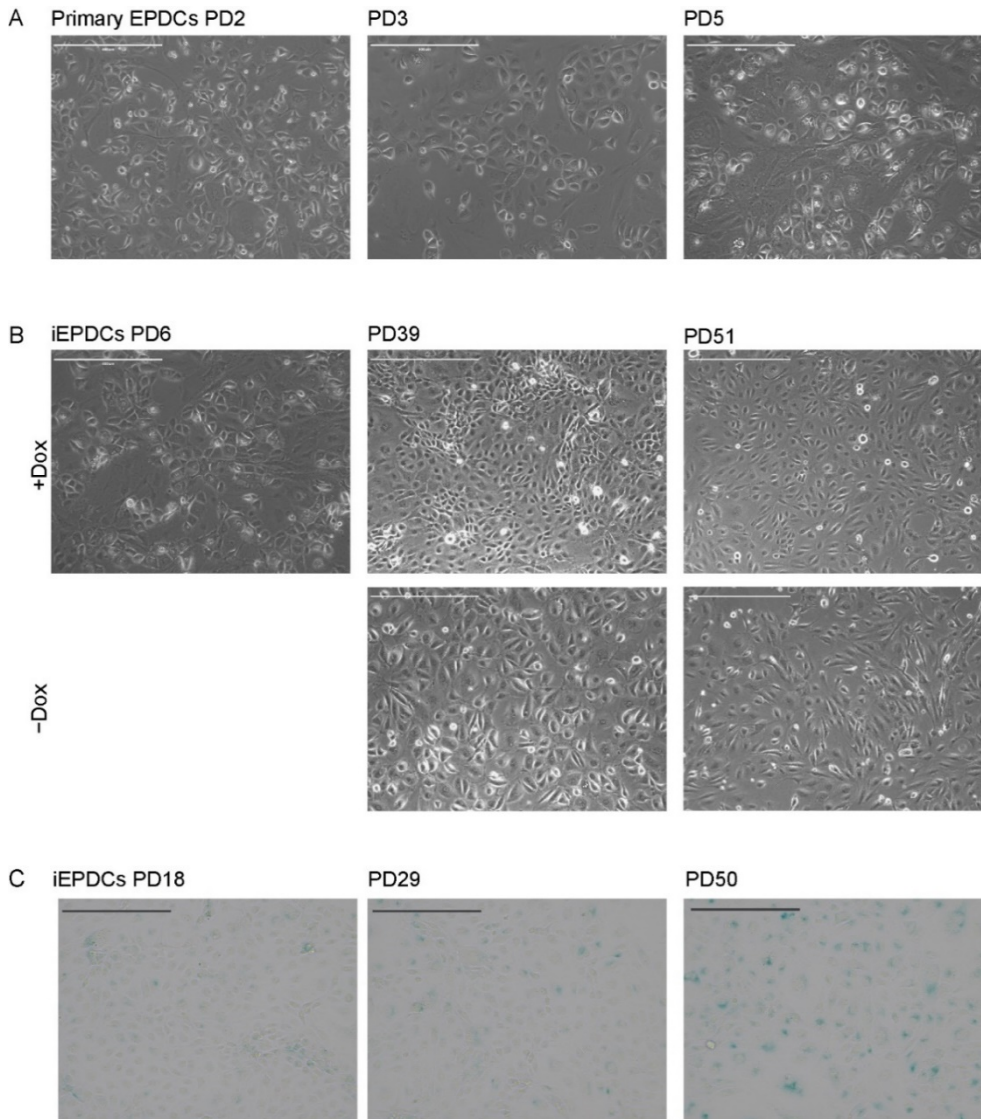
30. Bochmann, L.; Sarathchandra, P.; Mori, F.; Lara-Pezzi, E.; Lazzaro, D.; Rosenthal, N. Revealing new mouse epicardial cell markers through transcriptomics. *PLoS ONE* 2010, 5, doi:10.1371/journal.pone.0011429.
31. Gambardella, L.; McManus, S.A.; Moignard, V.; Sebkhan, D.; Delaune, A.; Andrews, S.; Bernard, W.G.; Morrison, M.A.; Riley, P.R.; Gottgens, B.; et al. BNC1 regulates cell heterogeneity in human pluripotent stem cell-derived epicardium. *Development* 2019, 146, doi:10.1242/dev.174441.
32. Moss, J.B.; Xavier-Neto, J.; Shapiro, M.D.; Nayeem, S.M.; McCaffery, P.; Drager, U.C.; Rosenthal, N. Dynamic patterns of retinoic acid synthesis and response in the developing mammalian heart. *Dev. Biol.* 1998, 199, 55–71, doi:10.1006/dbio.1998.8911.
33. Xavier-Neto, J.; Shapiro, M.D.; Houghton, L.; Rosenthal, N. Sequential programs of retinoic acid synthesis in the myocardial and epicardial layers of the developing avian heart. *Dev. Biol.* 2000, 219, 129–141, doi:10.1006/dbio.1999.9588.
34. Wilm, B.; Ipenberg, A.; Hastie, N.D.; Burch, J.B.; Bader, D.M. The serosal mesothelium is a major source of smooth muscle cells of the gut vasculature. *Development* 2005, 132, 5317–5328, doi:10.1242/dev.02141.
35. Smith, C.L.; Baek, S.T.; Sung, C.Y.; Tallquist, M.D. Epicardial-derived cell epithelial-to-mesenchymal transition and fate specification require PDGF receptor signaling. *Circ. Res.* 2011, 108, e15–e26, doi:10.1161/circresaha.110.235531.
36. Katz, T.C.; Singh, M.K.; Degenhardt, K.; Rivera-Feliciano, J.; Johnson, R.L.; Epstein, J.A.; Tabin, C.J. Distinct compartments of the proepicardial organ give rise to coronary vascular endothelial cells. *Dev. Cell* 2012, 22, 639–650, doi:10.1016/j.devcel.2012.01.012.
37. Compton, L.A.; Potash, D.A.; Mundell, N.A.; Barnett, J.V. Transforming growth factor-beta induces loss of epithelial character and smooth muscle cell differentiation in epicardial cells. *Dev. Dyn. Off. Publ. Am. Assoc. Anat.* 2006, 235, 82–93, doi:10.1002/dvdy.20629.
38. Saifi, O.; Ghandour, B.; Jaalouk, D.; Refaat, M.; Mahfouz, R. Myocardial regeneration: Role of epicardium and implicated genes. *Mol. Biol. Rep.* 2019, 46, 6661–6674, doi:10.1007/s11033-019-05075-0.
39. Maqsood, M.I.; Matin, M.M.; Bahrami, A.R.; Ghasroldasht, M.M. Immortality of cell lines: Challenges and advantages of establishment. *Cell Biol. Int.* 2013, 37, 1038–1045, doi:10.1002/cbin.10137.
40. Wall, I.; Toledo, G.S.; Jat, P. Recent advances in conditional cell immortalization technology. *Cell Gene Ther. Insights* 2016, 2, 339–355, doi:10.18609/cgti.2016.044.
41. Stepanenko, A.A.; Kavan, V.M. Immortalization and malignant transformation of eukaryotic cells. *Cytol. Genet.* 2012, 46, 96–129, doi:10.3103/S0095452712020041.
42. Rahman, N.A.; Rasil, A.N.H.M.; Meyding-Lamade, U.; Craemer, E.M.; Diah, S.; Tuah, A.A.; Muharram, S.H. Immortalized endothelial cell lines for in vitro blood-brain barrier models: A systematic review. *Brain Res.* 2016, 1642, 532–545, doi:10.1016/j.brainres.2016.04.024.
43. Ramboer, E.; De Craene, B.; De Kock, J.; Vanhaecke, T.; Berx, G.; Rogiers, V.; Vinken, M. Strategies for immortalization of primary hepatocytes. *J. Hepatol.* 2014, 61, 925–943, doi:10.1016/j.jhep.2014.05.046.
44. Sato, M.; Shay, J.W.; Minna, J.D. Immortalized normal human lung epithelial cell models for studying lung cancer biology. *Respir. Investig.* 2020, 58, 344–354, doi:10.1016/j.resinv.2020.04.005.
45. Choi, M.; Lee, C. Immortalization of primary keratinocytes and its application to skin research. *Biomol. Ther.* 2015, 23, 391–399, doi:10.4062/biomolther.2015.038.
46. Ke, Y.; Reddel, R.R.; Gerwin, B.I.; Reddel, H.K.; Somers, A.N.; McMenamin, M.G.; LaVeck, M.A.; Stahel, R.A.; Lechner, J.F.; Harris, C.C. Establishment of a human in vitro mesothelial cell model system for investigating mechanisms of asbestos-induced mesothelioma. *Am. J. Pathol.* 1989, 134, 979–991.
47. Fischereder, M.; Luckow, B.; Sitter, T.; Schroppel, B.; Banas, B.; Schlondorff, D. Immortalization and characterization of human peritoneal mesothelial cells. *Kidney Int.* 1997, 51, 2006–2012, doi:10.1038/ki.1997.273.

48. Pruett, N.; Singh, A.; Shankar, A.; Schrupp, D.S.; Hoang, C.D. Normal mesothelial cell lines newly derived from human pleural biopsy explants. *Am. J. Physiol. -Lung Cell.* 2020, 319, L652–L660, doi:10.1152/ajplung.00141.2020.
49. Lamouille, S.; Xu, J.; Derynck, R. Molecular mechanisms of epithelial-mesenchymal transition. *Nat. Rev. Mol. Cell Bio.* 2014, 15, 178–196, doi:10.1038/nrm3758.
50. Barrero, M.J.; Boue, S.; Belmonte, J.C.I. Epigenetic mechanisms that regulate cell identity. *Cell Stem Cell* 2010, 7, 565–570, doi:10.1016/j.stem.2010.10.009.
51. Thiagalingam, S. Epigenetic memory in development and disease: Unraveling the mechanism. *BBA Rev. Cancer* 2020, 1873, doi:10.1016/j.bbcan.2020.188349.
52. Li, V.C.; Kirschner, M.W. Molecular ties between the cell cycle and differentiation in embryonic stem cells. *Proc. Natl. Acad. Sci. USA* 2014, 111, 9503, doi:10.1073/pnas.1408638111.
53. Brown, G.; Hughes, P.J.; Michell, R.H. Cell differentiation and proliferation—Simultaneous but independent? *Exp. Cell Res.* 2003, 291, 282–288, doi:10.1016/S0014-4827(03)00393-8.
54. Hardwick, L.J.A.; Ali, F.R.; Azzarelli, R.; Philpott, A. Cell cycle regulation of proliferation versus differentiation in the central nervous system. *Cell Tissue Res.* 2015, 359, 187–200, doi:10.1007/s00441-014-1895-8.
55. Dong, C.Y.; Zhang, J.W.; Fang, S.; Liu, F.S. IGFBP5 increases cell invasion and inhibits cell proliferation by EMT and Akt signaling pathway in Glioblastoma multiforme cells. *Cell Div.* 2020, 15, doi:10.1186/s13008-020-00061-6.
56. Shin, S.; Buel, G.R.; Nagiec, M.J.; Han, M.J.; Roux, P.P.; Blenis, J.; Yoon, S.O. ERK2 regulates epithelial-to-mesenchymal plasticity through DOCK10-dependent Rac1/FoxO1 activation. *Proc. Natl. Acad. Sci. USA* 2019, 116, 2967–2976, doi:10.1073/pnas.1811923116.
57. Testa, J.R.; Berns, A. Preclinical models of malignant mesothelioma. *Front. Oncol.* 2020, 10, doi:10.3389/fonc.2020.00101.

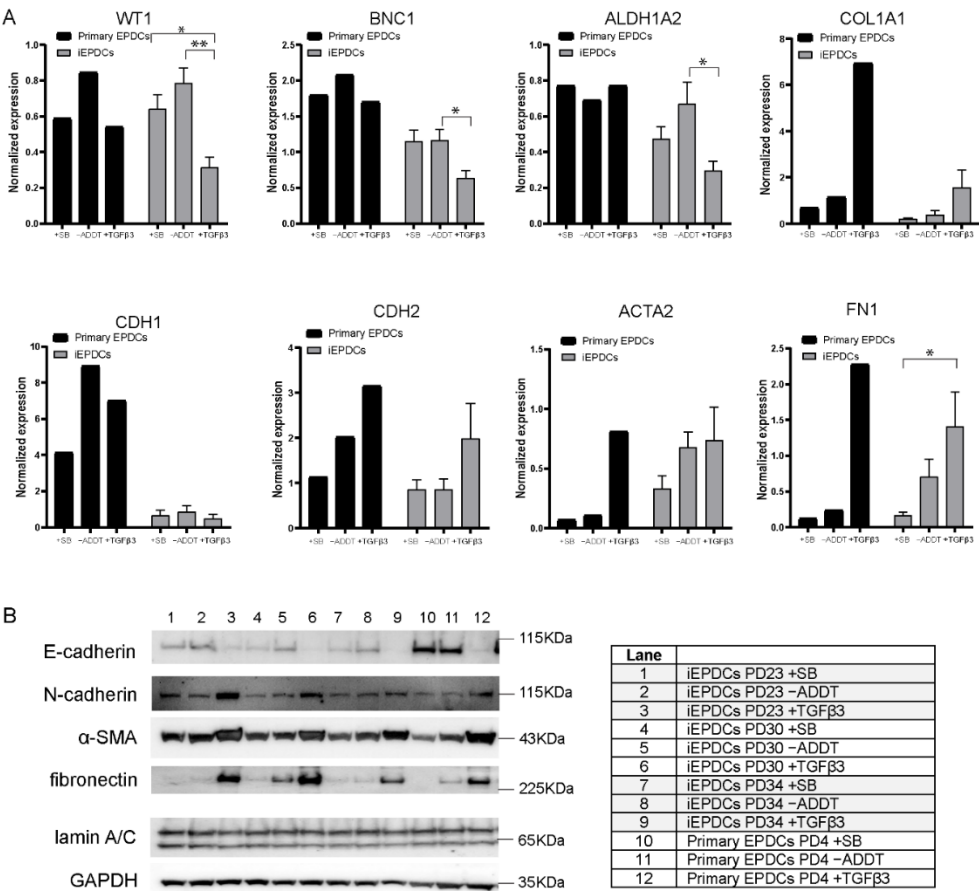
SUPPLEMENTAL FIGURES



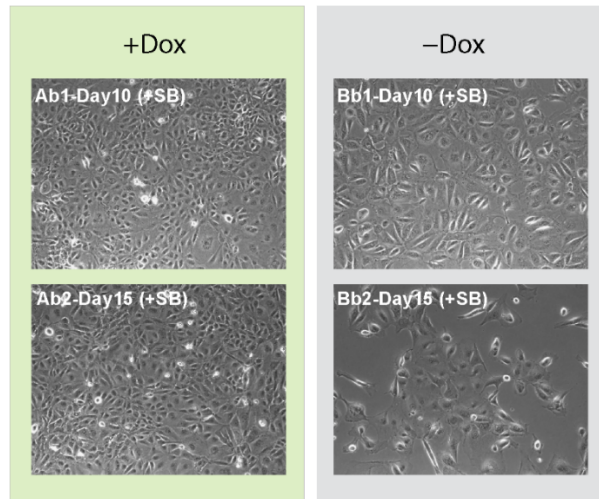
Supplemental Figure 1. Schematic overview of iEPDC generation. (A) Map of the LV shuttle plasmid to generate LV.iHsUBC.LT-WT. LTR, human immunodeficiency virus type 1 (HIV1) long terminal repeat; Ψ , HIV1 packaging signal; RRE, HIV1 Rev-responsive element; cPPT, HIV1 central polypurine tract and termination site; HsUBC, human ubiquitin C gene promoter; LT-WT, coding sequence of the wildtype SV40 LT protein; IRES, encephalomyocarditis virus internal ribosome entry site; tetR-KRAB, coding sequence of the hybrid tetracycline-controlled transcriptional repressor; WHVPRE, woodchuck hepatitis virus posttranscriptional regulatory element; tetO, tetracycline-responsive promoter element consisting of 7 repeats of a 19-nucleotide tetracycline operator sequence; AmpR, *Escherichia coli* β -lactamase gene; Ori, bacterial origin of replication (B) Diagram showing the derivation of epithelial and mesenchymal iEPDCs.



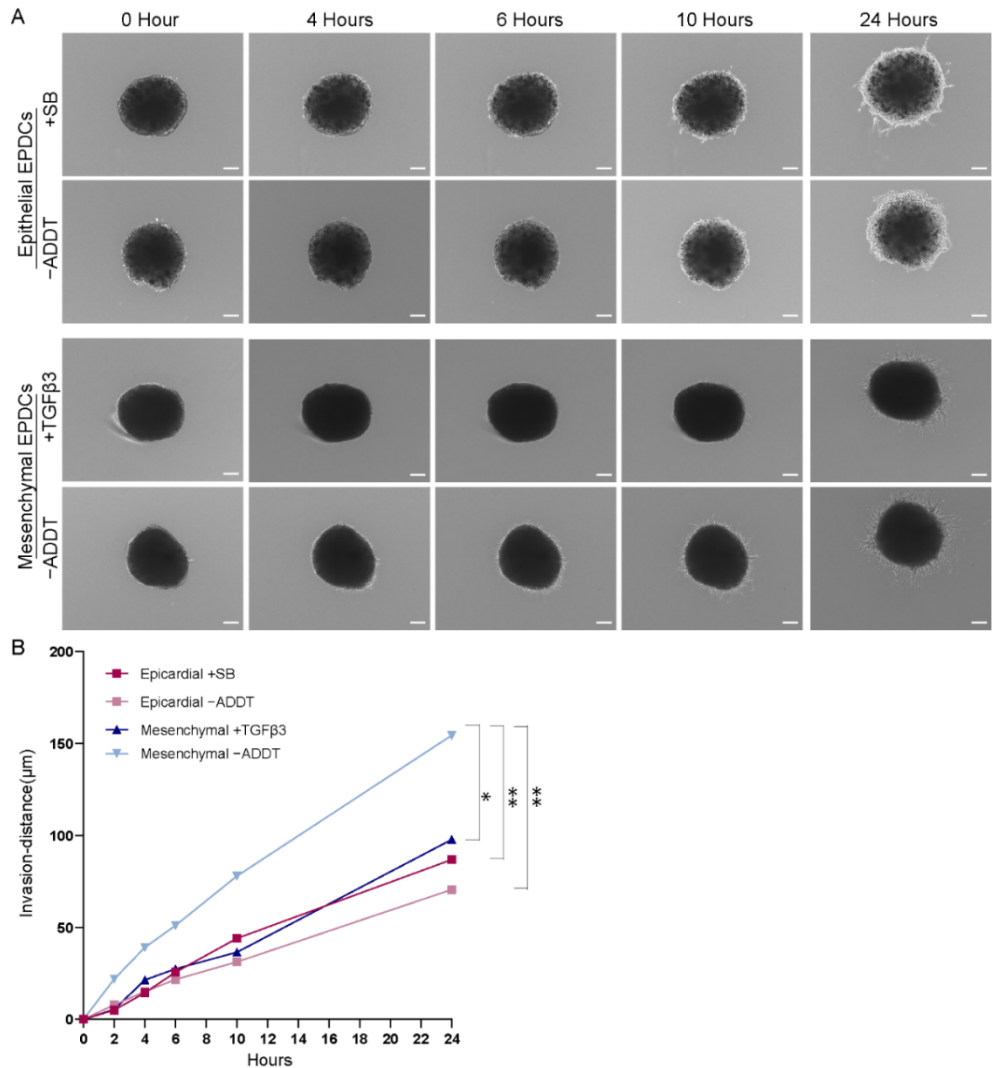
Supplemental Figure 2. Passaging of primary human EPDCs results in loss of their epithelial cuboidal morphology. (A) Representative phase contrast images of primary human EPDCs of PD2, -3 and -5 showing loss of cuboidal epithelial morphology by a fraction of the cells at PD5. (B) Representative phase contrast images of iEPDCs of PD6, -39 and -51. iEPDCs still have a cuboidal epithelial morphology at PD39 but start to display a more spindle-like appearance at PD51. (C) Bright field images of senescence β -galactosidase staining of iEPDCs at PD18, -29 and -50. Scale bar = 400 μ m.



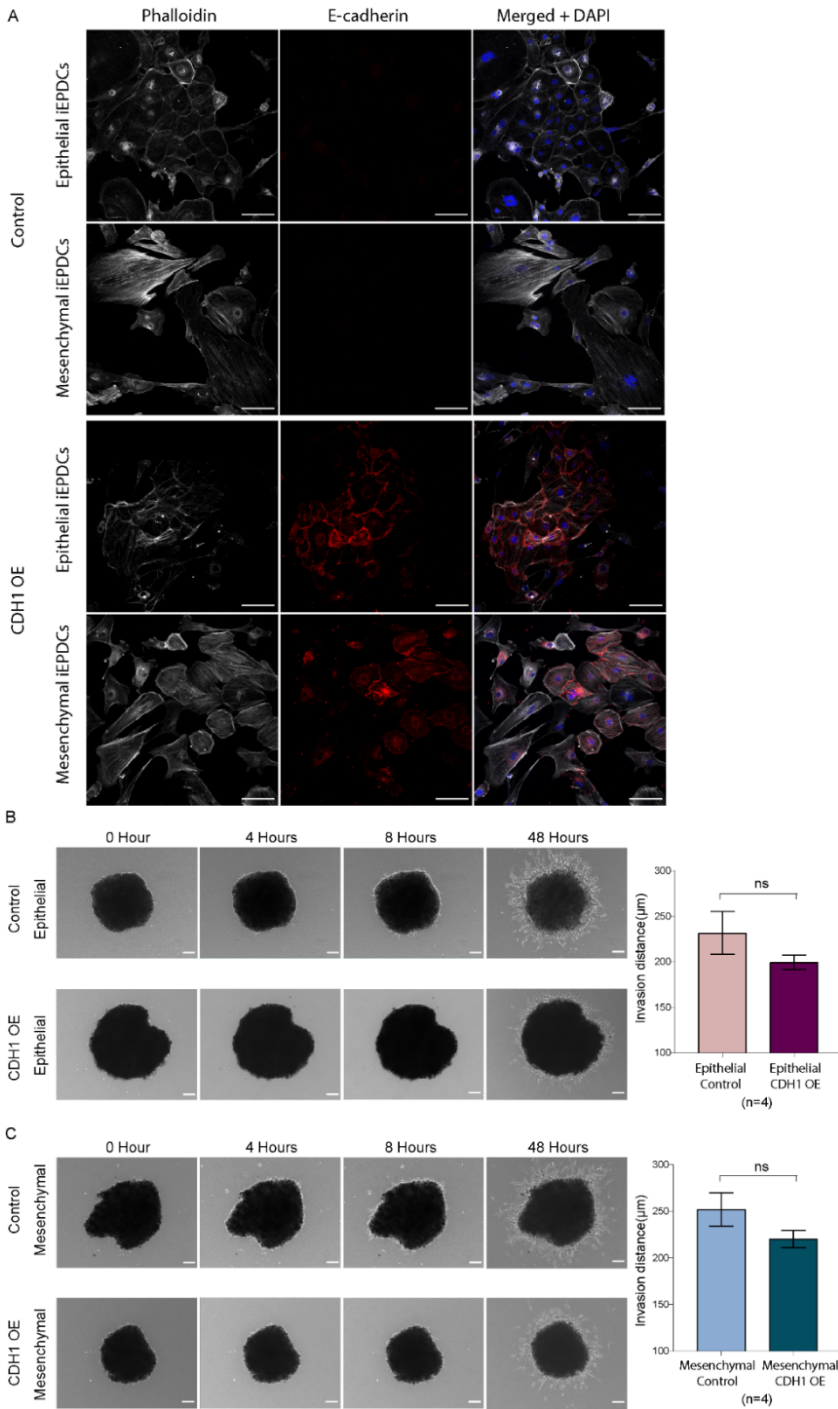
Supplemental Figure 3. Assessment by RT-qPCR and western blotting of epithelial and mesenchymal marker gene expression in primary human EPDCs and in iEPDCs. (A) RT-qPCR analysis. Black colored bars represent primary human EPDCs of PD5. Gray colored bars represent cumulative data of iEPDCs of PD25, -28, -30 and -35. For each sample, 3 technical replicates were performed. Data is shown as mean±SEM. * $P<0.05$, ** $P<0.01$. (B) Western blot analysis of primary EPDCs and of iEPDCs at PD23, -30 and -34 for E-cadherin, N-cadherin, α -smooth muscle actin (α -SMA) and fibronectin. iEPDCs and primary EPDCs were cultured without Dox under conditions that either inhibited (+SB) or stimulated (+TGF β 3) EMT. Lamin A/C and glyceraldehyde 3-phosphate dehydrogenase (GAPDH) served as loading controls. -ADDT, no additive.



Supplemental Figure 4. Appearance of iEPDCs after long-term culture in the presence of SB with or without Dox. Representative phase contrast images of iEPDCs cultured in the presence of SB and with or without Dox as indicated in **Fig. 4A**. The images in the left panel display the morphology of actively proliferating iEPDCs in the presence of SB; the images in the right panel show the morphology of cell cycle-arrested iEPDCs in the presence of SB.



Supplemental Figure 5. Invasion ability of epithelial and mesenchymal primary human EPDCs. (A) Representative images of primary human EPDC (PD4) aggregates in a 3D collagen gel-based invasion assay. Scale bar = 100 μm. (B) Quantification of EPDC invasion distance within 24 hours. The assay was performed in Dox-free complete medium with the indicated additives using either epithelial iEPDCs (*i.e.* iEPDCs pretreated with SB [10 μM] to preserve their cuboidal epithelial morphology) or with mesenchymal iEPDCs (*i.e.* iEPDCs pretreated for 5 days with TGFβ3 [1 ng/ml] to induce a spindle-like morphology). *P<0.05, **P<0.01. -ADDT, no additive.



Supplemental Figure 6. CDH1 overexpression reduces the invasion ability of mesenchymal EPDCs. (A) Immunostaining showing robust E-cadherin expression in iEPDCs (PD41) following CDH1 overexpression (OE). Scale bar = 100 μ m. (B) Left panel, representative images of epithelial iEPDCs overexpressing CDH1 in a collagen gel-based invasion assay. Right panel, quantification of epithelial iEPDC invasion distance within 48 hours. The epithelial iEPDCs were cultured in Dox-free complete medium with SB (10 μ M), which was left out of the medium 24 hours before the start of the invasion imaging. Scale bar = 100 μ m. (C) Left panel, representative images of mesenchymal iEPDCs overexpressing CDH1 in a collagen gel-based invasion assay. Right panel, quantification of mesenchymal iEPDC invasion distance after 48 hours. The mesenchymal iEPDCs were cultured in Dox-free complete medium with TGF β 3 (1 ng/ml) for 5 days before the start of the invasion imaging. Scale bar = 100 μ m.

SUPPLEMENTAL VIDEOS

<https://www.mdpi.com/article/10.3390/cells10082064/s1>.

Video S1: Epithelial iEPDC (+SB) migration, Video S2: Epithelial iEPDC (–ADDT) migration, Video S3: Mesenchymal iEPDCs (+TGF β 3) migration, Video S4: Mesenchymal iEPDCs (–ADDT) migration.

SUPPLEMENTAL METHODS

CDH1 overexpression in iEPDCs

Overexpression of human E-cadherin (CDH1) in iEPDCs was accomplished with an LV containing a bicistronic expression unit consisting of the human eukaryotic translation elongation factor 1 α gene promoter, the coding sequence of human CDH1, an encephalomyocarditis virus internal ribosomal entry site and the coding sequence of the *Aequorea victoria* enhanced green fluorescent protein. The shuttle plasmid for making this LV was obtained from Addgene (Watertown, MA; pHAGE-CDH1; plasmid number 116722). The production, purification and concentration of LV particles was done essentially as described in [1].

Senescence β -Galactosidase staining

To investigate senescence in iEPDCs at PD18, -29 and -50, a Senescence β -Galactosidase Staining Kit (#9860; Cell Signaling Technology, Leiden, the Netherlands) was applied as recommended by the manufacturer. Imaging acquisition was done with the EVOS FL Auto 2 Imaging System (Thermo Fisher Scientific).

Western blotting

Eight days after removal of Dox, iEPDCs at PD23, -30 and -34) and primary EPDCs were cultured for 5 days in complete medium containing SB (10 μ M), no additive or TGF β 3 (1 ng/ml). Next, cells were lysed in ice-cold RIPA Lysis and Extraction Buffer supplemented with Halt Protease Inhibitor Cocktail and the lysates were passed ≥ 3 times through a 30G needle and centrifuged at 16000 $\times g$ for 20 min at 4°C. The total protein concentration in each sample was determined

with the Pierce BCA Protein Assay Kit and 13 µg of each protein sample was subjected to polyacrylamide gel electrophoresis for subsequent blotting. For fibronectin and E-cadherin, a NuPAGE 3-8% Tris-Acetate Gel and corresponding running buffer were used for protein fractionation and lamin A/C served as loading control. For N-cadherin and α -smooth muscle actin, a Bolt 10% Bis-Tris Plus Gel and corresponding running buffer were used and glyceraldehyde 3-phosphate dehydrogenase (GAPDH) served as loading control. After electrophoresis, size-fractionated proteins were transferred to 0.45-µm polyvinylidene difluoride membranes (GE Healthcare, Chicago, IL) by wet electroblotting. Next, membranes were incubated for 1 hour in 2% ECL Prime Blocking Reagent in Tris-based saline/0.1% Tween-20 (TBST). Membranes were then incubated overnight at 4°C with primary antibodies in TBST/2% ECL Prime Blocking Reagent, washed 3 times with TBST and incubated for 1 hour with matching horseradish peroxidase-conjugated secondary antibodies. Following 3 washes with TBST, the membranes were incubated with SuperSignal West Femto Maximum Sensitivity Substrate and chemiluminescence was measured using the iBright FL1500 Imaging System (Thermo Fisher Scientific). After detection of the proteins of interest, the blots were stripped and immunostained for the loading controls lamin A/C and GAPDH. Details about the different reagents used for western blotting are provided in **Supplemental Table 2**.

E-cadherin immunostaining

iEPDCs were fixed with 4% paraformaldehyde in PBS, permeabilized with 0.5% Tween 20 (822184; Merck Millipore, Darmstadt, Germany) in PBS and non-specific epitopes were blocked with PBS containing 1% bovine serum albumin (A8022; Sigma-Aldrich, St. Louis, MO) and 0.05% Tween 20. Afterwards, iEPDCs were stained with rabbit anti-E-cadherin antibodies (Abcam, Cambridge, MA; ab40772; 1:500) overnight at 4°C. After 3 washes with 0.05% Tween in PBS, the cells were incubated with Alexa Fluor 647-conjugated donkey anti-rabbit IgG(H+L) (Thermo Fisher Scientific, Bleiswijk, the Netherlands A-31573; 1:250) and Alexa Fluor 594-conjugated phalloidin (Thermo Fisher Scientific A12381, 1:200) at room temperature for 1 hour. DAPI (300 nM; D3571; Thermo Fisher Scientific) was used to stain nuclei. All images were captured with a Leica TCS SP8 confocal laser scanning microscope (Leica Microsystems, Wetzlar, Germany).

Invasion assay of CDH1-overexpressing iEPDCs

Eight days after removal of Dox, the iEPDCs were cultured for 5 days in complete medium containing SB or TGFβ3 to keep epithelial iEPDCs or obtain mesenchymal iEPDCs, respectively. Next, aggregates of 20,000 epithelial iEPDCs, mesenchymal iEPDCs or primary EPDCs in a total volume of 30 µl were formed by the hanging drop technique. Twenty four hours before the invasion assay started, the epithelial iEPDCs in the hanging drop were given complete medium with or without SB while the clumps of mesenchymal EPDCs received complete medium with

or without TGFβ3. To measure their invasion ability, aggregates of iEPDCs that did or did not overexpress CDH1 were placed in drops of 3 mg/ml rat tail collagen I (354236; Corning Life Sciences, Amsterdam, the Netherlands) and cultured for the indicated time periods in EPDC culture medium. Time-lapse images were captured immediately with the EVOS FL Auto 2 Imaging System. The invasion distance of the cells away from the aggregates were measured with ImageJ 1.52p (National Institutes of Health [NIH], Bethesda, MA).

Supplemental Table 1. qPCR primers.

Gene		Sequence
GAPDH	Forward	AGCCACATCGCTCAGACAC
	Reverse	GCCCAATACGACCAAATCC
TBP	Forward	TGGAAAAGTTGTATTAACAGGTGCT
	Reverse	GCAAGGGTACATGAGAGCCA
HPRT1	Forward	CTCATGGACTGATTATGGACAGGAC
	Reverse	GCAGGTCAGCAAAGAACTTATAGCC
WT1	Forward	CAGCTTGAATGCATGACCTG
	Reverse	TATTCTGTATTGGGCTCCGC
BNC1	Forward	CCACCGTCAGTGTGACCAAT
	Reverse	CAATCTCCACCTGGCTTGTT
ALDH1A2	Forward	AACAAGGCCCTCACAGTGTC
	Reverse	TTCTGAGTACTCCCGCAAGC
CDH1	Forward	CCCGGTATCTTCCCCGC
	Reverse	CAGCCGCTTTCAGATTTTCAT
CDH2	Forward	CAGACCGACCCAAACAGCAAC
	Reverse	GCAGCAACAGTAAGGACAAACATC
ACTA2	Forward	CCGGGAGAAAATGACTCAAA
	Reverse	GAAGGAATAGCCACGCTCAG
COL1A1	Forward	CAGGCTGGTGTGATGGGATT
	Reverse	GGGCCTTGTTACCTCTCTC
FN1	Forward	CGTCATAGTGGAGGCACTGA
	Reverse	CAGACATTGTTCCCACTCA

Supplemental Table 2. Western blot reagents.

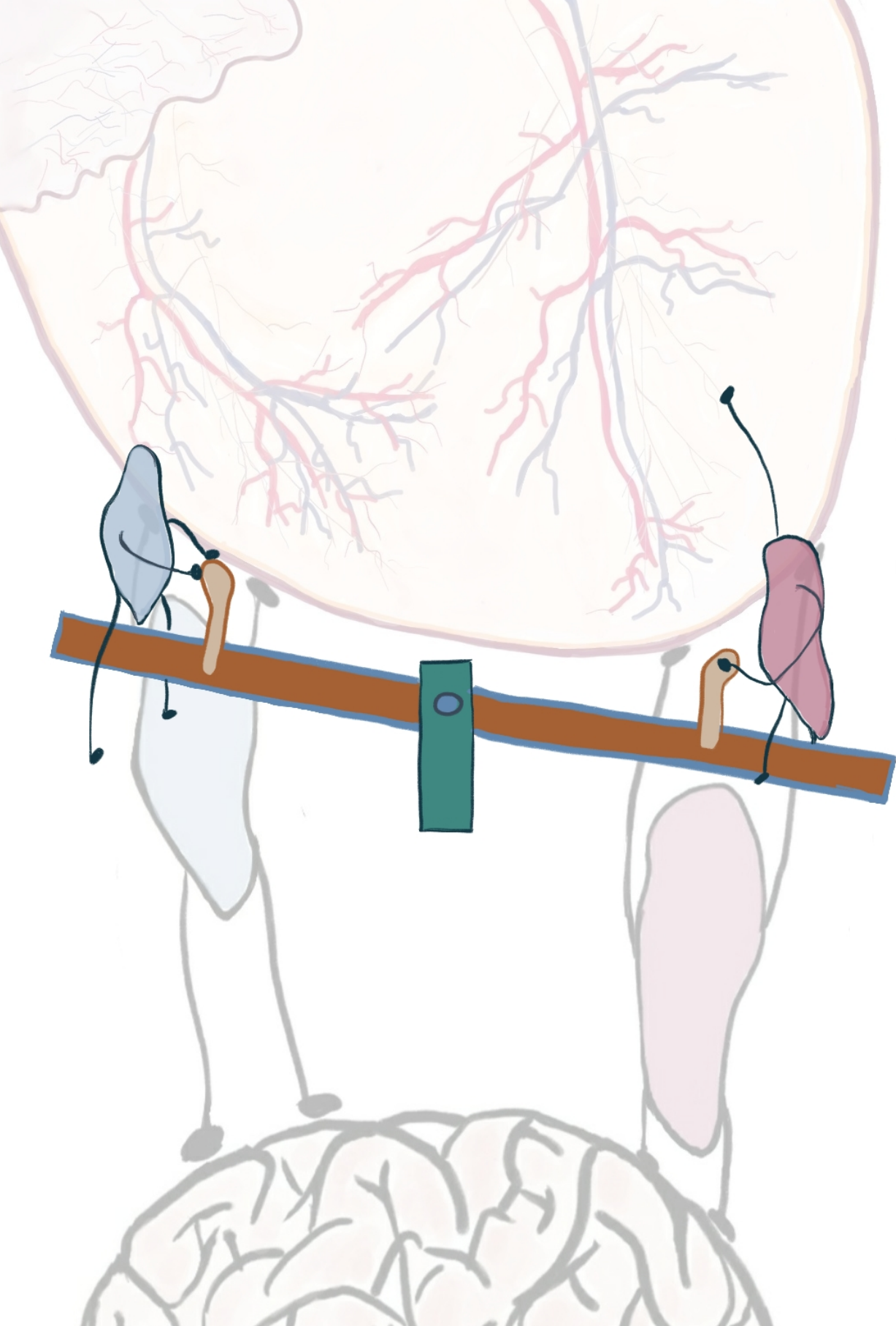
Device and Reagent	
RIPA Lysis and Extraction Buffer	89900; Thermo Fisher Scientific
Halt™ Protease Inhibitor Cocktail	87785; Thermo Fisher Scientific
Pierce BCA Protein Assay Kit	23227; Thermo Fisher Scientific
NuPAGE™ 3-8% Tris-Acetate Gel	EA03785BOX; Thermo Fisher Scientific
NuPAGE™ Tris-Acetate SDS Running Buffer (20X)	LA0041; Thermo Fisher Scientific
NuPAGE™ Transfer Buffer (20X)	NP00061; Thermo Fisher Scientific
Bolt™ 10% Bis-Tris Gel	NW00105BOX; Thermo Fisher Scientific
Bolt™ MOPS SDS Running Buffer (20X)	B000102; Thermo Fisher Scientific
Bolt™ Transfer Buffer (20X)	BT0006; Thermo Fisher Scientific
Mini Gel Tank and Blot Module Set	NW2000; Thermo Fisher Scientific
ECL Prime blocking reagent	RPN418V; Sigma-Aldrich
SuperSignal™ West Femto Maximum Sensitivity Substrate	34094; Thermo Fisher Scientific
Western Blot Stripping Buffer	21059; Thermo Fisher Scientific
iBright FL1500 Imaging System	Thermo Fisher Scientific
Antibody	
Mouse-anti-fibronectin	1:500; F6140; Sigma-Aldrich
Rabbit-anti-E-cadherin	1:5000; ab40772; Abcam
Mouse-anti-N-cadherin	1:200; C3865; Sigma-Aldrich
Rabbit-anti- α -smooth muscle actin (α SMA)	1:200; ab5694; Abcam
Rabbit-anti-Lamin A/C	1:5000; SC-20681; Santa Cruz
Mouse-anti-glyceraldehyde 3-phosphate dehydrogenase (GAPDH)	1:300; MAB374; Merck (Millipore)
HRP~Goat-anti-Mouse IgG(H&L)	1:25000; ab97040; Abcam
HRP~Goat-anti-Rabbit IgG(H&L)	1:25000; ab97080; Abcam

REFERENCE

1. Liu, J.; Volkers, L.; Jangsangthong, W.; Bart, C.I.; Engels, M.C.; Zhou, G.; Schali, M.J.; Ypey, D.L.; Pijnappels, D.A.; de Vries, A.A.F. Generation and primary characterization of iAM-1, a versatile new line of conditionally immortalized atrial myocytes with preserved cardiomyogenic differentiation capacity. *Cardiovasc. Res.* 2018, *114*, 1848–1859, doi:10.1093/cvr/cvy134.

PART III

CARDIAC SYMPATHETIC NERVOUS SYSTEM REMODELING AFTER CARDIAC DAMAGE



5

ACUTE MYOCARDIAL INFARCTION INDUCES NEURONAL
REMODELING IN MURINE SUPERIOR CERVICAL GANGLIA

Yang Ge^{1,2}, Lieke van Roon^{1,2}, Janine M. van Gils⁴, Conny J Munsteren¹, Anke M. Smits³, Marie-José T.H. Goumans³, Marco C. DeRuiter¹, Monique R.M. Jongbloed^{1,2}

1. Department of Anatomy & Embryology, Leiden University Medical Center, Einthovenweg 20, 2333 ZC Leiden, The Netherlands;

2. Department of Cardiology, Leiden University Medical Center, Albinusdreef 2, 2333 ZC Leiden, The Netherlands;

3. Department of Cell and Chemical Biology, Leiden University Medical Center, Einthovenweg 20, 2333 ZC Leiden, The Netherlands

4. Department of Nephrology, Leiden University Medical Center, Albinusdreef 2, 2333 ZC Leiden, The Netherlands;

ABSTRACT

A role for cardiac sympathetic hyperinnervation in arrhythmogenesis after myocardial infarction (MI) has increasingly been recognized. In humans and mice, the heart receives cervical as well as thoracic sympathetic contributions. In mice, superior cervical ganglia (SCG) have been shown to contribute significantly to myocardial sympathetic innervation of the left ventricular anterior wall. Of interest, the SCG is situated adjacent to the carotid body (CB), a small organ involved in oxygen and metabolic sensing. We investigated the remodeling of murine SCG, as well as the adjacent CB, over time after MI. Murine SCG were isolated from control mice, as well as 24 hours, 3 days, 7 days and 6 weeks after MI. SCG were stained for autonomic nervous system markers (Tubb3, TH and ChAT), as well as for neurotrophic factors (BDNF and NGF) and their receptors. Quantification of the staining-intensity as well as the neuronal size was performed in the entire SCG and in the adjacent CB. Our results show that ChAT and TH are co-expressed in SCG neuronal cells in control ganglia. After MI, neuronal remodeling occurs, with a significant increase in size of ganglionic cells and a decreased intensity of ChAT expression. This SCG remodeling was observed as early as 24 hours after infarction, with a peak at day 7, regressing within 6 weeks post-MI to basal levels. Of note, the most robust neuronal remodeling was observed at the region adjacent to the CB. An increase of neurotrophic factors (BDNF and NGF) was observed in the CB and neuronal cells, whereas the high affinity receptors for BDNF and NGF increased in the SCG after MI. These findings were concomitant with an increase in GAP43 expression indicating axonal outgrowth in the SCG. In conclusion, overt remodeling occurs after MI in the SCG as well as in the CB, suggesting an interaction of these 2 structures that might contribute to pathological cardiac hyperinnervation.

Keywords

Myocardial infarction, murine, superior cervical ganglion, neuronal remodeling, carotid body, neurotrophic factors, TrK, GAP43

INTRODUCTION

About one third of all global deaths are attributed to cardiovascular diseases (World Health Organization, 2017). In Western countries, the incidence of sudden cardiac death (SCD) is 50-100 per 100,000 which is attributed to coronary artery disease (CAD) in 70-80% of cases, despite the development of reperfusion strategies and medical therapies (Isbister and Semsarian, 2019). SCD after myocardial infarction (MI) has been classically linked to heterogeneous conduction in the infarct border zone caused by surviving cardiomyocytes surrounding the scar area, resulting in polymorphic ventricular tachycardia (VT) based on micro-re-entry (de Bakker et al., 1993; Wit, 2017). Interestingly, in the past decades a role for the cardiac autonomic nervous system in arrhythmogenesis after MI has increasingly been recognized (Zipes and Rubart, 2006; Li and Li, 2015). The heart is innervated by the autonomic nervous system, divided in sympathetic and parasympathetic branches, regulating cardiac function. In order to maintain a regular heartbeat, a balance is needed between sympathetic and parasympathetic tone. Parasympathetic input towards the heart is provided by (branches of) the vagal nerve that synapse in parasympathetic ganglia in the epicardial layer of the heart. Preganglionic cardiac sympathetic axons synapse with postganglionic sympathetic neurons in the sympathetic chain (Wink et al., 2020). In humans, cardiac input from the sympathetic chain is provided by both cervical as well as thoracic contributions (Kawashima, 2005; Wink et al., 2020).

A myriad of studies have reported a potential association of cardiac sympathetic hyperinnervation, usually defined as an increased amount of sympathetic nerve fibres in the area of damage, with SCD after MI. To date the exact underlying mechanism of the relation between sympathetic hyperinnervation and VT after MI is still uncertain. Likely, factors secreted by the ischemic myocardium retrogradely stimulate axonal outgrowth and remodeling of sympathetic ganglia, altering electrophysiological properties, thereby increasing the risk of VT and SCD (Han et al., 2012; O'Keeffe et al., 2016; Irie et al., 2017). Recent data shows an upregulation of nerve growth factor (NGF) in the ischemic zone after MI, that supports this concept (Ge et al., 2020).

Although several studies have shown sympathetic hyperinnervation as well as neuronal remodeling post-MI, the exact timeline of this phenomenon is less clear. In several species, neuronal remodeling has been described to occur 1 to 8 weeks after MI, characterized by increased expression of growth associated protein (GAP43) and synaptophysin—both markers for neuronal outgrowth—and increased amounts of tyrosine hydroxylase, suggesting an increase in innervation and a switch towards a more adrenergic phenotype (Nguyen et al., 2012; Ajjola et al., 2015; Li et al., 2015; Nakamura et al., 2016). Most studies, however, focus on the stellate ganglion, whereas limited information is available on the relevance of the other

ganglia providing sympathetic input to the heart. The superior cervical ganglion (SCG) gives input to the carotid plexus whose fibres run along the carotid arteries and provide sympathetic input towards the head where it stimulates parts of the eye, mouth and small blood vessels. The SCG also participates in innervation of the heart, providing the superior cardiac nerve that joins with postganglionic sympathetic fibres originating from other sympathetic ganglia at the cardiac plexus (Kawashima, 2005; Wink et al., 2020). Remarkably, in mice it has been shown that ganglionectomy of the SCG before MI leads to an almost entire loss of myocardial sympathetic innervation of the left ventricular anterior wall, in addition to a significantly reduction in chronic consequences of MI, such as myocardial inflammation, myocyte hypertrophy, and overall cardiac dysfunction (Ziegler et al., 2018). In human, it has been established that the SCG is involved in cardiac innervation (Kawashima, 2005), although the impact of a potential remodeling of this ganglion after MI, is unclear. In this respect, it may be relevant that the SCG is situated adjacent to the carotid body (CB), a small organ involved in oxygen, carbon and pH sensing, that has been shown to produce many neurotrophic factors (Lopez-Barneo et al., 2008). Of interest, Rocha et al. report that in rabbits the response of the chemo sensitive cardiac reflex of the CB was enhanced in the acute phase of MI (Rocha et al., 2003). Hypertonicity of the CB has been linked with cardiac disease such as hypertension and chronic heart failure. In rats with induced chronic heart failure, denervation of the CB performed early after MI, resulted in improved survival due to reduction of ventricular remodeling, less fibrosis and reduction of arrhythmias (Del Rio et al., 2013). Whether this is a transient phenomenon is unclear, as is the time-course of remodeling of the superior cervical ganglion and CB after MI.

Given the relevance of the SCG in cardiac innervation of the murine heart, as well as the still enigmatic role of this ganglion in the innervation of the human heart in health and disease, in the current study we investigated the remodeling of the murine SCG as well as the bordering CB over time after MI.

MATERIAL & METHODS

Animals

C57BL/6J (Jackson Laboratory) male mice of 13 weeks old (n=13) were used. All animal experiments were carried out according to the Guide for the Care and Use of Laboratory Animals published by NIH and approved by the Animal Ethics Committee of the Leiden University (License number AVD1160020185325), Leiden, The Netherlands.

Induction of MI and superior Cervical ganglia (SCG) isolation

Myocardial infarction was induced as previously described (Ge et al., 2020). Briefly, mice were anesthetized with 2% isoflurane, intubated and ventilated. The left anterior descending coronary artery (LAD) was permanently ligated and ischemia was confirmed by discoloration of the anterior wall of the left ventricle. The mice were given the analgesic drug Temgesic, 24 hours before and after the operation to relieve pain. As control, untreated mice (n=2) were included. All mice were maintained in a specific pathogen-free facility and regularly monitored. After 24h (n = 2; 4 SCG), 3 days (n = 3; 6 SCG), 7 days (n = 3; 6 SCG), or 6 weeks (n = 3; 6 SCG) post-MI mice as well as the healthy control mice (n=2; 4 SCG) were euthanized by CO₂ asphyxiation (**Fig. 1A**). For dissection of the left- and right SCG, an incision was made in the skin of the neck area, the submandibular glands were moved aside, whereafter the carotid artery bifurcation with the SCG could be captured bilaterally. After excision, both SCG were fixed with 4% paraformaldehyde (104005; Merck Millipore), and embedded in paraffin.

Immunofluorescence staining of sympathetic ganglia

The schematic illustration **Fig. 1B** shows the workflow schedule, during which a series of 5 µm-thick paraffin sections throughout each ganglion were used for immunostaining and subsequently analyzed. The sections were deparaffinized, pre-treated with Tris-EDTA buffer (pH 9) at 98°C for 12 min for antigen retrieval, and incubated with the following neuronal antibodies: anti-tyrosine hydroxylase (TH, a marker for sympathetic nerves)(Fisher Scientific PA14679; 1:1000), anti-choline acetyltransferase (ChAT, considered a marker for parasympathetic nerves)(Abcam ab181023; 1:1000), and anti-β-tubulin III (Tubb3, general nerve marker)(Santa Cruz; SC-80005; 1:1000) overnight at 4°C. On the second day, the sections were incubated with secondary antibodies donkey anti-rabbit Alexa Fluor 488 (Invitrogen A-21206; 1:250), donkey anti-sheep Alexa Fluor 568 (Invitrogen A21099; 1:250) and donkey anti-mouse Alexa Fluor 647 (Invitrogen A31571; 1:250) for 1 hour and followed by a 10 min nuclear staining with DAPI (Invitrogen D3571; 1:1000). The slides were mounted with ProLong Gold Antifade Mountant (Invitrogen P36930) and the images were captured with the Zeiss AxioscanZ1 microscope slide scanner.

For quantification, a minimum of 10 sections throughout each ganglion was analyzed, by including every 5th section; in case of longitudinally sectioned ganglia, shorter intervals were applied. In order to select cells in an unbiased way, an 1 mm² cross grid was placed with ImageJ on top of the image to aid in the random selection of cells for quantification (**Fig.1-B1**). When a cross overlapped at least $\frac{3}{4}$ with a cell, the region of interest (ROI) of the cytoplasm and nucleus was selected with ImageJ. After this was done for the whole section, the area of the

ROI template was applied to the TH and ChAT fluorescent channels of corresponding sections, after which the area of the cytoplasm and nucleus was measured with ImageJ.

To be able to quantify the dynamic remodeling of neurons in the area adjacent to the carotid body vs. the area remote from the carotid body, three images per ganglion were selected (4 ganglia per time point) that contained the CB adjacent to the SCG (Fig. 1-B2). Three images per ganglion that contained SCG area remote to the CB were also selected (Fig. 1-B2). Using ImageJ software (version 1.52p), a 500 x 500 μm square was placed within the SCG adjacent to the CB and in the remote region of the SCG. Within each square 20 cells were drawn in as ROI and the area and ChAT intensity were measured in ImageJ (version 1.52p).

Immunofluorescence detection and quantification of neurotrophic factors

5 μm -thick paraffin sections that contained the SCG adjacent to the CB were used for the study of neurotrophic factors (Fig. 1-B2). As described above, the sections were first deparaffinized and antigen retrieval was performed. Hereafter, the sections were incubated with the neurotrophic markers anti-brain derived neurotrophic factor (BDNF)(Abcam ab108319; 1:250, anti-nerve growth factor (NGF)(Abcam ab6199; 1:100) or the receptor anti-pan Neurotrophic Receptor Tyrosine Kinase (pan Trk)(Abcam ab181560; 1: 500) combined with anti-TH (Fisher Scientific PA14679; 1:1000) overnight at 4°C. Secondary antibodies, donkey anti-rabbit Alexa Fluor 488 (Invitrogen A-21206; 1:250) and donkey anti-sheep Alexa Fluor 568 (Invitrogen A21099; 1:250), were incubated to visualize the expression of corresponding factors and receptor, followed by a 10 min nuclear staining with DAPI (Invitrogen D3571: 1:1000).

Images were captured with Leica confocal SP8 microscopy under the same exposure time and gain settings. To quantify BDNF, NGF and pan-Trk expression, 3 sections of each ganglion and 4 ganglia of each timepoint were used to measure the corresponding fluorescence intensity in ImageJ (version 1.52p).

Immunohistochemical staining of growth-associated protein 43 and quantification

5 μm -thick paraffin sections were used to study neuronal remodeling using the Growth Associated Protein 43 (GAP43), a marker for nerve sprouting (Benowitz and Routtenberg, 1997; Korshunova and Mosevitsky, 2010) (Fig. 1-B3). As previously described, the sections were first deparaffinized and antigen retrieval was performed. Hereafter, the sections were incubated with the primary recombinant anti-GAP43 antibody (Abcam ab75810, 1:2000) overnight at 4°C. The next day, the primary antibody was washed away and thereafter the slides were incubated with the secondary biotinylated anti-rabbit IgG (H+L) antibody (Vector Laboratories BA-1000, 1:200) for 1 hour, followed by an incubation with ABC-AP (Vector Laboratories AK-5000) for 30 min. To visualize GAP43, the slides were incubated with alkaline phosphatase substrate

(Vector Laboratories SK-5105) in the dark for 5 minutes. The substrate was then washed away and the slides were counterstained with haematoxylin (Klinipath VWRK4085-9002) to visualize the nuclei. After dehydration the sections were mounted with Entellan (Merck 107961) mounting medium and all images were captured with the 3DHISTECH scanner.

To quantify GAP43 expression, 3 sections of each ganglion and 4 ganglia per time point were quantified. Individual sections were imported into ImageJ and the ganglion region was selected by hand with ImageJ selection function and set as ROI. To acquire the percentage of the GAP43+ area the measurements were performed as follows: within the green channel the total area of the ganglion was measured by setting the threshold on the maximum and the GAP43+ area was measured using the default threshold in ImageJ (version 1.52p).

Statistics

Data were presented as mean \pm standard error of the mean (SEM). One-way ANOVA and multiple comparisons followed by a Tukey's post hoc analysis or Dunnett's T3 multiple comparisons test when standard deviations (SDs) are different to determine statistically significant differences among groups. To compare the differences of neuronal cell size and ChAT intensity in the neuronal cells located adjacent versus remote to CB, the paired t-test was applied. Results were considered significantly different when the p value was <0.05 . GraphPad Prism (GraphPad Software, San Diego, CA, USA; version 9) was used for statistical analysis. Pearson correlation coefficients were used to test the linear relationship between two variants. R (version 4.0.2) was used for Pearson correlation coefficients and linear regression.

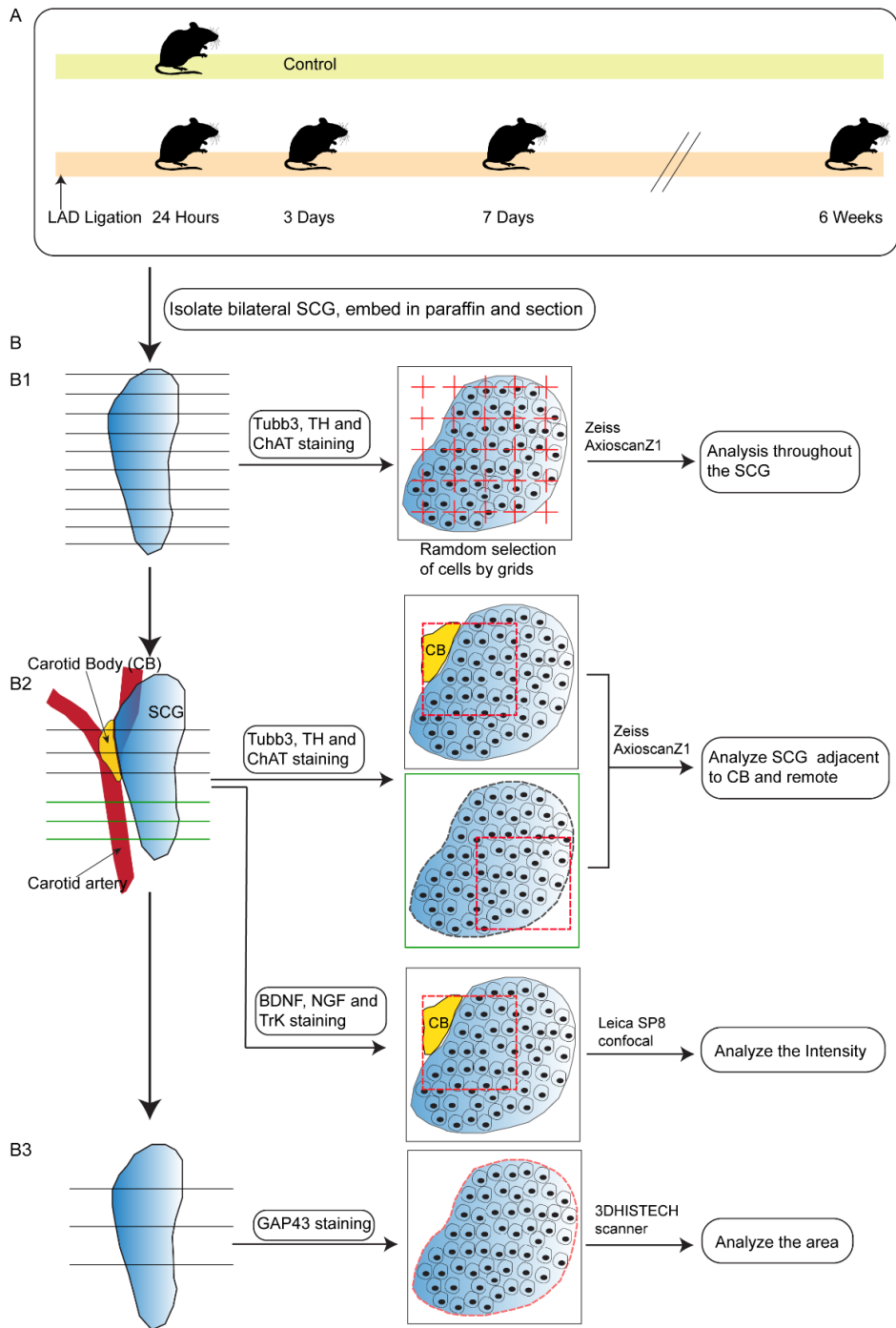


Figure 1. Schematic workflow of the time-course study. From the top to the bottom panels, the schematic diagram is a step-by-step illustration of the methods performed in this time-course study of SCG remodeling after MI. A. Representation of MI induction and the post-MI timepoints in mouse. B. Brief illustration of all study methods applied. Left panels display an overview of the sections chosen in each analysis. The midline panels explain the cells/regions selection for each analysis from a cross-sectioned view. B1. Analysis of ChAT and TH expression in complete SCG. B2. Analysis of ChAT and TH expression in the region adjacent versus remote to the CB. Quantification of neurotrophic factors and their receptors in the region adjacent to the CB. B3. Analysis of growth associated protein 43 (GAP43) in the SCG.

RESULTS

Superior cervical ganglia exhibit dynamic neuronal remodeling after acute myocardial infarction

To investigate the remodeling of the murine SCG over time post-MI, MI was induced in mice by permanent ligation of the LAD and the SCG was analyzed after 24 hours, 3 days, 7 days, and 6 weeks. Staining of serial sections of the murine SCG with the general nerve marker Tubb3 provided an overview of the distribution of neurons and nerves in each ganglion (**Fig. 2A**). Previous studies in sympathetic ganglia (i.e. stellate ganglia) in both rat and pig demonstrated the existence of ChAT+ neurons in sympathetic ganglia (Nguyen et al., 2012; Ajijola et al., 2015). We performed immunostainings for the parasympathetic marker ChAT as well as with the sympathetic TH marker in the SCG post-MI. This revealed a series of striking alterations in SCG neuronal cells in the different stages after MI compared to control SCG, referred to as dynamic neuronal remodeling. As shown in **Fig. 2A**, we observed many neuronal cells that expressed both TH and ChAT (TH+ ChAT+) in the SCG throughout the post-MI timeline.

Multiple control experiments were carried out to confirm the reliability of the detected TH+ChAT+ expression in murine SCG neuronal cells. Double immunostaining for ChAT and TH was performed on the nodose ganglion (NG), a well-described entirely parasympathetic ganglion. As reported by Bookout et. al (Bookout and Gautron, 2021), neuronal cells of the NG were only positive for ChAT, but not for TH (TH-ChAT+), and both TH- and TH+ neuronal cells were observed in the “bridge” between the NG and the SCG (**Supplemental Fig. 1A**). Moreover, no obvious difference in ChAT intensity was detected between the NG and SCG neuronal cells (**Supplemental Fig. 1A**). In addition, immunoblot analysis of protein lysates from either whole SCG tissue or nuclei showed the main presence of ChAT at the size of 69KDa as expected (**Supplemental Fig. 1B and C**), which reconfirmed the specific detection of ChAT in SCG. The cell lysate of non-neuronal cells (human epicardial cells) was used as negative control, due to the absence of ChAT expression in these cells. (**Supplemental Fig. 1C**). These findings indicate that no cross reaction between ChAT and TH occurred in the double immunostainings, and

support the specificity of the ChAT staining. Co-staining of TH and ChAT in a human sympathetic ganglion (stellate ganglion) presented with a similar ChAT staining pattern as observed in the mouse ganglia (**Supplemental Fig. 1D**).

Time course comparison of the SCG of healthy control mice vs. post-MI mice revealed obvious alterations of the ChAT expression in neuronal cells both in the level of expression as well as the intracellular location in the neuronal cell body. Quantification of the neuronal cell size of the entire SCG indicated that neuronal remodeling appears as early as 3 days post-MI and shows a significant increase at day 7 post-MI when compared to control animals (**Fig. 2B**). TH expression was steadily high throughout the timeline (**Fig. 2C**) whereas ChAT expression decreased as early as 24 hours post-MI, showed a significant decrease at day 7 post-MI as compared to control, and had returned to control values after 6 weeks post-MI (**Fig. 2D**). This alteration in ChAT expression is concomitant with a significant decrease of ChAT expression in the nuclei, with the most marked decrease at day 7 post-MI (**Fig. 2E**).

SCG neurons adjacent to the CB display robust neuronal enlargement

The most striking neuronal cell remodeling was observed in the region of the SCG most adjacent to the CB in post-MI mice. Therefore, further time course analysis was performed specifically of this region. As presented in **Fig. 3A**, post-MI SCG neuronal cells located adjacent to the CB exhibit an striking enlargement in cell size accompanied with a loss of ChAT expression, especially at day 3 post-MI, compared to a relatively even distribution in cell size and ChAT expression of control SCG. Pairwise presented data in **Supplemental Fig. 2A and B** show the distribution width of the neuronal cell size and ChAT intensity, indicating a varying degree of remodeling within each time point as well as the region within the post-MI SCG. When observing the changes over time, the alterations in the neuronal cells adjacent to the CB versus the neuronal cells located remotely demonstrated a clear remodeling, with a significant difference ($P < 0.01$) of the change in cell size (**Fig. 3B**). The ChAT intensity of the neuronal cells adjacent to the CB versus the neuronal cells located remotely was not significantly different (**Fig. 3C**).

As the enlarged neuronal cells displayed low expression of ChAT, especially a decrease in cytoplasmic ChAT 3 days post-MI (**Fig. 3A-C**), co-efficiency analysis was performed, to examine whether the cell enlargement caused the decrease of ChAT. This revealed a negative correlation between neuronal cell size and ChAT expression, which was significantly detectable in the SCG 24 hours, 3 days and 7 days post-MI (**Fig. 3D**). The correlation disappeared in SCG 6 weeks post-MI (**Fig. 3D**).

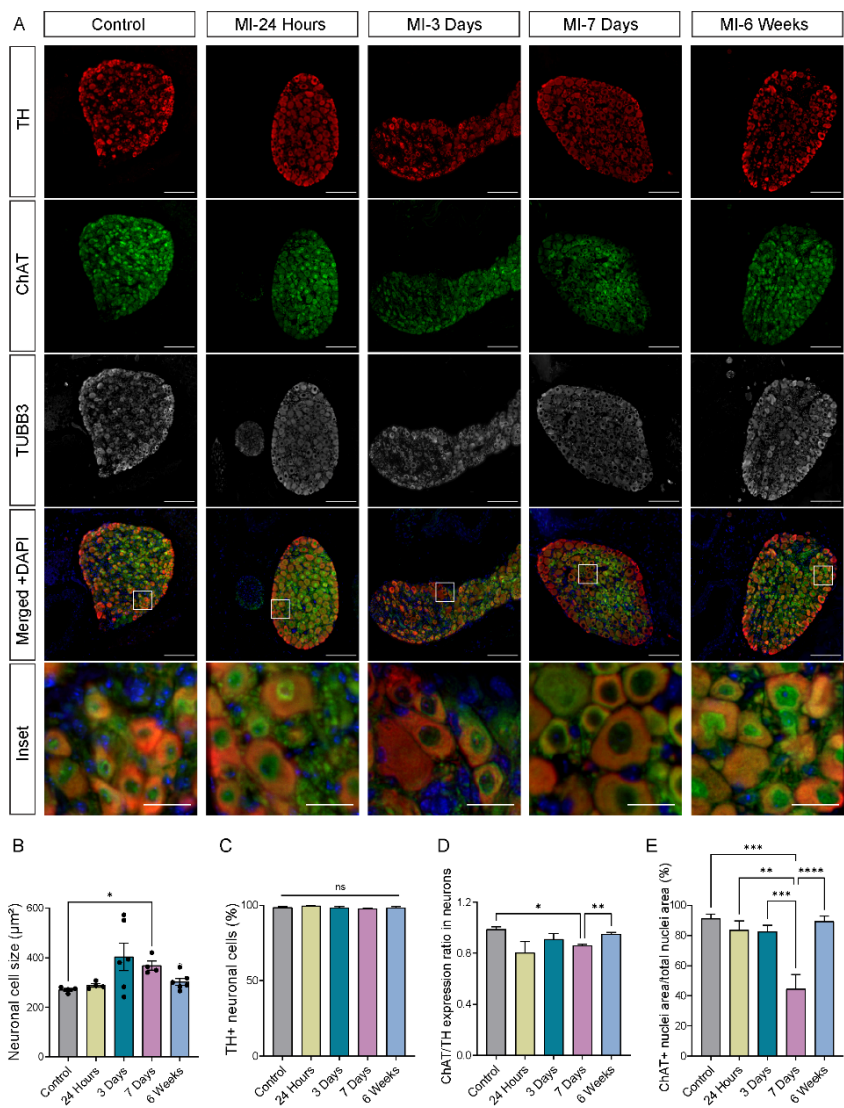


Figure 2. Superior cervical ganglia exhibit dynamic remodeling after MI. A. Immuno-fluorescence staining of TH (red), ChAT (green), Tubb3 (gray), and nuclei (blue) in SCG from control mice and mice post-MI at 24 hours, 3 days, 7 days, and 6 weeks. The enlarged regions are shown at the bottom panels. Scale bar = 100 µm in all panels, with exemption of the enlarged panels: here Scale bar = 20 µm. B. Average size of TH+ cells of each ganglion derived from control mice and post-MI mice at 24 hours, 3 days, 7 days, and 6 weeks. C. Percentage of sympathetic neurons that show high TH expression in all ganglia. D. Comparison of the area ratio of ChAT expression/TH expression in the SCG neuronal cells of each timepoint. E. Comparison of the expression of ChAT in neuronal nuclei in each timepoint. ns = not significantly different, * P< 0.05, ** P< 0.01, *** P<0.001, **** P< 0.0001.

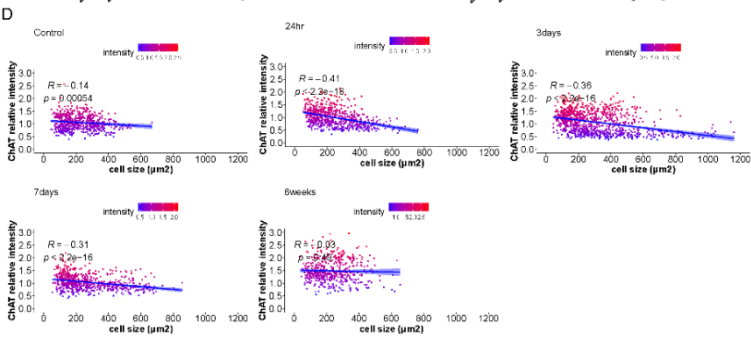
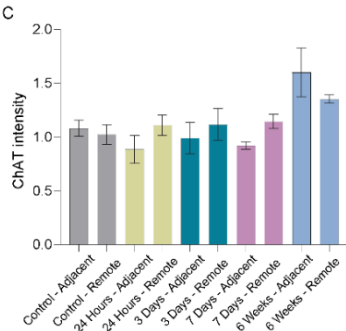
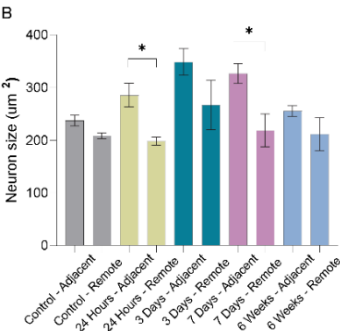
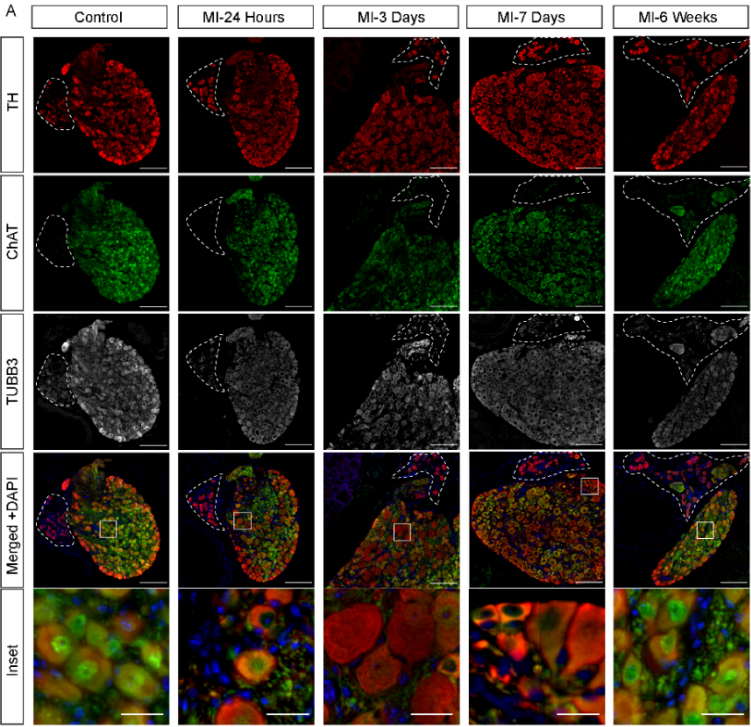


Figure 3. SCG neurons adjacent to the carotid body display robust neuronal enlargement. A. Immunofluorescence staining of TH (red), ChAT (green), Tubb3 (gray), and nuclei (blue) in SCG regions located adjacent to the CB (dashed lines) of control mice and post-MI mice at 24 hours, 3 days, 7 days, and 6 weeks. Enlarged region is shown at the bottom panels. Scale bar = 100 μm all panels, except in the enlarged panel, where Scale bar = 20 μm . B and C. Bar graphs that display the alterations of SCG neuronal cell size and the relative ChAT intensity in the region *adjacent* to the CB vs *remote*. D. ChAT intensity of neuronal cells are plotted against the neuronal cell size (μm^2) of SCG derived from control mice and post-MI mice at 24 hours, 3 days, 7 days, and 6 weeks. The lines indicate the linear regression of the plotted data. Light blue regions indicate the standard error of the mean (SEM) of ChAT intensity. Each point represents one neuronal cell. R demonstrates correlation coefficients at indicated P value. ** $P < 0.01$.

BDNF and NGF expression is increased in CB and neuronal cells after MI

Based on our observation that SCG neurons adjacent to the CB exhibited stronger remodeling post-MI, and as it has been shown that the CB type I glomus cells can be identified with the conventional marker TH and that these cells secrete neurotrophic factors during development as well as in response to environmental stimuli (Pulgar-Sepúlveda et al., 2018; Stocco et al., 2020), as a next step we assessed BDNF expression in the SCG and the CB. In the CB, glomus type I cells were recognized as TH+ cells, and analysis of BDNF expression indicated an increased expression of BDNF in type I glomus cells (i.e. TH+ cells) of the CB post-MI, which reached its highest peak and showed a significant difference at day 7 post-MI when compared to control (**Fig. 4A and B**). Notably, BDNF expression in the CB was significantly regressed at week 6 compared to day 7 post-MI, and returned to basal level (**Fig. 4B**).

In addition to BDNF, NGF, another well-known neurotrophic factor, was examined in both the CB and SCG neurons. Similar to BDNF, NGF expression in both the CB and SCG neurons reached the first small peak 24 hours post-MI, although not statistically significantly different from control due to the high variation (**Fig. 5A-C**). The second peak of NGF expression appeared at day 7 post-MI and the expression was significantly increased as compared to SCG neurons in control, followed by a drop 6 weeks post-MI (**Fig. 5A-C**).

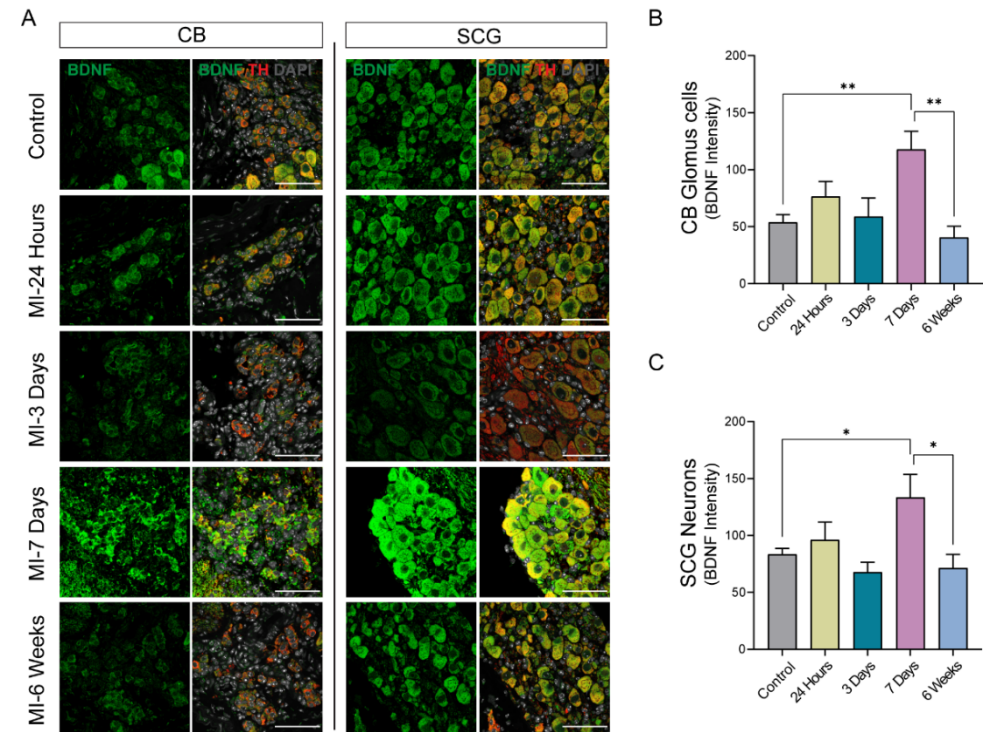


Figure 4. BDNF is increased in CB and neurons in SCG after MI. **A.** Immunofluorescence staining of BDNF (green), TH (red), and nuclei (DAPI, gray) in the CB and SCG neurons of control mice and mice post-MI at 24 hours, 3 days, 7 days, and 6 weeks. Scale bar = 100 μ m. **B** and **C.** BDNF intensity of the CB and SCG neurons at different timepoints post-MI were quantified by measuring fluorescence integrated density. Both the CB glomus type I cells and SCG neurons are recognized as TH⁺ cells. * $P < 0.05$, ** $P < 0.01$

High affinity receptors of BDNF and NGF in SCG neurons are increased after MI

Given the importance of the neurotrophic receptor (TrKA and TrKB) expression in neurons to facilitate the binding of neurotrophic factors (NGF and BDNF) and mediating their subsequent impact on neuronal survival and axonal growth (Ginty and Segal, 2002; Kuruville et al., 2004; Kimura et al., 2012), we investigated whether the high affinity receptors TrKA and TrKB were expressed in the SCG. Immunostaining of SCG, using a pan-Trk antibody, showed a low expression of Trk in control SCG neurons (**Fig. 6A**). According to the time course analysis, Trk expression in SCG neurons gradually increased and was significantly upregulated at day 7 post-MI. This upregulation, when compared to control, was still present at 6 weeks post-MI (**Fig. 6A and B**).

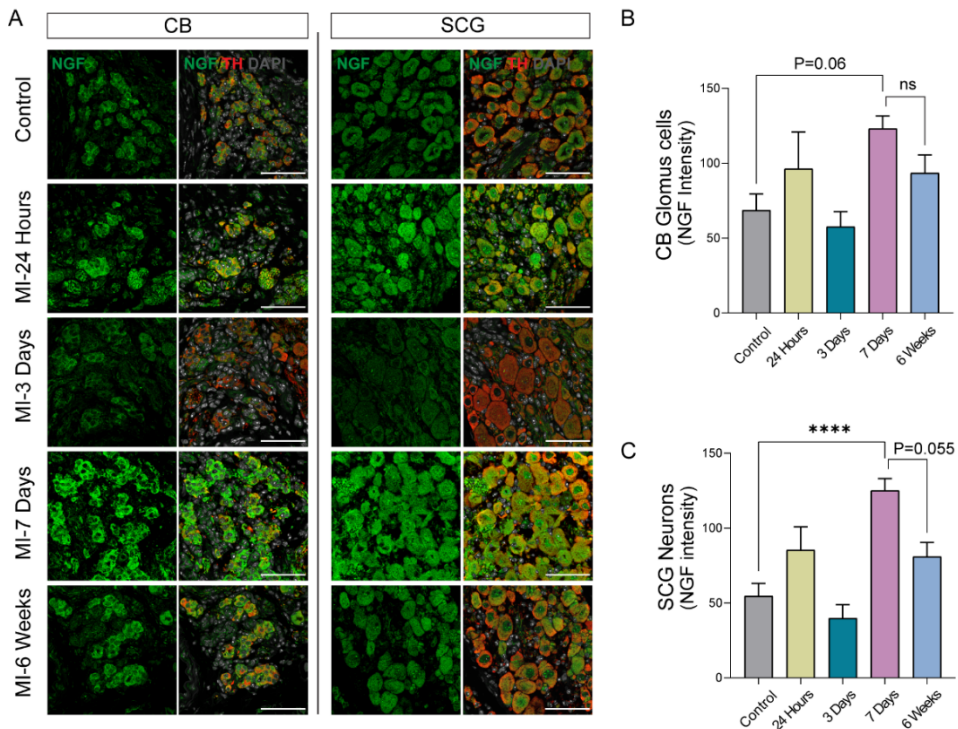


Figure 5. NGF is increased in CB and neurons in SCG after MI. **A.** Immunofluorescence staining of NGF (green), TH (red), and nuclei (DAPI, grey) in the CB and SCG neurons of healthy control mice and mice post-MI at 24 hours, 3 days, 7 days, and 6 weeks. Scale bar = 100 μ m. **B** and **C.** NGF intensity of the CB and SCG neurons at different timepoints post-MI were quantified by measuring fluorescence integrated density. Both the CB glomus cells and SCG neurons are recognized as TH⁺ cells. **** $P < 0.0001$.

GAP43 reveals neuronal outgrowth after MI

As we observed neuronal remodeling concomitant with an increased expression of the neurotrophic factors BDNF and NGF and their receptors, we postulated that this neuronal remodeling in SCG after MI mediates new axon formation and axonal elongation. SCG of control mice and mice post-MI were therefore immunostained for GAP43, a growth- and plasticity-related protein that is involved in axon elongation during early development and nerve regeneration (Holahan, 2017). As is shown in **Fig. 7A**, after MI, a very strong increase in GAP43 expression was observed in axons and, to a lesser extent, also inside the neuronal cell bodies, while in the control SCG a very low number of axons expressed GAP43. Time-course comparison indicated a significant upregulation of GAP43 expression at all examined time points after MI, with the highest peak at day 3 post-MI (**Fig. 7B**).

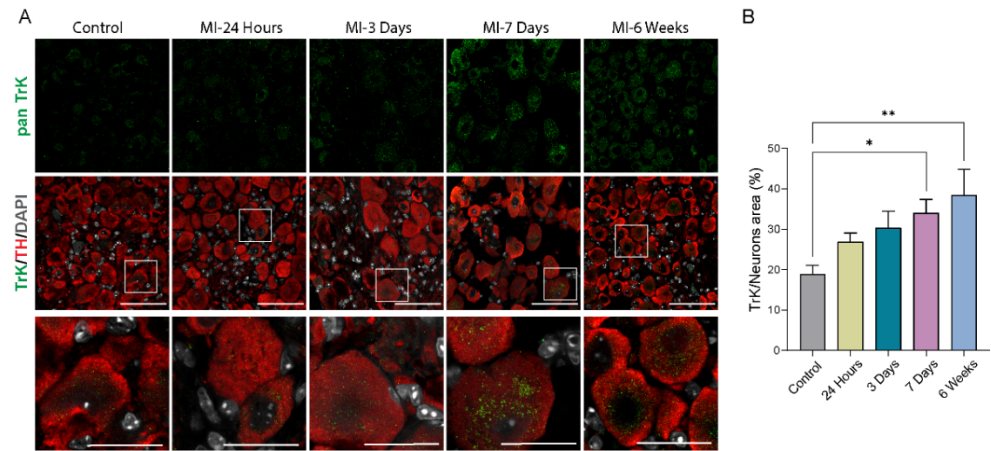


Figure 6. Increase in high affinity receptors for BDNF and NGF in SCG neurons after MI. **A.** Immunofluorescence staining of pan-Trk (green), TH (red), and nuclei (DAPI, gray) in SCG of control mice and mice post-MI at 24 hours, 3 days, 7 days, and 6 weeks. Representative images are shown in upper 2 panels and enlarged images in the lowest panels. Scale bar = 100 μ m. Scale bar = 20 μ m in enlarged panels. **B.** Time-course comparison of TrK expression in SCG. Percentage of TrK⁺ area out of the TH⁺ neuronal area is used to indicate TrK expression level. * $P < 0.05$, ** $P < 0.01$.

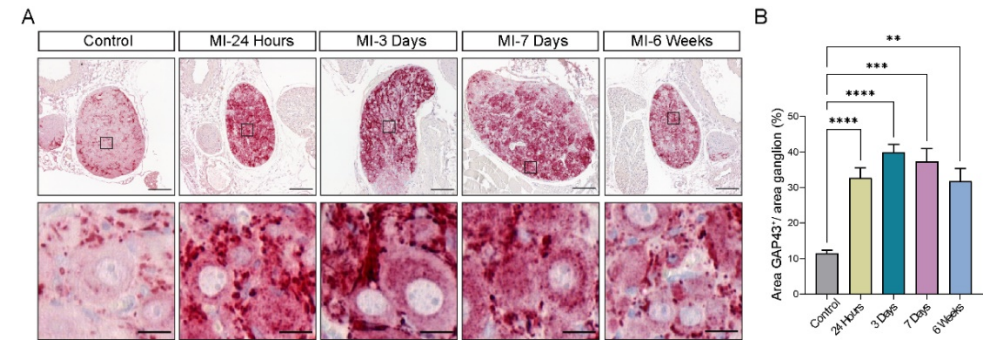


Figure 7. Growth Associated Protein 43 reveals neuronal outgrowth after MI. **A.** Representative images of immunohistochemistry staining of GAP43 in SCG from control mice and mice post-MI at 24 hours, 3 days, 7 days, and 6 weeks. Scale bar = 100 μ m. Lower panels are enlarged images, scale bar = 20 μ m. **B.** Time-course comparison of the GAP43 expression in SCG, percentage of GAP43⁺ area out of the ganglionic area is used to indicate the GAP43 expression level. ** $P < 0.01$, *** $P < 0.001$, **** $P < 0.0001$.

DISCUSSION

The role of the autonomic nervous system in post-MI arrhythmogenicity has gained increased attention over the past decades. Whereas vagal innervation is considered cardioprotective, sympathetic overdrive is associated with arrhythmias and sudden cardiac death (Fukuda et al., 2015; Hausenloy et al., 2019). Remarkably, although nerve tissue is generally notorious for its lack of regeneration capacity in adults, after cardiac damage the intriguing phenomenon of cardiac sympathetic hyperinnervation has been reported in multiple animal species, suggesting a renewed capacity of neuronal outgrowth of sympathetic neurons (Cao et al., 2000; Yokoyama et al., 2017). In line with this, several studies in human, rat, rabbit and pig, indicated neuronal and electrical remodeling in the stellate ganglia after MI (Ajjola et al., 2012; Han et al., 2012; Nguyen et al., 2012; Ajjola et al., 2015). In addition to the stellate ganglion and upper thoracic ganglia, the cardiac plexus also receives contributions from sympathetic nerves derived from the SCG that participate in cardiac ventricular innervation in both human and mouse (Pather et al., 2003; Kawashima, 2005; Ziegler et al., 2018). However, in contrast to the stellate ganglion, data on the time course of neural remodeling in the SCG - that is in close proximity to the oxygen- and PH-sensing CB - after MI is still limited. In the current study, we assessed the neuronal remodeling of murine entire SCG, including the CB, at several time points post-MI.

Our key findings are: i) Both ChAT and TH are co-expressed in SCG neuronal cells in healthy mice; ii) After MI, remodeling of the SCG occurs, with an increased size of ganglionic cells and a decreased intensity of ChAT expression; iii) Neuronal remodeling in the SCG starts already 24 hours after MI, reaches a peak at day 7 post-MI, after which a return to the healthy control situation is observed within 6 weeks post-MI; iv) The most robust neuronal remodeling of the SCG takes place at the region adjacent to the CB; v) An increase of neurotrophic factors (BDNF and NGF) occurs in the CB and neuronal cells, in the latter accompanied by a dynamic increase in the high affinity receptors of BDNF and NGF, concomitant with vi) an increase in axonal outgrowth in the SCG.

Expression of nerve markers - noticeable expression of ChAT in SCG. Sympathetic neuronal cells are generally considered as adrenergic cells, expressing the rate-limiting enzyme TH, that plays a pivotal controlling role in the synthetic pathway of catecholamines (adrenergic neurotransmitters) (Kobayashi and Nagatsu, 2012). In contrast, ChAT, the enzyme that catalyzes the synthesis of acetylcholine (cholinergic neurotransmitter in the peripheral nervous system) (Deutch and Roth, 2004) is generally considered as a marker for parasympathetic neurons. Remarkably, we observed neuronal cells that both express TH and ChAT in the mouse SCG. While we did observe TH+ChAT- in 3 days post-MI SCG and CB glomus type I cells, we did not detect TH in the parasympathetic nodose ganglion, indicating adequate

specificity of the antibody. In addition, this was supported by the detection of ChAT in different intracellular locations, either both in the cytoplasm and the nucleus or only in the cytoplasm, in SCG at different timepoints post-MI. Enriched biphenotypic neurons (ChAT+TH+) were also observed in human sympathetic ganglia in the current study. This is in contrast with what has been found in rat and pig sympathetic ganglia, where only few neurons are either biphenotypic or ChAT+ (Anderson et al., 2006; Ajijola et al., 2015), and no ChAT+ neurons were observed in rabbit sympathetic ganglia (Nguyen et al., 2012). These data indicate that phenotype differences might exist in sympathetic neurons among species, and the mouse model seems to resemble human ganglia in this respect, thus holding potential as an adequate model to study transdifferentiation (i.e. switch in neuronal phenotype) after cardiac damage (Olivas et al., 2016).

Neuronal remodeling. Post-MI time-course analysis demonstrated a neuronal remodeling of SCG which presented as a gradual decrease of ChAT expression and SCG neuronal cell enlargement with a remodeling starting already after 24 hours with a peak on day 7 and regression towards the control situation 6 weeks post-MI. These findings are in accordance with cardiac sympathetic re- and hyper-innervation post-MI (Kimura et al., 2007; Yokoyama et al., 2017). At the peak of remodeling on day 7 we observed a loss of nuclear ChAT. In both human and mouse it has been found that in younger subjects, ChAT was found mostly in neuronal nuclei whereas ChAT expression increased in neuronal cytoplasm in older individuals (Gill et al., 2007; Albers et al., 2014). We speculate that the stress response upon MI might induce a loss of nuclear ChAT, similar as seen with aging. It has previously been reported that the 69-kDa ChAT isoform can shift between the cytoplasmic and nuclear compartments, and nuclear ChAT can act as a transcriptional activator of a high affinity choline transporter (CHT1) which also regulates acetylcholine synthesis in neurons (Matsuo et al., 2011). The nuclear localization has also been shown to induce an epigenetic response (Winick-Ng and Rylett, 2018), which might also further mediate neuronal remodeling seen in SCG upon MI.

Neurotrophic factors & role CB. The finding that robust neuronal remodeling occurred in SCG neurons adjacent to the CB, suggests that the remodeling is potentially mediated by the CB. The CB, a neural crest derived structure located at the carotid bifurcation, is the main peripheral chemoreceptor in mammals (Pulgar-Sepúlveda et al., 2018). It can sense and respond to changes in blood flow, O₂- and CO₂ levels, PH as well as changes in metabolites such as glucose and lactate (Lopez-Barneo et al., 2008; Ortega-Saenz and Lopez-Barneo, 2020). In the CB, the type I glomus cells, that are immunoreactive for TH, express a wide range of growth factors and neurotrophic factors during development (Stocco et al., 2020). In our time-course analysis, after MI an increase in expression of neurotrophic factors (BDNF and NGF) in the type I glomus cells was observed. Of note, the peak of neuronal remodeling occurred when

highest levels of BDNF and NGF were expressed in the CB. Moreover, an upregulation of the TrK (the high affinity receptors of BDNF and NGF) receptor in the SCG neurons was observed alongside the upregulation of BDNF and NGF expression post-MI. This response was accompanied with neuronal cell enlargement and a decrease of ChAT expression. Surprisingly, levels of BDNF and NGF expression did not return to control levels at 6 weeks post-MI, whereas also the TrK expression in SCG neurons was maintained at high levels with a significant difference compared to control (Fig. 5B). Results indicate that neuronal remodeling is influenced by neurotrophic factors via a paracrine and autocrine effect, as was previously described (Davies, 1996; Cheng et al., 2011).

Although remodeling indicates a change in phenotype, the question is whether this actually contributed to an increase in new axons from the SCG. GAP43, a growth-associated protein, participates in the developmental regulation of axonal growth and the formation of new synapses, neurite outgrowth, and synaptogenesis after injury (Hou et al., 1998; Nguyen et al., 2009; Holahan, 2015). This might be related to its function in growth cones by stabilizing f-actin, preventing actin polymerization and promoting microtubule-based neurite outgrowth (He et al., 1997; Nguyen et al., 2009; Kusik et al., 2010). As its transcriptional expression is up-regulated in differentiating and regenerating neurons, though lowly expressed in mature neurons (Skene, 1989), it is a suitable marker to examine the neo-outgrowth of nerves after damage. In addition to previous findings of GAP43 expression in sprouting axons in infarcted heart (Zhou et al., 2004), in the current study, we showed a striking upregulation of the GAP43 expression in SCG neurons and axons post-MI, starting from as early as 24 hours post-MI compared to control.

In conclusion, overt remodeling towards an increased adrenergic phenotype occurs in the SCG as well as in the area of the CB, accompanied with an increase in axonal outgrowth in the SCG. The dynamics in expression of neurotrophic factors and their high affinity receptors, indicate a paracrine/autocrine neurotrophic effect. Results suggest an interaction of the SCG and CB after MI, that might contribute to pathological cardiac sympathetic hyperinnervation.

FUTURE PERSPECTIVES

In this time-course study, we show that the cholinergic marker ChAT is also expressed in SCG sympathetic neurons of the SCG and that expression of ChAT displays a dynamic transition, from expression in both cytoplasm and nucleus to only in cytoplasmic expression after MI. Further studies are required to study the functional implication of ChAT in adrenergic neurons and the mechanisms behind ChAT dynamic change caused by MI. Taking into account that the CB participates in SCG neuronal remodeling, as was indicated in the present study, the further

exploit of the potential interaction between CB and SCG could empower our integrative understanding of cardiac innervation after damage.

AUTHOR CONTRIBUTIONS

All authors contributed to the study conception and design. The experiments were designed by Y.G. and M.R.M.J. and performed by Y.G. and L.v.R.. Data collection and analysis were performed by Y.G. and L.v.R., supervised by J.M.v.G. and M.R.M.J. The first draft of the manuscript was written by Y.G., L.v.R., J.M.v.G. and M.R.M.J. and all authors commented on previous versions of the manuscript. All authors read and approved the final manuscript.

ACKNOWLEDGMENTS

We are grateful to Tessa van Herwaarden (Department of Cell and Chemical Biology, LUMC, Leiden, the Netherlands) for her help with induction of MI.

FUNDING

This work is supported by the Netherlands Organization for Scientific Research (NWO) [016.196.346 to M.R.M.J.], the Dutch Heart Foundation [2017T059 to A.M.S].

DECLARATION OF COMPETING INTEREST

The authors declare no competing interests.

REFERENCES

- Ajjola, O.A., Wisco, J.J., Lambert, H.W., Mahajan, A., Stark, E., Fishbein, M.C., et al. (2012). Extracardiac Neural Remodeling in Humans With Cardiomyopathy. *5*(5), 1010-1116. doi: 10.1161/CIRCEP.112.972836.
- Ajjola, O.A., Yagishita, D., Reddy, N.K., Yamakawa, K., Vaseghi, M., Downs, A.M., et al. (2015). Remodeling of stellate ganglion neurons after spatially targeted myocardial infarction: Neuropeptide and morphologic changes. *Heart Rhythm* 12(5), 1027-1035. doi: 10.1016/j.hrthm.2015.01.045.
- Albers, S., Inthathirath, F., Gill, S.K., Winick-Ng, W., Jaworski, E., Wong, D.Y., et al. (2014). Nuclear 82-kDa choline acetyltransferase decreases amyloidogenic APP metabolism in neurons from APP/PS1 transgenic mice. *Neurobiol Dis* 69, 32-42. doi: 10.1016/j.nbd.2014.05.008.
- Anderson, C.R., Bergner, A., and Murphy, S.M. (2006). How many types of cholinergic sympathetic neuron are there in the rat stellate ganglion? *Neuroscience* 140(2), 567-576. doi: <https://doi.org/10.1016/j.neuroscience.2006.02.021>.
- Benowitz, L.I., and Routtenberg, A. (1997). GAP-43: an intrinsic determinant of neuronal development and plasticity. *Trends Neurosci* 20(2), 84-91. doi: 10.1016/s0166-2236(96)10072-2.
- Bookout, A.L., and Gautron, L. (2021). Characterization of a cell bridge variant connecting the nodose and superior cervical ganglia in the mouse: Prevalence, anatomical features, and practical implications. *Journal of Comparative Neurology* 529(1), 111-128. doi: 10.1002/cne.24936.
- Cao, J.M., Chen, L.S., KenKnight, B.H., Ohara, T., Lee, M.H., Tsai, J., et al. (2000). Nerve sprouting and sudden cardiac death. *Circ Res* 86(7), 816-821. doi: 10.1161/01.res.86.7.816.
- Cheng, P.-L., Song, A.-H., Wong, Y.-H., Wang, S., Zhang, X., and Poo, M.-M. (2011). Self-amplifying autocrine actions of BDNF in axon development. *Proceedings of the National Academy of Sciences* 108(45), 18430. doi: 10.1073/pnas.1115907108.
- Davies, A.M. (1996). Paracrine and autocrine actions of neurotrophic factors. *Neurochemical Research* 21(7), 749-753. doi: 10.1007/BF02532296.
- de Bakker, J.M., van Capelle, F.J., Janse, M.J., Tasseron, S., Vermeulen, J.T., de Jonge, N., et al. (1993). Slow conduction in the infarcted human heart. 'Zigzag' course of activation. *Circulation* 88(3), 915-926. doi: 10.1161/01.cir.88.3.915.
- Del Rio, R., Marcus, N.J., and Schultz, H.D. (2013). Carotid chemoreceptor ablation improves survival in heart failure: rescuing autonomic control of cardiorespiratory function. *J Am Coll Cardiol* 62(25), 2422-2430. doi: 10.1016/j.jacc.2013.07.079.
- Deutch, A.Y., and Roth, R.H. (2004). "CHAPTER 9 - Pharmacology and Biochemistry of Synaptic Transmission: Classic Transmitters," in *From Molecules to Networks*, eds. J.H. Byrne & J.L. Roberts. (Burlington: Academic Press), 245-278.
- Fukuda, K., Kanazawa, H., Aizawa, Y., Ardell, J.L., and Shivkumar, K. (2015). Cardiac innervation and sudden cardiac death. *Circ Res* 116(12), 2005-2019. doi: 10.1161/circresaha.116.304679.
- Ge, Y., Smits, A.M., Van Munsteren, J.C., Gittenberger-De Groot, A.C., Poelmann, R.E., Van Brakel, T.J., et al. (2020). Human epicardium-derived cells reinforce cardiac sympathetic innervation. *Journal of Molecular and Cellular Cardiology* 143, 26-37. doi: 10.1016/j.yjmcc.2020.04.006.
- Gill, S.K., Ishak, M., Dobransky, T., Haroutunian, V., Davis, K.L., and Rylett, R.J. (2007). 82-kDa choline acetyltransferase is in nuclei of cholinergic neurons in human CNS and altered in aging and Alzheimer disease. *Neurobiol Aging* 28(7), 1028-1040. doi: 10.1016/j.neurobiolaging.2006.05.011.
- Ginty, D.D., and Segal, R.A. (2002). Retrograde neurotrophin signaling: Trk-ing along the axon. *Curr Opin Neurobiol* 12(3), 268-274. doi: 10.1016/s0959-4388(02)00326-4.
- Han, S., Kobayashi, K., Joung, B., Piccirillo, G., Maruyama, M., Vinters, H.V., et al. (2012). Electroanatomic remodeling of the left stellate ganglion after myocardial infarction. *J Am Coll Cardiol* 59(10), 954-961. doi: 10.1016/j.jacc.2011.11.030.

- Hausenloy, D.J., Bøtker, H.E., Ferdinandy, P., Heusch, G., Ng, G.A., Redington, A., et al. (2019). Cardiac innervation in acute myocardial ischaemia/reperfusion injury and cardioprotection. *Cardiovascular Research* 115(7), 1167-1177. doi: 10.1093/cvr/cvz053.
- He, Q., Dent, E.W., and Meiri, K.F. (1997). Modulation of actin filament behavior by GAP-43 (neuromodulin) is dependent on the phosphorylation status of serine 41, the protein kinase C site. *J Neurosci* 17(10), 3515-3524. doi: 10.1523/jneurosci.17-10-03515.1997.
- Holahan, M.R. (2015). GAP-43 in synaptic plasticity: molecular perspectives. *Research and Reports in Biochemistry* 5, 137-146. doi: 10.2147/Rrbc.S73846.
- Holahan, M.R. (2017). A Shift from a Pivotal to Supporting Role for the Growth-Associated Protein (GAP-43) in the Coordination of Axonal Structural and Functional Plasticity. *Front Cell Neurosci* 11, 266. doi: 10.3389/fncel.2017.00266.
- Hou, X.E., Lundmark, K., and Dahlstrom, A.B. (1998). Cellular reactions to axotomy in rat superior cervical ganglia includes apoptotic cell death. *Journal of Neurocytology* 27(6), 441-451. doi: 10.1023/A:1006988528655.
- Irie, T., Yamakawa, K., Hamon, D., Nakamura, K., Shivkumar, K., and Vaseghi, M. (2017). Cardiac sympathetic innervation via middle cervical and stellate ganglia and antiarrhythmic mechanism of bilateral stellectomy. *Am J Physiol Heart Circ Physiol* 312(3), H392-h405. doi: 10.1152/ajpheart.00644.2016.
- Isbister, J., and Semsarian, C. (2019). Sudden cardiac death: an update. *Internal Medicine Journal* 49(7), 826-833. doi: 10.1111/imj.14359.
- Kawashima, T. (2005). The autonomic nervous system of the human heart with special reference to its origin, course, and peripheral distribution. *Anatomy and Embryology* 209(6), 425-438. doi: 10.1007/s00429-005-0462-1.
- Kimura, K., Ieda, M., and Fukuda, K. (2012). Development, Maturation, and Transdifferentiation of Cardiac Sympathetic Nerves. *Circulation Research* 110(2), 325-336. doi: 10.1161/CIRCRESAHA.111.257253.
- Kimura, K., Ieda, M., Kanazawa, H., Yagi, T., Tsunoda, M., Ninomiya, S.-i., et al. (2007). Cardiac Sympathetic Rejuvenation. *Circulation Research* 100(12), 1755-1764. doi: 10.1161/01.RES.0000269828.62250.ab.
- Kobayashi, K., and Nagatsu, T. (2012). "Chapter 7 - Tyrosine Hydroxylase," in *Primer on the Autonomic Nervous System (Third Edition)*, eds. D. Robertson, I. Biaggioni, G. Burnstock, P.A. Low & J.F.R. Paton. (San Diego: Academic Press), 45-47.
- Korshunova, I., and Mosevitsky, M. (2010). Role of the growth-associated protein GAP-43 in NCAM-mediated neurite outgrowth. *Adv Exp Med Biol* 663, 169-182. doi: 10.1007/978-1-4419-1170-4_11.
- Kuruvilla, R., Zweifel, L.S., Glebova, N.O., Lonze, B.E., Valdez, G., Ye, H., et al. (2004). A neurotrophin signaling cascade coordinates sympathetic neuron development through differential control of TrkA trafficking and retrograde signaling. *Cell* 118(2), 243-255. doi: 10.1016/j.cell.2004.06.021.
- Kusik, B.W., Hammond, D.R., and Udvadia, A.J. (2010). Transcriptional regulatory regions of gap43 needed in developing and regenerating retinal ganglion cells. *Developmental dynamics : an official publication of the American Association of Anatomists* 239(2), 482-495. doi: 10.1002/dvdy.22190.
- Li, C.Y., and Li, Y.G. (2015). Cardiac Sympathetic Nerve Sprouting and Susceptibility to Ventricular Arrhythmias after Myocardial Infarction. *Cardiol Res Pract* 2015, 698368. doi: 10.1155/2015/698368.
- Li, Z., Wang, M., Zhang, Y., Zheng, S., Wang, X., and Hou, Y. (2015). The Effect of the Left Stellate Ganglion on Sympathetic Neural Remodeling of the Left Atrium in Rats Following Myocardial Infarction. *Pacing and Clinical Electrophysiology* 38(1), 107-114. doi: 10.1111/pace.12513.
- Lopez-Barneo, J., Ortega-Saenz, P., Pardal, R., Pascual, A., and Piruat, J.I. (2008). Carotid body oxygen sensing. *Eur Respir J* 32(5), 1386-1398. doi: 10.1183/09031936.00056408.

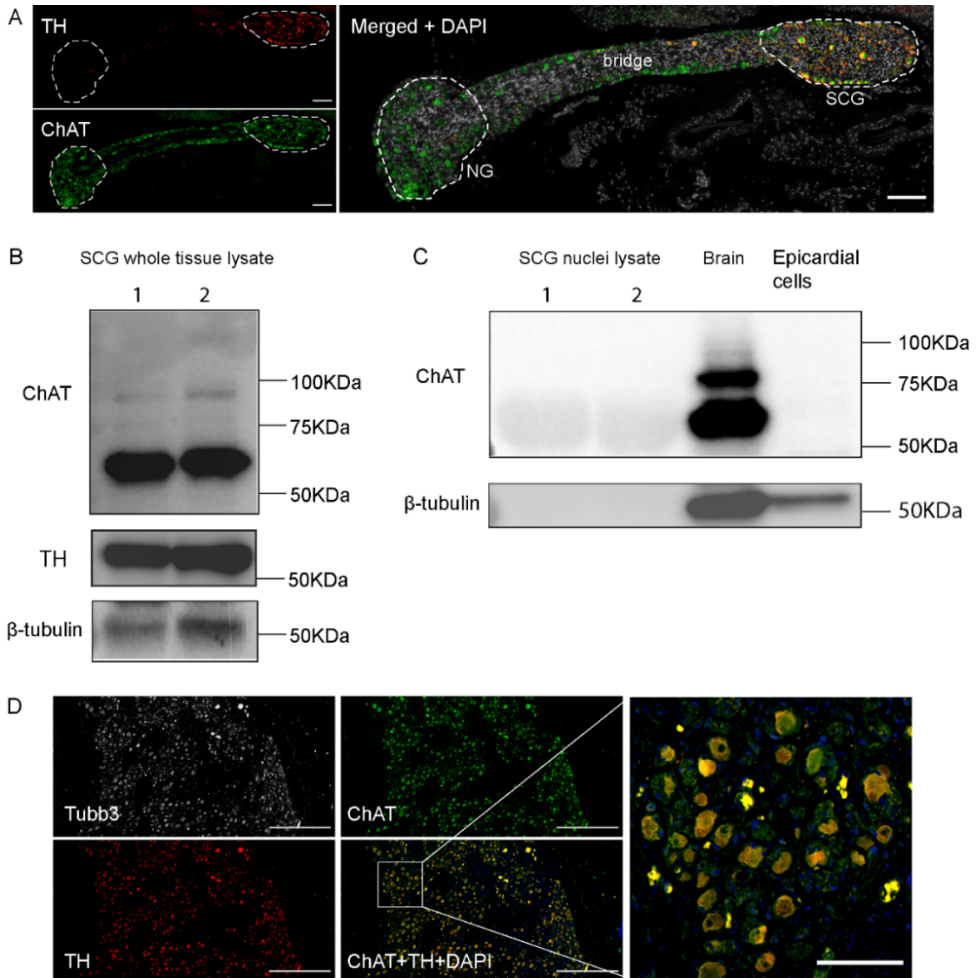
- Matsuo, A., Bellier, J.P., Nishimura, M., Yasuhara, O., Saito, N., and Kimura, H. (2011). Nuclear choline acetyltransferase activates transcription of a high-affinity choline transporter. *J Biol Chem* 286(7), 5836-5845. doi: 10.1074/jbc.M110.147611.
- Nakamura, K., Ajjola, O.A., Aliotta, E., Armour, J.A., Ardell, J.L., and Shivkumar, K. (2016). Pathological effects of chronic myocardial infarction on peripheral neurons mediating cardiac neurotransmission. *Auton Neurosci* 197, 34-40. doi: 10.1016/j.autneu.2016.05.001.
- Nguyen, B.L., Li, H., Fishbein, M.C., Lin, S.F., Gaudio, C., Chen, P.S., et al. (2012). Acute myocardial infarction induces bilateral stellate ganglia neural remodeling in rabbits. *Cardiovasc Pathol* 21(3), 143-148. doi: 10.1016/j.carpath.2011.08.001.
- Nguyen, L., He, Q., and Meiri, K.F. (2009). Regulation of GAP-43 at serine 41 acts as a switch to modulate both intrinsic and extrinsic behaviors of growing neurons, via altered membrane distribution. *Mol Cell Neurosci* 41(1), 62-73. doi: 10.1016/j.mcn.2009.01.011.
- O'Keeffe, G.W., Gutierrez, H., Howard, L., Laurie, C.W., Osorio, C., Gavaldà, N., et al. (2016). Region-specific role of growth differentiation factor-5 in the establishment of sympathetic innervation. *Neural Development* 11(1), 4. doi: 10.1186/s13064-016-0060-3.
- Olivas, A., Gardner, R.T., Wang, L., Ripplinger, C.M., Woodward, W.R., and Habecker, B.A. (2016). Myocardial Infarction Causes Transient Cholinergic Transdifferentiation of Cardiac Sympathetic Nerves via gp130. *J Neurosci* 36(2), 479-488. doi: 10.1523/jneurosci.3556-15.2016.
- Ortega-Saenz, P., and Lopez-Barneo, J. (2020). Physiology of the Carotid Body: From Molecules to Disease. *Annu Rev Physiol* 82, 127-149. doi: 10.1146/annurev-physiol-020518-114427.
- Pathar, N., Partab, P., Singh, B., and Satyapal, K.S. (2003). The sympathetic contributions to the cardiac plexus. *Surgical and Radiologic Anatomy* 25(3), 210-215. doi: 10.1007/s00276-003-0113-2.
- Pulgar-Sepúlveda, R., Varas, R., Iturriaga, R., Del Rio, R., and Ortiz, F.C. (2018). Carotid Body Type-I Cells Under Chronic Sustained Hypoxia: Focus on Metabolism and Membrane Excitability. *Frontiers in Physiology* 9(1282). doi: 10.3389/fphys.2018.01282.
- Rocha, I., Rosário, L.B., de Oliveira, E.I., Barros, M.A., and Silva-Carvalho, L. (2003). Enhancement of carotid chemoreceptor reflex and cardiac chemosensitive reflex in the acute phase of myocardial infarction of the anesthetized rabbit. *Basic Res Cardiol* 98(3), 175-180. doi: 10.1007/s00395-003-0407-x.
- Skene, J.H. (1989). Axonal growth-associated proteins. *Annu Rev Neurosci* 12, 127-156. doi: 10.1146/annurev.ne.12.030189.001015.
- Stocco, E., Barbon, S., Tortorella, C., Macchi, V., De Caro, R., and Porzionato, A. (2020). Growth Factors in the Carotid Body-An Update. *Int J Mol Sci* 21(19). doi: 10.3390/ijms21197267.
- Winick-Ng, W., and Rylett, R.J. (2018). Into the Fourth Dimension: Dysregulation of Genome Architecture in Aging and Alzheimer's Disease. *Front Mol Neurosci* 11, 60. doi: 10.3389/fnmol.2018.00060.
- Wink, J., van Delft, R., Notenboom, R.G.E., Wouters, P.F., DeRuiter, M.C., Plevier, J.W.M., et al. (2020). Human adult cardiac autonomic innervation: Controversies in anatomical knowledge and relevance for cardiac neuromodulation. *Auton Neurosci* 227, 102674. doi: 10.1016/j.autneu.2020.102674.
- Wit, A.L. (2017). Basic Electrophysiologic Mechanisms of Sudden Cardiac Death Caused by Acute Myocardial Ischemia and Infarction. *Card Electrophysiol Clin* 9(4), 525-536. doi: 10.1016/j.ccep.2017.07.004.
- World Health Organization (2017). Cardiovascular diseases (CVDs) [Online]. World Health Organization. Available: [https://www.who.int/news-room/fact-sheets/detail/cardiovascular-diseases-\(cvds\)](https://www.who.int/news-room/fact-sheets/detail/cardiovascular-diseases-(cvds)) [Accessed 17 May 2017].
- Yokoyama, T., Lee, J.K., Miwa, K., Ophhof, T., Tomoyama, S., Nakanishi, H., et al. (2017). Quantification of sympathetic hyperinnervation and denervation after myocardial infarction by three-dimensional assessment of the cardiac sympathetic network in cleared transparent murine hearts. *PLoS One* 12(7), e0182072. doi: 10.1371/journal.pone.0182072.

Zhou, S., Chen, L.S., Miyauchi, Y., Miyauchi, M., Kar, S., Kangavari, S., et al. (2004). Mechanisms of Cardiac Nerve Sprouting After Myocardial Infarction in Dogs. *Circulation Research* 95(1), 76-83. doi:10.1161/01.RES.0000133678.22968.e3.

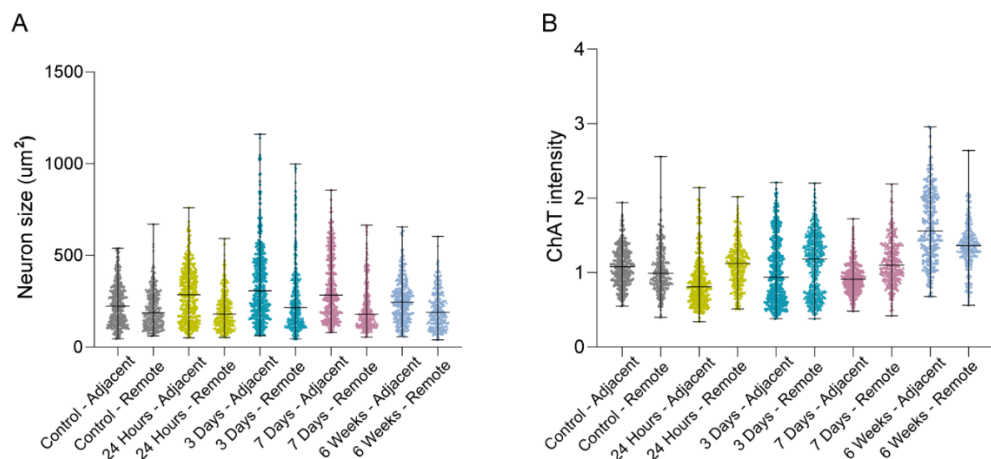
Ziegler, K.A., Ahles, A., Wille, T., Kerler, J., Ramanujam, D., and Engelhardt, S. (2018). Local sympathetic denervation attenuates myocardial inflammation and improves cardiac function after myocardial infarction in mice. *Cardiovasc Res* 114(2), 291-299. doi: 10.1093/cvr/cvx227.

Zipes, D.P., and Rubart, M. (2006). Neural modulation of cardiac arrhythmias and sudden cardiac death. *Heart Rhythm* 3(1), 108-113. doi: 10.1016/j.hrthm.2005.09.021.

SUPPLEMENTAL FIGURES



Supplemental Figure. 1 ChAT expression in murine nodose ganglion and human stellate ganglion. **A.** Immunofluorescence staining of TH (red) and ChAT (green) in murine NG, SCG, and the bridge between the ganglia. NG and SCG are indicated by dashed lines. Scale bar = 100 μ m. **B.** Immunoblot analysis of ChAT or β -tubulin (loading control) in protein lysates of 4 control murine SCG displayed the expression of ChAT isoforms in SCG. **C.** Immunoblot analysis of ChAT and β -tubulin (loading control) in nuclei protein lysates of 4 SCG, total cell protein lysates of murine brain (positive control), and total cell protein lysates of human epicardial cells (negative control). No detection of β -tubulin in SCG nuclei lysate is aimed to confirm no cytoplasm contamination. **D.** Immunofluorescence staining of Tubb3 (gray) TH (red), ChAT (green) and nuclei (blue) in human stellate ganglion, enlarged image of merged channels is shown in the rightest panel. Scale bar = 500 μ m. Scale bar in enlarged image = 100 μ m.



Supplemental Figure 2. Graphs related to figure 2. A. A. cell size overview of neurons adjacent or remote to CB in control SCG and post-MI SCG at different timepoints. Each dot represents a neuronal cell. Lines indicate the median \pm range of each dataset. B. A relative ChAT intensity overview of neurons adjacent or remote to CB in control SCG and post-MI SCG at different timepoints. Each dot represents a neuronal cell. Lines indicate the median \pm range of each dataset. Relative ChAT intensity was calculated as a fold change of fluorescence intensity of neuronal ChAT to the intensity of cholinergic nerves in each corresponding ganglion (internal reference).

SUPPLEMENTAL METHODS

Immunofluorescence staining of murine nodose ganglion and human stellate ganglion

A nodose ganglion was isolated from one of 6-week post-MI mice. A human stellate ganglion was obtained as redundant material from a stellate ganglion ablation surgery. All experiments were performed according to the guidelines of the Leiden University Medical Centre (Leiden, The Netherlands). The 5 μm -thick paraffin sections were deparaffinized, pre-treated with Tris-EDTA buffer (pH 9) at 98°C for 12 min for antigen retrieval, and incubated with anti-tyrosine hydroxylase (TH)(Fisher Scientific PA14679; 1:1000), anti-choline acetyl transferase (ChAT)(Abcam ab181023; 1:1000), and anti- β -tubulin III (Tubb3)(Santa Cruz; SC-80005; 1:1000) overnight at 4°C. On the second day, the sections were incubated with secondary antibodies donkey anti-rabbit Alexa Fluor 488 (Invitrogen A-21206; 1:250), donkey anti-sheep Alexa Fluor

568 (Invitrogen A21099; 1:250) and donkey anti-mouse Alexa Fluor 647 (Invitrogen A31571; 1:250) for 1 hour, and followed by a 10 min nuclear staining with DAPI (Invitrogen D3571: 1:1000) when indicated. The slides were mounted with ProLong Gold Antifade Mountant (Invitrogen P36930) and images were captured with the Zeiss AxioscanZ1.

Western Blotting

Protein of whole ganglia tissue lysate was extracted with RIPA lysis and extraction buffer (89900; ThermoFisher) supplemented with Protease inhibitor cocktail (87785; ThermoFisher). To extract protein from nuclear fraction of the ganglia, ganglionic cells were first dissociated by 30-minute incubation in 2.5% trypsin (25200056; Thermo Fisher Scientific) followed by 30-minute incubation in 5 mg/ml collagenase type II (LS004176; Worthington) at 37°C. After centrifuge the cell suspension at 300 rcf for 10 minutes, 100 µl nuclei lysis buffer (10 mM Tris-HCl, 10 mM NaCl, 3 mM MgCl₂, and 0.1%Nonidet™ P40 Substitute, 40 U/ml RNase in Nuclease-Free Water) was added into the cell pellet, cells were mixed well in nuclei lysis buffer and incubated on ice for 8 minutes. Centrifuge the nuclei suspension at 300 rcf for 5 minutes and wash twice with nuclei wash (1X PBS with 2.0% BSA). Nuclear protein was extracted with RIPA supplemented with Protease inhibitor.

20 µg of each protein was loaded in 8 % SDS-PAGE gel for electrophoresis. Following electrophoretic separation, the proteins were transferred to a polyvinylidene difluoride membrane by wet electroblotting. Afterwards, the membrane was incubated with 5% BSA in PBS-0.1% Tween 20 (PBST) for 1 hour at RT for blocking and probed with rabbit-anti-ChAT (Abcam ab181023; 1:2000) or sheep-anti-TH (Fisher Scientific PA14679; 1:2000) primary antibodies overnight at 4°C, followed by a 1-hour incubation with HRP~Donkey-anti-Rabbit IgG(H&L) (cell signalling #7074; 1:10,000) or HRP~Donkey-anti-goat IgG(H&L)(Jackson Immuno research 705035003; 1:10,000). The target protein was visualized with a WesternBright kit (Isogen life science). After stripping, the membrane was blocked for 1 hours and incubated with rabbit-anti-βtubulin followed by our incubation with HRP-linked antibody as a protein loading reference. Images were captured by C500 western blot imaging system (Azure biosystems).



6

LOW-INPUT NUCLEUS ISOLATION AND MULTIPLEXING WITH BARCODED ANTIBODIES OF MOUSE SYMPATHETIC GANGLIA FOR SINGLE-NUCLEUS RNA SEQUENCING

Yang Ge^{1,2}, Lieke van Roon¹, H. Sophia Chen^{1,2}, Ruben Methorst¹, Martin Paton², Marco C. DeRuiter¹, Szymon M. Kielbasa³, Monique R.M. Jongbloed^{1,2}

1. Department of Anatomy & Embryology, Leiden University Medical Center, Einthovenweg 20, 2333 ZC Leiden, The Netherlands;

2. Department of Cardiology, Leiden University Medical Center, Albinusdreef 2, 2333 ZC Leiden, The Netherlands;

3. Department of Medical Statistics and Bioinformatics, Leiden University Medical Center, Einthovenweg 20, 2333 ZC Leiden, The Netherlands;

6

Under peer review *Jove*

SUMMARY

This protocol describes the detailed low-input sample preparation for single-nucleus sequencing, which includes the dissection of mouse superior cervical and stellate ganglia, cell dissociation, cryo-preservation, nucleus isolation and hashtag barcoding.

ABSTRACT

The cardiac autonomic nervous system is crucial in controlling cardiac function, such as heart rate and cardiac contractility, and is divided into a sympathetic and parasympathetic branch. In healthy persons there is a balance between these two branches to maintain homeostasis. However, cardiac disease states such as myocardial infarction, heart failure and hypertension can induce remodeling of cells involved in cardiac innervation, which in turn is associated with adverse clinical outcome. Although a myriad of data is present on histological structure and function of the cardiac autonomic nervous system, its molecular biological architecture in health and disease is in many aspects still enigmatic. Novel technologies such as single cell RNA sequencing hold promise for genetic characterization of tissues on a single cell level, however the relatively large size of neurons may impede the standardized use of these techniques. Here, we took advantage of advanced droplet-based single-nucleus RNA sequencing (snRNA-seq), a promising method to characterize the biological architecture of cardiac sympathetic neurons in health and in disease. We demonstrate a stepwise approach to perform snRNA-seq of the bilateral superior cervical and stellate ganglia dissected from adult mice. This method enables long-term sample preservation maintaining an adequate RNA quality when samples cannot be fully collected within a short period of time. Nucleus-barcoding with hashtag barcoding antibody-oligos (HTOs) staining enables demultiplexing and the trace-back of distinct ganglionic samples during the afterward single nucleus analysis. The analysis results support successful nuclei capture of neuronal cells, glial cells and endothelial cells of the sympathetic ganglion by snRNA-seq. In summary, we provide a stepwise approach for single nucleus RNA sequencing of sympathetic cardiac ganglia, a method that has the potential for broad application also in studies of innervation of other organs and tissues.

INTRODUCTION

The autonomic nervous system (ANS) is a crucial part of the peripheral nervous system that maintains body homeostasis, including the adaption to environmental conditions and pathology (McCorry, 2007). As such, it is involved in regulation of multiple organ systems throughout the body such as the cardiovascular system, respiratory system, digestive system and endocrine system. The ANS is divided in sympathetic and parasympathetic branches. Spinal branches of the sympathetic nervous system synapse in ganglia of the sympathetic chain, situated bilaterally in a paravertebral position. The bilateral cervical and thoracic ganglia, especially the stellate ganglia, are important components participating in cardiac sympathetic innervation. In disease states, such as cardiac ischemia, neuronal remodeling can occur, resulting in a sympathetic overdrive (Li and Li, 2015), as was demonstrated in histological studies in human and several other animal species (Ajjola et al., 2012; Han et al., 2012; Nguyen et al., 2012; Ajjola et al., 2015). Currently, a detailed biological characterization of cardiac ischemia induced neuronal remodeling in cardiac sympathetic ganglia is lacking, and the fundamental biological characteristics of specialized neuronal cell types or subtypes within the cardiac sympathetic nervous system (SNS) in health and disease are not fully determined yet (Zeisel et al., 2018).

Novel technologies such as single cell RNA sequencing (scRNA-seq), have opened gateways for genetic characterization of small tissues on a single cell level. However, the relatively large size of neurons may impede the optimized use of these single cell techniques in humans. In addition, single cell sequencing requires a high-throughput of cells to recover a sufficient cell number due to a high loss in the sequencing process. This might prove to be challenging when studying small tissues that are hard to capture in one session and require multiple samples to introduce enough single cells for sequencing. Recently developed droplet-based single-nucleus RNA sequencing (snRNA-seq) technology (i.e. the 10x Chromium platform) allows the study of biological differences among single cells. snRNA-seq holds an advantage as compared to scRNA-seq for large cells (> 30 μm), that may not be captured in Gel Bead in Emulsions (GEMs), as well as for cells that are more difficult to dissociate and/or preserve (Bakken et al., 2018; Wu et al., 2019; Gaublomme et al., 2020). Heterogeneity, number of neuronal cells and other cells enriched in the cardiac SNS are important aspects to characterize the ANS in health and disease states. In addition, the organ or region-specific innervation by each sympathetic ganglion contributes to the complexity of the SNS, and cervical, stellate and thoracic ganglia of the sympathetic chain have been shown to innervate different regions of the heart (Zandstra et al., 2021).

Therefore, it is mandatory to perform single cell analysis of ganglionic cells derived from individual ganglia to study their biological architecture. Droplet-based snRNA-seq allows

transcriptome-wide expression profiling for a pool of thousands of cells from multiple samples at once with lower cost compared to plate-based sequencing platforms. This approach enables droplet-based snRNA-seq to be more suitable for cellular phenotype classification and new subpopulation identification of cells within a ganglion. Here, we provide—to our knowledge—for the first time a stepwise approach for identification, isolation and single nucleus RNA sequencing of sympathetic extrinsic cardiac ganglia, a method that has the potential for a broad application in studies of the characterization of ganglia innervating other related organs and tissues in health and disease.

PROTOCOL

Below we provide a protocol for snRNA-seq of murine cervical and cervicothoracic (stellate) ganglia. Female and male C57BL/6J mice (15-weeks old, n=2 for each sex, Charles River) were used in our setup. One additional Wnt/Cre; mT/mG mouse on a C57BL/6JLumc background was used to visualize the ganglia for dissection purposes. All animal experiments were carried out according to the Guide for Care and Use of Laboratory Animals published by NIH and approved by the Animal Ethics Committee of the Leiden University (License number AVD1160020185325, Leiden, the Netherlands).

1. Preparations

All steps are performed in a cell culture flow cabinet.

- 1.1. Clean the forceps and scissors by immersing the instruments in 70% ethanol for 20 minutes.
- 1.2. Prepare the ganglion medium containing; Neurobasal Medium (Gibco 21103049) supplemented with B-27plus (1x, Gibco A3582801), L-glutamine (2mM, Thermo Scientific 25030024) and Antibiotic-Antimycotic (1x, Gibco 15240096). Pre-warm the ganglion medium at room temperature.
- 1.3. Prepare the digestion solution: 0.25% Trypsin-EDTA (1:1; Thermo Fisher Scientific) and 1400U/ml collagenase type 2 dissolved in ganglion medium (Worthington LS004176).
- 1.4. Prepare material and fresh cold (4°C) buffers for nuclei isolation.

Pre-Separation Filters(30µm)	Miltenyi biotec130-041-407
------------------------------	----------------------------

Cell wash (0.04% BSA)	
DPBS (Ca ²⁺ ,Mg ²⁺ +free)	Gibco, 14190-169
Bovine Serum Albumin 10%	Sigma-Aldrich, A1595-50ML

Lysis buffer (10 mM Tris-HCl, 10 mM NaCl, 3 mM MgCl ₂ , and 0.1%Nonidet™ P40 Substitute, 40U/ml RNase in Nuclease-Free Water)	
Nuclease free water (not DEPC treated)	Invitrogen, AM9937
Trizma® Hydrochloride Solution, 1M, pH 7.4	Sigma-Aldrich, T2194
Sodium Chloride Solution, 5M	Sigma-Aldrich, 59222C
Magnesium Chloride Solution, 1M	Sigma-Aldrich, M1028
Nonidet™ P40 Substitute	Sigma-Aldrich, 74385
Protector RNase Inhibitor,40U/μl	Sigma-Aldrich, 3335399001

Nucleus Wash (1X PBS with 2.0% BSA and 0.2U/μl RNase Inhibitor)	
DPBS (Ca ²⁺ ,Mg ²⁺ +free)	Gibco, 14190-169
Bovine Serum Albumin 10%	Sigma-Aldrich, A1595-50ML
Protector RNase Inhibitor,40U/μl	Sigma-Aldrich, 3335399001

1.5. Preparation for nucleus hashtag antibody staining

ST staining buffer (ST-SB) (10 mM Tris-HCl, 146 mM NaCl, 21 mM MgCl ₂ , 1mM CaCl ₂ , 2% BSA, 0.02%Tween-20 in Nuclease-free water)	
Nuclease free water (not DEPC treated)	Invitrogen, AM9937

Trizma® Hydrochloride Solution, 1M, pH 7.4	Sigma-Aldrich, T2194
Sodium Chloride Solution, 5M	Sigma-Aldrich, 59222C
Magnesium Chloride Solution, 1M	Sigma-Aldrich, M1028
Calcium chloride solution, 1M	Sigma-Aldrich, 21115-100ML
Tween-20	Merck Millipore, 822184
Bovine Serum Albumin 10%	Sigma-Aldrich, A1595-50ML

FC receptor blocking solution (Human TruStain FcX, 422302)

Single nucleus hashtag antibodies (Mab414)

TotalSeq™-A0451 anti-Nuclear Pore Complex Proteins Hashtag 1 Antibody

TotalSeq™-A0452 anti-Nuclear Pore Complex Proteins Hashtag 2 Antibody

TotalSeq™-A0453 anti-Nuclear Pore Complex Proteins Hashtag 3 Antibody

TotalSeq™-A0461 anti-Nuclear Pore Complex Proteins Hashtag 11 Antibody

TotalSeq™-A0462 anti-Nuclear Pore Complex Proteins Hashtag 12 Antibody

TotalSeq™-A0463 anti-Nuclear Pore Complex Proteins Hashtag 13 Antibody

TotalSeq™-A0464 anti-Nuclear Pore Complex Proteins Hashtag 14 Antibody

TotalSeq™-A0465 anti-Nuclear Pore Complex Proteins Hashtag 15 Antibody

2. Dissection of adult mouse superior cervical ganglia (SCG) and stellate ganglia (StG)

2.1. Euthanize the mice. In the current study, a total of 4 C57BL6/J mice were euthanized by CO₂ asphyxiation. **Note:** Alternatively Isoflurane can be used followed by exsanguination when a large amount of blood needs to be collected for other study purposes.

2.2. Fix the mice on a dissection board with pins and douse with 70% ethanol to restrict contamination (shaving is not necessary). Under a stereo microscope; open up the skin of the neck region by making a midline cut with scissors, move the submandibular glands aside and remove the sternomastoid muscle in order to expose the common carotid artery and its bifurcation (**Fig. 1A, B**). Dissect the right and left carotid artery bifurcation and the tissue attached to it. Transfer each dissected piece of tissue into a separate 3.5 cm petri dish, containing cold PBS, and the SCG can be detected attached to the carotid bifurcation. Clean the SCG further by removing the artery and other attached tissue in the petri dish (**Fig. 1E**).

2.3. To dissect the StG, make a midline cut in the abdomen, followed by the opening of the diaphragm and the ventral thoracic wall. Remove the heart and lungs to expose the dorsal

thorax. The left and right StG can be detected anterolateral to the musculus colli longus (MCL) at the level of the first rib (Fig. 1C, D). Dissect both left and right StG with a forceps and separately transfer them into 3.5 cm petri dishes containing cold PBS (Fig. 1F).

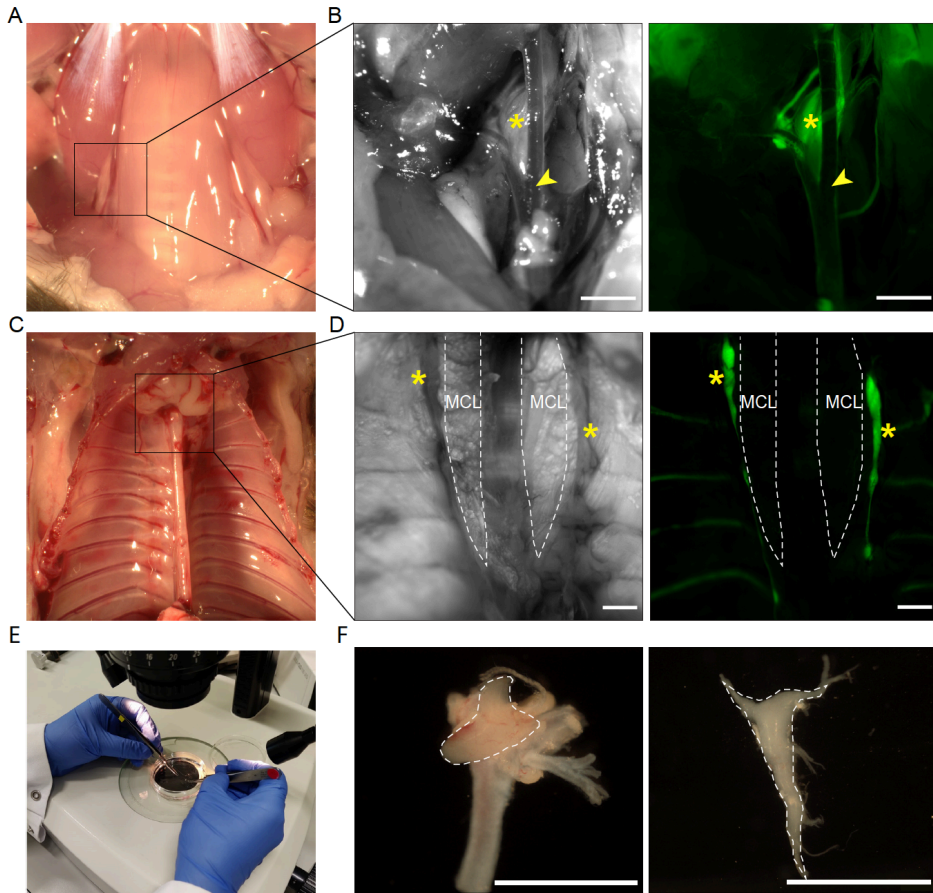


Figure 1. Dissection of adult mouse superior cervical ganglia (SCG) and stellate ganglia (StG). A. Bright field image of the location of the SCG. B. To facilitate visualization, a Wnt/Cre; mT/mG mouse was used. Asterisks indicate the SCG (eGFP+), arrowheads indicate the bifurcation of the carotid artery. C. Bright field image of the location of the StG. D. Asterisks indicate the StG (eGFP+), dashed lines indicate the musculus colli longus (MCL). E. Dissected ganglia are transferred into a petri dish separately for further cleaning under a stereo microscope. F. Left panel, the dissected SCG with the carotid artery still attached. Dashed line indicates the SCG. Right panel, the dissected and cleaned StG has the shape of an inverted triangle as indicated by the dashed line. Scale bar = 1000 μ m.

Steps 3-5 are summarized in **Figure 2**.

3. Isolation and cryopreservation of mouse ganglionic cells

3.1. Carefully transfer all SCG and StG into separate 1.5 ml Eppendorf tubes with a forceps. **Note:** The ganglia are prone to adhere to the wall of plastic pipette tips.

3.2. Add 500 μ l of 0.25% trypsin-EDTA solution into each Eppendorf tube and incubate in a shaking water bath at 37°C for 40 minutes. **Note:** This step is aimed to facilitate the digestion and cell release hereafter in collagenase type 2 solution.

3.3. Prepare a 15 ml Falcon tube containing 5 ml of ganglion medium for each sample.

3.4. Allow the ganglia to settle down at the bottom of the Eppendorf tubes. Collect the supernatant, transfer the supernatant into the prepared Falcon tubes and label each tube. Alternatively, the trypsin-EDTA supernatant can be aspirated without collection as very few dissociated cells can be detected in it. **Note:** A small amount of trypsin-EDTA solution (around 10-30 μ l) can be left in the Eppendorf tube to avoid removal of the ganglion. Avoid pipetting at this step because it may damage the ganglion and lead to low output of ganglionic cells afterwards.

3.5. Add 500 μ l collagenase type 2 solution into each Eppendorf tube and incubate in a shaking water bath at 37°C for 35-40 minutes. **Note:** The incubation time could vary depending on the age of mouse. Try to pipette the ganglion after 35 minutes, if the ganglion is still intact and does not dissociate, prolong the incubation time or increase the concentration of collagenase type 2 solution.

3.6. Pipette the ganglia in collagenase solution up and down for around 10 times or until tissue clumps can no longer be detected. Transfer the cell suspension into the corresponding Falcon tube that contains the ganglia culture medium and the trypsin-EDTA suspension.

3.7. Centrifuge the cell suspension for 10 min, 300 relative centrifugal force (rcf) at room temperature. Carefully discard the cell supernatant. **Note:** Because the ganglionic cells are dissociated from a single ganglion, the cell pellet may be too small to detect by eye; a small amount of supernatant can be left in the tube to avoid removal of the cell pellet.

3.8. Resuspend the ganglionic cells in 270 μ l heat-inactivated fetal bovine serum (FBS, low endotoxin; Biowest) and transfer each cell-FBS suspension into a 1 ml cryovial.

3.9. Count the cells by using a hemocytometer. Mix 5 μ l ganglionic cell suspension with 5 μ l 0.4% trypan blue dye (Bio-Rad 1450021) and load the mixture into a hemocytometer. Count

the total and live cell numbers under a microscope. The cell viability (live cell count/total cell count = viability %) is usually above 90% with this dissociation protocol. **Note:** Live cell count of a single ganglion (either SCG or StG) usually falls within the range of 9,000~60,000 cells when the ganglion is isolated from a mouse aged 12 to 16 weeks.

3.10. Add 30 μ l Dimethyl sulfoxide (DMSO; Sigma-Aldrich 67-68-5) into each cell-FBS suspension in the cryovials, mix well and transfer the cryovials to a Mr. Frosty (Thermo Fisher) or CoolCell container (Corning). Keep the container at -80°C overnight and transfer the cryovials into liquid nitrogen the next day for long-time preservation before sequencing.

4. Nucleus isolation

Left and right SCG isolated from four mice (in total 8 samples) were used as an example in the following nuclei preparation and sequencing preparation. Note: Keep everything on ice during the whole procedure.

4.1. Prepare 15 ml Falcon tubes with a MACS SmartStrainer (30 μ m; Miltenyi Biotec) on top. Pre-rinse the strainer with 1 ml ganglion medium.

4.2. Take out the cryovials from the liquid nitrogen and immediately thaw them in a water bath at 37°C. When a small pellet of ice is left in the cryovial, take the cryovials out of the water bath.

4.3. Recover the ganglionic cells by dropping 1 ml of ganglion medium into each cryovial while shaking carefully. Optional: To evaluate cell recovery, mix the cell suspension after recovery and take 5 μ l cell suspension out for live cell counting as describe in step 3.9.

4.4. Load each ganglionic cell suspension on a separate strainer (as prepared in step 4.1) and rinse each strainer with 4 to 5 ml ganglion medium.

4.5. Centrifuge the cell suspension for 5 min at 300 rcf, remove supernatant carefully and resuspend the cells in 50 μ l cell wash.

4.6. Transfer the cell suspension into a DNA/RNA LoBind 0.5 ml Eppendorf tube. Centrifuge the cell suspension at 500 rcf for 5 min at 4°C.

4.7. Remove 45 μ l supernatant, without touching the bottom of the tube to avoid dislodging the cell pellet, and add 45 μ l chilled Lysis Buffer. Gently pipette up and down using a 200ul pipette tip and incubate the cells for 8 min on ice.

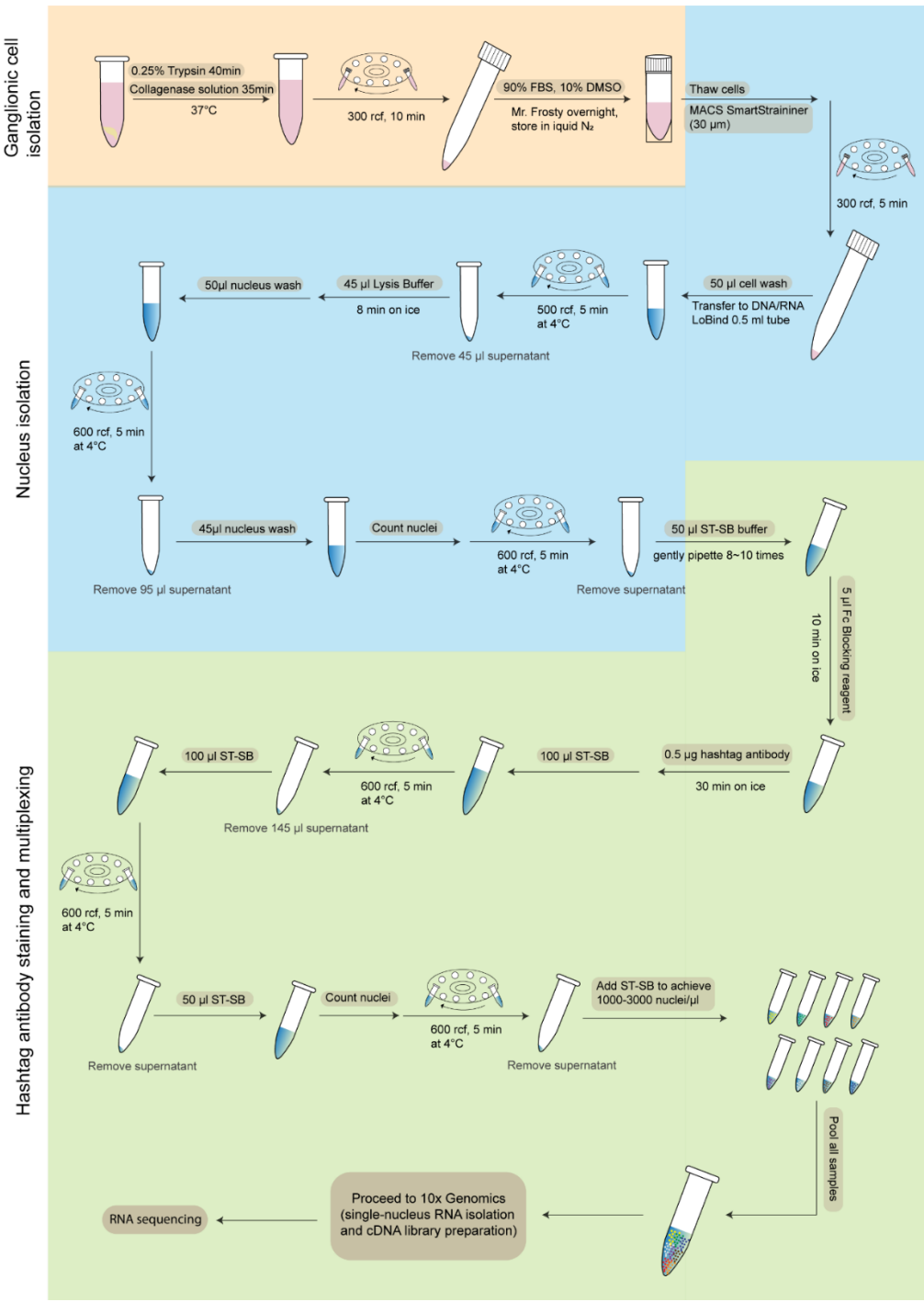


Figure 2. Workflow of sample preparation and hashtag staining-based multiplexing for snRNA-seq. The flowchart depicts the steps from the dissociation of ganglionic cells to hashtag antibody staining and multiplexing that are carried out for snRNA-seq.

4.8. Add 50 μ l cold Nuclei wash buffer to each tube. **Note:** Do not mix.

4.9. Centrifuge the nuclei suspension at 600 rcf for 5 min at 4°C. Remove 95 μ l of supernatant without disrupting the nuclei pellet. Then add 45 μ l chilled Nuclei wash buffer to the pellet. **Note:** Because of the invisibility of tiny nucleus pellets, a centrifuge with swinging buckets instead of fixed-angle rotors is recommended to facilitate supernatant removal. **Optional:** Take 5 μ l nuclei suspension, mix with 5 μ l 0.4% trypan blue to count and check the quality of nuclei under a microscope with a hemocytometer.

4.10. Centrifuge the nuclei suspension at 600 rcf for 5 min at 4°C. Remove the supernatant without touching the bottom of the tube to avoid dislodging the nuclei pellet.

5. Hashtag barcoding antibody-oligos (HTOs) staining and multiplexing

HTOs staining steps were modified and optimized for nuclei labelling of very low amounts of (ganglionic) nuclei according to previous application in cortical tissue by Gaublomme et al (Gaublomme et al., 2020).

5.1. Add 50 μ l ST-SB buffer to the nuclei pellet, gently pipette 8~10 times until nuclei are completely resuspended.

5.2. Add 5 μ l Fc Blocking reagent (Biolegend 422302) per 50 μ l of ST-SB/nuclei mix and incubate for 10 min on ice.

5.3. Add 1 μ l (0.5 μ g) of single nucleus hashtag antibody (Biolegend MAb414) per 50 μ l of ST-SB/nuclei mix and incubate for 30 min on ice. **Note:** Shorter incubation time leads to lower efficiency of hashtag labelling as is demonstrated in representative results below.

5.4. Add 100 μ l ST-SB to each tube, centrifuge the nuclei suspension for 5 min, 600 rcf at 4°C. **Note:** Do not mix.

5.5. Remove 145 μ l supernatant without disrupting the nuclei pellet. Repeat step 5.4.

5.6. Remove the supernatant without touching the bottom of the tube to avoid dislodging the nuclei pellet.

5.7. Resuspend the nuclei pellet in 50 μ l ST-SB, and gently mix the nuclei. Then take 5 μ l nuclei suspension and mix it with 5 μ l 0.4% trypan blue to count the nuclei under a microscope. A representative image of nuclei mixed with trypan blue and loaded in a hemocytometer is shown in **Fig. 3A**.

5.8. Centrifuge the nuclei suspension for 5 min at 600 rcf at 4°C.

5.9. Resuspend the nuclei in ST-SB to achieve a target nuclei concentration of 1000-3000 nuclei/ μ l for each sample according to corresponding the nuclei counts.

5.10. Pool samples to achieve the desired number of cells. For example, in this experiment 8 samples were equally pooled to achieve in total 25,000 nuclei to immediately proceed to 10x Genomics Chromium and afterwards snRNA-seq. **Note:** nucleus count usually falls within the range of 6,000~40,000 cells when the ganglion is isolated from a mouse aged 12 to 16 weeks. **Note:** Only around half of the total loaded nuclei can be captured by 10x Chromium. For example, we prepared a 25,000 nuclei mixture to ensure a capture of 10,000 nuclei by 10x Chromium which is needed for further library preparation and sequencing according to the 10x Genomics standard procedure.

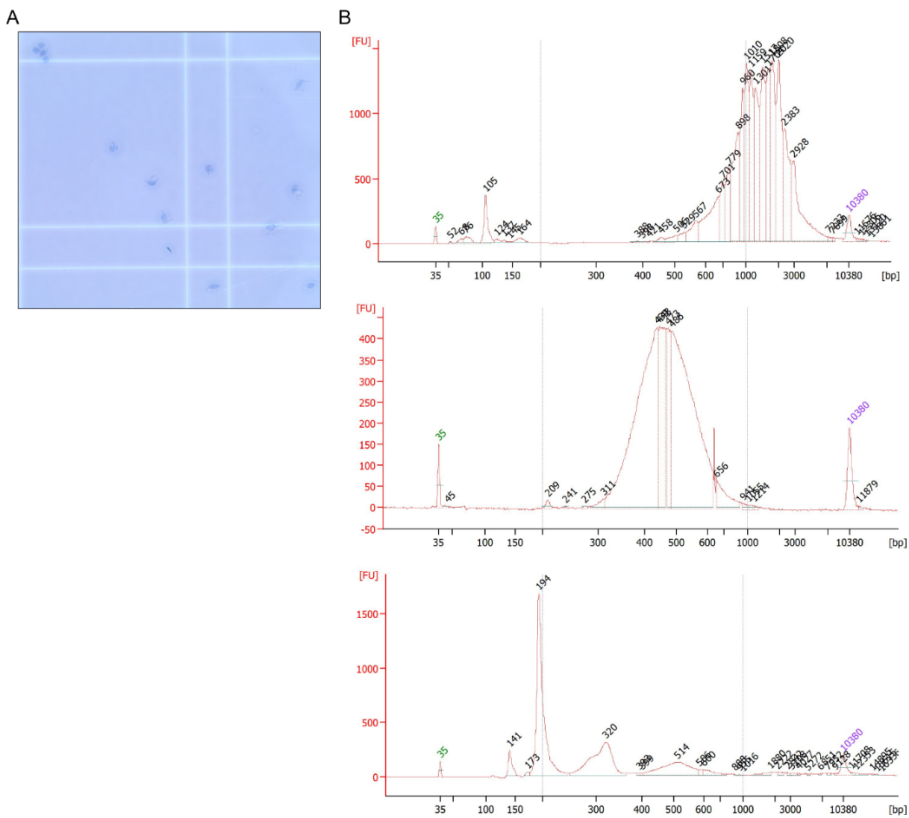


Figure 3. Quality control of nuclei isolation and gene expression library preparation. A. Brightfield image of the HTOs-stained nuclei. B. Bioanalyzer results of 1st strand cDNA (top), gene expression (GEX) library (middle) and hashtag oligo (HTO) library (bottom).

REPRESENTATIVE RESULTS

Quality control analysis of the single-nucleus cDNA library preparation and snRNA-seq.

Fig. 3B illustrates the quality control results of the 1st strand cDNA, gene expression (GEX) library and hashtag oligo (HTO) library which were checked with Bioanalyzer. The HTO-derived cDNAs are expected to be smaller than 180bp (135bp) and mRNA-derived cDNAs are larger than 300bp. A high quality GEX library can be detected as a broad peak from 300 to 1000bp and the HTO library is detected as a specific peak of 194bp. Seurat R package (version 4.0, Satija Lab) (Stuart et al., 2018) was used for pre-processing quality checks and downstream analyses. Demultiplexing of the snRNA-seq data was performed by identifying HTOs using Seurat in-built demultiplexing strategy. Demultiplexing results are visualized as a heatmap in **Fig. 4A**, singlets are recognized as the nuclei with only one highly-expressed HTO, while doublets with more than one highly-expressed HTO and negatives with no HTO expression. Of note, approximately 33% of the nuclei were detected as negatives with our 10-min HTO antibody incubation approach. We therefore further optimized the HTO staining protocol by prolonging the incubation time from 10 min to 30 min in a subsequent experiment, resulting in a great decrease of negatively labeled nuclei (**Fig. 4B**). These findings indicate that prolongation of antibody incubation time may improve hashing efficiency. Violin plots in **Fig. 4C** demonstrate the number of genes (nFeature_RNA), number of unique molecular identifiers (UMI) (nCount_RNA), and the percentage of mitochondrial counts (percent.MT) in our snRNA-seq dataset to identify outliers and low quality nuclei. Subsequently, doublets and negatives were removed based on demultiplexing results and gene expression counts were normalized using the default method in Seurat. 875 (2.71%) counts are detected as highly variable genes (**Fig. 4D**), which might model cellular heterogeneity, sex difference and/or laterality. To validate the accuracy of HTO sample segregation, expression of X Inactive Specific Transcript (Xist, expressed in the inactive female X chromosome) was assessed to identify male samples and female samples (**Fig. 4E**). Xist expression was in accordance with the hashtag labeling that HTO 1-4 labelled samples were female samples and HTO 5-8 labelled samples were male samples. This suggests curated HTO labelling is highly specific. snRNA-seq GEX was scaled and linear dimensional reduction (principle components analysis, PCA) was performed. Assessment of the principal components (PCs) (**Fig. 4F**) revealed true signal being present in the first 12-15 PCs. Cells were then clustered using 15 PCs followed by dimension reduction visualization (UMAP) to visualize our 14 individual clusters (**Fig. 4G**). Neuronal cells, known to highly express Tubb3, were represented by cluster 7 and 9 (**Fig. 4H**). Glial cells, known to be enriched with Fabp7 (Avraham et al., 2020), were represented by cluster 0,1, 3 and 5 (**Fig. 4I**). Endothelial cells were detected in cluster 6 with high expression of Pecam1 (**Fig. 4J**). Our results support successful nuclei capture of neuronal cells, glial cells and endothelial cells of the sympathetic ganglion using snRNA-seq.

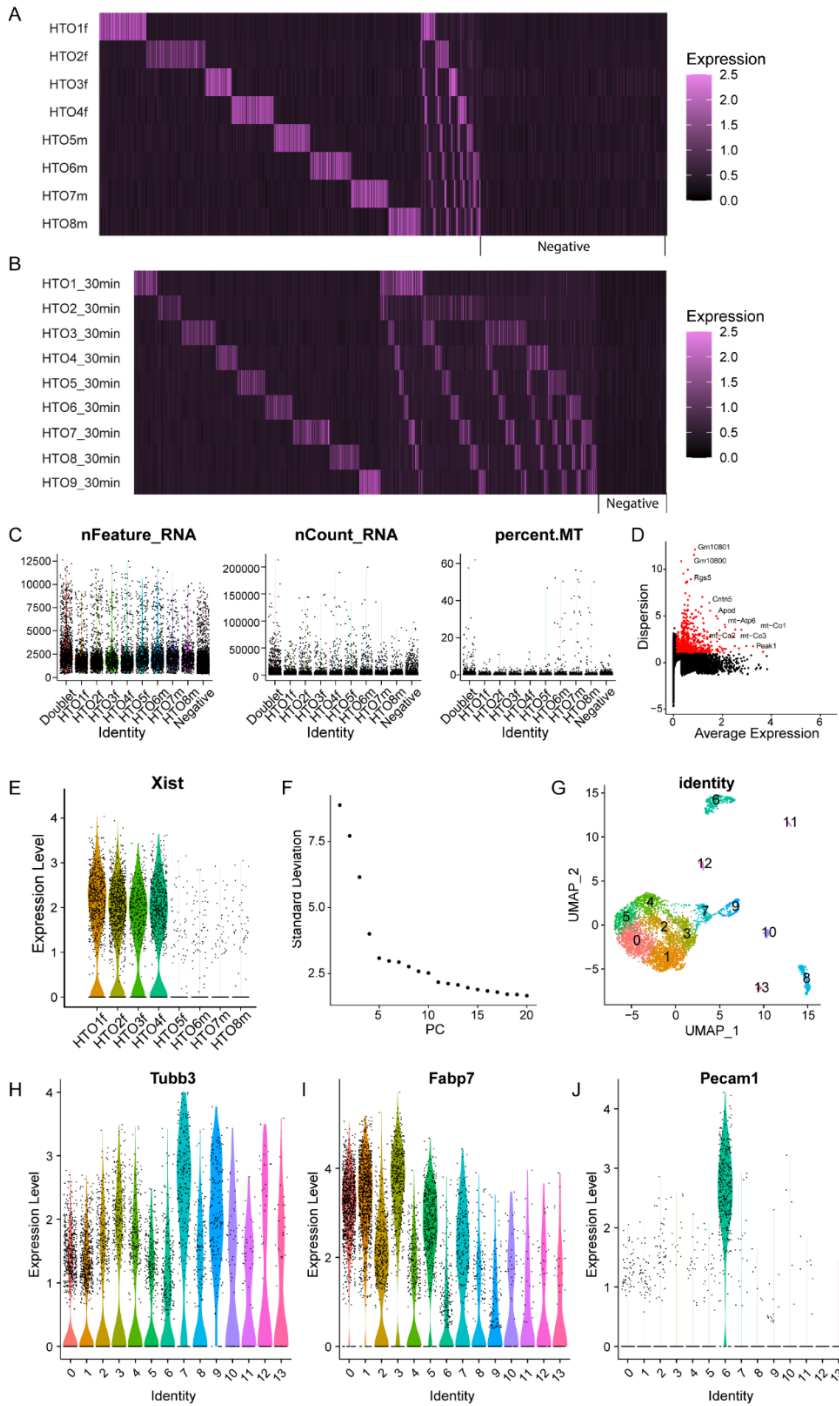


Figure 4. Quality control and analysis results of single nucleus sequencing. A-B. Heatmap of HTO demultiplexing reveals HTO staining in each nucleus. A. HTO staining achieved by performing 10-minute hashtag antibody incubation. B. HTO staining achieved by 30-min hashtag antibody incubation in a subsequent snRNA-seq experiment. Comparison of the number of negative-labelled nuclei shows a marked improvement of nucleus labeling after prolonging antibody incubation time. C. Violin plots of quality control metrics show the number of genes (nFeature_RNA), the number of UMIs (nCount_RNA), and the percentage of mitochondrial counts (percent.MT). D. Of the total 32,285 genes sequenced, 875 (2.71%) were identified as variable features as visualized in the scatter plot. E. Violin plot displaying female samples (high Xist expression) after demultiplexing using HTO labelled samples. F. Elbow plot of PCs to determine inclusion of true signal used for clustering. G. UMAP plot of the clustered snRNA-seq dataset. H-J. Violin plots of known cell type markers, such as Neuronal cells (Tubb3), glial cells (Fabp7) and endothelial cells (Pecam1) for cell type identification.

DISCUSSION

Here we describe a detailed protocol of the dissection of adult mouse superior cervical and stellate sympathetic ganglia, isolation and cryopreservation of the ganglionic cells, nuclei isolation and nucleus-barcoding with HTOs staining for multiplexing and snRNA-seq.

With this protocol, sympathetic ganglionic cells can easily be obtained by dissociating individual ganglion with commonly used trypsin and collagenase. Long-term preservation of isolated ganglionic cells is also readily achieved by freezing cells in FBS supplemented with 10% DMSO, which showed a high quality of recovery after thawing. Moreover, compared to conventional single-cell RNA sequencing, the use of droplet-based snRNA-seq of single murine sympathetic ganglia combined with the application of HTOs staining-based nucleus-barcoding has the following advantages: i) samples can be preserved for a long time until all samples are ready for further nuclei isolation; ii) nuclei of good quality isolated from multiple small-size ganglia can be pooled together for sequencing without a batch effect caused by sample preparation; iii) the ability to trace back the distinct ganglionic origin after sequencing by hashing; and iv) Cost-effectiveness, since only one library preparation is needed. Importantly, the described isolation and cell culture protocol provides a single uniform method for both murine cervical and stellate ganglia, and is potentially applicable to other ganglia, such as dorsal root ganglia, and other species such as human ganglia.

The first scRNA-seq study was published in 2009 (Tang et al., 2009), and the benefit of scRNA-seq in comparison with the transcriptomes of individual cells within a sample/biopsy highly promoted its applications in the field of cell biology. One of the major advantages of scRNA-seq is the ability to identify (novel) cell types and to reveal rare cell populations that could not be detected by bulk RNA-seq. The droplet-based scRNA-seq platform, i.e. the 10x Chromium platform used in this protocol, facilitates the capture of more cells and thus can provide an

aggregate view of the cell (sub)types and transcriptional heterogeneity of a large cell population as compared to a plate-base sequencing platform. However, the 10x Chromium platform is not suitable for cells larger than 50 μm , which limits its application in large cells such as human neurons (around 100 μm). The availability of the snRNA-seq technique overcomes this drawback, because of the small size of a nucleus. Moreover snRNA-seq is known as a useful method for gene-expression studies of highly interconnected and low recovered cells such as neurons as well as frozen tissues. snRNA-seq allows isolation of nuclei from tissues without prior cell dissociation, although we prefer to take a two-step nuclei isolation method that first dissociates the ganglion into single cells (which can be preserved in liquid nitrogen) followed by isolation of the single nuclei. Because of the tiny size of a mouse sympathetic ganglion, we found more nuclei yielded by a two-step nuclei isolation method as compared to direct one-step nuclei isolation from a mouse ganglion. The quality check of the cDNA, library and brief sequencing analysis supported the good nuclei/RNA quality. In addition, it makes the procedure logistically easier, since samples can be collected and stored before sending them collectively away for sequencing. Single nucleus analysis also revealed successful recovery and capture of neurons and glial cells that are of interest in our current projects. As the ganglion size is much larger in human and human neurons are difficult to dissociate and recover in our experience, one-step nuclei isolation instead of two-step nuclei isolation might be better for application of snRNA-sequencing in human sympathetic ganglia.

Another advantage of this protocol is the multiplexing with barcoded antibodies (Stoeckius et al., 2018). The mouse sympathetic ganglion is a tiny tissue (average size 0.1 mm^3), and the low amount of cells derived from an individual ganglion is insufficient for droplet-based sequencing, whereas pooling of several ganglia of different mice or different ganglia of a same mouse will cause the loss of either individual mouse information or individual ganglion information. As a solution, the HTOs staining step is easy to perform and enables the barcoded labelling of nuclei derived from different mice or different ganglia before nuclei pooling. The accuracy of HTOs demultiplexing is verified in this protocol by matched Xist expression in known female nuclei populations. Nuclei multiplexing with barcoded antibodies therefore reduces batch effects and lowers the sequencing cost.

A potential limitation of snRNA-seq might be that there may be differences between the RNA composition of the nucleus and cytoplasm due to the natural presence of nascent transcripts in nuclei, associated with early response to neuronal activities (Lacar et al., 2016; Lake et al., 2017). The nucleus and cytoplasm may also differ in transcripts depending on the state within the cell cycle (Grindberg et al., 2013). Less transcripts were detected in individual nuclei (~7000 genes) than in cells (~11000 genes) (Bakken et al., 2018). Therefore, scRNA-seq and snRNA-seq may yield different results at a transcript level. Nevertheless, the comparison

between scRNA-seq and snRNA-seq demonstrated similar capability to discriminate neuronal cell types of brain tissue (Bakken et al., 2018). To improve the discrimination between highly similar cell types or subtypes by snRNA-seq, more nuclei might be needed to compensate for the lower gene detection ability compared to scRNA-seq. Another limitation of snRNA-seq is the inability to select specific cellular populations due to the lack of an intact cell membrane, that is required for fluorescent activated cell sorting (FACS). Even though the accuracy of HTOs demultiplexing is sufficient, loss of some data is inevitable, as not all nuclei show an expression of a single HTO. Optimization of the staining time could minimize the amount of nuclei with double or negative expression of HTOs.

Taken together, here we provide — to our knowledge — for the first time a protocol for sequencing neuronal nuclei from sympathetic ganglia by means of an easy-to-follow workflow starting from ganglion isolation to nuclei preparation of low input of cells, followed by HTOs staining-based nucleus labelling for snRNA-seq. The protocol provides a detailed overview of all key steps that can be easily performed and can be applied to a diversity of ganglia in murine as well as in other species.

DISCLOSURES

The authors have nothing to disclose.

FUNDING

This work is supported by the Netherlands Organization for Scientific Research (NWO) [016.196.346 to M.R.M.J.].

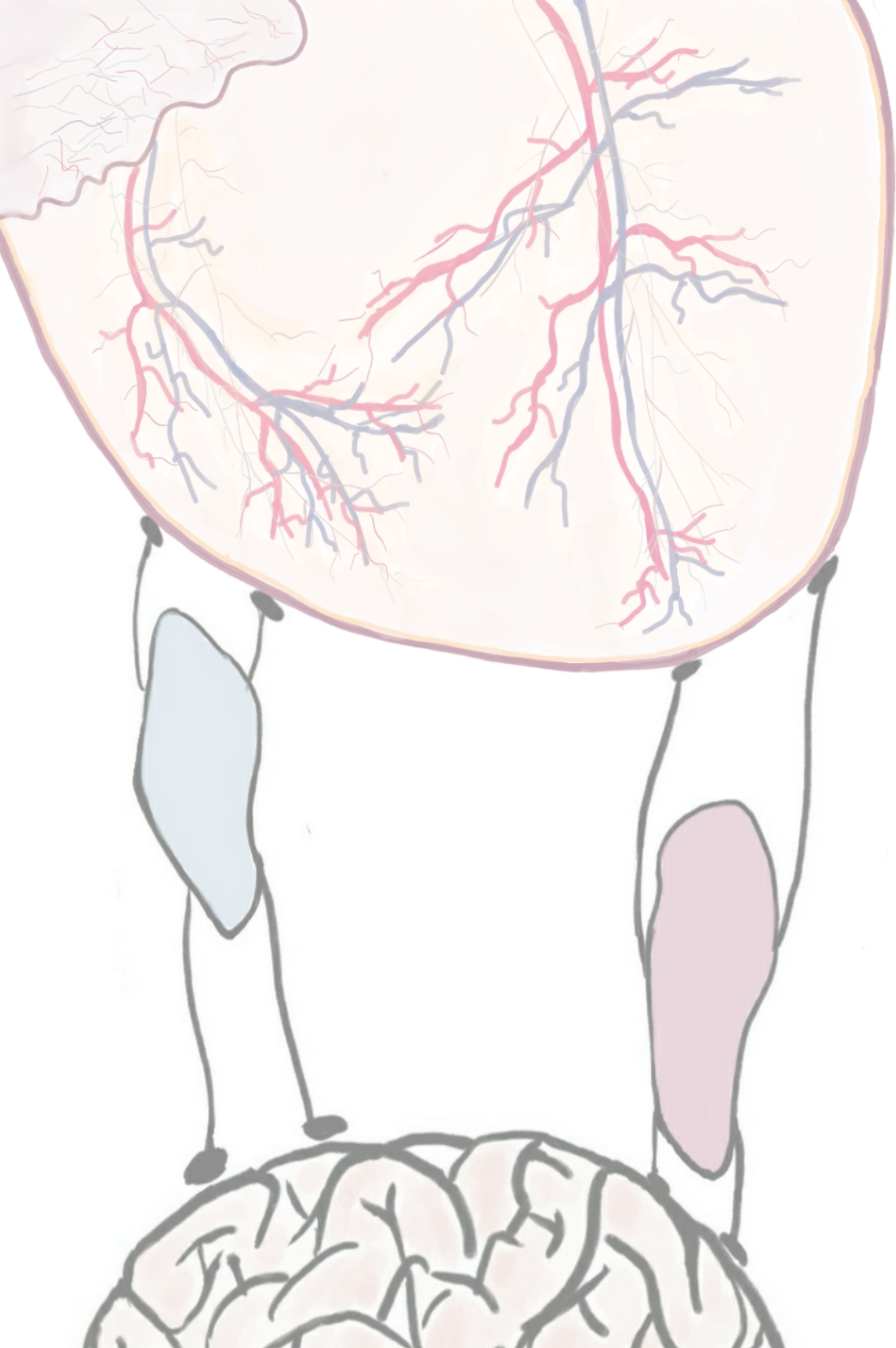
ACKNOWLEDGMENTS

We thank Susan L. Kloet (Department of Human Genetics, LUMC, Leiden, the Netherlands) for her help in experimental design and useful discussions. We thank Emile J. de Meijer (Department of Human Genetics, LUMC, Leiden, the Netherlands) for the help with single-nucleus RNA isolation and library preparation for sequencing.

REFERENCES

- Ajjjola, O.A., Wisco, J.J., Lambert, H.W., Mahajan, A., Stark, E., Fishbein, M.C., et al. (2012). Extracardiac Neural Remodeling in Humans With Cardiomyopathy. 5(5), 1010-1116. doi: 10.1161/CIRCEP.112.972836.
- Ajjjola, O.A., Yagishita, D., Reddy, N.K., Yamakawa, K., Vaseghi, M., Downs, A.M., et al. (2015). Remodeling of stellate ganglion neurons after spatially targeted myocardial infarction: Neuropeptide and morphologic changes. Heart Rhythm 12(5), 1027-1035. doi: 10.1016/j.hrthm.2015.01.045.

- Avraham, O., Deng, P.-Y., Jones, S., Kuruvilla, R., Semenkovich, C.F., Klyachko, V.A., et al. (2020). Satellite glial cells promote regenerative growth in sensory neurons. *Nature Communications* 11(1), 4891. doi: 10.1038/s41467-020-18642-y.
- Bakken, T.E., Hodge, R.D., Miller, J.A., Yao, Z., Nguyen, T.N., Aeversmann, B., et al. (2018). Single-nucleus and single-cell transcriptomes compared in matched cortical cell types. *PLoS One* 13(12), e0209648. doi: 10.1371/journal.pone.0209648.
- Gaublomme, J.T., Li, B., McCabe, C., Knecht, A., Yang, Y.M., Drokhlyansky, E., et al. (2020). Nuclei multiplexing with barcoded antibodies for single-nucleus genomics (vol 163, pg 447, 2021). *Nature Communications* 11(1). doi: 10.1038/s41467-020-19357-w.
- Grindberg, R.V., Yee-Greenbaum, J.L., McConnell, M.J., Novotny, M., O'Shaughnessy, A.L., Lambert, G.M., et al. (2013). RNA-sequencing from single nuclei. *Proceedings of the National Academy of Sciences* 110(49), 19802-19807. doi: 10.1073/pnas.1319700110.
- Han, S., Kobayashi, K., Joung, B., Piccirillo, G., Maruyama, M., Vinters, H.V., et al. (2012). Electroanatomic remodeling of the left stellate ganglion after myocardial infarction. *J Am Coll Cardiol* 59(10), 954-961. doi: 10.1016/j.jacc.2011.11.030.
- Lacar, B., Linker, S.B., Jaeger, B.N., Krishnaswami, S.R., Barron, J.J., Kelder, M.J.E., et al. (2016). Nuclear RNA-seq of single neurons reveals molecular signatures of activation. *Nature Communications* 7(1), 11022. doi: 10.1038/ncomms11022.
- Lake, B.B., Codeluppi, S., Yung, Y.C., Gao, D., Chun, J., Kharchenko, P.V., et al. (2017). A comparative strategy for single-nucleus and single-cell transcriptomes confirms accuracy in predicted cell-type expression from nuclear RNA. *Scientific Reports* 7(1), 6031. doi: 10.1038/s41598-017-04426-w.
- Li, C.-Y., and Li, Y.-G. (2015). Cardiac Sympathetic Nerve Sprouting and Susceptibility to Ventricular Arrhythmias after Myocardial Infarction. *Cardiology Research and Practice* 2015, 698368. doi: 10.1155/2015/698368.
- McCorry, L.K. (2007). Physiology of the autonomic nervous system. *Am J Pharm Educ* 71(4), 78. doi: 10.5688/aj710478.
- Nguyen, B.L., Li, H., Fishbein, M.C., Lin, S.F., Gaudio, C., Chen, P.S., et al. (2012). Acute myocardial infarction induces bilateral stellate ganglia neural remodeling in rabbits. *Cardiovasc Pathol* 21(3), 143-148. doi: 10.1016/j.carpath.2011.08.001.
- Stoeckius, M., Zheng, S., Houck-Loomis, B., Hao, S., Yeung, B.Z., Mauck, W.M., et al. (2018). Cell Hashing with barcoded antibodies enables multiplexing and doublet detection for single cell genomics. *Genome Biology* 19(1), 224. doi: 10.1186/s13059-018-1603-1.
- Stuart, T., Butler, A., Hoffman, P., Hafemeister, C., Papalexi, E., Mauck, W.M., et al. (2018). Comprehensive integration of single cell data. *bioRxiv*, 460147. doi: 10.1101/460147.
- Tang, F., Barbacioru, C., Wang, Y., Nordman, E., Lee, C., Xu, N., et al. (2009). mRNA-Seq whole-transcriptome analysis of a single cell. *Nat Methods* 6(5), 377-382. doi: 10.1038/nmeth.1315.
- Wu, H., Kirita, Y., Donnelly, E.L., and Humphreys, B.D. (2019). Advantages of Single-Nucleus over Single-Cell RNA Sequencing of Adult Kidney: Rare Cell Types and Novel Cell States Revealed in Fibrosis. *J Am Soc Nephrol* 30(1), 23-32. doi: 10.1681/asn.2018090912.
- Zandstra, T.E., Notenboom, R.G.E., Wink, J., Kiès, P., Vliegen, H.W., Egorova, A.D., et al. (2021). Asymmetry and Heterogeneity: Part and Parcel in Cardiac Autonomic Innervation and Function. *Frontiers in Physiology* 12(1569). doi: 10.3389/fphys.2021.665298.
- Zeisel, A., Hochgerner, H., Lönnerberg, P., Johnsson, A., Memic, F., van der Zwan, J., et al. (2018). Molecular Architecture of the Mouse Nervous System. *Cell* 174(4), 999-1014.e1022. doi: 10.1016/j.cell.2018.06.021.



7

SINGLE-NUCLEUS RNA SEQUENCING REVEALS THE CELLULAR COMPOSITION AND MOLECULAR SIGNATURE OF MURINE SUPERIOR CERVICAL GANGLIA

Yang Ge^{*1,2}, H. Sophia Chen^{* 1,2}, Ruben Methorst², Lieke van Roon^{1,2}, Marco de Ruiter¹, Szymon M. Kielbasa³, Monique R.M. Jongbloed^{1,2}

1. Department of Anatomy & Embryology, Leiden University Medical Center, Einthovenweg 20, 2333 ZC Leiden, The Netherlands;

2. Department of Cardiology, Leiden University Medical Center, Albinusdreef 2, 2333 ZC Leiden, The Netherlands;

3. Department of Cell and Chemical Biology, Leiden University Medical Center, Einthovenweg 20, 2333 ZC Leiden, The Netherlands;

4. Department of animal ..., Leiden University Medical Center, Albinusdreef 2, 2333 ZC Leiden, The Netherlands;

* Authors contribute equally

Manuscript in preparation

ABSTRACT

The superior cervical ganglion (SCG) provides sympathetic nerve fibers to the murine anterior myocardium, an area that can be involved in large transmural myocardial infarctions. It has been shown that overactivity of SCG is associated with adverse clinical outcome after myocardial infarction. Despite these findings and a plethora of knowledge regarding electrophysiological function and histology, the exact cellular composition and molecular signature of the SCG remains to be elucidated. Here, we report a single-nuclei RNA-sequencing (snRNA-seq) study on murine SCG in order to provide an overview of its variety in cellular compositions and focused laterally and sex differences. We identified 7 major cell types, among which 5 subtypes of neuronal cells and 4 subtypes of satellite glial cells were distinguished. Assessment of potential heterogeneity between sexes revealed differences in cellular distribution and gene expression. No obvious laterality differences were detected on this healthy murine SCG dataset. Our data provides insight into the heterogenous SCG cellular composition and gene expression in a normal healthy state, thus providing a resource for further disease-oriented studies.

Keywords

Single-nucleus RNA sequencing, superior cervical ganglion, cellular composition, molecular signature, sex differences, laterality differences

INTRODUCTION

The autonomic nervous system (ANS), which is divided in parasympathetic and sympathetic branches, strictly regulates multiple organ systems including the cardiovascular system [1]. Cardiac sympathetic innervation is mainly provided by nerve fibers from the bilateral superior cervical ganglia (SCG), stellate ganglia, and upper thoracic ganglia [2]. Each of these ganglia have been shown to innervate different regions of the heart [3]. The SCG projects nerve fibers to the anterior myocardium [4], an area which can be involved in large transmural myocardial infarctions after atherosclerotic occlusion of the left anterior descending coronary artery, and is regarded as a factor associated with adverse clinical outcome when overactive [5]. Upon myocardial infarction, cardiac sympathetic innervation can drastically change, with remodeling of sympathetic nerves and neurons resulting in sympathetic overdrive, which has been associated with adverse outcome in patients due to increased risk of ventricular arrhythmias [6, 7]. Changes in SCG structure and/or composition have also proven to be relevant in other diseases, such as diabetic sympathetic autonomic neuropathy and obesity [8-10].

Single-cell sequencing technologies allow for accurate exploration of the molecular signature of individual cells in complex tissues, such as sympathetic ganglia. A variety of previously unknown neuronal (sub)types in the SCG, stellate ganglia, and sympathetic chain ganglia have been identified using single-cell sequencing [11]. Similarly, different maturation and differentiation states of satellite glial cells in stellate ganglia have been identified [12]. Current literature focuses on subclassification of neuronal cells or specific non-neuronal cells in sympathetic ganglia. Although these findings are crucial to elucidate cell-type specific behavior in sympathetic ganglia, a complete outline of the cellular composition in the superior cervical ganglion is currently lacking, thus hampering interpretation of molecular changes at the single cell level in disease states.

It is hypothesized that individual healthy ganglia may already present differences in sex and laterality of the ganglia. Recently, significant transcriptomic differences between the male and female have been revealed in the left stellate ganglia in healthy adult mice [13]. Sympathetic ganglia show distinct laterality in terms of morphology (macroscopic and microscopic) and function, despite being symmetrically distributed along the paravertebral locations [14-17].

However, this classification of cellular phenotypes based on detailed molecular signatures is currently still lacking in the superior cervical ganglia. Here, we aim to provide an overview of potential sex-specific (male versus female) and side-specific (left versus right) differences of healthy adult murine SCG by assessment of heterogeneity in transcriptomic diversity at single nucleus resolution.

MATERIAL AND METHODS

Animals

Two female and two male C57BL/6J mice (Charles River Laboratories Inc, Wilmington, MA, USA), 15 weeks of age, were used for snRNA-seq. Animals were euthanized by CO₂ asphyxiation. This animal study was performed in accordance with the regulations of Animal welfare and rights in the Netherlands (The Animals Act 2011) and approved by the Animal Ethics Committee of the Leiden University Medical Center (Leiden, The Netherlands) (AVD1160020185325).

Cell dissociation

A protocol for the methods used here is described in detail in *Chapter 6*. Briefly, bilateral superior cervical ganglia (n=8) were identified, isolated, and collected in cold Dulbecco's phosphate-buffered saline (DPBS, Gibco, Grand Island, NY, USA). Next, the individual ganglia were incubated in a 0.25% Trypsin-EDTA solution (Thermo Fisher Scientific, Waltham, MA, USA) at 37°C for 40 min in separate tubes. After removal of Trypsin, 500 µl of 1400U/ml collagenase type 2 dissolved in supplemented Neurobasal Medium (1x, Gibco, Grand Island, NY, USA; 1x B-27plus (Gibco, Grand Island, NY, USA), 2mM L-glutamine (Thermo Scientific, Waltham, MA, USA) and, 1x Antibiotic-Antimycotic (Gibco, Grand Island, NY, USA)) was added and incubated at 37°C for 40 minutes. The dissociated cells were then carefully triturated with 1 ml pipette tips. After trituration, the cell suspension was transferred into the a 15 ml tube containing 5 ml supplemented Neurobasal Medium and spun down for 10 minutes at 300 rcf at room temperature. Thereafter, the supernatant was carefully removed, and the pellet was resuspended with 270 µl fetal bovine serum (Biowest LLC, Bradenton, FL, USA). 5 µl 0.4% Trypan blue dye (Bio-Rad Laboratories, Hercules, CA, USA) was added to 5ul of each cell suspension and live cell numbers were counted using a cell counter. 30 µl Dimethyl sulfoxide (Sigma-Aldrich, Saint Louis, MO, USA) was added into each cell suspension, mixed, and transferred into cryovials. Cryovials were kept in Corning Coolcell containers (Corning Incorporated, Corning, NY, USA) at -80°C overnight and transferred into liquid nitrogen the next day until further use.

Nucleus isolation and hashing

After thawing the cryovials at 37°C, 1 ml supplemented Neurobasal Medium was added. Each cell suspension was loaded into a MACS SmartStrainer (30 µm; Miltenyi Biotec) separately and rinsed with 5ml supplemented Neurobasal Medium. The cell suspension was centrifuged at 300 rcf for 5 minutes and supernatant was carefully removed and resuspended in 50 µl cell wash (0.04% BSA in DPBS) (Sigma-Aldrich, Saint Louis, MO, USA). Next, the cell suspension was

transferred into an Eppendorf DNA/RNA LoBind tube (EP0030108035) and centrifuged at 500 rcf for 5 minutes at 4°C. 45 µl supernatant was removed and replaced with 45 µl chilled Lysis Buffer (10 mM Tris-HCL, 10mM NaCl, 3 mM MgCl₂, 0.1% Nonidet P40 Substitute, 40 U/ml RNase inhibitor (Sigma-Aldrich, Saint Louis, MO, USA) in Nuclease-Free Water (ThermoFisher Scientific, Waltham, MA, USA)). After 8 minutes of incubation on ice, 50 µl cold nuclei wash buffer was added to each tube (1xDPBS with 2% BSA and 20 U/ml RNase Inhibitor) and spun down at 600 rcf for 5 minutes at 4°C. 95 µl of supernatant was removed and 45 µl chilled Nuclei wash buffer was added to the pellet. Next, the nuclei suspension was centrifuged at 600 rcf for 5 minutes at 4°C and the supernatant was removed. 50 µl ST staining buffer (ST-SB) (10 mM Tris-HCL, 146 mM NaCl, 21 mM MgCl₂, 1 mM CaCl₂, 2% BSA, 0.02% Tween-20 in Nuclease-free water) was added to the nuclei pellet and resuspended carefully. 5 µl Fc Blocking reagent (Biolegend, San Diego, CA, USA) was added per 50 µl of ST-SB/nuclei mix and incubated for 10 minutes on ice. 1 µl of unique hashtag-oligos antibodies (HTO, Mab414) were added per 50 µl of ST-SB/nuclei mix to all 8 superior cervical ganglia samples and incubated for 10 minutes on ice. 100 µl of ST-SB was added to each sample and spun down for 5 minutes at 600 rcf at 4°C. 145 µl supernatant was removed and the previous step was repeated once. After removing the supernatant and resuspending the nuclei pellet in 50 µl ST-SB, nuclei were counted. Next, nuclei suspensions were centrifuged for 5 minutes at 600 rcf at 4°C and resuspended in ST-SB to reach the target nuclei concentration of 1,000-3,000 nuclei/µl for each sample and individual samples were pooled together.

Single nuclei library preparation and sequencing

Single nuclei gene expression libraries were generated on the 10x Genomics Chromium platform using the Chromium Next GEM Single Cell 3' Library & Gel Bead Kit v3.1 and Chromium Next GEM Chip G Single Cell Kit (10x Genomics, Pleasanton, CA, USA) according to the manufacturer's protocol. TotalSeq-A hashtag libraries were generated using the Chromium Single Cell 3' Feature Barcode Library Kit (10x Genomics) according to the manufacturer's protocol. Gene expression and hashtag libraries were sequenced on a NovaSeq 6000 S4 flow cell with PE150bp sequencing using v1.5 chemistry (Illumina, San Diego, CA, USA).

snRNA-seq data analysis

Cell Ranger software v4.0.0 (10x Genomics) was used for library demultiplexing, fastq file generation and read alignment. The resulting matrices contain the number of unique molecular identifiers (UMIs) per gene or per hashtag barcoding antibody-oligo (HTO) for each cell. Downstream analyses were performed by using R 4.0.5 and the R package Seurat (version 4.0.2, Satija Lab) [18]. Nuclei were included in analysis if passing the following criteria: i)

nFeature > 500 and nCount < 15000; ii) percent.mito < 5% and percent.RP < 3%; iii) the individual nuclei showed clear expression of a single HTO.

Normalization counts were normalized, scaled with default thresholds in Seurat

Dimension reduction and clustering. Principal component analysis was performed to identify major sources of variation within the dataset. The elbow plot was used to assess inclusion of principal components that would be used for downstream analyses. In total, 20 PCs were included. Clustering was performed with a resolution of 0.5. Dimension reduction was performed using UMAP reduction.

Heatmaps. Function FindVariableFeatures from Seurat was used to identify highly variable genes of the dataset. The top 500 highly variable genes were employed to generate a heatmap to show hierarchical clustering.

Differential gene expression analysis. Function FindAllMarkers from Seurat was used to find differential expression genes (DEGs) of each cluster by comparing the gene expression of every cluster to all remaining clusters. The list of DEGs per cluster with adjusted p-value < 0.05 (Wilcoxon rank sum test) was used for a Gene Ontology (GO) enrichment analysis using the default Kolmogorov–Smirnov test.

Subtypes of neurons analysis. To subcluster neurons, 13 PCs were included in clustering and dimension reduction (resolution=0.4, k.param=10). DEGs analysis of subclusters was performed with Function FindAllMarkers from Seurat.

Subtypes of glial cells analysis. DEGs analysis was performed with Function FindAllMarkers by comparing the gene expression of each glial cell cluster to the other glial cell clusters.

Sex differences and bilaterality differences analysis. Sex information and bilaterality information of each nucleus was assigned according to HTO expression. DEGs between male and female (or left versus right) were generated with Function FindMarkers from Seurat R package and GO enrichment analyses was performed on significant DEGs.

RESULTS

Single nucleus clustering and cell type identification of mouse SCG

Droplet-based high-throughput single nucleus RNA sequencing was performed on a HTO barcoded nuclei suspension of 8 adult murine SCG. After read quality control, alignment and quality control, a total of 4,721 high quality single nuclei were used for subsequent analysis. SCG nuclei were clustered and 12 major clusters were identified (**Fig. 1A**). There was sufficient

integration of all eight samples, indicating that differences in sample preparation were minimal (**Fig. 1B**). Next, the top 500 variably expressed genes together with the top 20 DEGs of each cluster were used to identify major cell types and clusters of similar molecular characteristics (i.e. cluster 4 and 9 as stromal cells), based on known cell markers (**Fig. 1C**, **Supplemental Fig. 1A**, **Supplemental Table 1**).

To further extrapolate cell type identity of these clusters, expression levels of multiple known marker genes for every cell type were visualized (**Figure 1C and Supplemental Figure 1B**): *S100b* and *Fabp7* for satellite glial cells [12]; *Tubb3* and *TH* for adrenergic neurons [19]; *Sox10* and *Ncmip* for Schwann cells [20]; *Vwf* and *Pecam1* for endothelial cells [21]; *Acta2* and *Myh11* for vascular smooth muscle cells (vSMAs) [22]; *Col1a1* and *Dcn* for stromal cells; *Ccr5* and *Cd14* for immune cells. Nuclei clustering and DEGs analysis indicated cellular heterogeneity of neuronal subtypes (cluster 6-7), satellite glial cell subtypes (cluster 0-3) and stromal cell subtypes (*Lum+* stromal cells and *Cldn1+* stromal cells) as was reported previously in other sympathetic and sensory ganglia [12, 23, 24].

In total, we identified seven major cell types in the SCG, including neuronal cells, satellite glial cells, Schwann cells, endothelial cells, smooth muscle cells, stromal cells and immune cells (**Fig. 1**).

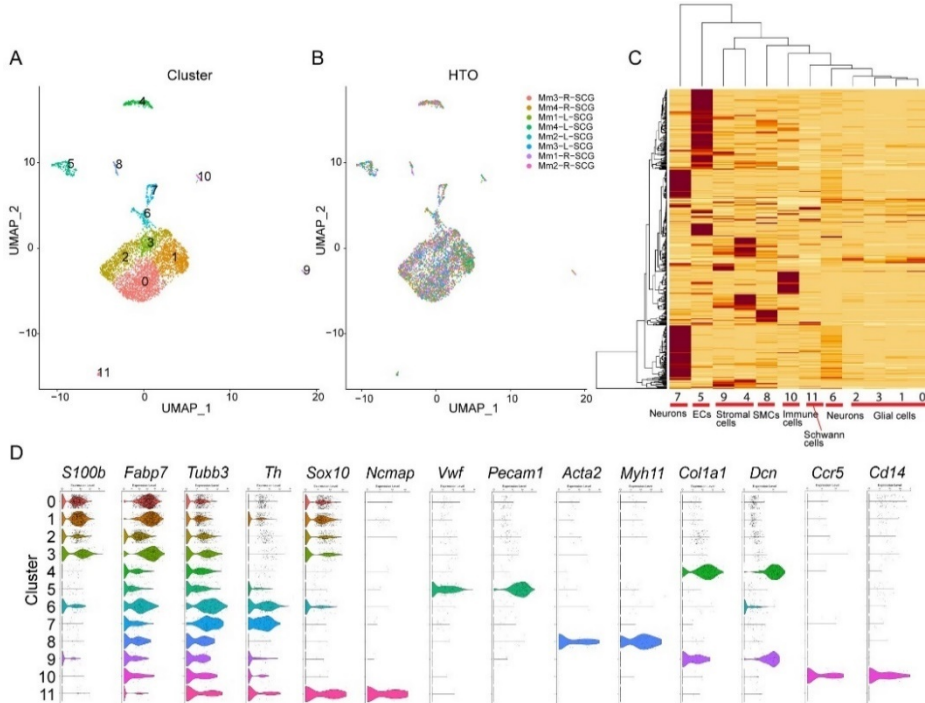


Figure 1. Single nuclei clustering and cell type identification. A. UMAP plot of 4,721 single nuclei with cell clusters highlighted. B. UMAP plot of single nuclei with HTO labels highlighted. C. Heatmap and hierarchical clustering based on expression of top 500 most variable genes. D. Violin plots displaying marker gene expression of known cell types for each cluster.

Heterogeneity among mouse SCG neurons

To characterize SCG neuronal subtypes, neuron clusters were subclustered. Subclustering analysis revealed five major subtypes of neurons (3 subclusters from original cluster 6 and 2 subclusters from original cluster 7 (**Fig. 2A, B**). All neuronal subclusters were similarly represented in all eight individual samples (**Supplemental Fig. S2**). DEGs analysis of each subclusters revealed several marker genes of neuronal subtypes (**Fig. 2C**).

Almost all SCG neuronal subtypes expressed *Dbh* (Dopamine beta-hydroxylase, converting dopamine to norepinephrine) which is known to be mainly expressed in neurosecretory vesicles in sympathetic neurons [25]. *Snap25* (Synaptosomal-Associated Protein, a presynaptic plasma membrane protein involved in neurotransmitter release) showed heterogenous expression between the individual neuronal clusters [26] (**Fig. 2D**).

Recently reported marker genes in mouse thoracic ganglia were compared to marker genes in the mouse SCG. In thoracic ganglia the following neuronal subtypes were identified: 5 subtypes of nonadrenergic neurons (NA1-5), 2 subtypes of acetylcholinergic neurons (Ach1-2) and 1 type of glutamatergic neurons (Glut) [24]. We examined the expression of these published neuronal sub-type marker genes in our dataset, which revealed that only NA4 neurons are detectable in the mouse SCG (**Fig. 2E-L**). The other neuronal subpopulation in mouse SCG could not be assigned to previously known subtypes.

Differential gene expression analysis among the neuronal subclusters indicated a distinct gene expression profile of the five neuronal subclusters in SCG neurons (**Fig. 2M**) and potential distinct functions which was further suggested by Gene Ontology (GO) enrichment analysis (**Supplemental Fig. 3**). Using this approach, we identified the following neuronal subpopulations; *Apoe*⁺ neurons, *Kcnq1*⁺/*Nrg3*⁺ neurons, *Kcnq1*/*Nrg3*⁺ neurons, *Map1b*⁺ neurons and *Chl1*⁺ neurons. Ultimately, our findings are indicative of cellular heterogeneity of nonadrenergic neurons in the SCG.

Heterogeneity of mouse SCG satellite glial cells

The important function of glial cells in the central nervous system (CNS) has been recognized for decades [27]. Although the relevance of glial cells in the peripheral nervous system has also been getting more awareness recently, still little is known about glial cells in the sympathetic ganglia [28]. Recently the presence of satellite glial subtypes with different functions have

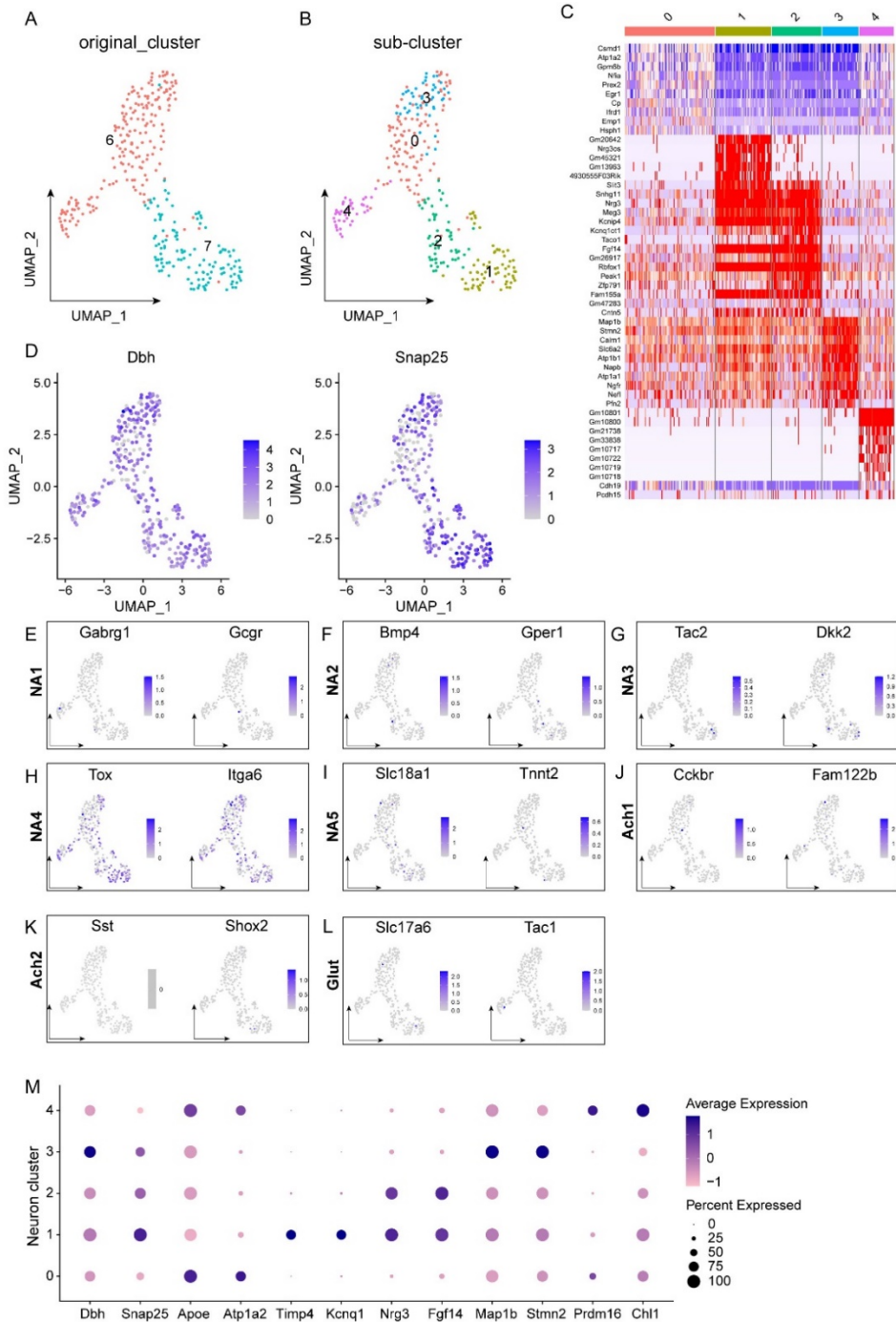


Figure 2. Identification of neuronal subtypes and markers of mouse SCG neurons. A. UMAP plot of 316

neuronal cells grouped by original cell clustering. B. Subclustering of 316 neuronal cells shown in A resulted in 5 cellular subtypes. C. Heatmap of top 10 DEGs of each neuronal subcluster. D. Overview of a well-known adrenergic neuron marker (*Dbh*) and synapse marker (*Snap25*) of neuronal clusters. E-L. Derivation of previously published neuronal subtypes with UMAP expression plots: E-I. Subtypes of adrenergic sympathetic neurons; J-K. cholinergic neurons and L. glutamatergic neurons. M. Expression of marker genes identified using subclustering of mouse SCG neuronal cells.

been identified, although their precise role is still unclear [23]. General markers for satellite glial cells (*Fabp7* and *S100b*) are currently used as the main identifiers for satellite glial cells in the peripheral nervous system. To facilitate the analysis of SCG satellite glial cells, satellite glial cells (cluster 0-3) were extracted from the whole dataset with the original clustering signatures (**Fig. 3A**) using *Fabp7* and *S100b*. All satellite glial sub-clusters were similarly represented over all eight individual samples (**Supplemental Fig. 4**). Differential gene expression analysis among the glial clusters revealed their distinct gene expression patterns (**Fig. 3B**). The expression of known sympathetic- and sensory-specific glial markers[23] were assessed in SCG (**Fig. 3C-E**). Consistent with previous findings [23], only sympathetic-specific, but almost no sensory-specific, satellite glial cells were present in murine SCG (**Fig. 3C, D**). General cell type gene markers of the satellite glial cells generally expressed in the peripheral nervous system, were examined in SCG as shown in **Figure 3E**. Results revealed that while expression of common satellite glial cells markers is present in all glial subtypes, enrichment of these markers vastly differs. Marker gene identification and GO pathway analysis of glial subclusters revealed the potential different functions of the different satellite glial cells: immuno-responsive satellite glial cells (cluster 0), which are enriched with genes such as *Junb*, *Irf1* and *Cxcl10*; fatty acid metabolic-enriched *Ptprz1*⁺ satellite glial cells (cluster 1); migration-enriched *Ntrk3*⁺ satellite glial cells (cluster 2) and *Dbi/Tuba1a*-enriched satellite glial cells (cluster 3) (**Fig. 3F, Supplemental Fig. 5**).

Glial cells are considered to communicate with other glial cells and neighbouring neurons via gap junctions. They also have a role in supporting neurons after injury, showing alterations in expression of gap junctions in response to injury [28-30]. A variety of gap junctions and other gene markers which are known to be enriched in the CNS and sensory ganglia were examined. *Cdh19* and *Sox10* are enriched in SCG satellite glial cells, while *Gfap* which is known to be highly enriched in the CNS [31], is absent in healthy mouse SCG glial cells (**Fig. 4**). Potassium channel protein *Kcnj10* was mainly expressed in cluster 0 and 1 of SCG glial cells (**Fig. 4**). Different from *Gja1* as the main type of gap junction found in sensory glial cells, SCG satellite glial cells exclusively expressed *Gjc3* in all subclusters (**Fig. 4**). Moreover, we found SCG satellite glial cells to express the ATP purinergic receptor *P2rx7*, which was enriched in cluster 0 and 2 (**Fig. 4**). Thus, we identified heterogeneity in gap junction, ion channel, and receptor expression between different glial cell subtypes, indicating that different glial cell populations may play a different role in sympathetic innervation. Moreover, we observed NGF receptor (*Ngfr*)

expression in all SCG satellite glial cells which indicates their neurotrophic factor-responsive property (Fig. 4).

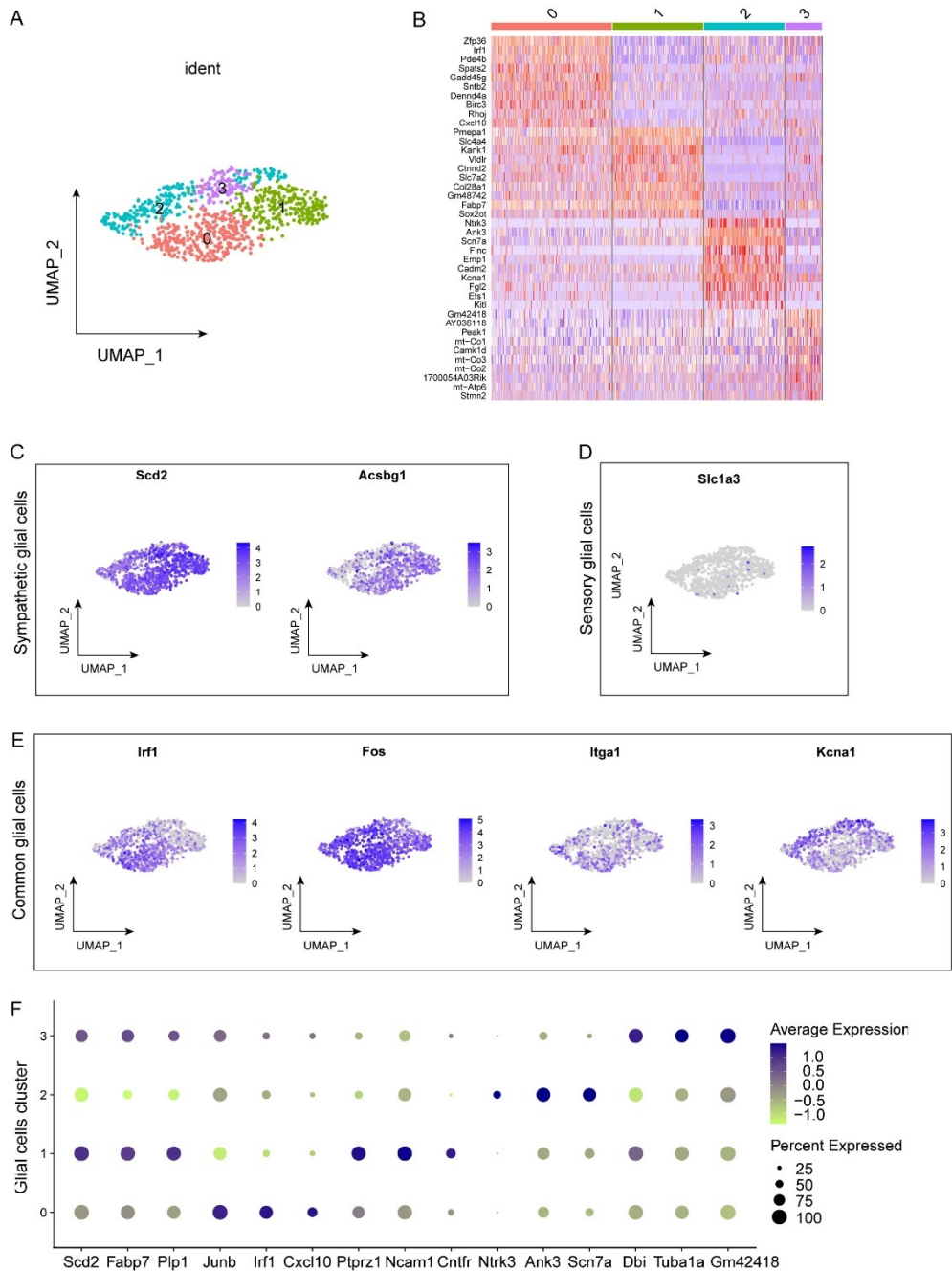


Figure 3. Identification of cellular subtypes and markers of SCG satellite glial cells. A. UMAP plot of 933 glial cells. B. Heatmap of top 10 DEGs of each glial cell population. C. Feature plot overview of two known markers of the sympathetic ganglion-specific glial cells (*Scd2* and *Acsbg1*). D. Feature plot overview of a known marker of the sensory ganglion-specific glial cells (*Sc11a3*). E. Feature plots of previously published common glial cell markers. F. Expression of marker genes of mouse SCG glial cells.

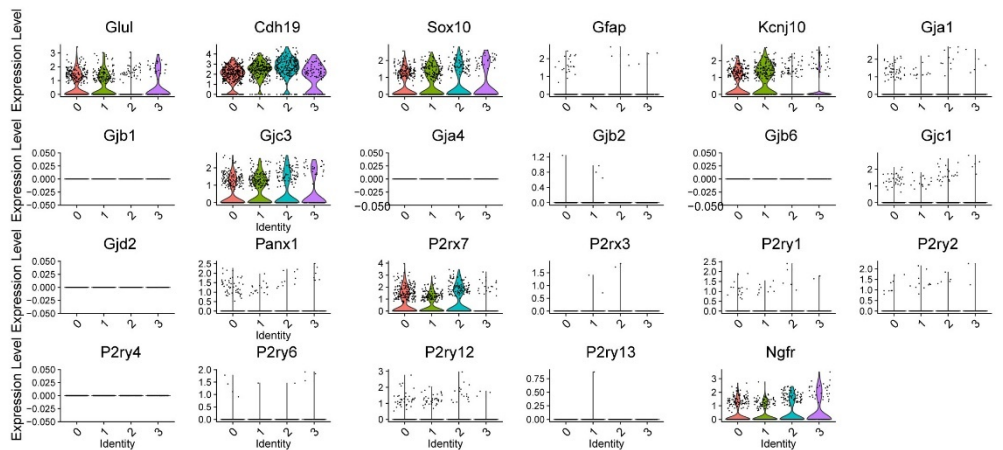


Figure 4. Mouse SCG glial cells have distinct gene expression from CNS and sensory ganglionic glial cells. Violin plots displaying expression of known CNS and sensory ganglionic glial cell marker genes in SCG glial cells.

snRNA-seq reveals sex differences in cellular distribution and gene expression of satellite glial cells in the SCG

Sex differences have received close attention in recent years and have been revealed in both health and disease in multiple organs/systems [32–34]. To date, a few studies of mouse and rat stellate ganglia based on bulk RNA sequencing have indicated transcriptomic differences between male and female [35, 36], however no molecular differences between sexes have been reported at single cell level. In the current study, we performed further analysis of SCG snRNA-seq data to detect molecular differences between male and female at single cell level. Single nuclei were annotated with sex information according to HTO labelling (Fig. 5A). The percentage of the nucleus numbers in each cluster/total nucleus number (to correct for differences in cell size of the different clusters) of corresponding sex was separately calculated and compared (Fig. 5B). The results indicate sex difference in cellular distribution in the mouse SCG, especially in the satellite glial cells (cluster 0–2). Differential gene expression analysis of satellite glial cells and neurons further demonstrated transcriptomic differences in satellite glial cells (cluster 0–3) between male and female, however no sex difference was detectable in neuronal clusters (Clusters 6 and 7, except for X-linked gene *Xist*) (Fig. 5C).

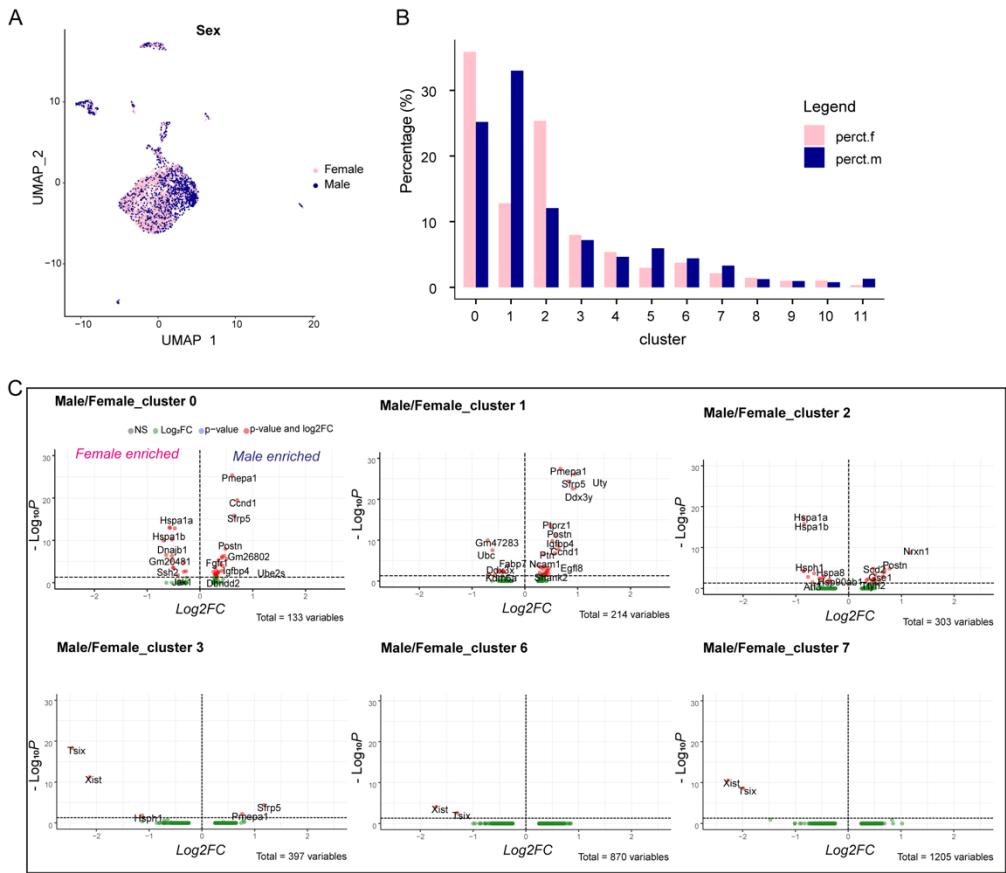


Figure 5. Sex difference analysis of mouse SCG cells. A. UMAP plot of mouse SCG cells colored by sex. B. Bar plot parallely showing cellular distribution in male and female SCG. Percentage = # nuclei per cluster / # of total nuclei. C. Volcano plot showing differentially expressed genes between male and female SCG satellite glial cells and neurons.

Examination of potential sidedness differences in cellular distribution or gene expression of murine SCG cells

Left and right sympathetic ganglia are known to unevenly innervate different regions of an organ or tissue, e.g. left dominant innervation of the posterior regions of ventricles by stellate ganglia [3]. The underlying molecular signatures driving these laterality differences are unknown and remains to be investigated.

To compare left and right mouse SCG, all sequenced nuclei were assigned with their laterality identification according to HTO labelling (Fig. 6A), wherafter cellular composition of the left and right SCG was determined and compared (Fig. 6B). Results revealed no obvious sidedness

differences in cellular distribution. Differential gene expression analysis of satellite glial cells and neurons indicated minor transcriptomic differences only in Junb⁺ satellite glial cells between left and right SCG (Fig. 6C). The results suggest no obvious differences between left and right SCG in a healthy state.

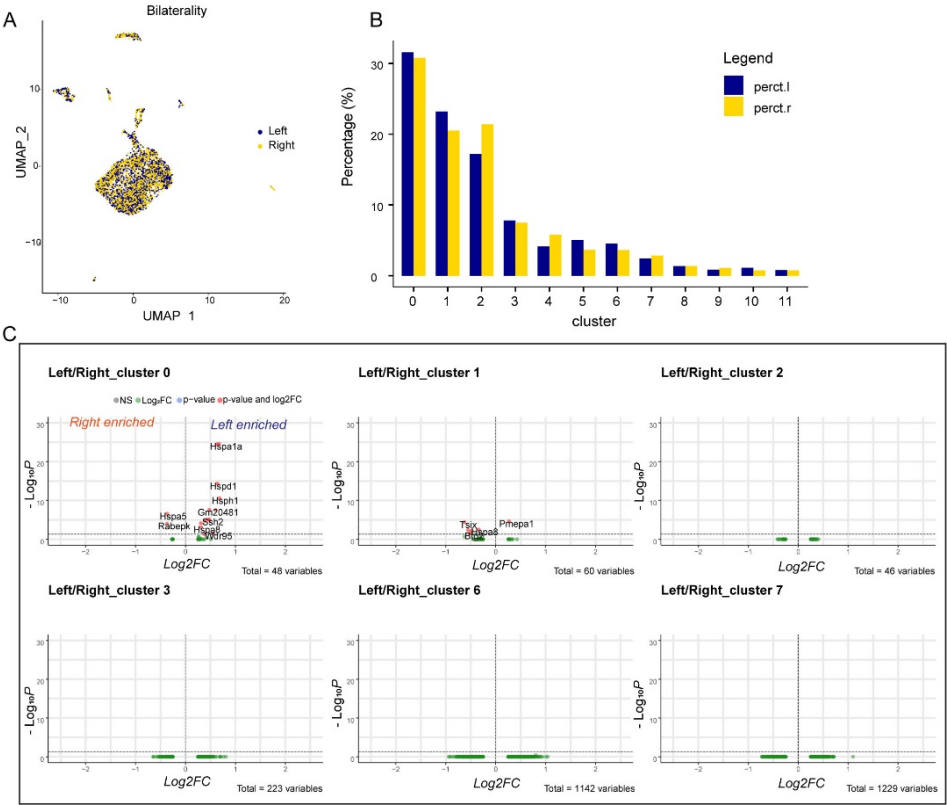


Figure 6. Sidedness analysis of mouse SCG cells. A. UMAP plot of mouse SCG cells coloured by bilaterality identification. B. Bar plot parellessly showing cellular cluster distribution in left and right SCG. Percentage = # nuclei in cluster / # total nuclei. C. Volcano plot showing differentially expressed genes between left and right SCG satellite glial cells and neurons.

DISCUSSION

Superior cervical ganglia are important components of the cardiac sympathetic nervous system. We have previously demonstrated neuronal cell remodeling in the SCG after MI [Chapter 5]. It is well-known that ganglia are mainly composed of neuronal cells with surrounding glial cells (the majority of which are satellite glial cells), and the emerging importance of glial cells in ganglia has been recently been made aware [28, 37]. However, due

to the lack of a clear molecular signature of glial cell populations in the SCG, characterization of glial cells was not included in our previous study [Chapter 5]. In the current study, we performed snRNA-seq of healthy SCG and aimed to create a reference of the cellular composition and to identify the molecular characteristics of neuronal and satellite glial cells at healthy baseline, which can be further utilized for disease investigation.

We identified seven major cell types in the SCG, including 1). neuronal cells; 2). satellite glial cells; 3). Schwann cells; 4). endothelial cells; 5). smooth muscle cells; 6). fibroblast cells 7). stromal cells and 8). immune cells. The general cellular composition of SCG is similar to the composition of other sympathetic ganglia and sensory ganglia, however SCG display obvious differences especially in molecular signatures of neuronal cells and satellite glial cells.

Neurons in SCG. Furlan and colleagues have shown adrenergic, cholinergic and glutamatergic neurons in the mouse stellate ganglion [24]. However, only adrenergic neurons were detected in SCG, which indicates that the SCG biologically differs from the stellate ganglion. Of note, histological analysis of SCG did reveal cells with a cholinergic phenotype in the SCG [chapter 5]. In this regard, it is striking that we did not find these cells in our snRNA-seq data consistent with previous finding of no cholinergic neurons by single cell RNA sequencing [23]. A potential explanation might be: i) We used high throughput droplet-based 10X Genomics Chromium approach which has limited ability to detect especially low abundance transcripts [38]; ii) Previous studies, including ours, are mostly based on immune-histological staining of cholinergic markers (i.e. choline acetyltransferase), cross reaction with other proteins might happen. Studies including PCR or sequencing with Smartseq2 will be required for further exploration.

Our snRNA-seq analysis identified five distinct subtypes of adrenergic neurons in the SCG. Several noteworthy marker genes were found. Synaptosome Associated Protein 25 (*Snap25*) which is a presynaptic plasma membrane protein and plays an important role in the synaptic function in the neuronal system [26]. *Kcnq1* encodes a voltage-gated potassium channel, which regulates neuronal excitability and contributes to dysregulation of cardiac function in cases with genetic mutations [39, 40]. Among SCG neurons, cluster 1 neurons exhibited high expression of *Snap25* and *Kcnq1*, which might indicate that they are actively synaptic-coupled neurons in the SCG. Cluster 3 neurons showed high expression of *Dbh* which is required in adrenergic neurons to convert dopamine to neurotransmitter norepinephrine. This cluster of neurons also showed a high expression of Tyrosine hydroxylase (*Th*). Previous work showed that Th⁺ neurons are situated at the outer region of SCG as was observed with immunostaining [Chapter 5]. Moreover, we also found that this cluster of neurons have high expression of *Map1b* and *Stmn2* which are necessary for the stability of neuronal microtubules and normal axonal outgrowth and regeneration [41, 42]. Interestingly, cluster 0 and 4 neurons displayed

a high expression of Brain-type fatty acid-binding protein 7 (*Fabp7*). *Fabp7* is usually considered as a glial cell marker, however, it was also previously found in neural stem cells and brain neural precursors [43, 44]. This might suggest the existence of neural precursor cells in adult mouse SCG, although further investigation is needed to substantiate this.

Satellite glial cells in SCG. With snRNA-seq analysis, we detected four major subtypes of satellite glial cells in mouse SCG. To have a brief understanding of these satellite cells, we used glial cells of the CNS and sensory ganglia as guidance for our cell type characterization, since more is known about these CNS and sensory glial cells compared to sympathetic ganglia. Cluster 0 satellite cells exhibited a clearly distinct expression of the transcript factor *Junb*, interferon-inducible gene *Irf1* and antimicrobial gene *Cxc10*. GO analysis demonstrated their distinct enrichment in immune-responsive pathways, which endows the similarity functions of this cluster of glial cells to microglial cells in the CNS [45, 46]. Cluster 1 satellite glial cells, showing high expression of *Ptprz1* and *Ncam*, are enriched in the pathways involving ensheathment of neurons and axons. Astrocytes and oligodendrocytes are the glial cells in the CNS with an established function in supporting neurons by their ensheathment [47, 48]. The molecular and functional similarity between cluster 1 satellite glial cells and these CNS glial cells however needs further biological validation. Remarkably, cluster 2 glial cells expressed the lowest level of *Fabp7* and exclusively expressed neurotrophin binding receptor *Ntrk3* and *Ank3* (originally found at initial segment axons and nodes of Ranvier [49]). Combined with GO analysis, cluster 2 glial cells might thus be involved in stimulation by neurotrophin and supporting axon development. The molecular print of cluster 3 glial cells is currently unclear, although a high expression of *Dbi*, *Tuba1a* and *GM42418* was detected with snRNA-seq. Furthermore, our results reveal enrichment of gap junction *Gjc3*, instead of *Gja1* that is found in CNS and sensory ganglionic glial cells. SCG satellite glial cells also express purinergic ATP receptor *P2rx7* and nerve growth factor receptor *Ngfr*.

Sex differences in mouse SCG. Baleys and colleagues have previously reported sex differences of mouse sympathetic ganglia with bulk RNA-seq technology [35]. However, the analysis of total mRNA extracted from whole tissue may lead to the loss of information, especially of low-enriched cells. Furthermore, it carries a risk of inclusion data of cell types that are not related to the SCG due to imprecise SCG isolation, e.g. cells from the carotid artery or carotid body that lie in close proximity to the SCG. Our snRNA-seq data elucidates the advantages that even low enriched neurons and other cell types can be extracted and analyzed separately to avoid information bias. The current snRNA-seq analysis also revealed sex differences of the SCG as was found with bulk RNA-seq [35], however differences were mainly detected in satellite glial cells, and not in neuronal cells. Moreover, by performing snRNA-seq, we could outline the

distribution of the different cell types in the SCG and, to our knowledge, these results are the first showing sex differences in the SCG at the single nucleus level.

Sidedness of mouse SCG. Asymmetry in cardiac innervation is widely recognized and left and right stellate ganglia show a regionalized distribution of their area of coverage [3]. Therefore in the current study, a comparison of bilateral ganglia was performed to evaluate whether SCG show laterality differences at transcriptomic level. Results indicated only minor differences in a single cluster of satellite glial cells, but no noticeable differences of SCG with respect to cellular distribution. Although no obvious laterality differences were shown at healthy conditions, it would be of interest to evaluate whether cardiac injury would cause differential changes of gene expression and cellular distribution in SCG. We strive to take the influence of cardiac damage into account in our future studies.

In summary, snRNA-seq endowed us the ability to identify the cellular composition and molecular signature of murine SCG in the healthy state. Cellular heterogeneity and subtypes of neuronal cells and satellite glial cells were revealed in healthy mouse SCG, although further biological validation is mandatory. The data of the current study provides a reference baseline to further investigate SCG remodeling at single nucleus resolution, including sex-specific and bilaterality-specific responses to cardiovascular disease.

Limitations of the study

Sample size was limited due to a variety of factors. Subclustering of neurons was performed on a limited amount of cells in some of the subclusters. This can explain difficulties to properly characterize neuronal and glial cell subtypes based on cellular pathways, unique gene expression markers, and cellular composition. Histological and/or electrophysiological validation is necessary to elucidate the actual role of identified subtypes of neuronal cells and glial cells.

DISCLOSURES

The authors have nothing to disclose.

FUNDING

This work is supported by the Netherlands Organization for Scientific Research (NWO) [016.196.346 to M.R.M.J.].

ACKNOWLEDGEMENTS

We thank Conny van Munsteren (Department of Anatomy and Embryology, LUMC, Leiden, the Netherlands) for her help in the arrangement of experimental animals and tissue preparation. We thank Susan L. Kloet (Department of Human Genetics, LUMC, Leiden, the Netherlands) for her help in experimental design and useful discussions. We thank Emile J. de Meijer (Department of Human Genetics, LUMC, Leiden, the Netherlands) for the help with single-nucleus RNA isolation and library preparation for sequencing.

REFERENCES

1. McCorry, L.K., *Physiology of the autonomic nervous system*. Am J Pharm Educ, 2007. 71(4): p. 78.
2. Wink, J., et al., *Human adult cardiac autonomic innervation: Controversies in anatomical knowledge and relevance for cardiac neuromodulation*. Auton Neurosci, 2020. 227: p. 102674.
3. Zandstra, T.E., et al., *Asymmetry and Heterogeneity: Part and Parcel in Cardiac Autonomic Innervation and Function*. Frontiers in Physiology, 2021. 12(1569).
4. Manousiouthakis, E., et al., *Venous endothelin guides sympathetic innervation of the developing mouse heart*. Nat Commun, 2014. 5: p. 3918.
5. Stone, P.H., et al., *Prognostic significance of location and type of myocardial infarction: independent adverse outcome associated with anterior location*. J Am Coll Cardiol, 1988. 11(3): p. 453-63.
6. Li, C.Y. and Y.G. Li, *Cardiac Sympathetic Nerve Sprouting and Susceptibility to Ventricular Arrhythmias after Myocardial Infarction*. Cardiol Res Pract, 2015. 2015: p. 698368.
7. Oh, Y.S., et al., *Spatial distribution of nerve sprouting after myocardial infarction in mice*. Heart Rhythm, 2006. 3(6): p. 728-36.
8. Stefanidis, A., et al., *Insights into the neurochemical signature of the Innervation of Beige Fat*. Mol Metab, 2018. 11: p. 47-58.
9. Li, G., et al., *Co-expression changes of lncRNAs and mRNAs in the cervical sympathetic ganglia in diabetic cardiac autonomic neuropathic rats*. J Neurosci Res, 2017. 95(8): p. 1690-1699.
10. Carroll, S.L., et al., *Ganglion-specific patterns of diabetes-modulated gene expression are established in prevertebral and paravertebral sympathetic ganglia prior to the development of neuroaxonal dystrophy*. J Neuropathol Exp Neurol, 2004. 63(11): p. 1144-54.
11. Furlan, A., et al., *Visceral motor neuron diversity delineates a cellular basis for nipple- and pilo-erection muscle control*. Nat Neurosci, 2016. 19(10): p. 1331-40.
12. van Weperen, V.Y.H., et al., *Single-cell transcriptomic profiling of satellite glial cells in stellate ganglia reveals developmental and functional axial dynamics*. Glia, 2021. 69(5): p. 1281-1291.
13. Bayles, R.G., et al., *Sex differences in sympathetic gene expression and cardiac neurochemistry in Wistar Kyoto rats*. PLoS One, 2019. 14(6): p. e0218133.
14. Kwon, O.J., et al., *Morphological Spectra of Adult Human Stellate Ganglia: Implications for Thoracic Sympathetic Denervation*. Anat Rec (Hoboken), 2018. 301(7): p. 1244-1250.
15. Wang, F.B., et al., *Axons of Passage and Inputs to Superior Cervical Ganglion in Rat*. Anat Rec (Hoboken), 2018. 301(11): p. 1906-1916.
16. Meijborg, V.M.F., et al., *Stellate ganglion stimulation causes spatiotemporal changes in ventricular repolarization in pig*. Heart Rhythm, 2020. 17(5 Pt A): p. 795-803.
17. Zhou, W., et al., *Effect of stellate ganglia stimulation on global and regional left ventricular function as assessed by speckle tracking echocardiography*. Am J Physiol Heart Circ Physiol, 2013. 304(6): p. H840-7.

18. Stuart, T., et al., *Comprehensive Integration of Single-Cell Data*. Cell, 2019. 177(7): p. 1888-1902 e21.
19. Gervasi, N.M., et al., *The local expression and trafficking of tyrosine hydroxylase mRNA in the axons of sympathetic neurons*. Rna, 2016. 22(6): p. 883-95.
20. Finsch, M., et al., *Sox10 is required for Schwann cell identity and progression beyond the immature Schwann cell stage*. J Cell Biol, 2010. 189(4): p. 701-12.
21. Goncharov, N.V., et al., *Markers of Endothelial Cells in Normal and Pathological Conditions*. Biochemistry (Moscow), Supplement Series A: Membrane and Cell Biology, 2020. 14(3): p. 167-183.
22. Milewicz, D.M., et al., *Altered Smooth Muscle Cell Force Generation as a Driver of Thoracic Aortic Aneurysms and Dissections*. Arteriosclerosis, Thrombosis, and Vascular Biology, 2017. 37(1): p. 26-34.
23. Mapps, A.A., et al., *Diversity of satellite glia in sympathetic and sensory ganglia*. bioRxiv, 2021: p. 2021.05.25.445647.
24. Furlan, A., et al., *Visceral motor neuron diversity delineates a cellular basis for nipple- and pilo-erection muscle control*. Nature Neuroscience, 2016. 19(10): p. 1331-1340.
25. Ernsberger, U., et al., *The expression of dopamine beta-hydroxylase, tyrosine hydroxylase, and Phox2 transcription factors in sympathetic neurons: evidence for common regulation during noradrenergic induction and diverging regulation later in development*. Mech Dev, 2000. 92(2): p. 169-77.
26. Gibbins, I.L., et al., *Heterogeneous expression of SNAP-25 and synaptic vesicle proteins by central and peripheral inputs to sympathetic neurons*. J Comp Neurol, 2003. 459(1): p. 25-43.
27. Allen, N.J. and D.A. Lyons, *Glia as architects of central nervous system formation and function*. Science (New York, N.Y.), 2018. 362(6411): p. 181-185.
28. Hanani, M. and D.C. Spray, *Emerging importance of satellite glia in nervous system function and dysfunction*. Nature Reviews Neuroscience, 2020. 21(9): p. 485-498.
29. Ji, R.R., C.R. Donnelly, and M. Nedergaard, *Astrocytes in chronic pain and itch*. Nat Rev Neurosci, 2019. 20(11): p. 667-685.
30. Huang, T.-Y., V. Belzer, and M. Hanani, *Gap junctions in dorsal root ganglia: Possible contribution to visceral pain*. European Journal of Pain, 2010. 14(1): p. 49.e1-49.e11.
31. Hol, E.M. and M. Pekny, *Glial fibrillary acidic protein (GFAP) and the astrocyte intermediate filament system in diseases of the central nervous system*. Curr Opin Cell Biol, 2015. 32: p. 121-30.
32. Klein, S.L. and K.L. Flanagan, *Sex differences in immune responses*. Nature Reviews Immunology, 2016. 16(10): p. 626-638.
33. Mecklenburg, J., et al., *Transcriptomic sex differences in sensory neuronal populations of mice*. Scientific Reports, 2020. 10(1): p. 15278.
34. Lam, C.S.P., et al., *Sex differences in heart failure*. European Heart Journal, 2019. 40(47): p. 3859-3868c.
35. Bayles, R.G., et al., *Transcriptomic and neurochemical analysis of the stellate ganglia in mice highlights sex differences (vol 8, 8963, 2018)*. Scientific Reports, 2019. 9.
36. Bayles, R.G., et al., *Sex differences in sympathetic gene expression and cardiac neurochemistry in Wistar Kyoto rats*. Plos One, 2019. 14(6).
37. Blackburn, D., et al., *Astrocyte function and role in motor neuron disease: a future therapeutic target?* Glia, 2009. 57(12): p. 1251-64.
38. Wang, X., et al., *Direct Comparative Analyses of 10X Genomics Chromium and Smart-seq2*. Genomics, Proteomics & Bioinformatics, 2021.

39. Goldman, A.M., et al., *Arrhythmia in heart and brain: KCNQ1 mutations link epilepsy and sudden unexplained death*. Sci Transl Med, 2009. 1(2): p. 2ra6.
40. Liin, S.I., R. Barro-Soria, and H.P. Larsson, *The KCNQ1 channel - remarkable flexibility in gating allows for functional versatility*. The Journal of physiology, 2015. 593(12): p. 2605-2615.
41. González-Billault, C., et al., *A role of MAP1B in Reelin-dependent neuronal migration*. Cereb Cortex, 2005. 15(8): p. 1134-45.
42. Klim, J.R., et al., *ALS-implicated protein TDP-43 sustains levels of STMN2, a mediator of motor neuron growth and repair*. Nature Neuroscience, 2019. 22(2): p. 167-179.
43. Yun, S.-W., et al., *Neural stem cell specific fluorescent chemical probe binding to FABP7*. Proceedings of the National Academy of Sciences, 2012. 109(26): p. 10214-10217.
44. Gerstner, J.R., et al., *Brain fatty acid binding protein (Fabp7) is diurnally regulated in astrocytes and hippocampal granule cell precursors in adult rodent brain*. PLoS One, 2008. 3(2): p. e1631.
45. Butovsky, O. and H.L. Weiner, *Microglial signatures and their role in health and disease*. Nature Reviews Neuroscience, 2018. 19(10): p. 622-635.
46. Bachiller, S., et al., *Microglia in Neurological Diseases: A Road Map to Brain-Disease Dependent-Inflammatory Response*. Frontiers in Cellular Neuroscience, 2018. 12(488).
47. Allen, N.J. and C. Eroglu, *Cell Biology of Astrocyte-Synapse Interactions*. Neuron, 2017. 96(3): p. 697-708.
48. Hughes, A.N. and B. Appel, *Oligodendrocytes express synaptic proteins that modulate myelin sheath formation*. Nature Communications, 2019. 10(1): p. 4125.
49. Dzhashiashvili, Y., et al., *Nodes of Ranvier and axon initial segments are ankyrin G-dependent domains that assemble by distinct mechanisms*. J Cell Biol, 2007. 177(5): p. 857-70.

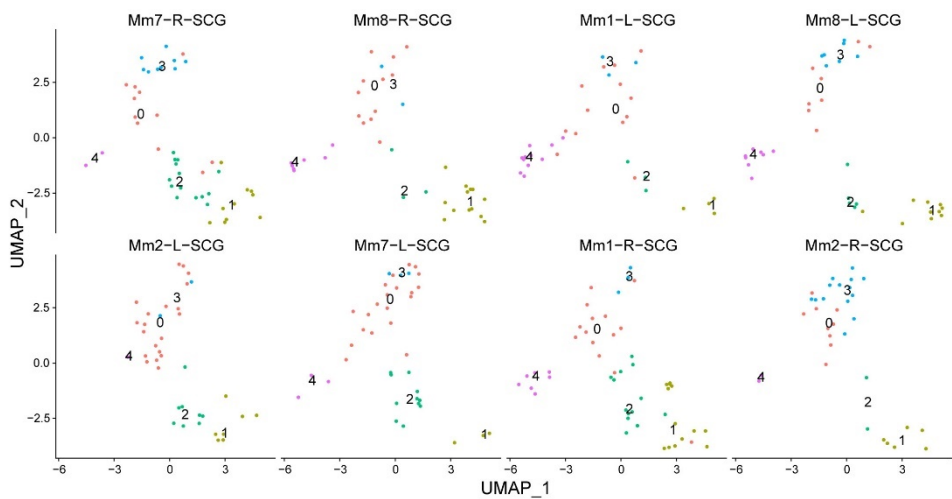
A

0 1 2 3 4 5 6 7 8 9 10 11

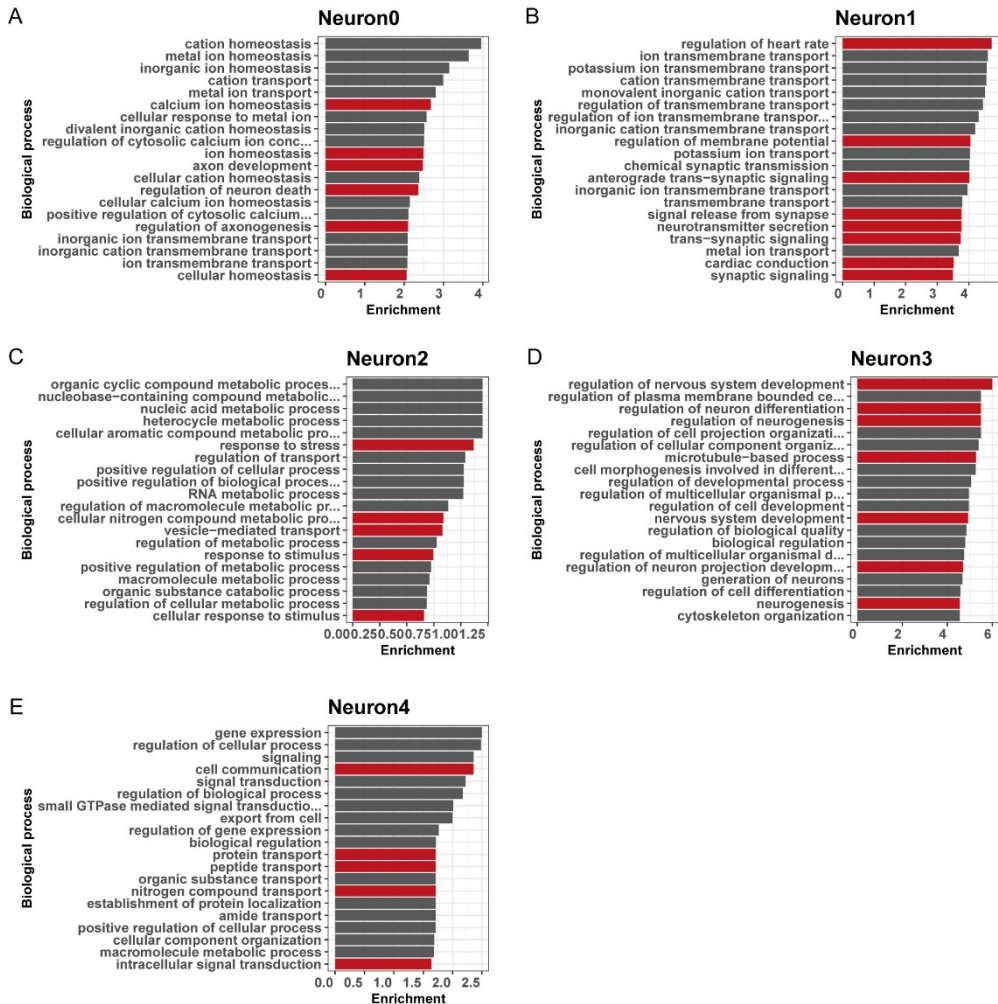
Jun
Zk338
Irf1
Gark69
Dnajb1
Acot1
4533424G08084
Densin4
Sv2c
Cdc10
Muc6d
Ptnpa1
Pncr1
Fabp7
Soc44
Tapan18
Cultr1
Lgr4
Gdnf
Omef42
Nrk3
Avk3
Scn7a
Kcnk1
Cadm2
Pnc
Emp1
Fgfr3
Mazn3
Irfap
Du
Agos
Cdc1
Cks
mt-Ccl
Ggn271
Cck4
Lip1b
Hatt2bc
Snecd
Lum
Ggpd
Gsc3
Csf1
Cnsp22
Dcn
Apod
H2
Gn
Ftr
Cyr1
Pecan1
Pthcn
Eng
Pab1
Mak4
Adams1
Pbrg
Selo
Cm1000
Cm1000
Gncd418
Sme2
Lip11
Ndg4
Map1b
Sld2
Alp1b
Lnc2
Nrg3
Pam15a
Fgf14
Serp11
Rfx1
Cnsp2
Kcnk4
Syn
Cnsp3
Mg2
Mg11
Abcc9
Acot1
Natk3
Ras
Pdk3
Pdk3
Pcl1
Cacna1c
Ighf3
Sncl
Sst2
Ighf2
Klf8
Cav1
Map
Tenn2
Pcn1
Cdk8
Rbm47
Mef12b
Mcl1
Pcl1
Cdk4
Alh15
H2-Eb1
Sclb
Lym
Dcp2
Pv
Cnsp3
Lnc3
Fmr2
Fmr2
Mpc
Mpc
Pmp22



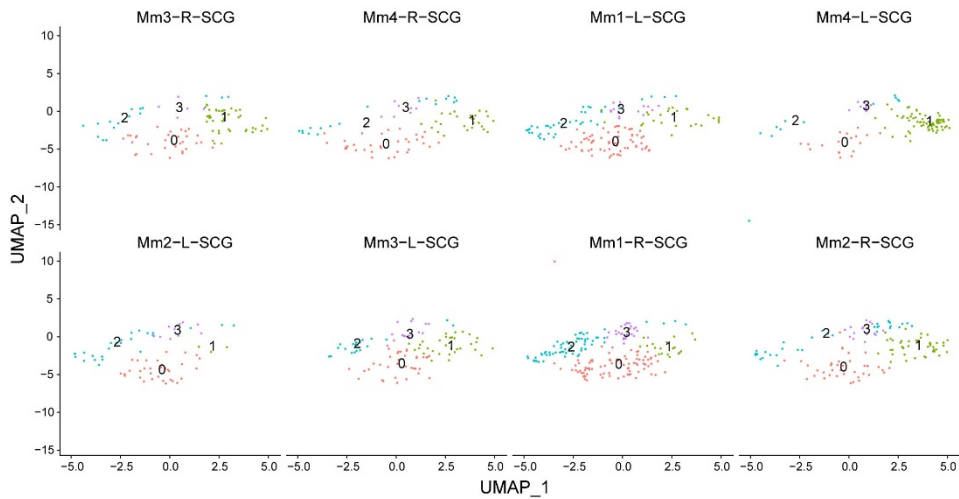
Supplemental Figure 1. Single nuclei clustering segregation and marker gene expression. A. Heatmap of top 10 DEGs of each cluster in mouse SCG showing the distinct gene expression patterns among clusters. B. UMAP showing expression of genes characteristic for major cell types in mouse SCG. Dashed lines indicate the boundaries of each cluster.



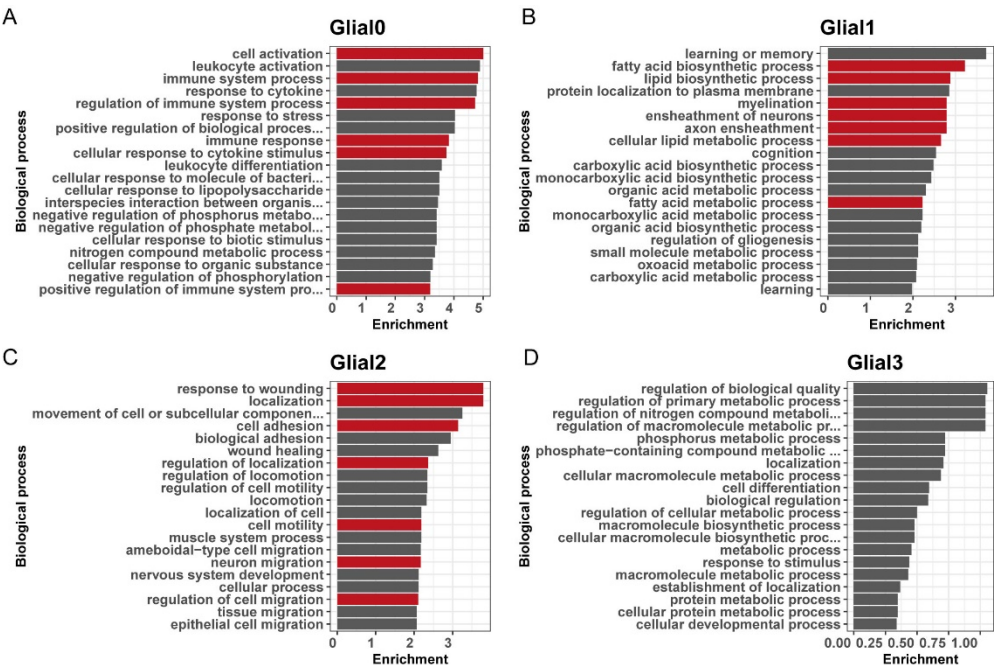
Supplemental Figure 2. UMAP plots of neuronal sub-clustering in eight individual samples.



Supplemental Figure 3. Glial cell subtype pathway identification. A-E. GO analysis of cellular subtypes (neuronal subcluster 0-4) in mouse SCG. Top 20 enriched biological process terms are shown.



Supplemental Figure 4. UMAP plots of satellite glial cell sub-clustering in eight individual samples.



Supplemental Figure 5. Glial cell subtype pathway identification. A-D. GO analysis of cellular subtypes (glial subcluster 0-3) in mouse SCG. Top 20 enriched biological process terms are shown.

Supplemental Table 1. DEGs of all clusters in mouse SCG

cluster	p_val	avg_log2FC	pct.1 (the specific cluster)	pct.2(the remaining clusters)	p_val_adj	gene
0	5,58E-251	1,155186	0,998	0,888	1,80E-246	Jun
0	8,96E-229	1,031058	0,997	0,863	2,89E-224	Junb
0	8,20E-223	0,990578	0,997	0,843	2,65E-218	Egr1
0	6,80E-221	0,959515	0,998	0,895	2,20E-216	Fos
0	1,14E-213	1,198485	0,937	0,572	3,67E-209	Zfp36
0	3,56E-203	1,146808	0,918	0,551	1,15E-198	Socs3
0	5,72E-193	1,229066	0,882	0,513	1,85E-188	Irf1
0	6,17E-182	1,123039	0,936	0,622	1,99E-177	Ccn1
0	8,22E-182	1,645215	0,78	0,42	2,65E-177	Gadd45g
0	3,55E-178	1,374782	0,883	0,562	1,15E-173	Dnajb1
0	2,74E-173	1,151691	0,875	0,532	8,86E-169	Phlda1
0	2,53E-170	1,124138	0,931	0,671	8,18E-166	Cebpd
0	2,98E-170	1,083206	0,89	0,553	9,61E-166	H2-Q4
0	7,98E-160	1,315184	0,66	0,282	2,57E-155	Acot1
0	7,39E-154	1,025383	0,924	0,699	2,38E-149	Jmjd1c
0	4,35E-147	0,937521	0,788	0,393	1,41E-142	Nop58
0	2,70E-144	1,025688	0,926	0,693	8,71E-140	Mt1
0	1,63E-142	0,997645	0,971	0,854	5,26E-138	Hspa1b
0	1,80E-137	0,722827	0,999	0,994	5,82E-133	Apoe
0	1,82E-136	0,87159	0,677	0,272	5,87E-132	Egr2
1	4,22E-198	1,105106	0,966	0,606	1,36E-193	Mboat2
1	1,02E-194	0,911269	0,995	0,863	3,29E-190	Scd2

1	1,22E-189	1,129088	0,967	0,633	3,94E-185	Pmepa1
1	6,19E-168	0,952881	0,973	0,661	2,00E-163	Lpar1
1	5,64E-158	1,0126	0,938	0,561	1,82E-153	Ptprz1
1	1,21E-154	0,829092	0,989	0,816	3,91E-150	Qk
1	6,49E-152	0,943986	0,876	0,46	2,09E-147	Mmd2
1	5,46E-140	0,909348	0,972	0,702	1,76E-135	Scd1
1	3,08E-139	1,107847	0,981	0,746	9,93E-135	Fabp7
1	1,26E-136	0,772041	0,995	0,821	4,08E-132	Abca8a
1	2,84E-134	1,064059	0,88	0,509	9,18E-130	Slc4a4
1	3,63E-134	0,871611	0,954	0,69	1,17E-129	Ptn
1	3,38E-132	0,944397	0,899	0,563	1,09E-127	Mapre2
1	1,64E-127	0,961361	0,818	0,44	5,31E-123	Tspan18
1	1,31E-126	1,003404	0,858	0,494	4,22E-122	Col28a1
1	3,71E-126	0,753898	0,996	0,9	1,20E-121	Dbi
1	4,25E-126	0,96837	0,901	0,544	1,37E-121	Lgr4
1	1,04E-125	0,848611	0,911	0,521	3,36E-121	Ttyh1
1	5,80E-124	0,744506	0,986	0,804	1,87E-119	Ncam1
1	4,80E-123	0,971833	0,743	0,342	1,55E-118	Grid1
2	1,08E-280	2,164069	0,521	0,065	3,48E-276	Ntrk3
2	2,10E-238	1,709265	0,943	0,693	6,77E-234	Ank3
2	1,94E-233	1,979247	0,867	0,495	6,27E-229	Scn7a
2	4,97E-185	1,687359	0,772	0,4	1,61E-180	Kcna1
2	1,16E-170	2,090916	0,82	0,519	3,76E-166	Cadm2
2	5,25E-139	1,210694	0,939	0,745	1,69E-134	Cdh19
2	3,66E-129	1,017289	0,973	0,808	1,18E-124	Nkain2

2	3,45E-126	1,634771	0,366	0,079	1,11E-121	Flnc
2	1,88E-122	1,221902	0,963	0,85	6,09E-118	Stard13
2	5,30E-122	1,6946	0,589	0,237	1,71E-117	Emp1
2	1,40E-118	0,968883	0,924	0,836	4,53E-114	Utrn
2	1,67E-114	1,54439	0,476	0,158	5,39E-110	Fgl2
2	6,16E-96	1,295345	0,71	0,461	1,99E-91	lqgap2
2	5,29E-90	1,051097	0,826	0,627	1,71E-85	Zfp536
2	1,50E-78	0,929312	0,902	0,781	4,85E-74	Zswim6
2	1,25E-74	1,119485	0,829	0,666	4,04E-70	Pcdh9
2	5,17E-73	1,161342	0,599	0,352	1,67E-68	Hbegf
2	2,28E-72	0,616814	0,983	0,932	7,35E-68	Dst
2	1,51E-69	0,968401	0,851	0,746	4,88E-65	Fosb
2	3,21E-69	0,747687	0,901	0,767	1,04E-64	Chl1
3	8,18E-62	0,969157	0,961	0,918	2,64E-57	Dbi
3	8,37E-50	0,962317	1	0,996	2,70E-45	Apoe
3	5,49E-36	0,428216	1	1	1,77E-31	Gm42418
3	1,59E-33	0,914624	0,886	0,789	5,12E-29	Fabp7
3	7,38E-33	0,562599	0,986	0,991	2,38E-28	Cmss1
3	3,66E-27	0,757622	0,878	0,868	1,18E-22	Cst3
3	8,72E-27	0,832419	0,8	0,799	2,81E-22	Ckb
3	5,53E-26	0,510104	0,992	0,996	1,78E-21	AY036118
3	1,47E-22	0,575833	0,869	0,898	4,76E-18	Fth1
3	5,09E-22	0,656334	0,811	0,817	1,64E-17	mt-Co1
3	2,34E-20	0,642612	0,839	0,89	7,56E-16	Tuba1a
3	1,81E-19	0,550096	0,892	0,913	5,86E-15	Tmsb4x

3	1,85E-19	0,625355	0,861	0,823	5,99E-15	Atp1a2
3	4,55E-19	0,765657	0,814	0,857	1,47E-14	mt-Co3
3	8,64E-19	0,563014	0,897	0,891	2,79E-14	Scd2
3	1,61E-18	0,478728	0,917	0,944	5,21E-14	Cd9
3	1,44E-16	0,693519	0,8	0,763	4,66E-12	Mt1
3	9,35E-16	0,564472	0,803	0,867	3,02E-11	Rplp1
3	3,10E-15	0,702077	0,719	0,712	1,00E-10	Fads2
3	7,55E-15	0,508344	0,919	0,972	2,44E-10	Ubb
4	0	4,726438	0,95	0,062	0	Smoc2
4	0	4,049333	0,882	0,044	0	Lum
4	0	3,909641	0,676	0,032	0	Gfpt2
4	0	3,691319	0,857	0,034	0	Gpc3
4	0	3,595781	0,803	0,03	0	Ebf2
4	0	3,335434	0,84	0,052	0	Crispld2
4	0	3,194692	0,803	0,066	0	Col1a1
4	0	3,146537	0,748	0,011	0	Egfr
4	0	3,12974	0,773	0,031	0	Inpp4b
4	0	2,977498	0,718	0,023	0	Ccl11
4	0	2,942344	0,739	0,047	0	Ror1
4	0	2,901629	0,668	0,009	0	Pdgfra
4	0	2,686553	0,714	0,048	0	Pid1
4	0	2,597557	0,731	0,044	0	Vit
4	0	2,375251	0,639	0,024	0	Tgfb1
4	0	2,256682	0,664	0,021	0	Bnc2
4	0	2,241282	0,571	0,01	0	Scara5

4	0	2,224234	0,538	0,017	0	Steap4
4	2,90E-300	2,343071	0,462	0,012	9,38E-296	Myoc
4	2,66E-299	2,839869	0,782	0,066	8,57E-295	Abi3bp
5	0	5,128264	0,995	0,039	0	Flt1
5	0	4,516822	0,946	0,026	0	Cyyr1
5	0	3,957327	0,955	0,05	0	Pecam1
5	0	3,600954	0,936	0,017	0	Prkch
5	0	3,593843	0,941	0,049	0	Eng
5	0	3,559848	0,886	0,022	0	Mecom
5	0	3,516593	0,842	0,012	0	Gm20663
5	0	3,404249	0,906	0,017	0	Adgrl4
5	0	3,376597	0,906	0,031	0	Ptpnb
5	0	3,371025	0,941	0,018	0	Adgrf5
5	0	3,123947	0,678	0,031	0	Slco2a1
5	0	3,120217	0,866	0,027	0	Emcn
5	0	3,082306	0,891	0,017	0	Cdh5
5	0	2,967538	0,743	0,04	0	Cxcl12
5	0	2,904818	0,842	0,015	0	Shank3
5	0	2,902043	0,891	0,021	0	Fli1
5	0	2,851468	0,886	0,039	0	Podxl
5	0	2,804952	0,866	0,019	0	Kdr
5	0	2,778672	0,847	0,042	0	Slfn5
5	0	2,626263	0,748	0,016	0	Cdh13
6	1,80E-116	4,918355	0,314	0,02	5,82E-112	Gm10801
6	1,19E-103	4,720511	0,298	0,021	3,84E-99	Gm10800

6	6,55E-62	2,022162	1	1	2,11E-57	Gm42418
6	3,53E-60	2,080351	0,859	0,458	1,14E-55	Stmn2
6	4,04E-58	1,861813	0,937	0,702	1,30E-53	Uchl1
6	2,56E-56	1,805287	0,869	0,51	8,28E-52	Prph
6	7,29E-56	1,762126	0,874	0,494	2,35E-51	Tubb3
6	8,63E-56	1,832048	0,665	0,231	2,79E-51	Ndrd4
6	1,17E-54	1,549535	0,476	0,112	3,78E-50	Pirt
6	1,75E-53	1,499952	0,995	0,996	5,66E-49	AY036118
6	3,94E-53	1,387789	1	0,99	1,27E-48	Cmss1
6	6,68E-51	1,471733	0,555	0,161	2,16E-46	Basp1
6	5,14E-50	1,898765	0,958	0,804	1,66E-45	Map1b
6	6,26E-50	2,153109	0,901	0,637	2,02E-45	Slc6a2
6	3,79E-49	1,757346	0,764	0,355	1,22E-44	Cyb561
6	6,61E-49	1,601678	0,518	0,147	2,13E-44	Rab3c
6	2,68E-48	1,743264	0,806	0,441	8,65E-44	Pcsk1n
6	2,00E-47	1,747337	0,707	0,297	6,47E-43	Syt4
6	3,83E-46	1,539747	0,775	0,382	1,24E-41	Syt1
6	1,74E-44	1,492519	0,607	0,218	5,62E-40	Bex2
7	0	2,77176	0,808	0,027	0	Gm26871
7	0	2,761974	0,856	0,041	0	Erc2
7	0	2,533693	0,784	0,023	0	9530059014Rik
7	0	2,507673	0,848	0,041	0	Gpr158
7	0	2,47224	0,872	0,038	0	Ptpn2
7	0	2,438466	0,728	0,018	0	C130073E24Rik
7	0	2,335411	0,792	0,025	0	Kcnb2

7	0	2,175881	0,712	0,024	0	Shisa9
7	0	2,109083	0,784	0,027	0	Hs3st5
7	0	1,786868	0,536	0,008	0	Gm20642
7	0	1,742581	0,48	0,004	0	Nrg3os
7	0	1,641719	0,448	0,004	0	Gm45321
7	0	1,266802	0,36	0,001	0	Gm2516
7	0	1,265201	0,456	0,004	0	4930587E11Rik
7	0	1,238337	0,464	0,004	0	Gm45323
7	3,67E-303	1,729972	0,496	0,008	1,19E-298	Gm13963
7	7,12E-303	0,973718	0,424	0,005	2,30E-298	Timp4
7	3,00E-297	2,71025	0,84	0,043	9,69E-293	Cacna2d3
7	8,54E-293	1,759724	0,688	0,025	2,76E-288	Srrm4
7	1,18E-290	3,025272	0,88	0,051	3,81E-286	Ryr2
8	0	3,496526	0,703	0,01	0	Myh11
8	0	3,311048	0,625	0,009	0	Abcc9
8	0	3,239672	0,672	0,011	0	Ano1
8	0	2,311215	0,547	0,003	0	Mrvi1
8	5,62E-230	1,452957	0,391	0,004	1,82E-225	Des
8	7,90E-228	1,821674	0,406	0,005	2,55E-223	Ndufa4l2
8	1,16E-220	3,388257	0,828	0,033	3,74E-216	Notch3
8	1,23E-213	5,259622	0,906	0,044	3,96E-209	Rgs5
8	2,19E-212	1,209482	0,328	0,003	7,08E-208	Aoc3
8	3,99E-206	3,037071	0,422	0,006	1,29E-201	Acta2
8	5,56E-182	1,804938	0,359	0,005	1,79E-177	Kcnj8
8	7,85E-158	2,013145	0,469	0,013	2,53E-153	Sdc1

8	5,26E-156	1,746464	0,406	0,009	1,70E-151	Cap2
8	2,99E-151	1,459359	0,328	0,005	9,65E-147	Angpt1
8	7,36E-146	2,165652	0,547	0,021	2,38E-141	Gm17276
8	1,21E-144	3,016445	0,5	0,017	3,90E-140	Cacnb2
8	1,89E-136	2,612237	0,406	0,011	6,10E-132	Trpc3
8	1,24E-126	2,076352	0,391	0,011	4,00E-122	Ngf
8	3,94E-118	2,922934	0,547	0,027	1,27E-113	Rgs6
8	1,08E-117	2,076446	0,391	0,012	3,49E-113	Lin7a
9	0	2,819295	0,739	0,008	0	Cldn1
9	0	2,32761	0,739	0,009	0	Ildr2
9	0	1,557562	0,522	0,002	0	Stra6
9	0	1,520011	0,435	0,001	0	Slc6a13
9	0	1,305872	0,413	0,001	0	Lypd2
9	2,90E-291	0,936488	0,304	0	9,36E-287	Mpzl2
9	7,49E-283	2,888788	0,826	0,016	2,42E-278	Thbs4
9	7,75E-268	2,057361	0,717	0,012	2,50E-263	Lbp
9	1,77E-186	1,566679	0,457	0,007	5,72E-182	Moxd1
9	8,75E-186	5,044909	0,978	0,044	2,82E-181	Bnc2
9	4,61E-177	3,223915	0,87	0,034	1,49E-172	Stxbp6
9	1,41E-173	2,595863	0,87	0,035	4,56E-169	Lmo7
9	4,30E-173	2,124606	0,674	0,019	1,39E-168	Mfap5
9	5,26E-170	5,045211	0,957	0,048	1,70E-165	Igfbp6
9	3,50E-155	1,376672	0,326	0,004	1,13E-150	Fbln1
9	2,49E-151	1,629242	0,435	0,008	8,05E-147	Col4a3
9	8,65E-145	2,665384	0,674	0,025	2,79E-140	Itgbl1

9	7,73E-144	1,00449	0,37	0,006	2,49E-139	Omd
9	2,88E-140	1,998228	0,587	0,018	9,30E-136	Cfh
9	4,19E-134	3,06093	0,826	0,044	1,35E-129	Klf5
10	0	3,929504	0,744	0,002	0	Cd86
10	0	3,673243	0,698	0,004	0	Rbm47
10	0	3,528198	0,767	0,001	0	Mir142hg
10	0	3,387477	0,512	0,001	0	Blnk
10	0	3,034705	0,605	0,002	0	Ptprc
10	0	2,63694	0,535	0,001	0	Nlrp3
10	0	2,383334	0,488	0,003	0	C1qa
10	0	2,296911	0,488	0,002	0	Spi1
10	0	2,158548	0,442	0,001	0	Lilrb4a
10	0	1,991559	0,419	0,001	0	C1qc
10	5,89E-300	2,353846	0,488	0,003	1,90E-295	C1qb
10	1,44E-299	2,007822	0,488	0,003	4,66E-295	Laptm5
10	3,71E-292	1,766681	0,326	0	1,20E-287	Gm30489
10	1,99E-291	2,892125	0,488	0,003	6,43E-287	Lyz2
10	5,17E-288	1,867723	0,302	0	1,67E-283	Lilr4b
10	7,56E-283	3,355917	0,605	0,007	2,44E-278	Pik3ap1
10	1,06E-274	1,768351	0,395	0,002	3,43E-270	Ikzf1
10	1,54E-268	1,481916	0,302	0	4,98E-264	Cd53
10	2,08E-268	2,543725	0,442	0,003	6,73E-264	Syk
10	8,17E-263	3,500216	0,535	0,005	2,64E-258	Mrc1
11	1,38E-214	2,541152	0,389	0,003	4,44E-210	Gldn
11	1,17E-200	2,619507	0,472	0,005	3,79E-196	Ncmap

11	2,38E-186	2,012751	0,333	0,002	7,68E-182	B230206H07Rik
11	5,67E-150	1,41521	0,278	0,002	1,83E-145	Cldn19
11	3,57E-114	1,542084	0,306	0,004	1,15E-109	Fa2h
11	4,12E-106	2,463933	0,611	0,023	1,33E-101	Bcas1
11	9,19E-92	2,233328	0,5	0,018	2,97E-87	Arhgap19
11	1,32E-88	2,889457	0,528	0,021	4,27E-84	Drp2
11	1,10E-74	1,840785	0,361	0,011	3,54E-70	Dusp15
11	2,74E-74	2,929182	0,639	0,038	8,85E-70	Stxbp6
11	2,94E-71	1,98468	0,306	0,008	9,50E-67	Emid1
11	1,01E-69	2,24402	0,444	0,019	3,27E-65	Ugt8a
11	8,61E-67	1,988055	0,333	0,01	2,78E-62	Plip
11	4,07E-60	2,711392	0,75	0,07	1,32E-55	Nfasc
11	3,21E-49	3,456207	0,778	0,098	1,03E-44	Prx
11	2,15E-47	4,567284	0,944	0,17	6,93E-43	Ctnna3
11	1,09E-46	1,990057	0,361	0,019	3,52E-42	Gm15541
11	2,89E-44	2,124599	0,333	0,017	9,32E-40	Mlip
11	9,10E-44	3,075827	0,667	0,075	2,94E-39	Lrrtm3
11	4,69E-40	2,329292	0,472	0,039	1,52E-35	Gm16168



8

GENERAL DISCUSSION

THE RELEVANCE OF THE SUPERIOR CERVICAL GANGLION FOR CARDIAC AUTONOMIC INNERVATION IN HEALTH AND DISEASE: SYSTEMATIC REVIEW - PART 1: MORPHOLOGICAL CONSIDERATIONS

Yang Ge^{1,2}, H. Sophia Chen^{1,2}, Jan Schoones³, Marco C. DeRuiter², Monique R.M. Jongbloed^{1,2}

1. Department of Anatomy & Embryology, Leiden University Medical Center, Einthovenweg 20, 2333 ZC Leiden, The Netherlands;
2. Department of Cardiology, Leiden University Medical Center, Albinusdreef 2, 2333 ZC Leiden, The Netherlands;
3. Walaeus library of the Leiden University Medical Center, Albinusdreef 2, 2333 ZC Leiden, The Netherlands

Adapted manuscript in preparation, with an additional discussion for this thesis

ABSTRACT

Cardiac autonomic innervation is of major importance for maintaining homeostasis, including the adaption to environmental conditions in healthy as well as in pathological states. The autonomic nervous system is divided in sympathetic and parasympathetic branches. Spinal branches of the sympathetic nervous system synapse in ganglia of the sympathetic chain, that is situated bilaterally in a paravertebral position. In humans and animal models, the heart receives cervical as well as thoracic sympathetic contributions. Bilateral cervical and thoracic ganglia, especially the stellate ganglia, are important components participating in cardiac sympathetic innervation. In disease states, such as cardiac ischemia, neuronal remodeling can occur, resulting in a sympathetic overdrive. In particular, the role of cardiac sympathetic hyperinnervation in arrhythmogenesis after myocardial infarction, has gained increasing attention over the past decades. The superior cervical ganglion is situated at the bifurcation of the common carotid arteries, that provides a relatively easily accessible anatomical landmark. This rather superficial position of the superior cervical ganglia, especially in comparison with the stellate ganglia, that are found at a deeper position within the thorax, likely facilitated the choice of these ganglia for many experimental studies on cardiac innervation in health and disease. However, the reports on the clinical relevance of contributions of cervical ganglia to cardiac innervation have been controversial, and these ganglia also contribute to the innervation of other structures in the head and neck, including the iris and submandibular gland. In this review, we aim to systematically investigate current evidence, as well as to expose current controversies, on the contribution of the superior cervical ganglia to cardiac innervation in health and disease in human and other animal models. This chapter encompasses part 1 of the review in preparation: Morphological data. In addition, a general discussion for this thesis is included.

INTRODUCTION

A balanced function of the cardiac autonomic nervous system is essential to maintain cardiovascular homeostasis. Cardiac innervation is provided by the autonomic nervous system, which is organised in sympathetic and parasympathetic branches. A balance between sympathetic and parasympathetic tone is mandatory to maintain a regular heartbeat. Parasympathetic innervation of the heart is provided by branches of the vagal nerve that synapse close to the target organ, i.e., in parasympathetic ganglia situated at the epicardial surface of the heart. For sympathetic innervation, preganglionic cardiac sympathetic axons synapse with postganglionic sympathetic neurons in the sympathetic chain (1). In contrast to nerve supply at the abdominal level, postganglionic axons towards the heart do not route via the gray ramus communicans and spinal nerve, but originate directly from the sympathetic chain ganglia. In humans, this innervation from the sympathetic chain is likely provided by both cervical and thoracic ganglia, although the exact level of ganglia contributing to the heart is still controversial (1).

Interest in cardiac autonomic innervation has increased in the past decades, as a myriad of studies have reported alteration in cardiac innervation, both morphologically as well as functionally, after cardiac damage. An especially intriguing phenomenon, is the so-called cardiac sympathetic hyperinnervation, that can occur after cardiac damage, such as myocardial infarction (2,3). This hyperinnervation is characterised by an increased amount of sympathetic nerve fibres in the area of damage and has been related to ventricular arrhythmias and sudden cardiac death after myocardial infarction (MI). Although several excellent mechanistic studies have been performed, to date the exact underlying relation between the occurrence of sympathetic hyperinnervation and ventricular arrhythmias after MI is still uncertain. Apparently sympathetic ganglia, which are renowned for their limited growth potential after birth, retrieve their potential for fast outgrowth after cardiac damage. These findings have prompted researchers in the field to study prerequisites for cardiac innervation in health and disease.

Although the stellate ganglion is generally accepted to provide the majority of cardiac innervation, also other ganglia have been proposed to provide their contributions in health and disease, including the thoracic and cervical ganglia (1,4). In addition, sidedness seems relevant in cardiac autonomic innervation (5), as well as the sex of the subject (6). In animal models, many studies have taken advantage of the relatively good accessibility of the superior cervical ganglion (SCG), that is located at a specific anatomical landmark location, at the bifurcation of the common carotid arteries (**Figure 1**).

In contrast, the stellate ganglia (consisting of the fused inferior cervical ganglion with the first thoracic ganglion) that are most renowned for their contribution to cardiac innervation, are located at a deeper location in the thorax, just below the subclavian artery at the level of the 7th cervical vertebra (**Figure 1**). Although cervical ganglia have indeed been shown to contribute to cardiac innervation both in animal models as well as in human, reports in literature differ (1), and these ganglia also contribute to innervation of other structures in the head and neck, including the iris, jaw, submandibular gland, the pineal gland and the carotid body (7–9). The SCG is in close spatial orientation with both the carotid body, a chemoreceptor sensitive organ that can respond to changes in blood O₂, CO₂ pH, and with the ganglion nodosum, the inferior ganglion of the vagal nerve (10,11).

As the SCG is used for studying cardiac innervation in a myriad of reports, including in our own studies (12), in this review, we aimed to systematically investigate current evidence, as well as to expose current controversies and gaps in knowledge, on the contribution of the SCG to cardiac innervation in health and disease in human and other animal models, considering potentially relevant aspects such as sex and sidedness.

MATERIALS AND METHODS

Research questions. Our research questions are defined as follows:

1. What is the morphological evidence that the SCG is involved in cardiac innervation in human and in other animal species, in health as well as in cardiac disease?
2. What is the functional evidence that the SCG is involved in cardiac innervation in human and in other animal species, in health as well as in cardiac disease?
3. Is sidedness relevant (i.e., using left or right sided SCG) to study cardiac innervation?
4. Have sex differences been studied and/or encountered?
5. Which controversies are encountered, and which questions are potentially unanswered by current data?
6. And finally, derived from these data: Is the use of the SCG in experimental setting an adequate structure to study cardiac innervation in health and disease?

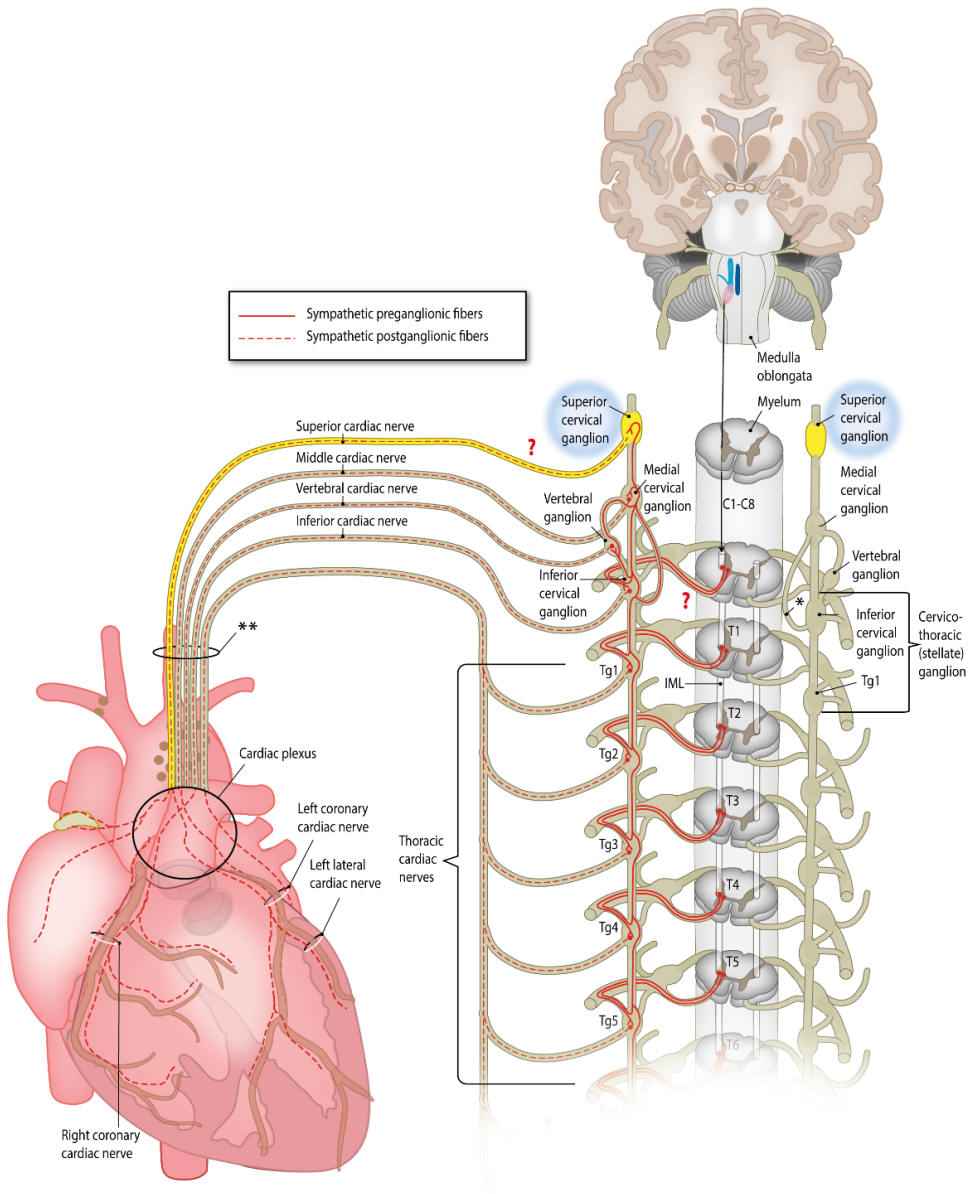
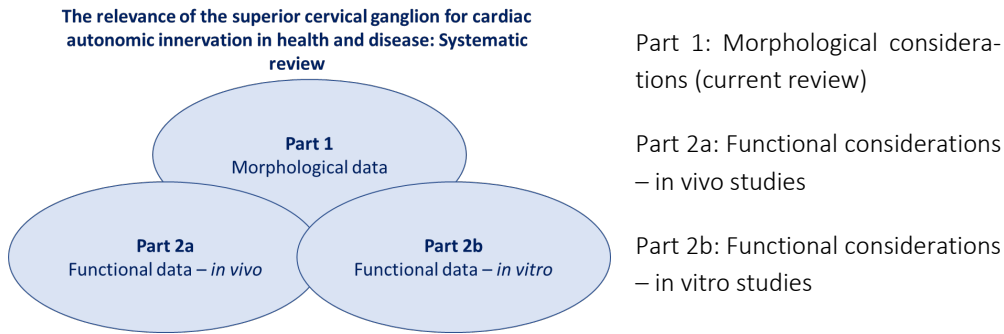


Figure 1: Anatomy of the cardiac sympathetic autonomic nervous system. The superior cervical ganglia are bilaterally indicated in bright yellow. (The figure is adapted from Wink et al. Auton Neurosci. 2020.)

We aim to provide the answer to these research questions in 3 parts:



Search strategy. The systematic review was performed based on the Preferred Reporting Items for Systematic Reviews and Meta Analyses (PRISMA) checklist (<http://prisma-statement.org/prismastatement/Checklist.aspx>), using the same workflow as in previous systematic reviews from our group (1,13,14). A comprehensive literature search was performed in PubMed, Embase, Web of Science, and Cochrane Library. The search strategy was carried out by using key words for “superior cervical ganglion” and “heart”, combined with “innervation” and “nerve growth factor”. Duplicate articles were removed. The complete query can be found in **Appendix A**.

Selection of articles. Inclusion: Papers were considered eligible to be included when there was a combination of SCG with morphological or functional data in original research papers. All articles published after 1975 were included. Both studies in health and in disease models were included, and all animal species including human. Both prenatal and postnatal studies were included. In vitro studies were also included (Part 2b), as long as an interdependent effect of SCG and myocardium or vice versa was studied. Relevant articles found in the references of papers included via the query, were also included, as long as they were original articles and published after 1975. Retrograde labeling studies were considered as morphological studies.

Exclusion: Studies in which the heart and SCG were studied independently, i.e., when no morphological or functional relationship was studied, were considered not eligible to answer our research questions and were therefore excluded. For example, when the effect of certain substances was studied independently on the heart and on the SCG, but no causal effect of the alterations in SCG on the heart or vice versa was described, the paper was excluded. In addition, we excluded papers that contained only information on the heart, only information on ganglia (without any relation to the heart), or papers describing other ganglia than the SCG (unless the SCG was described as well). Papers describing the SCG in relation to other organs than the heart were excluded. We included only original papers; therefore, reviews and book

chapters were excluded. Other reasons to exclude the paper were: non-English papers, papers that could not be retrieved after significant effort and papers that were from journals that were listed as predatory journal (<https://predatoryjournals.com/publishers/>). With regard to date of publication, we excluded studies that were published before 1975, partly because of the difficulties to retrieve several older papers.

Data extraction and appraisal. All abstracts were screened for eligibility by two independent observers (H.S.C. and M.R.M.J.) taking into account the selection criteria described above. In case of disagreement, differences between the observers' judgements were discussed to seek consensus.

After selection, all included papers were evaluated in light of the 5 research questions described above and categorised based on 1. Morphological data; 2. Functional data, in each section taking the following parameters into account data on species, disease model (health or disease), sidedness and sex.

Quality assessment. Quality assessment of included articles was performed with the Quality Appraisal for Cadaveric Studies (QUACS scale) for morphological studies (Part 1). The original QUACX score is composed of 13 parameters (15). As statistical analyses were not performed in any of the included studies with regard to the SCG, we omitted this parameter and based our score on and evaluation of the other 12 parameters, rendering a score of 12/12 (100%) the maximum score that could be obtained. If only part of the criteria for a specific parameter was met, 0.5 point (instead of 1 point) was assigned. For functional studies, the SYRCLE's risk of bias tool and CAMARADES 10-item quality checklist will be used (Part 2a, in preparation and not described in this thesis). The methodological quality of the included studies was first rated independently by two authors (H.S.C. and M.R.M.J.). After comparing and discussing the individual scores for each article, a consensus score was achieved for each of the 21 articles included in this review (**Table 2**).

RESULTS

1. Study selection.

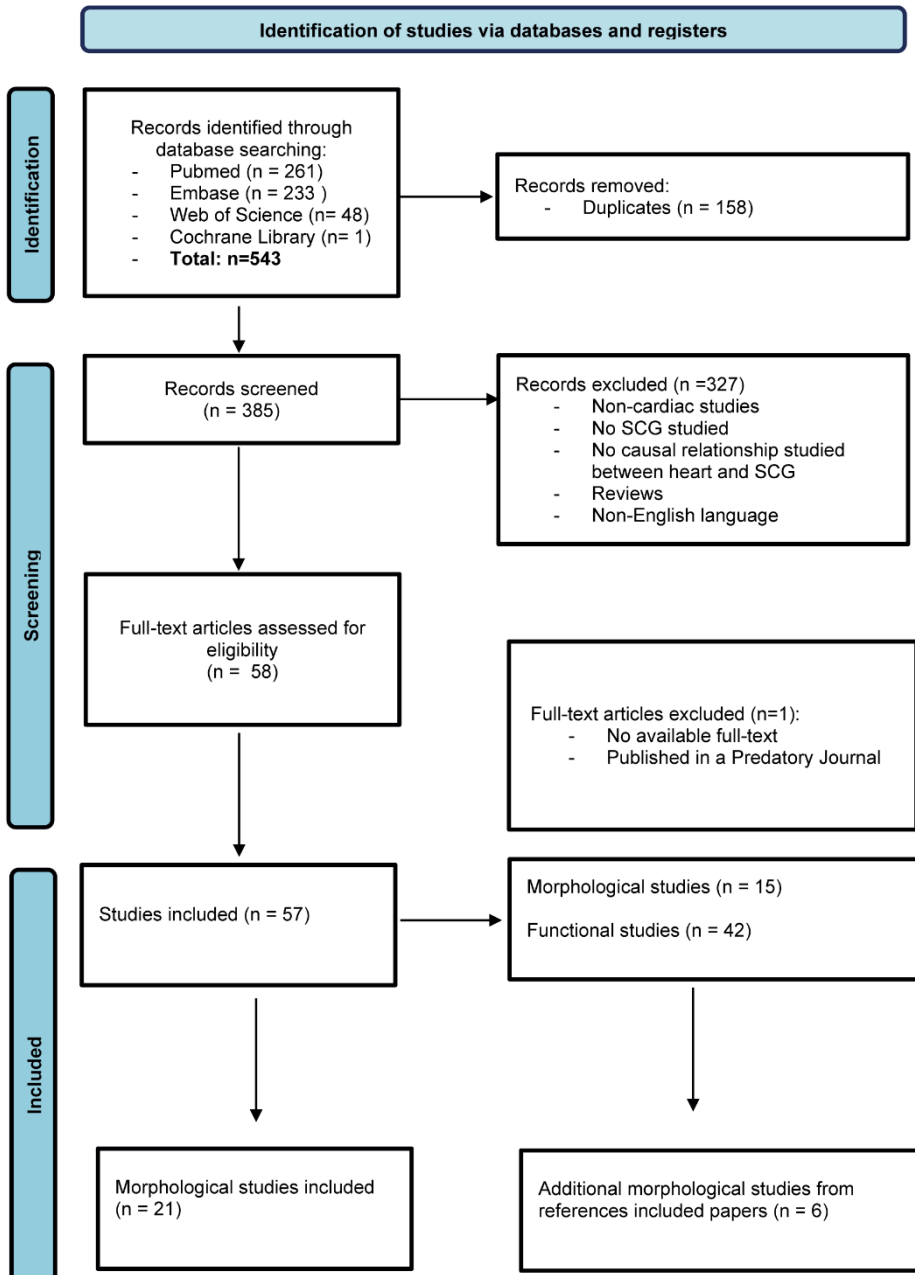
The search results and study selection flowchart are reported in **Flowchart 1**. From the initial **543** records identified through database searching and cited reference searching, **158** were duplicates and a total of **327** records were excluded because the studies did not meet our inclusion criteria, leaving **58** records available. One study was published in a predatory journal, leaving **57** studies considered eligible for inclusion in this review. Of these, **15** were morphological studies, and **42** were functional studies. As described above, the current review (Part 1) focusses on morphological papers. Next to the originally included **15** papers, we added **6** papers that fulfilled the inclusion criteria derived from screening references, leading to the **21** papers that were evaluated.

2. Overview of included studies.

Table 1 provides an overview of the 21 morphological studies included in part 1 of the systematic review. A total of 4 studies was performed in human, and 17 in other species: monkey (n=8), dog (n=3), cat (n=2), rat (n=1), shrew (n=1), chick (n=2). In one of the studies describing monkeys, also the primate Philippine Tarsier was included. No morphological studies were found in mice (*Mus musculus*). Two studies were performed in prenatal stages (17,18), both in chick, the remaining 19 papers concerned postnatal stages in mammals.

3. Quality assessment

Table 2 provides the quality assessment of the 21 included studies. Quality scores ranges from 46% to 67%. In the majority of morphological studies, a thorough description of results was presented, either with or without details on consistency of data with regard to number or percentages of cases in which observations were made. The far majority of studies adequately discussed findings in the context of contemporary evidence. Most studies adequately supported their description of data with photographs and/or drawings. The relatively low scores could be attributed largely to deficient data on education of dissecting researchers and on the number of observers, that was lacking in all of the included studies. In addition, distinctly indicated study limitations and clinical implications were lacking in the majority of the morphological manuscripts included. Approximately half of the included studies specified the sex of the specimen used (21,23,28,30,31,33–36).



Flowchart 1: PRISMA flow diagram (16).

Table 1: Results part 1: Included morphological papers

#	Author	Year	Species	Title paper	Original query or added from references
1	Kirby(17)	1980	Chick	<i>Developing innervation of the chick heart: a histofluorescence and light microscopy study of sympathetic innervation</i>	from references
2	Armour(20)	1981	Dog	<i>Localization of sympathetic postganglionic neurons of physiologically identified cardiac nerves in dog</i>	Original
3	Billman(21)	1982	Monkey	<i>A description of the upper thoracic autonomic nervous system in the rhesus monkey (Macaca Mulatta)</i>	Original
4	Hopkins(20)	1984	Dog	<i>Localization of sympathetic postganglionic and parasympathetic preganglionic neurons which innervate different regions of the dog heart</i>	Original
5	Shih(22)	1985	Cat	<i>Horseradish peroxidase localization of the sympathetic postganglionic neurons innervating the cat heart</i>	from references
6	Janes(23)	1986	Human	<i>Anatomy of human extrinsic cardiac nerves and ganglia</i>	Original
7	Wu(24)	1988	Cat	<i>Sympathetic postganglionic innervation of the cardiac coronary artery in cats</i>	from references
8	Pardini(25)	1989	Rat	<i>Organization of the sympathetic postganglionic innervation of the rat heart</i>	Original
9	Chuang(26)	1992	Monkey	<i>Localization of the sympathetic postganglionic neurons innervating cardiac coronary artery with horseradish peroxidase in monkeys</i>	from references
10	Hirakawa(27)	1993	Dog	<i>Sympathetic innervation of the young canine heart using antero- and retrograde axonal tracer methods</i>	Original
11	Verberne(18)	1999	Chick	<i>Contribution of the cervical sympathetic ganglia to the Innervation of the pharyngeal arch arteries and the heart in the chick embryo</i>	Original
12	Pather(28)	2003	Human	<i>The sympathetic contributions to the cardiac plexus</i>	Original
13	Chuang(29)	2004	Monkey	<i>Horseradish peroxidase localization of sympathetic postganglionic and parasympathetic preganglionic neurons innervating the monkey heart</i>	Original
14	Kawashima (1)(30)	2005	Human	<i>Topological changes of the human autonomic cardiac nervous system in individuals with a retroesophageal right subclavian artery: two case reports and a brief review</i>	Original
15	Kawashima (2)(31)	2005	Monkey	<i>Comparative anatomical Study of the autonomic cardiac nervous system in macaque monkeys</i>	Original

16	Kawashima (3)(32)	2005	Human	<i>The autonomic nervous system of the human heart with special reference to its origin, course, and peripheral distribution</i>	from references
17	Tanaka(33)	2007	Shrew	<i>Gross anatomical study of the sympathetic cardiac nerves in the house musk shrew (Suncus murinus)</i>	original
18	Kawashima(34)	2008	Monkey	<i>Systematic morphology and evolutionary anatomy of the autonomic cardiac nervous system in the lesser apes, gibbons (Hylobatidae)</i>	from references
19	Kawashima(35)	2009	Monkey	<i>Comparative anatomy and evolution of the cardiac innervation in new world monkeys (Platyrrhini, E. Geoffroy, 1812)</i>	original
20	Kawashima(36)	2011	Monkey	<i>Comparative morphological configuration of the cardiac nervous system in lorises and galagos (Infraorder Lorisiformes, Strepsirrhini, Primates) with evolutionary perspective</i>	original
21	Kawashima(37)	2013	Philippine Tarsier	<i>Evolutionary anatomy and phyletic implication of the extrinsic cardiac nervous system in the Philippine Tarsier (Tarsius syrichta, Primates) in comparisons with Strepsirrhines and New World Monkeys</i>	original

Table 2 Quality assessment of included papers

Study	Subjects				Methods				Limitations reported	QUACS score (%)
	<i>n</i> *	Species	Age (years)	Weight	Sex (M/F)	Type	Data on sidedness	Condition and setting		
Kirby et al (1980)	NR	Chick	4 days of incubation - 3 days after hatching	NR	NR	Histomorphology	Yes	Health: NR	NR	50
Armour et al (1981)	38	Dog	NR	12-20 kg	Either sex, number NR	Retrograde labeling Macromorphology	Yes	Health: NR Setting: Unilateral thoracotomy with identification of a cardiac nerve by measuring cardiovascular responses to stimulation, injection of 30% aqueous HRP into the nerve, re-anesthesia on the third postoperative day by overdose of	NR	63

									sodium pentobarbital, followed by fixation and removal of tissue							
Billman et al (1982)	10	Monkey	NR	NR	10/0	Macromorphology	Yes	Health: NR Setting: freshly killed or obtained no later than 24h post mortem	Fixation: No fixative used	NR	46					
Hopkins et al (1984)	27	Dog	NR	12-18 kg	Either sex, number NR	Retrograde labeling Macromorphology	Yes	Health: NR Setting: Unilateral thoracotomy with injection of 30% aqueous HRP or wheat germ agglutinin-HRP in a variety of regions of the heart, re-anesthesia on the third postoperative day by overdose of sodium pentobarbital, followed by fixation and removal of tissue	Fixation: perfusion with 1.0% paraformaldehyde, 1.25%glutaraldehyde in phosphate buffer (pH7.4), ganglia stored in 10% sucrose in phosphate buffer until processing Sections: Frozen sections, 40um Stain(ing): HRP and neutral red	Leakage of HRP from the injection site could have been picked up by thoracic neuronal elements other than those in the heart	67					
Shih et al (1985)	15	Cat	NR	2.0-4.0 kg	Either sex, number NR	Retrograde labeling Histomorphology	Yes	Health: NR Setting: Right thoracotomy with injection of 20% HRP in a variety of regions of the	Fixation:1.25% glutaraldehyde, 1% paraformaldehyde in 0.1M phosphate buffer (pH7.4), ganglia stored	NR	58					

Janes et al (1986)	23	Human	6-89	NR	15/8	Autopsy (n=10) and embalmed (n=13) cadavers Macromorphology y Histomorphology	Yes	heart, re- anesthesia after 72-96h with sodium pentobarbital followed by fixation and removal of tissue	in 10% sucrose- phosphate buffer Sections: Frozen sections, 40 um Stain(ing): HRP and neutral red	NR	67
Wu et al (1988)	28	Cat	NR	2.0-4.0 kg	Either sex, number NR	Retrograde labeling Histomorphology	Yes	Health: NR Setting: Unilateral thoracotomy with dissection of a variety of coronary arteries and enclosement with a silicone tubing impregnated with 40% HRP in 1% dimethyl sulfoxide solution, re-anesthesia 4 days	Fixation: 1.25% glutaraldehyde and 1% paraformaldehyde in 0.1M phosphate buffer (pH7.4), ganglia were stored in 10% sucrose- phosphate buffer Sections: Frozen sections, 40um Stain(ing): HRP and neutral red	NR	58

Pardini et al (1989)	69		Rat	NR	250-350 g	NR	Retrograde labeling Histomorphology	Yes	Health: NR Setting: Mid-sternal thoracotomy with injection of Diamidino Yellow into left or right ventricular free wall or surface of the heart, re-anesthesia 96-120 hours later followed by fixation and removal of tissue	Fixation: 10% buffered formalin Sections: Frozen sections, 20 um Stain(ing): no staining/Diamidino Yellow?	NR	54
Chuang et al (1992)	Monkey	Adult, exact age NR	4.0-7.0 kg	Either sex, number NR			Retrograde labeling Histomorphology	Yes	Health: NR Setting: Unilateral thoracotomy with dissection of a variety of coronary arteries and enclosement with a silicone tubing impregnated with 2mg HRP in 5ul 2% dimethyl sulfoxide solution, re-anesthesia after 84-96 hours with fixation and removal of tissue	Fixation: 1.25% glutaraldehyde plus 1% paraformaldehyde in 0.1M phosphate buffer (pH 7.4), ganglia were stored in 10% sucrose-phosphate buffer Sections: Frozen sections, 40 um Stain(ing): HRP	NR	67
Hirakawa et al	23	Dog	>2 months	2.5-3.5 kg	Either sex,		Retrograde labeling	Yes	Health: NR	Fixation: Perfusion with 2.5% formalin and 1%	NR	63

(1993)					number NR	Macromorphology y Histomorphology		Setting: Unilateral thoracotomy with injection of 3-4% wheat germ agglutinin HRP into various regions of the heart	glutaraldehyde, ganglia stored in 30% sucrose in phosphate buffer until processing Sections: Frozen sections, 50um Stain(ing): HRP and neutral red		
Verberne et al (1999)	24	Chick (n=3) and Quail (n=21)	Stage HH10-13	NR	NR	Histomorphology	No	Health: NR	Fixation: ethanol-acetic acid for 24-72hr Embedding: paraffin Sections: 5 um Staining: tyrosine hydroxylase and haematoxylin	NR	58
Pather et al (2003)	8 21	Human	18-55 <0	NR	4/4 11/10	Type cadavers NR Macromorphology y Histomorphology	Yes	Health: NR	Fixation: formalized (Solution NR) Embedding: paraffin Sections: 0.1um*** Stain(ing): hematoxylin and eosin	NR	58
Chuang et al (2004)	16	Monke y	Adult, exact age NR	4.0-8.0 kg	Either sex, number NR	Retrograde labeling Macromorphology y Histomorphology	Yes	Health: NR Setting: Unilateral thoracotomy with injection of HRP in a variety of regions of the heart, reanesthesia with sodium pentobarbital after 84-96 hours	Fixation: Perfusion with 1.25% glutaraldehyde and 1% paraformaldehyde in 0.1M phosphate buffer (pH7.4) and subsequently 10% sucrose in 0.1M phosphate buffer (pH 7.4), ganglia stored in 10% sucrose-phosphate buffer for 24 hours	NR	63

									aorta with 0.01M phosphate buffer (pH 7.2), followed by 4% paraformaldehyde and labeling of the blood vessels by injection of neoprene latex, fixation and removal of tissues									
Kawashima et al (2008)	10	Monkey	5 adults, 2 subadult, 3 infants, exact age NR	NR	8/2		Macromorphology	Yes	Health: NR	Fixation: 10% formaldehyde solution and/or preserved in 70% alcohol for more than 10 years	NR							
Kawashima et al (2009)	12	Monkey	7 adults, 1 juvenile, 2 subadult, exact age NR	NR	4/7 1 unknown		Macromorphology	Yes	Health: clearly abnormal heart, abnormal surrounding great vessels, and/or a heart position associated with a condition such as diaphragmatic hernia, thorax abnormality or pregnancy were excluded	Fixation: 10% formaldehyde solution and/or preserved in 70% for at least 3 years	NR							
Kawashima et al (2011)	7	Monkey	3 adults, 2 subadult, 2 infant, exact age NR	NR	3/4		Macromorphology	No**	Health: clearly abnormal heart, abnormal surrounding great vessels, and/or a	Fixation: 10% formaldehyde solution and/or preserved with 30-70% alcohol for at least 3 years	NR							

Kawashima et al (2013)	3	Monkey	adult, exact age NR	NR	NR	Macromorphology	Yes	heart position associated with a condition such as diaphragmatic hernia, thorax abnormality or pregnancy were excluded	Health: NR	Fixation: 10% formaldehyde solution and/or preserved in 70% alcohol for more than 10 years	NR	54
------------------------	---	--------	---------------------	----	----	-----------------	-----	--	------------	--	----	----

4. The relevance of the SCG for cardiac innervation: Morphological data

In many of the included studies, the evidence of morphological contributions of the SCG to cardiac innervation was not the primary objective of the study. In our analysis, we only included data that was specifically related to the SCG and/or superior cardiac nerve. **Table 3** outlines the primary objectives/aims of the included papers, and provides a summary of the main findings related to SCG contributions to cardiac sympathetic innervation. Findings are discussed below, per developmental stage (prenatal versus postnatal) and per species.

Table 3: Objectives and summary of main results of included studies

Study	Objective	Results
<i>Chick/Quail</i>		
	Kirby et al (1980)	No connections from SCG to the heart
<i>Shrew</i>	Verberne et al (1999)	No connection between the SCG and the heart
	Tanaka et al (2007)	The nerve originating from the SCG descended to reach the aortic arch and formed nerve plexuses after reaching the arterial pole supplying nerves to the ventral wall of the ventricle
<i>Rat</i>		3% of the labeled somata were found bilaterally in the SCG after injection of the left ventricular free wall 1% of the labeled somata were found bilaterally in the SCG after injection of the right ventricular free wall
<i>Cat</i>		No HRP-positive neurons where observed in the superior cervical ganglia after injections into the apex Occasionally labeled cells in the bilateral SCG after injection into the ventral wall of the RV Occasionally labeled cells in the bilateral SCG after injection into the dorsal wall of the LV Occasionally labeled cells in the right SCG after injection into the Sinoatrial nodal region No HRP-positive neurons where observed in the superior cervical ganglia after injections into pericardial sac Few cells in the SCG after application of HRP to the main trunk of the left coronaries

		To trace the innervation of the terminal branches of the coronary arteries	Occasionally some labeled cells in the SCG after application of HRP to the main trunk of the right coronaries Few cells in the LSCG, no neuron in the RSCG after HRP application to the terminal branch of the ventral descending vessel of the left coronary artery No neurons in the SCG after HRP application to the terminal branch of the dorsal descending vessel of the right coronary artery or pericardial sac
<i>Dog</i>			
	Armour et al (1981)	To determine the locations of the cells of origin of cardiac postganglionic sympathetic fibers	Occasional labeled neurons were located in the caudal regions of the ipsilateral superior cervical ganglion No labeled neurons were observed contralaterally No exclusive origin for any individual cardiac nerve
	Hopkins et al (1984)	To determine whether a topographical organization related to regions of the heart exists within cervicothoracic ganglia and whether specific regions of the heart with specific functions are innervated by neurons in specific locations in the ganglia	Innervation of a specific region of the heart does not arise from neurons in one locus of a ganglion. Very few sympathetic cardiac postganglionic neurons are found in the superior cervical ganglia.
	Hirakawa et al (1993)	To determine the origin of cardiac sympathetic postganglionic fibers and to demonstrate their distribution in the heart	A small number of labeled cells found in bilateral SCG after injection of tracers into various regions of the heart
<i>Monkey</i>			
	Billman et al (1982)	To present a detailed description of the cervical and upper thoracic ANS anatomy	No branches from the SCG to the heart
	Chuang et al (1992)	To study the postganglionic neurons innervating the cardiac coronary artery	After application of HRP to the main trunk of the left coronary artery 98.3% labeled neurons were localized in the SCG (the right SCG (57.4%) appeared to be more densely labeled than the left (44.6%)) After application of HRP to the main trunk of the right coronary artery 97.1% labeled neurons were found in the SCG (the right SCG (61%) appeared more densely labeled than the left (36%)) After application of HRP to the terminal branch of the ventral descending vessel of the left coronary artery 62.6% labeled neurons were observed in the right and 36.1% in the left SCG After application of HRP to the terminal branch of the dorsal descending vessel of the left coronary artery, 96.2% labeled neurons were found in the SCG on both sides (the left SCG (54.6%) appeared more densely labeled than the right (41.6%))

				There were no HRP-labeled neurons in the SCG after application to the internal surface of the pericardial sac
	Chuang et al (2004)		To investigate the autonomic neurons innervating the heart	Sympathetic postganglionic neurons innervating the heart are located predominantly in the superior cervical ganglion
	Kawashima (2) et al (2005)		To clarify the general morphology of the autonomic cardiac nervous system	The superior cardiac nerve originating from the superior cervical ganglion is usually absent
	Kawashima et al (2008)		To study when the vertebral ganglion consistently appears in primate evolution To study how the composition of the cervicothoracic ganglion is associated with primate evolution To study when the middle cervical ganglia (MCG) developed the communicating branches with the spinal cervical nerves To study when the superior cardiac nerve originating from the SCG and thoracic cardiac nerve appear consistently	The superior cardiac nerve originated from the SCG in 65% (4 rights, 9 left) The superior cardiac nerve originated from the sympathetic trunk in 50% (5 right, 5 left)
	Kawashima et al (2009)		To report on the anatomy of the autonomic cardiac nervous system	SCG is consistently present The superior cardiac nerve never originated from the SCG, but from the sympathetic trunk between the SCG and MCG in 41.7%
	Kawashima et al (2011)		To describe the detailed systematic morphology of the autonomic cardiac nervous system To update and provide additional information on the surrounding nervous system To examine the intraspecific and interspecific variation in the autonomic nervous system To determine whether family-dependent morphology exists To examine the relationship between the autonomic cardiac nervous system and its surrounding structures To consider the common morphology from an evolutionary perspective within the lineage	SCG is consistently present The superior cardiac nerve never originated from the SCG, but from the sympathetic trunk between the SCG and MCG in 21.4%
	Kawashima et al (2013)		To elucidate the general morphology of and variations in the extrinsic cardiac nervous system To test the hypothesis that the morphology of the cardiac innervation is a conservative structure preserving its phylogeny	No cardiac nerves arising from the SCG

		To consider whether the tarsier's morphology is more similar to that of the strepsirrhini or new world monkeys To update and provide additional information on the relationship between the neglected cardiac nervous system and its surrounding structures		
<i>Human</i>				
	Janes et al (1986)	To describe the anatomy of the extrinsic cardiac nerves and ganglia	No cardiopulmonary nerves arising from the SCG	
	Pather et al (2003)	To determine the cervical and thoracic sympathetic contributions to the cardiac plexus	100% incidence of SCG in both fetal and adult cases All sympathetic contributions from the cervical sympathetic trunks were found to arborize directly in the deep cardiac plexus	
	Kawashima (1) et al (2005)	To investigate the topological changes of the human autonomic cardiac nervous system in retroesophageal right subclavian artery (a branchial arterial anomaly) compared to the normal autonomic cardiac nervous system	Case 1: the superior cardiac nerves arising from both the SCG and sympathetic trunk between SCG and MCG were observed on the right side, not on the left side Case 2: the superior cardiac nerves arising from the SCG and sympathetic trunk between SCG and MCG were observed on both sides	
	Kawashima (3) et al (2005)	To clarify the detailed morphology of the entire autonomic cardiac nerves, including both sympathetic and parasympathetic nerves	The SCG was observed in all cases The superior cardiac nerve originating from the SCG was observed in 88.9% (15 right, 17 left) The superior cardiac nerve originating from the sympathetic trunk between the SCG and MCG was observed in 69.4% (11 right, 14 left)	

Prenatal studies.

Both prenatal studies that were included, were performed in chick. In the study of Kirby et al., aimed at studying the developing sympathetic innervation in the chick with regard to postnatal innervation, histomorphological techniques (catecholamine histofluorescence and silver preparations) were used. The authors report that all nerve branches from the superior cervical ganglia were directed cranially along the carotid arteries. No fluorescent postganglionic fibres could be traced directly from the SCG to the heart, nor accompanying the vagal nerves through the chick neck (17). In the study of Verberne et al. it was hypothesized that the cervical ganglia might contribute to cardiac sympathetic innervation. Both histo-morphological techniques (thyroxin hydroxylase (TH), marker for sympathetic nerve tissue; and HNK1, marker for migrating neural crest and nerve tissue) and heterospecific transplantation using quail chick-chimeras (visualisation of quail cells in chick with the quail nuclear antibody QCPN) were used to study specifically the contribution of the chick cervical sympathetic ganglia to the developing heart and great arteries. Of note, in the chick heart, sympathetic innervation is derived from the sympathetic neural crest (i.e. *trunk* neural crest arising from somite 1-20) (18). In this study both trunk neural crest chimeras and cardiac neural crest chimera were made. The chick cervical sympathetic chain consists of 14 sympathetic ganglia, and the authors showed that the sympathetic neural crest gives rise to cervical ganglia 4-14 in chick, as well as to carotid paraganglia. Tracing of cells of cardiac neural crest chimeras, showed QCPN positive cells in satellite cells of the SCG, however neuronal somata were negative. Three levels in the cervical sympathetic trunk (superior, middle and inferior) were observed to contribute TH⁺ nerve fibres to the heart. The authors report that the SCG contributes to the carotid nerve (18). The carotid nerve, or carotid sinus nerve, is known as a branch of the glossopharyngeal nerve, involved in innervation of the carotid sinus and carotid body (38). Remarkably, Verberne et al. describe the *carotid nerve* as a thyroxin hydroxylase positive nerve, while the vagus and glossopharyngeal nerves are TH negative. The TH⁺ carotid nerve along its course joined the parasympathetic nodose ganglion, via which it contributed to nerve fibres in cardiac vagal branches that enter the heart via both the arterial and venous poles (18). The carotid nerve also contributed to nerve fibres that were connected to the developing baro-and chemoreceptors in the outflow tract of the heart, thus suggesting a role of the SCG in sensory afferent innervation (18). No evidence for an contribution to sympathetic innervation was presented.

Postnatal studies.

Morphological data on SCG in relation to cardiac innervation in human. A total of 4 human studies were included, 3 in healthy subjects (23,28,32) and 1 in subjects with an aberrant right subclavian artery (30).

The position of the SCG in human is described behind the bifurcation of the common carotid artery and between the first to third cervical vertebrae (4). Nerve branches can originate from the SCG. In our previous papers, we have used the nomenclature as proposed by Kawashima who describes cardiac nerves as nerves connecting to the heart either “with direct connections or connections via the cardiac plexus” (1,5,32). The superior cardiac nerve is described as arising from the SCG and from the sympathetic trunk between the superior and middle cervical ganglia (4), and in its course usually follows the common carotid arteries. The cardiac plexus receives contributions from cardiac nerves and branches (30).

As previously observed, data in human on morphological observations of contributions of the SCG in humans is controversial (1). In 1986, Janes reported that no cardiopulmonary nerves were observed to originate from the SCG (23). In contrast, in 2003 Pather, based on data derived from 21 fetuses and 8 adults, reported the presence of the SCG in all specimen. The superior cardiac nerve (also present in all specimen examined) was reported to arise from the SCG in 53% of cases (31/58 sides, from which 16/29 on the right side and 15/29 on the left side) (28). All sympathetic contributions from the cervical sympathetic trunks were found to branch directly into the deep cardiac plexus. In line with this are the reports from Kawashima in 2005, where the SCG was also observed in all cases (32). It was found that the SCG communicates with spinal level C1-C3, and the SCG showed communicating branches with the spinal nerves on all sides. A superior cardiac nerve originating from the SCG was observed on 32/36 sides (88.9%: 15 right sides, 17 left sides). The superior cardiac nerve originated from the sympathetic trunk between the superior and the middle cervical ganglia on 25 sides (69.4%; 11 right sides, 14 left sides). Of note, in three right sides the superior cardiac nerve did not originate from the SCG or the cervical sympathetic trunk between the superior and the middle cervical ganglia. Therefore, although an apparent difference between the right and left sides was not observed, the frequency of the right superior cardiac nerve might be slightly less than the left. It was also reported that the SCG and stellate ganglia were consistent in size, position and communicating branches, whereas middle cervical and vertebral ganglia were variable (32). In 2 human cases with an aberrant right subclavian artery the superior cardiac nerve was also found to arise from the SCG. In the first case, a superior cardiac nerves arising from both the SCG and sympathetic trunk between SCG and MCG was observed on the right side, but not on the left side. In the second case, the superior cardiac nerves arising from the SCG and sympathetic trunk between SCG and MCG were observed on both sides (30).

Morphological data on SCG in relation to cardiac innervation in monkey. A total of 8 studies in different species of monkeys were included: one paper in the Rhesus Monkey (*Macaca Mulatta*) (21), one in Taiwan monkey (29), one in Macaque Monkey (31), one in the Gibbons (*Hylobatidae*) (34), in New World Monkeys (*Platyrrhini*) (35), Lorises and Galagos (36), in the Philippine Tarsier of the *Tarsiidae* family (37) and in one study the species of the monkey was not specified (26).

In 1982, Billman et al. described the position of the SCG in the monkey medial to the nodose ganglion, and dorsal to the carotid sinus area (21). Conform the situation described in mouse, a connection was observed between the SCG and the nodose ganglion (11). It was described in this study in the rhesus monkey that the carotid sinus receives nerves from the ipsilateral SCG as well as from the glossopharyngeal nerves, that are likely respectively efferent and afferent fibers (21). No direct sympathetic branches from the SCG to the heart were observed. Studies using retrograde labeling with horseradish peroxidase (HRP), however, supported nerve connections between the SCG and the heart (26). In 1992, Chuan et al. studied the localization of sympathetic postganglionic neurons innervating the coronary arteries, by injection of HRP to the proximal part of the right coronary artery (RCA) and left coronary artery (LCA), as well as to the distal branches of the ventral and dorsal descending arteries of the RCA and LCA. After sacrificing the animals, the paravertebral ganglia including the SCG were examined. Results show that after application of HRP in the proximal part of the RCA, and the proximal and distal part of the LCA, HRP positive cells could be localized mainly in the right SCG, and next in the left SCG. After HRP injection in the distal branches of the dorsal descending vessels of the RCA, labeled cells could be found mainly in the left SCG and next in the right SCG (26). In 2004, Chuang et al. examined several autonomic ganglia, including the SCG after injections of HRP in the subepicardial and myocardial layers in different cardiac regions. After injection in most locations, labeled cells could be found in the SCG, with exception of the posterior upper part of the left ventricle. Specifically, results showed that after injection of HRP in the cardiac apex, the region of the sino-atrial node, and in the right ventricle, HRP labeled sympathetic neurons were found only in the right SCG in 64.8% and in the left SCG in 35%. Also HRP injection in the left ventricle, lead to tracing of the labeled sympathetic cells mainly in the left SCG (51%) or right SCG (38.6%) (29). Between 2005 and 2013, 5 studies in monkeys were performed by Kawashima et al. in a variety of monkey species, that met the inclusion criteria of our review. As summarised in **Table 4**, several monkey interspecies-differences, a.o. regarding the presence of the superior cardiac nerve, were noted. For instance, a superior cardiac nerve arising from the SCG was absent in Rhesus monkeys (21), however could consistently be observed in New World Monkeys (35). An evolutionary summary figure based on several landmark studies in different monkey species, is provided in **Figure 2**.

Table 4: Evolutionary differences between different monkey species

Billman et al (1982)	Rhesus Monkeys	No branches from the SCG to the heart
Chuang et al (1992)	Monkeys, not specified	Labeling of the left coronary artery stem: → 98.3% labeled neurons localized in the SCG Labeling of the right coronary artery → 97.1% labeled neurons localized in the SCG No labeled neurons in the SCG after application to the internal surface of the pericardial sac
Chuang et al (2004)	Taiwan Monkeys	Sympathetic postganglionic neurons innervating the heart are located predominantly in the superior cervical ganglion
Kawashima (2) et al (2005)	Macaque Monkeys	The superior cardiac nerve originating from the superior cervical ganglion is usually absent
Kawashima et al (2008)	Lesser Apes, Gibbons	The superior cardiac nerve originated from the SCG in 65% (4 rights, 9 left) The superior cardiac nerve originated from the sympathetic trunk in 50% (5 right, 5 left)
Kawashima et al (2009)	New World Monkeys (Platyrrhini)	SCG is consistently present The superior cardiac nerve never originated from the SCG, but from the sympathetic trunk between the SCG and MCG in 41.7%
Kawashima et al (2011)	Lorises and Galagos	SCG is consistently present The superior cardiac nerve never originated from the SCG, but from the sympathetic trunk between the SCG and MCG in 21.4%
Kawashima et al (2013)	Philippine Tarsier (Comparisons With Strepsirrhines and New World Monkeys)	No cardiac nerves arising from the SCG

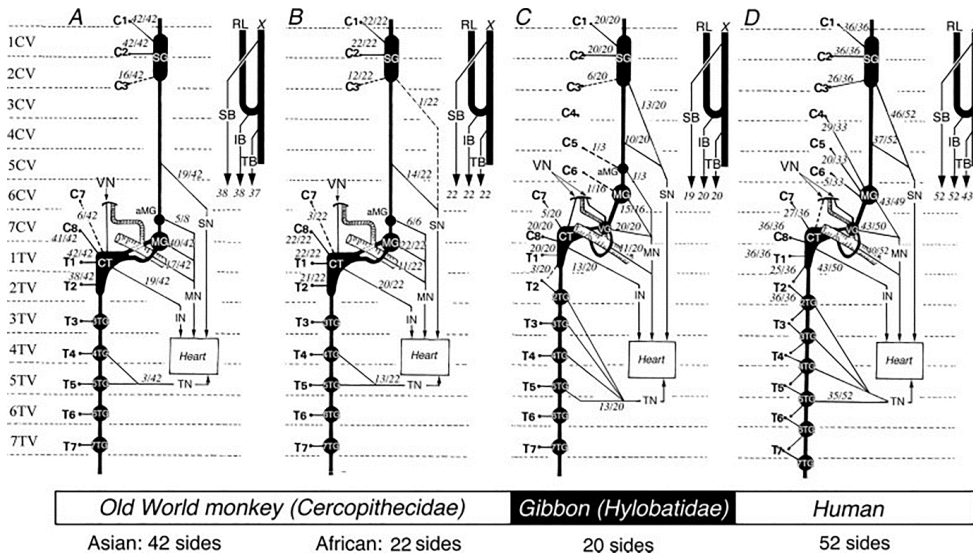


Figure 2: Evolutionary overview of cardiac sympathetic innervation. SG: Superior cervical ganglion. Source: Derived with the permission from Kawashima et al. Anat Rec. 2008 (Copyright Clearance Center 2021). The Figure represents a summary of data derived from studies in different monkey species.

Morphological data on SCG in relation to cardiac innervation in dogs. We included 3 studies in dogs (20,27,39). In all studies, retrograde labeling was performed, as well as micromorphology and/or histomorphology. In 1981, Armour et al. labeled cardiac nerves in dogs with HRP based on physiological identification, and found only sporadically retrogradely labeled neurons in the caudal pole of the ipsilateral SCG. No labeled neurons were observed on the contralateral side. Of note, in more than half of the SCG, no retrogradely labeled neurons could be traced back after injection of HRP into the cardiac nerves (39). In 1984, Hopkins et al. found corresponding data in dogs, with only very few sympathetic cardiac postganglionic neurons that could be traced back after HRP injection in the heart, intraventricular cavity, pericardial sac and aortic arch (20). Hirakawa et al, in 1993 reported similar findings after injecting HRP in various regions in the dog heart, with only a small number of labeled cells traced back into the bilateral SCG (27). After injections into the sino-atrial node, labeled cells could be traced back bilaterally in several ganglia, including the SCG (27). This was also the case after injection into the right or left atrium, although only few cells were observed in comparison to the other ganglia examined. No cells could be traced back into the left SCG after injection of HRP into the wall of the right ventricle (27).

Morphological data on SCG in relation to cardiac innervation in cats. We included 2 studies in cats (22,24). In all studies, retrograde labeling was performed, as well as micromorphology and/or histomorphology. Data in the cat show similar results as in dogs, with no or only very few cells that could be traced back into the SCG after injections of HRP into the heart (summarised in **Table 3**) (22,24)

Morphological data on SCG in relation to cardiac innervation in rat. In 1989, Pardini et al. described the organization of cardiac sympathetic innervation in rat, using both histomorphology and retrograde labeling with Diamidino Yellow injections into the right and left ventricle (25). Results show that labeled cells could be traced back bilaterally in an area ranging from the SCG until the 6th thoracic ganglion. However, only a small minority of cells of traced cells were found bilaterally in the SCG after injection of the left ventricular and right ventricular free wall (3% and 1% respectively).

Morphological data on SCG in relation to cardiac innervation in shrew. In shrew, Tanaka et al. found, based on macromorphological studies, that the nerve originating from the left SCG descended to reach the aortic arch and formed nerve plexuses after reaching the arterial pole, supplying nerves to the ventral wall of the ventricle (33).

No studies providing morphological data on morphological contributions of the SCG in mouse were included.

DISCUSSION

In this systematic review, we assessed the existing literature on the morphological relevance of the superior cervical ganglion for cardiac innervation in health and disease stages. Key findings are 1. The superior cervical ganglion could be identified in all species examined; 2. Morphological evidence of a contribution of the SCG to cardiac innervation differs between species and even within species, such as evidence in monkeys; 3. A superior cardiac nerve innervating the heart could be found in the majority of human studies; 4. In the majority of retrograde labeling tracing studies, labeled cells could be found in the SCG after injections in the heart, however these cells formed a minority of cells as compared to contributions of other (cervical/thoracic/cervicothoracic) ganglia; 5. Functional studies will be needed to point out the functional consequences of these cells for cardiac sympathetic innervation.

Of note, although many experimental function studies are performed in mouse and rat, only 1 morphological study was found in rat, but none in the mouse (*Mus musculus*). Remarkably, in mice it has been shown that ganglionectomy of the SCG before MI leads to an almost entire loss of myocardial sympathetic innervation of the left ventricular anterior wall, in addition to a significantly reduction in chronic consequences of MI, such as myocardial inflammation, myocyte hypertrophy, and overall cardiac dysfunction (40).

Our query provided studies concerning both prenatal and postnatal stages. Prenatal SCG have the advantage that they are more prone to sprout during co-culturing *in vitro* than postnatal ganglia, at least in control (“healthy”) settings. The embryological origin of the cervical sympathetic chain ganglia is still debated. Based on the observation that cellular clusters will expand from the thoracic to the cervical region (41), it has been speculated that cervical ganglia are generated from the thoracic sympathetic chain (4,42). As there are only 3-4 cervical ganglia in the cervical region whereas at the thoracic level each spinal level has a corresponding ganglion, alternatively, it has been suggested that the development of sympathetic ganglia is associated initially with the intersegmental vessels (43). The limited number of cervical ganglia could in this perspective be attributed to regression of most of the cervical intersegmental arteries, and subsequent remodeling and fusion of the corresponding ganglia. The upper 4 cervical ganglia would thus eventually form the superior cervical sympathetic ganglion, anatomically related or induced by the developing external carotid artery (43). In our review, 2 prenatal studies were included - both performed in chick - that did not show a clear contribution of the SCG to sympathetic innervation in the chick heart during the stages examined. However, as it was observed that the SCG contributes to the (TH+) carotid nerve during development (18), a contribution of the SCG to parasympathetic innervation of the heart, is not excluded.

The superior cervical ganglion (SCG) is a remarkable organ, that has an unique spatial anatomical localisation. It is situated at between the branching point of the common carotid arteries, in close proximity to the carotid body, which it innervates. The innervation pattern however, is much broader than the cardiovascular system alone. Nerve fibers originating from the SCG run along both carotid arteries, and will provide sympathetic input towards the head where it stimulates parts of the eye (iris), mouth and small blood vessels. In this respect, it may be relevant that the SCG is situated adjacent to the above mentioned carotid body (CB), by itself an intriguing structure, involved in oxygen, carbon and pH sensing, that has been shown to produce many neurotrophic factors (44). With regard to cardiovascular disease states, a role of the carotid body in hypertension has been indicated (45). In addition to the spatial relation with the carotid body, there are several studies in literature that indicate a connection of the sympathetic SCG with the parasympathetic nodose ganglion in mouse (11) (**Figure 3**), a finding that was also observed in monkeys in the current review (21). Given this evidence as well as the observation that the SCG contributes to the carotid nerve during development as described above (18), a contribution of the SCG to parasympathetic innervation of the heart, is possible.

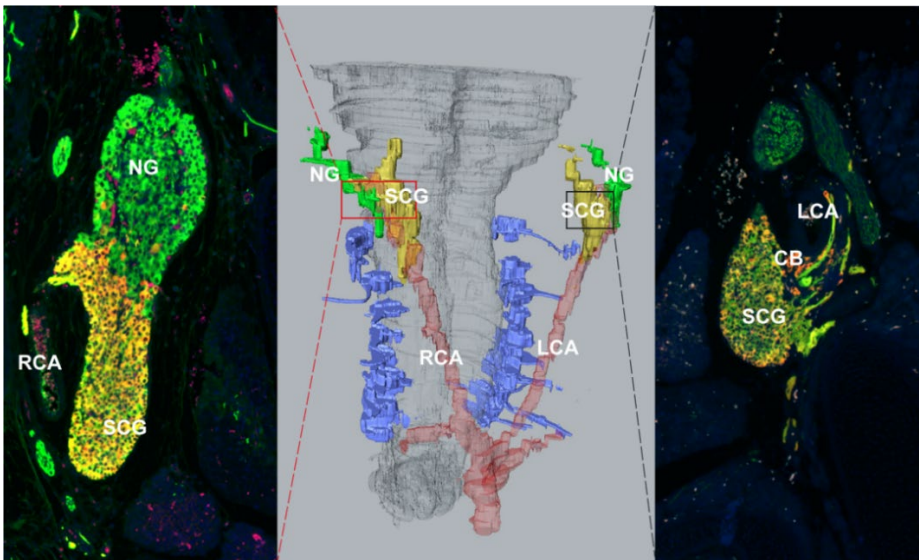
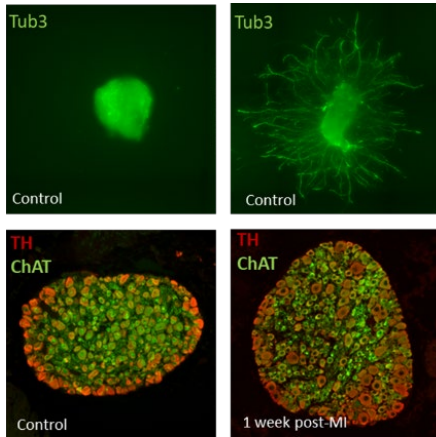


Figure 3. Connection of the sympathetic SCG with the nodose ganglion and carotid body in mouse. The middle panel shows a 3D reconstruction image of an adult mouse spinal cord, carotid arteries (indicated in red), SCG (yellow) and NG (green). SCG, superior cervical ganglion; NG, nodose ganglion; RCA, right carotid artery; LCA, left carotid artery; CB, carotid body.

General discussion of findings in light of the thesis. In Chapter 5 of this thesis, the presence of cholinergic cells in the SCG was described based on histopathological findings in healthy SCG as well as after MI, although the clinical/functional implications are at present unclear. The role of the autonomic nervous system in post-MI arrhythmogenicity has gained increasing attention over the past decades. Vagal innervation is considered as cardioprotective, whereas



At the left, sympathetic ganglion of sham-operated mice. At the right, sympathetic ganglion 7 days after occlusion of the left anterior descending coronary artery. An increase in neurite outgrowth, and remodeling of neuron size and expression (upregulation of TH) can be observed.

a sympathetic overdrive is associated with arrhythmias and sudden cardiac death (48,49). A myriad of studies in human, rat, rabbit and pig, have indicated neuronal and electrical remodeling in the stellate ganglia after MI (50–52). In contrast to the stellate ganglion, data on the time course of neural remodeling in the SCG – as indicated situated in close proximity to carotid body - after MI is still limited. It has been previously reported in rabbits that the response of the chemo sensitive cardiac reflex of the carotid body was enhanced in the acute phase of MI (53), and hypertonicity of the carotid has been linked with cardiac disease such as hypertension and chronic heart failure. In rats with induced chronic heart failure, denervation of the carotid body performed early after MI, resulted in improved

survival due to reduction of ventricular remodeling, diminished fibrosis and reduction of arrhythmias(54). Whether this is only a transient phenomenon is unclear, as is the time-course of remodeling of the SCG and the carotid after MI. Therefore in Chapter 5, we assessed the neuronal remodeling of the murine SCG, including the carotid body, at several time points post-MI. Of interest, we found ganglionic remodeling not only in the SCG, but also in the carotid body, with overt upregulation of expression of several neurotrophic factors. Generally, a remodeling towards a more sympathetic phenotype was observed, which would fit the hypothesis of a higher sympathetic tone underlying cardiac arrhythmogenesis after MI.

The finding of remodeling of SCG after MI, prompted the investigation of the molecular pathways involved in disease states. The exact molecular signature and cellular composition of the SCG in the control/healthy is however, also still largely unexplored. This inspired us to perform RNA sequencing at the single cell level. As our ultimate desire is to translate our findings in animal models to the human situation, we strived for applying a method that can ultimately also be applied on human tissues. In Chapter 6, we describe the development of a method for single-nucleus RNA sequencing (snRNA-seq) of murine ganglia using low-input

nucleus isolation and multiplexing with barcoded antibodies. The advantage of this method is, amongst other practical advantages, the possibility to also apply it to human neurons, that are larger than murine neurons and not suitable for single cell RNA seq. In Chapter 7, we took advantage for this method to study the molecular and genetic signature of the SCG and provide reference data for interpretation of our results of snRNA-seq after MI-R, that is currently ongoing.

Our aim to review the morphological contributions of the SCG to cardiac innervation was partly motivated by the findings of our *in vitro* studies, where we observed that murine embryonic SCG cultured with adult myocardium have a high tendency to sprout towards myocardium. Remarkably, as described in Chapter 2 of this thesis, we show that adding human epicardial derived cells (EPDCs) to our cell cultures, significantly increased this sprouting. Moreover, we found during subsequent studies that the sex of the donor of the EPDC, influenced the length and density of nerve sprouting, with a higher sprouting capacity observed in the presence of male EPDCs, as is described in Chapter 3. We propose the SLIT2/ROBO pathway as a potential candidate involved in these sex-differences observed. This also clinically relevant in light of the increasing attention for differences in presentation and outcome of cardiovascular disease between males and females (55).

Future perspectives. Our next step in studying the relevance of the SCG in health and disease, will be to systematically review the *functional* evidence of contributions of SCG ganglia in cardiac innervation, both *in vivo* and *in vitro*. With regard to the contribution of human EPDCs to cardiac innervation and the role of sex therein, we strive to further study the relevance of the SLIT2 /ROBO pathway. As a next step in the experiments described in Chapter 2 and 3, we aim to further validate our results by performing *SLIT2* knockdown and overexpression in male and female EPDCs and to evaluate the presence of the receptors of SLIT2 (ROBO receptors) on cardiac sympathetic autonomic ganglia, including the SCG. In addition, we strive towards increasingly progressing our experiments to human tissues. As a first step in this approach, taking into account the limited availability of human tissues as well as several other impediments described in Chapter 4, we have developed a human proliferative EPDC cell line (hiEPDCs), to facilitate their use in experiments. The Cardiology dept. of LUMC also houses a human proliferate atrial myocardial cell line (hiACMs), that together with the hiEPDCs provides a promising experimental model for our cardiac innervation studies in health and disease. We ultimately strive to also develop an inducible neuronal cell line (hiNeurons) which will be the focus of future studies. With regard to the experiments mentioned in Chapter 5, our next step will be to further explore the significance of expression of cholinergic factors, by performing i.a. qPCR of SCG and determining levels of catecholamines. With regard to Chapters 6 and 7, our next step will be to explore the molecular and genetic remodeling of SCG on the single

nucleus level after MI. Data presented in Chapter 7 will have an important function to serve as reference in interpretation of these data. In our future experiments with snRNA-seq, we will also take the sex of the donor into account, and aim to explore differential pathways involved in ganglion growth and remodeling in health and disease in both male and female. Finally, our next projects will aim at electrophysiological consequences of neuronal remodeling with regard to arrhythmogenesis.

REFERENCES

1. Wink J, van Delft R, Notenboom RGE, Wouters PF, DeRuiter MC, Plevier JWM, et al. Human adult cardiac autonomic innervation: Controversies in anatomical knowledge and relevance for cardiac neuromodulation. *Auton Neurosci Basic Clin* [Internet]. 2020;227(September 2019):102674. Available from: <https://doi.org/10.1016/j.autneu.2020.102674>
2. Li CY, Li YG. Cardiac Sympathetic Nerve Sprouting and Susceptibility to Ventricular Arrhythmias after Myocardial Infarction. *Cardiol Res Pr*. 2015;2015:1–8.
3. Zipes DP, Rubart M. Neural modulation of cardiac arrhythmias and sudden cardiac death. *Hear Rhythm Off J Hear Rhythm Soc*. 2006;3(1):108.
4. Kawashima T. The autonomic nervous system of the human heart with special reference to its origin, course, and peripheral distribution. *Anat Embryol (Berl)*. 2005;209(6):425–38.
5. Zandstra TE, Notenboom RGE, Wink J, Kiès P, Vliegen HW, Egorova AD, et al. Asymmetry and Heterogeneity: Part and Parcel in Cardiac Autonomic Innervation and Function. *Front Physiol*. 2021;12(September):1–15.
6. Smetana P, Malik M. Sex differences in cardiac autonomic regulation and in repolarisation electrocardiography. *Pflugers Arch Eur J Physiol*. 2013;465(5):699–717.
7. Razipour SE, Zarrintan S, Mathkour M, Iwanaga J, Dumont AS, Shane Tubbs R. Review of the External Carotid plexus: Anatomy, Function, and Clinical Manifestations. *Anat Cell Biol*. 2021;54(2):137–42.
8. De Stefano ME, Leone L, Lombardi L, Paggi P. Lack of dystrophin leads to the selective loss of superior cervical ganglion neurons projecting to muscular targets in genetically dystrophic mdx mice. *Neurobiol Dis*. 2005;20(3):929–42.
9. Fedele MLM, Galiana MD, Golombek DA, Muñoz EM, Plano SA. Alterations in metabolism and diurnal rhythms following bilateral surgical removal of the superior cervical ganglia in rats. *Front Endocrinol (Lausanne)*. 2018;8(JAN):1–10.
10. Brognara F, Felipe ISA, Salgado HC, Paton JFR. Autonomic innervation of the carotid body as a determinant of its sensitivity: Implications for cardiovascular physiology and pathology. *Cardiovasc Res*. 2021;117(4):1015–32.
11. Bookout AL, Gautron L. Characterization of a cell bridge variant connecting the nodose and superior cervical ganglia in the mouse: Prevalence, anatomical features, and practical implications. *J Comp Neurol*. 2021;529(1):111–28.
12. Ge Y, Smits AM, van Munsteren JC, Gittenberger-de Groot AC, Poelmann RE, van Brakel TJ, et al. Human epicardium-derived cells reinforce cardiac sympathetic innervation. *J Mol Cell Cardiol* [Internet]. 2020;143:26–37. Available from: <https://doi.org/10.1016/j.yjmcc.2020.04.006>
13. Engele LJ, Mulder BJM, Schoones JW, Kiès P, Egorova AD, Vliegen HW, et al. The coronary arteries in adults after the arterial switch operation: A systematic review. *J Cardiovasc Dev Dis*. 2021;8(9):1–18.
14. Koppel CJ, Jongbloed MRM, Kiès P, Hazekamp MG, Mertens BJA, Schalijs MJ, et al. Coronary anomalies in tetralogy of Fallot – A meta-analysis. *Int J Cardiol*. 2020;306:78–85.
15. Wilke J, Krause F, Niederer D, Engeroff T, Nürnberger F, Vogt L, et al. Appraising the methodological quality of cadaveric studies: Validation of the QUACS scale. *J Anat*. 2015;226(5):440–6.

16. Page MJ, McKenzie JE, Bossuyt PM, Boutron I, Hoffmann TC, Mulrow CD, et al. The PRISMA 2020 statement: An updated guideline for reporting systematic reviews. *BMJ*. 2021;372.
17. Kirby ML, McKenzie JW, Weidman TA. Developing innervation of the chick heart: A histofluorescence and light microscopic study of sympathetic innervation. *Anat Rec*. 1980;196(3):333–40.
18. Verberne ME, Gittenberger-De Groot AC, Van Iperen L, Poelmann RE. Contribution of the cervical sympathetic ganglia to the innervation of the pharyngeal arch arteries and the heart in the chick embryo. *Anat Rec*. 1999;255(4):407–19.
19. Kawashima T, Sasaki H. Morphological comparison of the cardiac autonomic nervous system between normal and abnormal great arterial branching pattern with a brief review of the literature. *Auton Neurosci Basic Clin*. 2007;132(1–2):37–43.
20. Hopkins DA, Armour JA. Localization of sympathetic postganglionic and parasympathetic preganglionic neurons which innervate different regions of the dog heart. *J Comp Neurol*. 1984;229(2):186–98.
21. Billman GE, Dickey DT, Stone HL. A description of the upper thoracic autonomic nervous system in the rhesus monkey (*Macaca mulatta*). *Am J Primatol*. 1982;2(2):159–66.
22. Shih CJ, Chuang KS, Tsai SH, Liu JC. Horseradish peroxidase localization of the sympathetic postganglionic neurons innervating the cat heart. *J Auton Nerv Syst*. 1985;13(3):179–89.
23. Janes RD, Christopher Brandys J, Hopkins DA, Johnstone DE, Murphy DA, Armour JA. Anatomy of human extrinsic cardiac nerves and ganglia. *Am J Cardiol*. 1986;57(4):299–309.
24. Wu JJ, Chuang KS, Shih CJ, Liu JC. Sympathetic postganglionic innervation of the cardiac coronary artery in cats. *J Auton Nerv Syst*. 1988;24(3):215–20.
25. Pardini BJ, Lund DD, Schmid PG. Organization of the sympathetic postganglionic innervation of the rat heart. *J Auton Nerv Syst*. 1989;28(3):193–201.
26. Chuang KS, Liu JC, Liu NH, Lin MT. Localization of the sympathetic postganglionic neurons innervating cardiac coronary artery with horseradish peroxidase in monkeys. *Chin J Physiol*. 1992;35(3):219–26.
27. Hirakawa N, Morimoto M, Totoki T. Sympathetic innervation of the young canine heart using antero- and retrograde axonal tracer methods. *Brain Res Bull*. 1993;31(6):673–80.
28. Pather N, Partab P, Singh B, Satyapal KS. The sympathetic contributions to the cardiac plexus. *Surg Radiol Anat*. 2003;25(3–4):210–5.
29. Chuang KS, Liu WC, Liou NH, Liu JC. Horseradish peroxidase localization of sympathetic postganglionic and parasympathetic preganglionic neurons innervating the monkey heart. *Chin J Physiol*. 2004;47(2):95–9.
30. Kawashima T, Sasaki H. Topological changes of the human autonomic cardiac nervous system in individuals with a retroesophageal right subclavian artery: Two case reports and a brief review. *Anat Embryol (Berl)*. 2005;210(4):327–34.
31. Kawashima T, Sato K, Akita K, Sasaki H. Comparative anatomical study of the autonomic cardiac nervous system in macaque monkeys. *J Morphol*. 2005;266(1):112–24.
32. Kawashima T. The autonomic nervous system of the human heart with special reference to its origin, course, and peripheral distribution. *Anat Embryol (Berl)*. 2005;209(6):425–38.
33. Tanaka A, Tanaka S, Miyamoto K, Yi SQ, Nakatani T. Gross anatomical study of the sympathetic cardiac nerves in the house musk shrew (*Suncus murinus*). *Anat Rec*. 2007;290(5):468–76.
34. Kawashima T, Thorington RW, Kunimatsu Y, Whatton JF. Systematic morphology and evolutionary anatomy of the autonomic cardiac nervous system in the lesser apes, gibbons (*Hylobatidae*). *Anat Rec*. 2008;291(8):939–59.
35. Kawashima T, Thorington RW, Whatton JF. Comparative anatomy and evolution of the cardiac innervation in new world monkeys (*Platyrrhini*, E. Geoffroy, 1812). *Anat Rec*. 2009;292(5):670–91.

36. Kawashima T, Thorington RW. Comparative Morphological Configuration of the Cardiac Nervous System in Lorises and Galagos (Infraorder Lorisiformes, Strepsirrhini, Primates) with Evolutionary Perspective. *Anat Rec.* 2011;294(3):412–26.
37. Kawashima T, Thorington RW, Murakami K, Sato F. Evolutionary Anatomy and Phyletic Implication of the Extrinsic Cardiac Nervous System in the Philippine Tarsier (*Tarsius syrichta*, Primates) in Comparisons With Strepsirrhines and New World Monkeys. *Anat Rec.* 2013;296(5):798–806.
38. Porzionato A, Macchi V, Stecco C, De Caro R. The Carotid Sinus Nerve—Structure, Function, and Clinical Implications. *Anat Rec.* 2019;302(4):575–87.
39. Armour JA, Hopkins DA. Localization of sympathetic postganglionic neurons of physiologically identified cardiac nerves in the dog. *J Comp Neurol.* 1981;202(2):169–84.
40. Ziegler KA, Ahles A, Wille T, Kerler J, Ramanujam D, Engelhardt S. Local sympathetic denervation attenuates myocardial inflammation and improves cardiac function after myocardial infarction in mice. *Cardiovasc Res.* 2018;114(2):291–9.
41. Sadler TW. Embryology of neural tube development. *Am J Med Genet C Semin Med Genet.* 2005 May;135C(1):2–8.
42. Rubin E. Development of the rat superior cervical ganglion: Ganglion cell maturation. *J Neurosci.* 1985;5(3):673–84.
43. Kanagasuntheram R, Dharshini P. The cervical sympathetic trunk--a new hypothesis. *Ann Acad Med Singapore.* 1994 Nov;23(6):923–8.
44. López-Barneo J, Ortega-Sáenz P, Pardo R, Pascual A, Piruat JL. Carotid body oxygen sensing. *Eur Respir J [Internet].* 2008 Nov 1;32(5):1386 LP – 1398.
45. Abdala AP, McBryde FD, Marina N, Hendy EB, Engelman ZJ, Fudim M, et al. Hypertension is critically dependent on the carotid body input in the spontaneously hypertensive rat. *J Physiol.* 2012 Sep;590(17):4269–77.
46. Debinski W, Kuchel O, Buu NT, Tremblay J, Hamet P. Atrial natriuretic factor constitutes an intrinsic functional unit within superior cervical ganglia of the rat. *Neuroscience.* 1990;36(1):21–6.
47. Debinski W, Kuchel O, Buu NT, Cantin M, Genest J. Atrial natriuretic factor partially inhibits the stimulated catecholamine synthesis in superior cervical ganglia of the rat. *Neurosci Lett.* 1987 Jun;77(1):92–6.
48. Fukuda K, Kanazawa H, Aizawa Y, Ardell JL, Shivkumar K. Cardiac innervation and sudden cardiac death. *Circ Res.* 2015 Jun;116(12):2005–19.
49. Hausenloy DJ, Bøtker HE, Ferdinandy P, Heusch G, Ng GA, Redington A, et al. Cardiac innervation in acute myocardial ischaemia/reperfusion injury and cardioprotection. *Cardiovasc Res.* 2019 Jun;115(7):1167–77.
50. Ajjola OA, Yagishita D, Reddy NK, Yamakawa K, Vaseghi M, Downs AM, et al. Remodeling of stellate ganglion neurons after spatially targeted myocardial infarction: Neuropeptide and morphologic changes. *Hear Rhythm.* 2015 May;12(5):1027–35.
51. Nguyen TP, Sovari AA, Pezhouman A, Iyer S, Cao H, Ko CY, et al. Increased susceptibility of spontaneously hypertensive rats to ventricular tachyarrhythmias in early hypertension. *J Physiol [Internet].* 2016;594(6):1689–707.
52. Han S, Kobayashi K, Joung B, Piccirillo G, Maruyama M, Vinters H V, et al. Electroanatomic remodeling of the left stellate ganglion after myocardial infarction. *J Am Coll Cardiol.* 2012 Mar;59(10):954–61.
53. Rocha I, Rosário LB, de Oliveira EI, Barros MA, Silva-Carvalho L. Enhancement of carotid chemoreceptor reflex and cardiac chemosensitive reflex in the acute phase of myocardial infarction of the anesthetized rabbit. *Basic Res Cardiol.* 2003 May;98(3):175–80.
54. Del Rio R, Marcus NJ, Schultz HD. Carotid chemoreceptor ablation improves survival in heart failure: rescuing autonomic control of cardiorespiratory function. *J Am Coll Cardiol.* 2013 Dec;62(25):2422–30.

55. E. Davis, D.A. Gorog, C. Rihal, A. Prasad, M. Srinivasan, "Mind the gap" acute coronary syndrome in women: A contemporary review of current clinical evidence, *Int J Cardiol* 227 (2017) 840-849.

SUPPLEMENTAL FILES

Appendix A: Query

Date: 7-10-2021.

Databases:

PubMed

<http://www.ncbi.nlm.nih.gov/pubmed?otool=leiden>

Triple strategy:

- Superior cervical ganglion (main subject) & Heart
- Superior cervical ganglion & Heart innervation
- Superior cervical ganglion & Heart & Nerve Growth Factors

```
((("Superior Cervical Ganglion"[majr] OR "superior cervical ganglion"[ti] OR "superior cervical ganglia"[ti] OR "superior cervical gangli*" [ti] OR "ganglion cervicale superius"[ti] OR "ganglion cervical superior"[ti] OR "ganglion cervicale"[ti]) AND ("Heart"[mesh] OR "Cardiovascular System"[mesh] OR "Cardiovascular"[tw] OR "Cardiac"[tw] OR "myocardial"[tw] OR "Heart"[tw] OR "Heart Diseases"[mesh] OR "Cardiovascular Diseases"[mesh] OR "Arrhythmia"[tw] OR "Myocardial infarction"[tw] OR "cardiac overload"[tw] OR "cardiac damage"[tw] OR "heart failure"[tw] OR "cardiac damage"[tw] OR "myocardial reperfusion"[tw] OR "cardiac innervation"[tw] OR "arrhythmias"[tw] OR "atrial"[tw] OR "ventricular"[tw])) OR ((("Superior Cervical Ganglion"[Mesh] OR "superior cervical ganglion"[tw] OR "superior cervical ganglia"[tw] OR "superior cervical gangli*" [tw] OR "ganglion cervicale superius"[tw] OR "ganglion cervical superior"[tw] OR "ganglion cervicale"[tw]) AND ("Heart/innervation"[majr])) OR (("Superior Cervical Ganglion"[Mesh] OR "superior cervical ganglion"[tw] OR "superior cervical ganglia"[tw] OR "superior cervical gangli*" [tw] OR "ganglion cervicale superius"[tw] OR "ganglion cervical superior"[tw] OR "ganglion cervicale"[tw]) AND ("Heart"[mesh] OR "Cardiovascular System"[mesh] OR "Cardiovascular"[tw] OR "Cardiac"[tw] OR "myocardial"[tw] OR "Heart"[tw] OR "Heart Diseases"[mesh] OR "Cardiovascular Diseases"[mesh] OR "Arrhythmia"[tw] OR "Myocardial infarction"[tw] OR "cardiac overload"[tw] OR "cardiac damage"[tw] OR "heart failure"[tw] OR "cardiac damage"[tw] OR "myocardial reperfusion"[tw] OR "cardiac innervation"[tw] OR "arrhythmias"[tw] OR "atrial"[tw] OR "ventricular"[tw]) AND ("Nerve Growth Factors"[Mesh] OR "Nerve Growth Factors"[tw] OR "Nerve Growth Factor"[tw] OR "Neurite Outgrowth Factor"[tw] OR "Neurite Outgrowth Factors"[tw] OR "Neuronal Growth Associated Protein"[tw] OR "Neuronal Growth Associated Proteins"[tw] OR "Neuronotrophic Factor"[tw] OR "Neuronotrophic Factors"[tw] OR "Neurotrophic Factor"[tw] OR "Neurotrophic Factors"[tw] OR "Neurotrophic Protein"[tw] OR "Neurotrophic Proteins"[tw] OR "Neurotrophin"[tw] OR "Neurotrophins"[tw] OR "Glia Maturation Factor"[tw] OR "Glia Maturation Factors"[tw] OR "Glial Cell Line-Derived Neurotrophic Factor"[tw] OR "Glial Cell Line-Derived Neurotrophic Factors"[tw] OR "Nerve Growth Factor"[tw] OR "Nerve Growth Factors"[tw] OR "Netrin"[tw] OR "Netrin-1"[tw] OR "Netrins"[tw])
```

OR "Neuregulin"[tw] OR "Neuregulin-1"[tw] OR "Neuregulins"[tw] OR "Neurotrophin 3"[tw] OR "Neurturin"[tw] OR "Neurturins"[tw]))

Embase. <http://ovidsp.ovid.com/ovidweb.cgi?T=JS&PAGE=main&MODE=ovid&D=oemezd>

((("Superior Cervical Ganglion"/ OR "superior cervical ganglion".ti OR "superior cervical ganglia".ti OR "superior cervical gangli*".ti OR "ganglion cervicale superius".ti OR "ganglion cervical superior".ti OR "ganglion cervicale".ti) AND (exp *"Heart"/ OR exp *"Cardiovascular System"/ OR "Cardiovascular".ti,ab OR "Cardiac".ti,ab OR "myocardial".ti,ab OR "Heart".ti,ab OR exp *"Heart Disease"/ OR exp *"Cardiovascular Disease"/ OR "Arrhythmia".ti,ab OR "Myocardial infarction".ti,ab OR "cardiac overload".ti,ab OR "cardiac damage".ti,ab OR "heart failure".ti,ab OR "cardiac damage".ti,ab OR "myocardial reperfusion".ti,ab OR "cardiac innervation".ti,ab OR "arrhythmias".ti,ab OR "atrial".ti,ab OR "ventricular".ti,ab)) OR ((("Superior Cervical Ganglion"/ OR "superior cervical ganglion".ti,ab OR "superior cervical ganglia".ti,ab OR "superior cervical gangli*".ti,ab OR "ganglion cervicale superius".ti,ab OR "ganglion cervical superior".ti,ab OR "ganglion cervicale".ti,ab) AND (exp *"Heart"/ OR exp *"Cardiovascular System"/ OR "Cardiovascular".ti,ab OR "Cardiac".ti,ab OR "myocardial".ti,ab OR "Heart".ti,ab OR exp *"Heart Disease"/ OR exp *"Cardiovascular Disease"/ OR "Arrhythmia".ti,ab OR "Myocardial infarction".ti,ab OR "cardiac overload".ti,ab OR "cardiac damage".ti,ab OR "heart failure".ti,ab OR "cardiac damage".ti,ab OR "myocardial reperfusion".ti,ab OR "cardiac innervation".ti,ab OR "arrhythmias".ti,ab OR "atrial".ti,ab OR "ventricular".ti,ab) AND (exp *"neurotrophic factor"/ OR *"Nerve Growth Factor"/ OR "Nerve Growth Factors".ti,ab OR "Nerve Growth Factor".ti,ab OR "Neurite Outgrowth Factor".ti,ab OR "Neurite Outgrowth Factors".ti,ab OR "Neuronal Growth Associated Protein".ti,ab OR "Neuronal Growth Associated Proteins".ti,ab OR "Neuronotrophic Factor".ti,ab OR "Neuronotrophic Factors".ti,ab OR "Neurotrophic Factor".ti,ab OR "Neurotrophic Factors".ti,ab OR "Neurotrophic Protein".ti,ab OR "Neurotrophic Proteins".ti,ab OR "Neurotrophin".ti,ab OR "Neurotrophins".ti,ab OR "Glia Maturation Factor".ti,ab OR "Glia Maturation Factors".ti,ab OR "Glial Cell Line-Derived Neurotrophic Factor".ti,ab OR "Glial Cell Line-Derived Neurotrophic Factors".ti,ab OR "Nerve Growth Factor".ti,ab OR "Nerve Growth Factors".ti,ab OR "Netrin".ti,ab OR "Netrin-1".ti,ab OR "Netrins".ti,ab OR "Neuregulin".ti,ab OR "Neuregulin-1".ti,ab OR "Neuregulins".ti,ab OR "Neurotrophin 3".ti,ab OR "Neurturin".ti,ab OR "Neurturins".ti,ab))) NOT (conference review or conference abstract).pt

Web of Science. <http://isiknowledge.com/wos>

((("Superior Cervical Ganglion" OR "superior cervical ganglion" OR "superior cervical ganglia" OR "superior cervical gangli*" OR "ganglion cervicale superius" OR "ganglion cervical superior" OR "ganglion cervicale") AND (ti=("Heart" OR "Cardiovascular System" OR "Cardiovascular" OR "Cardiac" OR "myocardial" OR "Heart" OR "Heart Disease" OR "Cardiovascular Disease" OR "Arrhythmia" OR "Myocardial infarction" OR "cardiac overload" OR "cardiac damage" OR "heart failure" OR "cardiac damage" OR "myocardial reperfusion" OR "cardiac innervation" OR "arrhythmias" OR "atrial" OR "ventricular") OR ab=("Heart" OR "Cardiovascular System" OR "Cardiovascular" OR "Cardiac" OR "myocardial" OR "Heart" OR "Heart Disease" OR "Cardiovascular Disease" OR "Arrhythmia" OR "Myocardial infarction" OR "cardiac overload" OR "cardiac damage" OR "heart failure" OR "cardiac damage" OR "myocardial reperfusion" OR "cardiac innervation" OR "arrhythmias" OR "atrial" OR "ventricular")))) OR ((("Superior Cervical Ganglion" OR "superior cervical ganglion" OR "superior cervical ganglia" OR "superior cervical gangli*" OR "ganglion cervicale superius" OR "ganglion cervical superior" OR "ganglion cervicale") OR ab=("Superior Cervical Ganglion" OR "superior cervical ganglion" OR "superior cervical ganglia" OR "superior cervical gangli*" OR "ganglion cervicale superius" OR "ganglion cervical superior" OR "ganglion cervicale")) AND (ti=("Heart" OR "Cardiovascular System" OR "Cardiovascular" OR "Cardiac" OR "myocardial" OR "Heart" OR "Heart Disease" OR "Cardiovascular

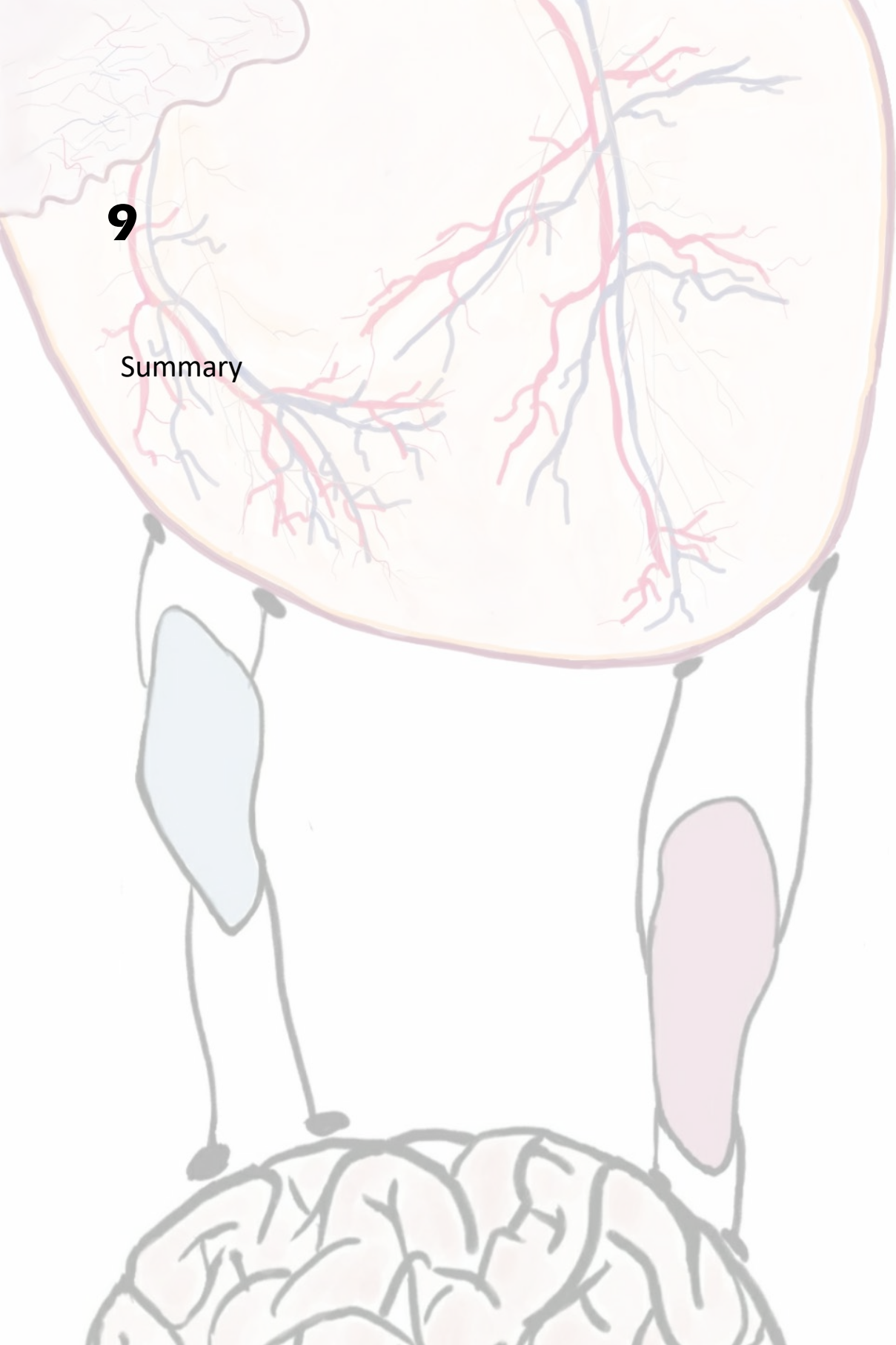
Disease" OR "Arrhythmia" OR "Myocardial infarction" OR "cardiac overload" OR "cardiac damage" OR "heart failure" OR "cardiac damage" OR "myocardial reperfusion" OR "cardiac innervation" OR "arrhythmias" OR "atrial" OR "ventricular") OR ab=("Heart" OR "Cardiovascular System" OR "Cardiovascular" OR "Cardiac" OR "myocardial" OR "Heart" OR "Heart Disease" OR "Cardiovascular Disease" OR "Arrhythmia" OR "Myocardial infarction" OR "cardiac overload" OR "cardiac damage" OR "heart failure" OR "cardiac damage" OR "myocardial reperfusion" OR "cardiac innervation" OR "arrhythmias" OR "atrial" OR "ventricular")) AND (ti=("neurotrophic factor" OR "Nerve Growth Factor" OR "Nerve Growth Factors" OR "Nerve Growth Factor" OR "Neurite Outgrowth Factor" OR "Neurite Outgrowth Factors" OR "Neuronal Growth Associated Protein" OR "Neuronal Growth Associated Proteins" OR "Neuronotrophic Factor" OR "Neuronotrophic Factors" OR "Neurotrophic Factor" OR "Neurotrophic Factors" OR "Neurotrophic Protein" OR "Neurotrophic Proteins" OR "Neurotrophin" OR "Neurotrophins" OR "Glia Maturation Factor" OR "Glia Maturation Factors" OR "Glial Cell Line-Derived Neurotrophic Factor" OR "Glial Cell Line-Derived Neurotrophic Factors" OR "Nerve Growth Factor" OR "Nerve Growth Factors" OR "Netrin" OR "Netrin-1" OR "Netrins" OR "Neuregulin" OR "Neuregulin-1" OR "Neuregulins" OR "Neurotrophin 3" OR "Neurturin" OR "Neurturins") OR ab=("neurotrophic factor" OR "Nerve Growth Factor" OR "Nerve Growth Factors" OR "Nerve Growth Factor" OR "Neurite Outgrowth Factor" OR "Neurite Outgrowth Factors" OR "Neuronal Growth Associated Protein" OR "Neuronal Growth Associated Proteins" OR "Neuronotrophic Factor" OR "Neuronotrophic Factors" OR "Neurotrophic Factor" OR "Neurotrophic Factors" OR "Neurotrophic Protein" OR "Neurotrophic Proteins" OR "Neurotrophin" OR "Neurotrophins" OR "Glia Maturation Factor" OR "Glia Maturation Factors" OR "Glial Cell Line-Derived Neurotrophic Factor" OR "Glial Cell Line-Derived Neurotrophic Factors" OR "Nerve Growth Factor" OR "Nerve Growth Factors" OR "Netrin" OR "Netrin-1" OR "Netrins" OR "Neuregulin" OR "Neuregulin-1" OR "Neuregulins" OR "Neurotrophin 3" OR "Neurturin" OR "Neurturins")))) NOT dt=(meeting abstract)

Cochrane. <https://www.cochranelibrary.com/advanced-search/search-manager>

((("Superior Cervical Ganglion" OR "superior cervical ganglion" OR "superior cervical ganglia" OR "superior cervical gangli*" OR "ganglion cervicale superius" OR "ganglion cervical superior" OR "ganglion cervicale") AND ("Heart" OR "Cardiovascular System" OR "Cardiovascular" OR "Cardiac" OR "myocardial" OR "Heart" OR "Heart Disease" OR "Cardiovascular Disease" OR "Arrhythmia" OR "Myocardial infarction" OR "cardiac overload" OR "cardiac damage" OR "heart failure" OR "cardiac damage" OR "myocardial reperfusion" OR "cardiac innervation" OR "arrhythmias" OR "atrial" OR "ventricular"))):ti,ab,kw

9

Summary



Summary

About one third of all global deaths are attributed to cardiovascular diseases (World Health Organization 2017). Sudden cardiac death (SCD) is a worldwide public health challenge and is commonly associated with ischemic heart disease. SCD after myocardial infarction (MI) is classically attributed to heterogeneous conduction in the infarct border zone. However autonomic hyperinnervation (especially sympathetic hyperinnervation) after MI has also been related to sudden cardiac death in a myriad of reports. The heart is innervated by the autonomic nervous system, which can be divided into sympathetic and parasympathetic parts. The balance between cardiac sympathetic and parasympathetic innervation is critical for maintaining normal cardiac function. Excessive sympathetic activation can be pro-arrhythmogenic. Post-MI hyperinnervation is most often linked to an increase of sympathetic nerve sprouting, which has been discovered in both patients and animal models. This phenomenon of post-MI sympathetic hyperinnervation has raised growing awareness on the important role of pathological innervation patterns in arrhythmogenesis, however the mechanism is not clear yet.

In **Chapter 1**, a general introduction to this thesis is provided. The heart is a self-excitation organ and is composed of three layers, from outermost to innermost the epicardium, myocardium and endocardium are encountered. Although the outer layer, the epicardium is a thin layer of cells, it plays an essential role in cardiac development. During development, epicardium-derived cells (EPDCs) can migrate into the subepicardial space and differentiate into several cardiac cell types. In addition, they have the ability to influence myocardial growth and coronary vessel patterning via paracrine effects. The cardiac autonomic nervous system, another critical element of a functional heart, regulates heart rate, contraction force and atrioventricular conduction velocity to adjust the body's adaption to different conditions. In this chapter, the development of epicardium and cardiac autonomic nervous system is introduced, as well as their dynamic changes in cardiac diseases, such as MI.

In **Chapter 2**, the role of EPDCs in promoting cardiac sympathetic re-/hyperinnervation after cardiac damage is elucidated *in vitro*. Sympathetic ganglia were co-cultured with mesenchymal EPDCs and/or myocardium, and neurite outgrowth and sprouting density were assessed. A significant increase in neurite density and directional (i.e. towards myocardium) outgrowth was observed when ganglia were co-cultured with a combination of EPDCs and myocardium, as compared to cultures with EPDCs or myocardium alone. The promotional effect of mesenchymal EPDCs on sympathetic neurite sprouting via paracrine signaling was confirmed by culturing PC12 cells in conditioned EPDC-medium, and a role of NGF, Endothelin-1 and SEMA3A in the process was also demonstrated in this study.

In **Chapter 3**, the influence of the sex of the donor that EPDCs are derived from on cardiac sympathetic innervation was studied. Co-cultures were performed of sympathetic ganglia with myocardium and activated EPDCs. Combinations of both male and female cellular components were included in the co-cultures to elucidate the impact of sex on cardiac sympathetic re-/hyperinnervation *in vitro*. The key findings include: i) EPDCs promote sympathetic neurite outgrowth *in vitro* and increase the directional neurite projection towards myocardium; ii) In the presence of EPDCs, male sympathetic ganglia exhibit higher cardiac sympathetic outgrowth than female ganglia; iii) Male EPDCs in a female setting can increase the cardiac sympathetic neurite outgrowth to a level that is comparable to the level of outgrowth in an entirely male environment. We propose the Slit2/ROBO-pathway as a potential candidate influencing these differential findings in male and female EPDCs. The findings in this chapter underline the potential relevance of sex differences in post-MI cardiac hyperinnervation. These data also suggest that sex should be taken into account when considering injection of cells for cell therapy in male and female patients.

In **Chapter 4**, an polyclonal line of inducible proliferative human EPDCs (iEPDCs) was established to facilitate in-vitro study using EPDCs, such as exploring the mechanism of their impact on cardiac sympathetic outgrowth. Inducible proliferation was achieved by doxycycline-controlled expression of simian virus 40 large T antigen (LT) with a repressor-based lentiviral Tet-On system. After doxycycline removal, LT expression ceased and the iEPDCs regained their cuboidal epithelial morphology and could undergo epithelial-to-mesenchymal transition (EMT) after stimulation with transforming growth factor β 3, similar as primary EPDCs. This was confirmed by RT-qPCR analysis and (immune)cytochemical staining. Collagen gel-based cell invasion assays demonstrated that mesenchymal iEPDCs, like primary EPDCs, possess increased invasion and migration capacities as compared to their epithelial counterparts. In addition, mesenchymal iEPDCs stimulated sympathetic neurite outgrowth similarly to primary EPDCs. This renders iEPDCs a highly useful new model for studying human epicardial properties *in vitro*.

Post-MI sympathetic hyperinnervation is most often linked to an increase of sympathetic nerve sprouting from cardiac sympathetic ganglia. In **Chapter 5**, the remodeling process of cardiac sympathetic ganglia after MI was explored. The superior cervical ganglia (SCG), situated adjacent to the carotid body (CB), contribute to cardiac ventricular sympathetic innervation. Remodeling of SCG at 24 hours, 3 days, 7 days and 6 weeks after MI was investigated with histological evaluation. SCG remodeling was observed as early as 24 hours after infarction, with a peak at day 7, regressing within 6 weeks post-MI to basal levels with a significant increase in neuron size and a decreased intensity of ChAT expression. Moreover, the most robust neuronal remodeling was observed at the region adjacent to the CB with an

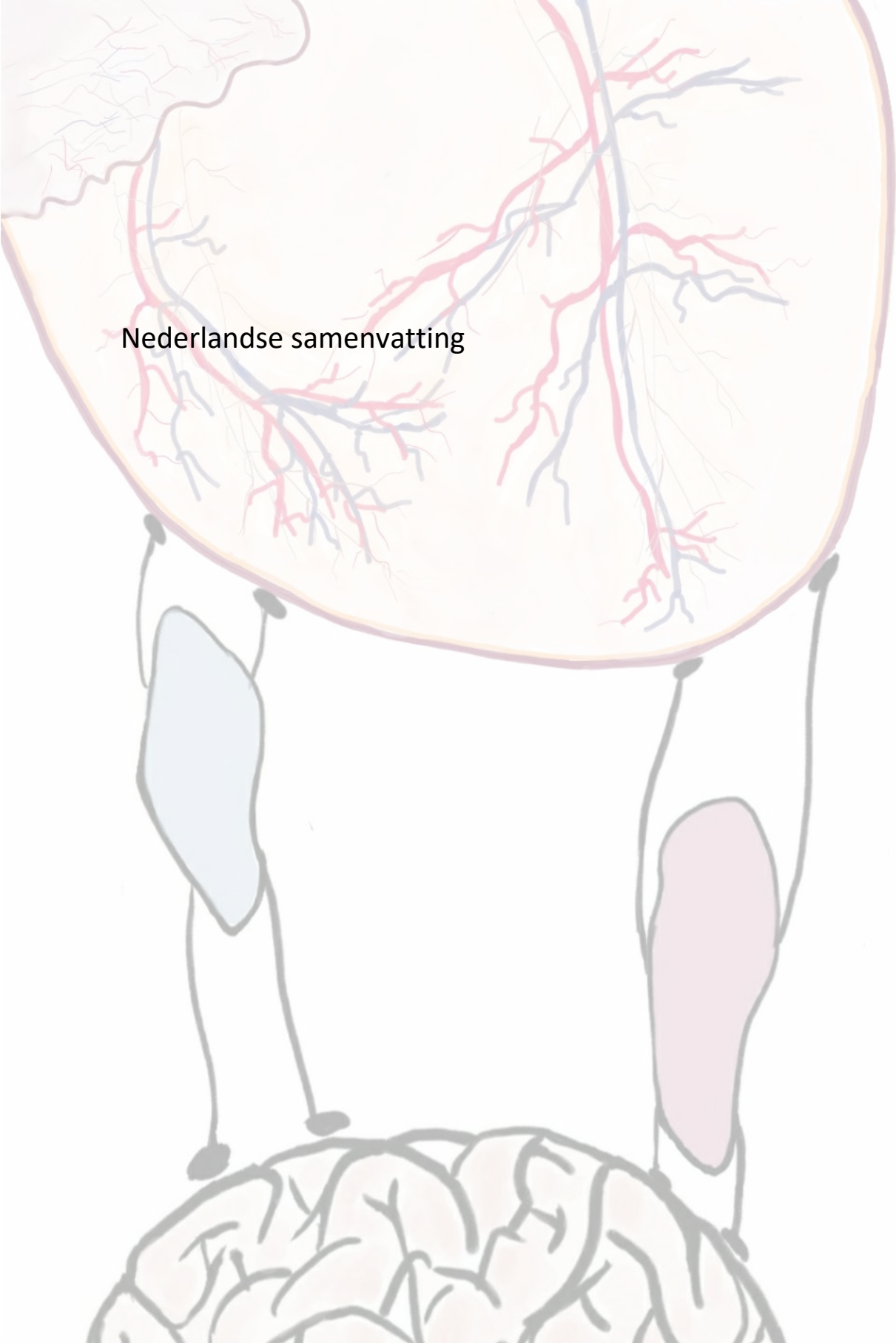
increase of neurotrophic factors. Furthermore, the high affinity receptors of BDNF and NGF increased in the SCG after MI. We concluded that overt remodeling occurs in the SCG as well as in the CB, suggesting an interaction of these 2 structures after MI, that might contribute to pathological cardiac hyperinnervation.

Chapter 6 describes a detailed low-input sample preparation method for single-nucleus sequencing, which includes the dissection of mouse superior cervical and stellate ganglia, cell dissociation, cryo-preservation, nucleus isolation and hashtag barcoding. The method has the potential for broad application also in studies of innervation of other organs and tissues.

Chapter 7 applies the method described in Chapter 6 to explore SCG remodeling after MI with single nucleus RNA sequencing (snRNA-seq) technology. snRNA-seq of healthy murine SCGs was performed, creating a template of the cellular composition of the SCG. The molecular signatures of neuronal and satellite glial cells at healthy baseline were identified, which will be utilized for investigation of disease models in future studies.

Chapter 8 provides a systematic review of current morphological evidence on the contribution of the SCG to cardiac innervation in health and disease in human and other animal models. A general discussion in relation to the work presented in this thesis, is also included in this chapter.

Nederlandse samenvatting



Samenvatting

Ongeveer een derde van alle sterfgevallen wereldwijd wordt toegeschreven aan hart- en vaatziekten (World Health Organization 2017). Plotse hartdood is een significante uitdaging voor de volksgezondheid en wordt vaak geassocieerd met ischemische hartziekte. Plotse hartdood na een myocardinfarct (MI) wordt klassiek toegeschreven aan heterogene geleiding in het grensgebied van het infarct. Autonome hyperinnervatie (vooral sympathische hyperinnervatie) na MI is echter ook in verband gebracht met plotse hartdood in een toenemend aantal artikelen. Het hart wordt geïnnerveerd door het autonome zenuwstelsel, dat kan worden onderverdeeld in een sympathische en een parasympatische component. De balans tussen cardiale sympathische en parasympatische innervatie is van cruciaal belang voor het behoud van een normale hartfunctie. Overmatige sympathische activatie kan pro-aritmogeen zijn. Post-MI hyperinnervatie is meestal geassocieerd met een toename van sympathische zenuwen, hetgeen is beschreven bij zowel mensen als in diermodellen. Dit fenomeen van post-MI sympathische hyperinnervatie heeft geleid tot een groeiend bewustzijn van de belangrijke rol van pathologische innervatiepatronen in aritmogenese, echter de onderliggende mechanismen zijn nog onduidelijk.

In **hoofdstuk 1** wordt een algemene inleiding van het proefschrift gegeven. Het hart is een zelf exciterend orgaan dat is opgebouwd in drie lagen, van buiten naar binnen: het epicardium, het myocardium en het endocardium. Hoewel de buitenste laag, het epicardium, slechts een dunne laag cellen is, speelt het een essentiële rol bij de ontwikkeling van het hart. Tijdens de ontwikkeling kunnen van epicardium afgeleide cellen (EPDCs) migreren naar de subepicardiale ruimte en differentiëren in verschillende hartceltypen. Bovendien hebben ze het vermogen om de myocardiële groei en coronaire vaatpatronen te beïnvloeden via paracrine effecten. Het cardiale autonome zenuwstelsel, zoals hierboven beschreven een ander cruciaal element van een functioneel hart, reguleert de hartslag, contractiekracht en atrioventriculaire geleidingssnelheid om de functie van het hart aan verschillende omstandigheden aan te passen. In dit inleidende hoofdstuk worden de ontwikkeling van het epicardium en het cardiale autonome zenuwstelsel geïntroduceerd, evenals hun dynamische veranderingen tijdens hartziekten, zoals MI.

In **Hoofdstuk 2** wordt de rol van EPDCs in het bevorderen van cardiale sympathische re-/hyperinnervatie na hartschade *in vitro* toegelicht. Sympathische ganglia werden samen gekweekt met mesenchymale EPDCs en/of myocardium, en de uitgroei van neurieten en de dichtheid van zenuwuitlopers werden beoordeeld. Een significante toename in neurietdichtheid en een directionele (d.w.z. naar het myocardium toe) uitgroei werd waargenomen wanneer ganglia samen werden gekweekt met een combinatie van EPDCs en myocardium, in vergelijking met kweken met EPDCs of myocardium alleen. Het bevorderende

effect van mesenchymale EPDCs op de uitgroei van sympathische neurieten via paracrine signalering werd bevestigd door het kweken van PC12-cellen in geconditioneerd EPDC-medium. Eveneens werd in deze studie een rol van NGF, Endothelin-1 en SEMA3A in dit proces aangetoond.

In **Hoofdstuk 3** werd de invloed van het geslacht van de donor van de EPDCs op cardiale sympathische innervatie bestudeerd. Co-culturen werden uitgevoerd van sympathische ganglia met myocardium en geactiveerde EPDCs. Combinaties van zowel mannelijke als vrouwelijke cellulaire componenten werden in de co-culturen opgenomen om de sekse-impact op cardiale sympathische re-/hyperinnervatie *in vitro* op te helderen. De belangrijkste bevindingen waren: i) EPDCs bevorderen de uitgroei van sympathische neurieten *in vitro* en bevorderen de directionele uitgroei van neurieten naar het myocardium; ii) In aanwezigheid van EPDCs vertonen mannelijke sympathische ganglia een hogere cardiale sympathische uitgroei dan vrouwelijke ganglia; iii) Mannelijke EPDCs in een vrouwelijke setting kunnen de uitgroei van cardiale sympathische neurieten verhogen tot een niveau dat vergelijkbaar is met het niveau van uitgroei in een volledig mannelijke omgeving. Tot slot werd de SLIT2/ROBO-pathway voorgesteld als een potentiële kandidaat die deze differentiële bevindingen in mannelijke en vrouwelijke EPDCs beïnvloedt. De bevindingen in dit hoofdstuk ondersteunen de mogelijke relevantie van sekseverschillen bij post-MI cardiale hyperinnervatie. Deze gegevens suggereren ook dat er rekening dient te worden gehouden met geslacht bij eventuele injectie van cellen voor celtherapie bij mannelijke en vrouwelijke patiënten.

In **Hoofdstuk 4** werd een polyclonale lijn van induceerbare proliferatieve humane EPDCs (iEPDCs) opgezet om *in vitro* onderzoek met EPDCs te vergemakkelijken, zoals het onderzoeken van het mechanisme van hun invloed op cardiale sympathische uitgroei. Induceerbare proliferatie werd bereikt door doxycycline-gecontroleerde expressie van simian virus 40 large T antigen (LT) met een op repressie gebaseerd lentiviraal Tet-On-systeem. Na verwijdering van doxycycline stopte de LT-expressie en kregen de iEPDCs hun kubusvormige epitheliale morfologie terug en konden ze epitheliale-naar-mesenchymale overgang (EMT) ondergaan na stimulatie met transforming growth factor β 3, vergelijkbaar met primaire EPDCs. Dit werd bevestigd door RT-qPCR-analyse en (immuun)cytochemische kleuringen. Invasie-tests op een collageengel toonden aan dat mesenchymale iEPDCs, zoals primaire EPDCs, verhoogde invasie- en migratiecapaciteiten bezitten in vergelijking met hun epitheliale tegenhangers. Bovendien stimuleerden mesenchymale iEPDCs de uitgroei van sympathische neurieten op dezelfde manier als primaire EPDCs. Dit maakt iEPDCs tot een zeer nuttig nieuw model voor het bestuderen van menselijke epicardiale eigenschappen *in vitro*.

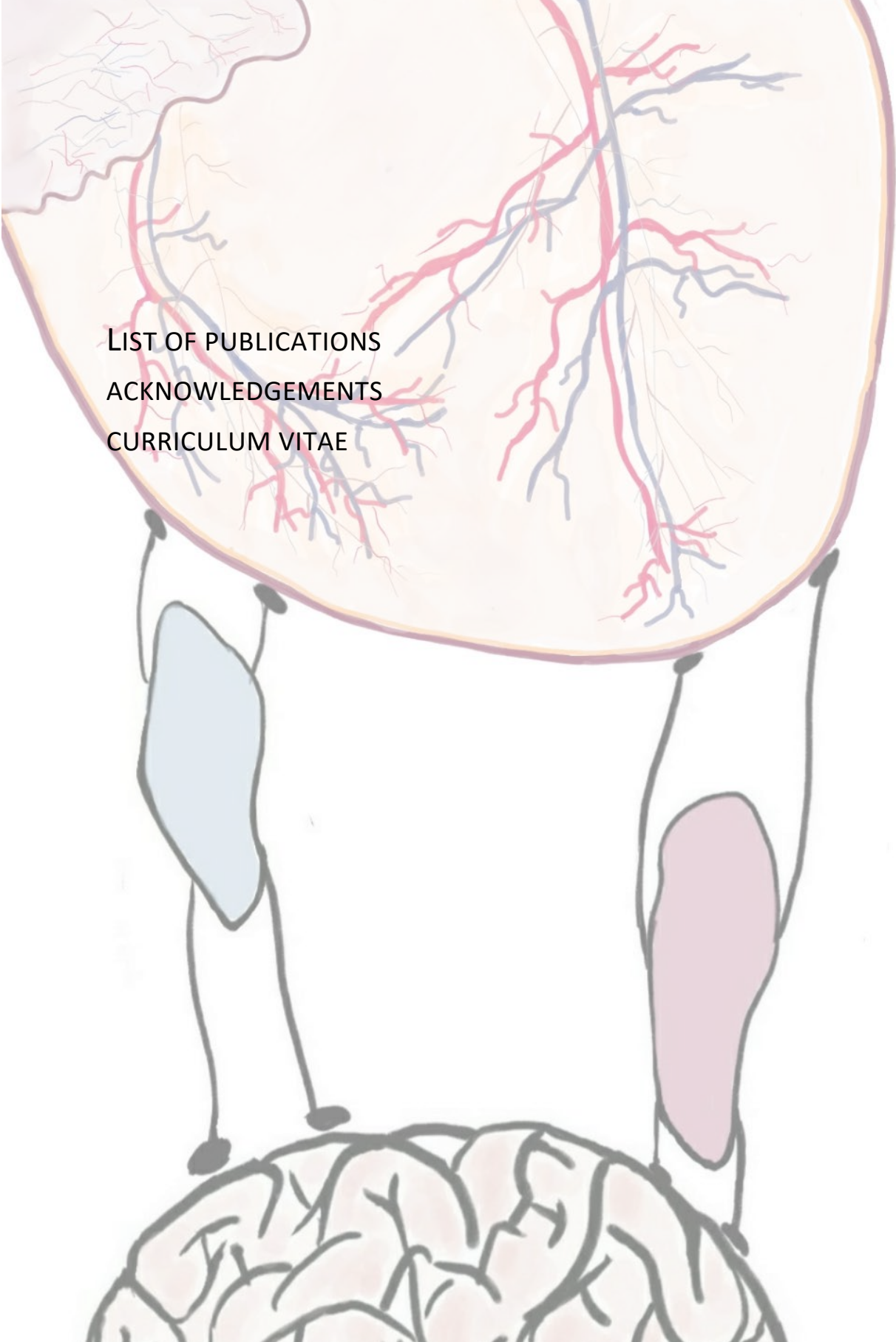
Sympathische hyperinnervatie na een MI wordt meestal in verband gebracht met een toename van de sympathische zenuwen die ontspruiten uit sympathische cardiale ganglia. In

Hoofdstuk 5 werd het remodeleringsproces van cardiale sympathische ganglia na MI onderzocht. De superior cervicale ganglia (SCG), gelegen naast het carotislichaampje, dragen bij aan de cardiale ventriculaire sympathische innervatie. Remodelering van SCG op 24 uur, 3 dagen, 7 dagen en 6 weken na MI werd onderzocht met behulp van histologische evaluatie. SCG-remodelering werd al 24 uur na het infarct waargenomen, met een piek op dag 7, waarna binnen 6 weken na MI het uitgangsniveau weer bereikt werd. De remodelering ging gepaard met een significante toename van de neuron grootte en een verminderde intensiteit van ChAT-expressie. Bovendien werd de meest robuuste neuronale remodelering waargenomen in de regio naast de carotislichaampje met een toename van expressie van neurotrofe factoren ter plaatse. Bovendien namen receptoren met hoge affiniteit voor BDNF en NGF toe in de SCG na MI. We concludeerden dat evidente remodelering optreedt in zowel de SCG als in het carotislichaampje, wat een interactie suggereert van deze 2 structuren na MI, die zou kunnen bijdragen aan pathologische cardiale hyperinnervatie.

In **Hoofdstuk 6** wordt een methode beschreven voor het isoleren van kernen uit een lage hoeveelheid cellen, voor single-nucleus RNA sequencing. Er wordt een stapsgewijze benadering gepresenteerd die het potentieel heeft voor een brede toepassing, onder andere bij het bestuderen van de genetische paden die betrokken zijn bij de innervatie van andere organen en weefsels.

Hoofdstuk 7 past de in Hoofdstuk 6 beschreven methode toe om SCG-remodelering na MI te onderzoeken met behulp van single nucleus RNA sequencing technologie (snRNA-seq). snRNA-seq werd uitgevoerd in SCG van gezonde muizen, waardoor een model van de cellulaire samenstelling van de SCG kon worden gecreëerd. De moleculaire kenmerken van neuronale en satelliet-gliacellen in een gezonde uitgangssituatie werden geïdentificeerd, en zullen verder worden gebruikt voor onderzoek in ziektemodellen in toekomstige studies.

In **Hoofdstuk 8** werd de huidige morfologische kennis met betrekking tot de bijdrage van de SCG aan de cardiale innervatie systematisch gereviewed, zowel in gezonde als in ziektemodellen in dier en de mens. Dit hoofdstuk omvat tevens een algemene discussie met betrekking tot het werk dat in dit proefschrift wordt gepresenteerd.



LIST OF PUBLICATIONS

ACKNOWLEDGEMENTS

CURRICULUM VITAE

PUBLICATIONS

Yang Ge, Anke M. Smits, Jia Liu, Juan Zhang, Daniel Pijnappels, Thomas van Brakel, Marie-José Goumans, Monique RM. Jongbloed, Antoine A.F. de Vries. Generation, characterization and application of inducible proliferative adult human epicardium-derived cells. *Cells*. 2021 Aug 12;10(8):2064.

Alex Neagu, Emiel van Genderen, Irene Escudero, Lucas Verwegen, Dorota Kurek, Johannes Lehmann, Jente Stel, René A. M. Dirks, Guido van Mierlo, Alex Maas, Cindy Eleveld, Yang Ge, Alexander. T. den Dekker, Rutger W. W. Brouwer, Wilfred F. J. van IJcken, Miha Modic, Micha Drukker, Joop H. Jansen, Nicolas C. Rivron, Esther B. Baart, Hendrik Marks & Derk ten Berge. In vitro capture and characterization of embryonic rosette-stage pluripotency between naive and primed states. *Nature Cell Biology*, volume 22, pages534–545 (2020).

Yang Ge, Anke M. Smits, J. Conny van Munsteren, Adriana C. Gittenberger-de Groot, Robert E. Poelmann, Thomas J. van Brakel, Martin J. Schalij, Marie-José Goumans, Marco C. DeRuiter, Monique RM. Jongbloed. Human epicardium-derived cells reinforce cardiac sympathetic innervation. *J Mol Cell Cardiol* 2020 Jun;143:26-37.

Yang Ge, Yiyi Gong, Zhiwei Xu, Yanan Lu, Wei Fu. The Application of Sheet Technology in Cartilage Tissue Engineering. *Tissue Eng Part B Rev*. 2016 Apr;22(2):114-24.

Yongxuan Peng, Yang Ge, Haibo Zhang , Jinfen Liu, Haifa Hong, Yanan Lu. Positional Relationship Between the Pulmonary Venous Confluence-Vertical Vein and Atria in Infracardiac Total Anomalous Pulmonary Venous Connection. *Pediatr Cardiol*. 2016 Feb;37(2):372-7.

Xiaomin He, Bei Feng, Chuanpei Huang, Hao Wang, Yang Ge, Renjie Hu, Meng Yin, Zhiwei Xu, Wei Wang, Wei Fu, Jinghao Zheng. Electrospun gelatin/polycaprolactone nanofibrous membranes combined with a coculture of bone marrow stromal cells and chondrocytes for cartilage engineering. *Int J Nanomedicine*. 2015 Mar 17;10:2089-99.

Under Peer Review Or Revision

Yang Ge, Lieke van Roon, Janine M. van Gils, Conny J Munsteren, Anke M. Smits, Marie-José T. H. Goumans, Marco C. DeRuiter, Monique R.M. Jongbloed. Acute myocardial infarction induces neuronal remodeling in murine superior cervical ganglia. Under revision *Frontiers in cardiovascular medicine*.

Yang Ge, Lieke van Roon, H. Sophia Chen, Ruben Methorst, Martin Paton, Marco C. DeRuiter, Szymon M. Kielbasa, Monique R.M. Jongbloed Low-input nucleus isolation and multiplexing with barcoded antibodies of mouse sympathetic ganglia for single-nucleus RNA sequencing. Under peer review *JOVE*

ACKNOWLEDGEMENTS

First of all, I would like to thank my co-promotor and group leader Dr Jongbloed. Thank you for welcoming me in your group and introducing me a new world of the cardiovascular research in epicardium and cardiac innervation. As a cardiologist and scientific researcher at the same time, although you've always been fully occupied every day, you could always empty your agenda and make some time to provide me enough guidance and discussion. I would also thanks for your trust on me in the past years, which is the foundation of my self-confidence and braveness of telling my thoughts.

I would like to thank my promotor Prof. Dr. De Ruiter (Dept. of Anatomy and Embryology). Thanks for your guidance and worthful suggestions and rephrase in my research discussion.

I would like to thank my promotor Prof. Dr. Schalij (Dept. of Cardiology, LUMC board). Thank you for providing me opportunity to do my PhD study here and thanks for your trust during my research activities in these years.

I would also like to express my great thanks to Prof. Goumans and Dr. Smits (the Dept. of Cell and Chemical Biology). Thanks for your guidance especially in epicardium and molecular biology aspect, and useful suggestions during each-time research discussion.

Dear Dr. de Vries and Dr. Pijnappels, thank you for your collaboration and willingness to share your knowledge in the iEPDCs project. I would also like to thank Juan for her help in the same project and Jia, Mai, Gurpreet, Aniek, Sven, Minka, Balázs, Cindy, Pim, Niels, Tim in the department of Cardiology.

Dear every friendly colleague in the “old” and “new” Department of Anatomy and Embryology. It is really my honor to have been working and hanging out with you together.

Please let me express my great appreciation to every lovely colleague in Jongbloed's group and the Carver group (Sophia, Tjitske, Claire Glashan, Joshua, Ruben, Fleur, Claire Koppel, Tamara, Michiel, Liza, Esther, Tom, Boudewijn, Annemarie, Vera...). A special word of thanks goes to Conny, without whom there would never be so many embryonic ganglia to make my studies come true; Lieke, your wonderful help with quantifying ganglia remodeling, nucleus isolation and best team work ever; Janine, your recent collaboration with the group and willingness to provide your experience and knowledge to help me during my last but critical steps approaching towards this thesis; Bert, your instruction in 3D reconstruction in my first year and your beautiful artwork with sharpening the pictures of this thesis cover.

Another special thank must go to Tessa who worked in the Department of Cell and Chemical Biology. It was quite tough at the beginning of my study as you may still remember, thanks for your experienced skills in EPDCs isolation and the share of the cells to make my research life easier.

Thanks to Szymon Kielbasa, who provided useful suggestions and his expertise in the snRNA-seq project.

My dear paranymp and best friends, Karina and Sophia, we discussed scientific questions and help each other, I really enjoyed the dinners and the Korean drama with you. I will always remember “Horse head and \$3500”...

My dear colleague and best friend Xueying, thanks for sharing your knowledge about single cell data analysis. I also enjoyed our each-time accompany, chatting and dinner together.

My previous supervisor during internship: Dr. Derk ten Berge, you provided me the internship position in your group and I gained a lot of knowledge of not only biological molecular aspects but also the language.

My friends I met in Erasmus Medical Center and Leiden: 张爽, 刘俊, 吴斌, 蔡宗辉, 鲁涛, 丁世豪, Katja, Viola, Oleh, Lettine, Maria, 张肖冰, 曹旭, 杨蔚, 杨晓宇, 罗毅鑫和小徐, 何南南, 王芳, 罗卓艺和欧阳, 王莹, 周恩晨, 马瑾, 宋晓月, 王迪, 段飞波, 赵之涵, 商鹏。

My previous supervisor during master: Prof. Dr. Yanan Lu (鲁亚南) and Dr. Wei Fu (付炜), you initiated my interest in cardiovascular surgery and basic research.

The last but not the least a special word of thanks goes to Thomas Reyna for his wonderful flute teaching.

My dear parents, I could not wish for better parents! 致我最亲爱的父母, 感谢你们这些年来的支持! 致我最亲爱的家人, 我很幸运有你们这些可爱的家人们!

All of the beautiful moments in the past years in LUMC, in the Netherlands, I will never forget...

CURRICULUM VITAE

Yang Ge was born on 22nd of April 1990 in Lanzhou, Gansu province, China, where she finished her high school study in 2008. In the same year she started her clinical medicine study in Weifang Medical University, during which she did her medical internship in Qingdao, Shandong, China. During the internship, she became interested in the congenital heart disease and cardiac development. Therefore, she started her master at the Department of Cardiothoracic Surgery at Shanghai Children's Medical Center, Shanghai Jiao Tong University, Shanghai, China (supervised by Prof. Dr. Y. Lu and Dr. W.Fu). In 2015, she got a scholarship from Shanghai Jiao Tong University to finish her 6-month research internship at the Department of Cell Biology at Erasmus Medical Center, where she obtained knowledge about mouse embryonic stem cells and epiblast stem cells (supervised by Dr. D. ten Berge). In 2016, she finished her master thesis and obtained her master degree of Medicine.

In the same year she finished her master, she decided to move to the Netherlands to continue her studying and research activity. She started to work as a PhD student at the Department of Anatomy & Embryology and the Department of Cardiology at Leiden University Medical Center (LUMC) (promotors: Prof. Dr. M.C. DeRuiter and Prof. Dr. M.J. Schalij; co-promotor: Dr. M.R.M. Jongbloed). Her research focused on cardiac innervation, especially the (re)modeling of cardiac sympathetic innervation (after cardiac damage) and the contribution of the epicardium/epicardium-derived cells during this process. The work is presented in this thesis.

She will start her resident training of Pediatric Surgeon at the Xinhua hospital, Shanghai, China in January 2022. She aspires to become a pediatric cardiothoracic surgeon after resident training and keep active in cardiac research.